Dissertation
submitted to the
Combined Faculties for the Natural Sciences and for Mathematics
of the Ruperto-Carola University of Heidelberg, Germany
for the degree of
Doctor of Natural Sciences

presented by

Diplom-Physiker Martin Haas
born in Freiburg im Breisgau, Germany

Oral examination: July 5th, 2006

Theory Advances

in

High-Precision Two-Photon Spectroscopy

Referees: **Prof. Dr. Christoph H. Keitel**

Prof. Dr. Markus K. Oberthaler

Zusammenfassung

Die Hochpräzisionsspektroskopie von Zweiphotonübergängen in Wasserstoff und wasserstoffartigen Systemen stellt ein außergewöhnliches Instrument für experimentelle Tests fundamentaler Theorien dar. In der Analyse dieser Experimente spielt die theoretische Physik eine wichtige Rolle bei der Modellierung zeitaufgelöster Spektren, der Berechnung präziser Übergangsmatrixelemente und der Korrektur systematischer Effekte. In dieser Arbeit wird die für diese Experimente relevante Zweiphotonen-Anregungsdynamik detailliert untersucht, ausgehend von der Dynamik eines einzelnen Atoms bis hin zu einem Monte Carlo Modell, das zur Analyse von Atomstrahlexperimenten verwendet werden kann. Die dynamischen Polarisierbarkeiten der entsprechenden S– und D–Zustände, die die Größe des dynamischen Stark Effekts bestimmen, und die zugehörigen Übergangsmatrixelemente werden berechnet. Dabei werden relativistische Korrekturen, Strahlungskorrekturen und Korrekturen zur Laserfeld-Dipolnäherung jeweils in führender Ordnung berücksichtigt. Ein wichtiger verbreiternder Effekt auf die experimentell beobachteten Spektren der $1S$–$2S$ Wasserstoffspektroskopie am Max–Planck–Institut für Quantenoptik (MPQ) wird identifiziert und quantitativ beschrieben, ebenso wie systematische Effekte, die frequenzverschiebend wirken. Es werden entsprechende mögliche Verbesserungen des Versuchsaufbaus vorgeschlagen. Durch Verknüpfung der Ergebnisse wiederholter MPQ-Messungen der Wasserstoff $1S$–$2S$ Absolutfrequenz mit Resultaten anderer Experimente, werden in Zusammenarbeit mit der Forschungsgruppe des MPQ unabhängige und stringente Einschränkungen der möglichen Drift des magnetischen Moments des Cäsiumkerns und der Feinstrukturkonstante abgeleitet.

Abstract

High-precision two-photon spectroscopy of hydrogen and hydrogenlike systems constitutes an exceptional tool for experimental tests of fundamental theories. In the analysis of these experiments, theory also plays a vital role in the modeling of time-resolved spectra, the calculation of precise transition matrix elements, and the correction of a number of systematic effects. This thesis gives a detailed analysis of the relevant two-photon excitation dynamics, starting from the single-atom response and leading to a Monte Carlo model which can be used for the analysis of atomic beam experiments. Dynamic polarizabilities of relevant S and D states, quantifying the dynamic Stark shift, and transition matrix elements among these states are calculated, taking into account leading-order relativistic, radiative and non-dipole laser-field effects. An important broadening effect of the experimentally observed spectra in the hydrogen $1S$–$2S$ spectroscopy experiment at the Max–Planck–Institut für Quantenoptik (MPQ) is identified and quantitatively described, as well as systematic frequency shifts. Corresponding possible improvements to the experimental setup are proposed. By combining the results of repeated MPQ hydrogen $1S$–$2S$ measurements and other experiments, in collaboration with the MPQ group, separate stringent limits on the possible drift of the magnetic moment of the cesium nucleus and the finestructure constant are deduced.

In connection with the work on this thesis, the following articles were published in refereed journals:

- U. D. Jentschura, J. Evers, M. Haas and C. H. Keitel: *Lamb Shift of Laser-Dressed Atomic States*
  Phys. Rev. Lett. **91**, 253601 (2003).

- M. Fischer, N. Kolachevsky, M. Zimmermann, R. Holzwarth, Th. Udem and T. W. Hänsch; M. Abgrall, J. Grünert, I. Maksimovic, S. Bize, H. Marion, F. Pereira Dos Santos, P. Lemonde, G. Santarelli, P. Laurent, A. Clairon, and C. Salomon; M. Haas, U. D. Jentschura, and C. H. Keitel: *New Limits on the Drift of Fundamental Constants from Laboratory Measurements*
  Phys. Rev. Lett. **92**, 230802 (2004).

- M. Haas, U. D. Jentschura and C. H. Keitel: *Comparison of Classical and Second Quantized Description of the Dynamic Stark Shift*
  Am. J. Phys. **74**, 77 (2006).

  [selected for volume 5, issue 1 of the "Virtual Journal of Ultrafast Science" (`http://www.vjultrafast.org`), publishers: APS, AIP]

- M. Haas, U. D. Jentschura and C. H. Keitel; N. Kolachevsky, M. Herrmann, P. Fendel, M. Fischer, R. Holzwarth, Th. Udem and T. W. Hänsch; M. O Scully, G. A. Agarwal: *Two-photon Excitation Dynamics in Bound Two-body Coulomb Systems Including AC Stark Shift and Ionization*
  Phys. Rev. A **73**, 052501 (2006).

Unrefereed conference proceedings:

- A. Staudt, G. R. Mocken, M. Haas and C. H. Keitel: *Quantum dynamics beyond the dipole approximation: From two-electron ions to more complex systems*
  Conference Proceedings "Atoms and Plasmas in Super-Intense Laser Fields", Vol. 88, D. Batani, C. J. Joachain and S. Martellucci (Eds.), Societa italiana di fisica, Bologna (2004).

- M. Haas, U. D. Jentschura and C. H. Keitel: *Dynamischer Stark-Effekt in der Hochpräzisionsspektroskopie*
  Conference Proceedings Riezlern (2005).

- M. Haas, U. D. Jentschura and C. H. Keitel: *QED Corrections to the Dynamic Polarizability*
  AIP Conference Proceedings (LEAP'05) **796**, 317 (2005).

Article to be submitted:

- N. Kolachevsky, M. Haas, U. D. Jentschura, M. Herrmann, M. Fischer, R. Holzwarth, Th. Udem, C. H. Keitel and T. W. Hänsch: *Photoionization Broadening of the $1S$–$2S$ Transition in a Beam of Atomic Hydrogen*
  to be submitted to JETP (2006).

Contents

1 Introduction **1**

2 Two-Photon Excitation Dynamics **7**

2.1 Introduction 7

2.2 Basic quantum dynamics 8

2.2.1 Analytic solution for constant intensity 12

2.2.2 Quantum dynamics including spontaneous decay 16

2.3 Generalizations of the equations of motion 21

2.3.1 Motion in a standing wave and time-dependent intensity 22

2.3.2 Further generalizations 26

2.4 Analytic solution including ionization and spontaneous decay 27

3 Transition Matrix Elements and Dynamic Polarizability **31**

3.1 Introduction 31

3.2 Overview of the interactions of atom, laser mode and vacuum 32

3.2.1 Second-order perturbation 34

3.2.2 Fourth order perturbation 36

3.2.3 Transition matrix elements 36

3.3 Calculation of two-photon transition matrix elements 37

3.3.1 Calculational method 37

3.3.2 Results for two-photon transitions 40

3.4 Dynamic Stark effect 43

3.4.1 Classical field approach 43

3.4.2 Second-quantized approach 46

3.5 Calculation of the AC Stark shift 47

3.5.1 Matrix elements 48

3.5.2 Results for two-photon transitions 49
3.6 Calculation of the photoionization cross section 53
3.7 Combined induced-spontaneous two-photon decay 56
3.8 Conclusion 58

4 Relativistic and Radiative Corrections to Dynamic Processes 61
4.1 Perturbation to the dynamic polarizability 62
4.2 Perturbation to the transition matrix element 64
4.3 Potential for relativistic corrections 65
4.4 Potential for radiative corrections 66
4.5 Calculation of relativistic and radiative corrections 67
4.5.1 Wavefunction contributions 67
4.5.2 Eigenenergy contributions 70
4.5.3 Hamiltonian contributions 71
4.5.4 Results for S–S transitions 72
4.6 Beyond the dipole approximation 78
4.6.1 Field-configuration dependent corrections 78
4.6.2 Results for two-photon transitions 80
4.7 Lamb shift of laser dressed states 83

5 Monte Carlo Investigations and Lineshape 87
5.1 Introduction 87
5.2 Experimental setup 89
5.3 Implementation of the simulation 91
5.4 Photoionization broadening of the $1S$–$2S$ transition line shape 92
5.4.1 Introduction 92
5.4.2 Experimentally observed broadening and shift coefficients 93
5.4.3 Simulated broadening and shift coefficients 94
5.4.4 Comparison 96
5.4.5 Laser line width 97
5.5 Effects of nozzle freezing 98
5.6 Effect of laser beam misalignment 100
5.6.1 The $\alpha\theta$-term 103
5.6.2 The α^2-term 104

5.7 Conclusion 105

6 $1S$–$2S$ Spectroscopy and Possible Drift of Fundamental Constants 107

6.1 Data analysis and systematic effects 108

6.1.1 MPQ data analysis procedure 108

6.1.2 Models for the velocity distribution 111

6.1.3 Full line shape model and Lorentz data analysis 113

6.1.4 Weighting and χ^2_r in the data regression 116

6.1.5 Effect of unsteady power calibration 119

6.1.6 Freezing nozzle 122

6.1.7 Power-dependent line shape model 123

6.2 Test of the drift of fundamental constants 125

6.2.1 Introduction 125

6.2.2 Analysis of the laboratory measurements 126

6.2.3 Results 131

7 Conclusion 133

7.1 General conclusion 133

7.2 Proposals for future experiments 134

A Some comparisons with the literature 137

A.1 The $1S$–$2S$ transition 137

A.2 The $1S$–$3S$ transition 138

A.3 Light shifts 139

B Explicit Polarizabilities and Transition Matrix Elements 141

Bibliography 143

Chapter 1

Introduction

In the vivid history of atomic physics and matter-light interaction, experiment and theory have stimulated a number of mutual developments and greatly profited from each other's progress.

In the early nineteenth century, before the discovery of Brownian motion, the existence of atoms was a controversial, if not a philosophical question, and the debate whether light was made up of particles or was a wave phenomenon, was seemingly decided in favor of the wave nature, as the equations of electrodynamics were established by James Clerk Maxwell. The observation of dark lines in the solar spectrum in 1802 by William Wollaston and independently in 1813 by Joseph von Fraunhofer should mark a starting point in the challenges to theory to explain light-matter interactions on the microscopic level beyond the Maxwell equations and in the quest for experiments to discover new physical phenomena and test prevailing theories.

The phenomenological description of the wavelengths of the hydrogen absorption lines by Johann Balmer and Johannes Rydberg was first successfully explained in 1913 by Niels Bohr, introducing an atomic model in which the electron orbiting the nucleus can occupy only discrete energy levels, and the quantized energy differences in transitions among these levels would lead to the characteristic lines in the absorption spectrum. This model was the first building block of quantum mechanics, which was quickly emerging in the following years through the additional works of Erwin Schrödinger, Werner Heisenberg, Max Born and Wolfgang Pauli, to name only a few. In this framework of early quantum mechanics, the solution to the two-body problem of the hydrogen atom could explain in a very fundamental way the atomic energy levels of the Bohr model. Spectroscopy experiments with high resolution showed, however, that there was a fine structure in the main lines of atomic spectra, first discovered by Albert Michelson and Edward Morley in 1887. This small splitting of the main absorption lines was first interpreted in 1916 by Arnold Sommerfeld as being a consequence of relativistic corrections to the energy levels of Bohr's atomic model.

This realization that quantum mechanics based on Schrödinger theory was not sufficient to fully describe the hydrogen spectrum, among other reasons, initiated the search for a relativistic generalization of the Schrödinger equation. In 1928, Paul Dirac succeeded in

introducing a relativistic wave equation for electrons, laying the foundation of relativistic quantum mechanics. The Dirac equation also requires the existence of so-called antiparticles for the electrons of ordinary matter. In fact, shortly after the prediction of these so-called positrons, Carl Anderson could detect the new particles in cosmic rays in 1932.

By means of exciting atomic hydrogen to the $2S$ state by electron impact and probing the metastable atoms with radio waves, in 1947, Willis Lamb and Robert Retherford found a tiny frequency splitting separating the $2s_{1/2}$ and $2p_{1/2}$ states [1,2], which in Dirac theory are assigned equal energies. The lifting of this degeneracy is caused by effects which can only be described by the quantum field theory of electromagnetism, quantum electrodynamics (QED), as developed by Richard Feynman, Freeman Dyson, Julian Schwinger, and Sin-Itiro Tomonaga in the 1940s. Applied to bound states of the hydrogen atoms, QED can explain the Lamb shift as a result of interactions of the bound electron with the electromagnetic vacuum, the so-called self-energy shift, by the vacuum polarization of virtual particle-antiparticle pairs close to the nucleus, and higher order effects.

Quantum electrodynamics is currently the most refined and accurate theory of the electromagnetic interaction. Up to date, this theory has been tested by a large number of experiments and has prevailed in the most precise tests. A prominent example is the measurement of the electron magnetic moment in units of the Bohr magneton, g, which according to Dirac theory should have a value of exactly 2. QED predicts deviations from $g-2$ on the order of 10^{-4}, which could be experimentally confirmed to a relative accuracy of 10^{-12} [3]. Similar measurements of the muon anomalous magnetic moment [4] are equally in agreement with theoretical values of QED.

Current comparisons of QED predictions with Lamb shift measurements of the $1S$ ground state [5–7] rely on high-precision two-photon spectroscopy comparing transitions like $1S$–$2S$ and $2S$–$4S/4D$. The experimental precision of the results in the optical regime even surpasses the precision of radio frequency measurements of the classic $2S$–$2P$ Lamb shift. However, the comparisons of the calculated Lamb shift with experimental observations are currently limited by the experimental precision of the value of the proton charge radius, which cannot be calculated ab initio within QED. This value is needed as input to the QED calculations to account for the deviation from a nuclear Coulomb potential due to the finite proton size. Reversing the situation and having faith in QED, the proton charge radius can be determined [8] more precisely than by any other method, even though it is a very small correction to the energy levels of the hydrogen atom. Some of the latest QED predictions for optical transition frequencies [9] are given with relative uncertainties which are even smaller than the predictions for the electron g factor, which previously was the most accurate prediction of QED.

High-precision spectroscopy of two-photon transitions also plays a key role in the determination of fundamental constants. In particular, the Rydberg constant

$$R_\infty = \frac{m_\mathrm{e}\, e^4}{8\,\epsilon_0^2\, h^3 c} = \frac{m_\mathrm{e}\, c\, \alpha^2}{2\, h} \tag{1.1}$$

originally introduced already in the phenomenological formula for the wavelengths of the Fraunhofer lines by Johannes Rydberg, can be determined by high-precision two-photon spectroscopy of the two-photon $1S$–$2S$, $2S$–nS, $2S$–nD with very high accuracy [5, 6,

10, 11]. In addition to its decisive role in spectroscopy, the Rydberg constant is also an important pivotal point in the determination of the constituent constants m_e, e, and h in the regular adjustment of the CODATA self-consistent set of physical constants [12].

Frequency measurements constitute the most accurate measurements in physics, because they amount to counting the number of cycles of the periodic process under consideration and comparing this number to the number of cycles a reference oscillator undergoes in the same time interval. For this reason, the most precise current atomic clocks [13] are based on a microwave oscillator locked to the cesium ground state hyperfine structure transition. The cycles of the microwave field, oscillating at about 9 GHz, can be counted by an electronic circuit.

The absolute measurement of optical frequencies is much more difficult in principle, because the oscillations are so fast that electronic counting is impossible. A very sophisticated method to count optical cycles relies on phase-coherent harmonic frequency chains [14–16]. These chains allow to connect microwave frequencies and optical frequencies by means of successive steps of harmonic generation stages, but present immense technical challenges, because they require stable transfer oscillators in a range of different frequency domains. Also, one usually can only measure frequencies that are close to one specific target frequency. The recent advent of the optical frequency comb technique [17,18] has provided the decisive leap ahead in optical frequency metrology, bridging the gap between the microwave regime and optical frequencies in one single step, providing a ruler in frequency space for any optical frequency.

Since optical frequencies are larger than the cesium microwave frequency by many orders of magnitude, clocks based on optical oscillators could become much more accurate than today's microwave atomic clocks. Turning the difficulties with the metrology of optical frequencies to an advantage, future atomic clocks could rely on an extremely narrow two-photon transition like the $1S$–$2S$ transition in hydrogen as an oscillator, and the frequency comb as the clockwork, building up an all-optical clock.

Although QED has up to now passed all experimental tests with flying colors, it is probably not the final description of the electromagnetic interaction. A theory unifying all fundamental interactions is a persistent challenge to theoretical physics. In such a "grand unified theory", the four fundamental forces, gravity, electromagnetism, weak and strong force, and the fundamental particles, would be described in one common framework and, ideally, this theory would have only very few free parameters. In the current standard model of particle physics, in which all interactions except gravity are unified, there are 19 free parameters describing, e.g., the interaction strengths and masses of the particles, and since neutrinos probably have a finite rest mass, 10 additional parameters might be required. The fine structure constant

$$\alpha = \frac{e^2}{4\pi\epsilon_0\,\hbar\,c}\,, \tag{1.2}$$

which is the coupling constant of the electromagnetic interaction, is one example of such a free parameter and is of fundamental importance in QED. For example, the fact that $\alpha \approx 1/137$ at the low energies considered in atomic physics, allows for an expansion of many quantities of interest in $Z\alpha$ for low nuclear charge Z, permitting calculations using

perturbation theory. The actual value of the fine structure constant, however, cannot be inferred within the framework of QED.

The search for unified theories therefore also aims at explaining physical constants which are as yet free parameters. Generalized Kaluza-Klein theories [19] and modern string theories [20,21] allow for, or even predict [22] tiny time variations of fundamental parameters like, e.g., the fine structure constant α. In these theories, α is linked to the size of extra compact dimensions of a higher-dimensional space-time, and as a dynamical variable of the theory it could vary on cosmological time scales. For tests of these predictions, high-precision spectroscopy can provide valuable contributions. The possible drift of the fine structure constant would be observable as a tiny drift of optical transition frequencies which are measurable with high precision in laboratory experiments. Together with complementary results of astronomical spectroscopy experiments and investigations of nuclear processes on a geological time scale, high-precision spectroscopy therefore opens an opportunity to put experimental constraints on, or select among, alternative unified theories.

One important advantage of laboratory experiments is that a very tight control of systematic effects is possible and that one can repeat the experiment under improved conditions. Very generally, the improvement of the accuracy and the precision of high-precision spectroscopy experiments requires a very detailed study of systematic effects, aiming to minimize perturbing influences on the measurement both by experimental and theoretical means.

In this thesis, a number of theoretical contributions to the interplay between experiment and theory of high-precision two-photon spectroscopy are presented. Investigations of the coherent population dynamics in the density matrix formalism of quantum optics are performed as well as calculations of important matrix elements in the framework of non-relativistic atomic physics. Relativistic and QED corrections to these matrix elements and corrections beyond the dipole approximation are calculated, which surpass the currently accessible experimental precision. Numerical Monte Carlo simulations, bringing to light collective phenomena and systematic effects, and independent validity checks of the data analysis procedure used by the $1S$–$2S$ hydrogen spectroscopy group of T. W. Hänsch at the Max–Planck–Institut für Quantenoptik (MPQ) are carried out. Finally, by analyzing the results of high-precision experiments, in cooperation with the MPQ precision spectroscopy group, separate limits to the possible drift of two fundamental constants are derived.

Specifically, in chapter 2 the excitation dynamics of a hydrogenlike system on two-photon resonance with a driving laser is investigated. In contrast to many other processes in quantum optics, the two-photon excitation of the hydrogen $1S$–$2S$ transition can not be obtained via a steady-state calculation, because one-photon resonant ionization introduces a strong loss channel, which requires the fully time-dependent treatment of the excitation process. The canonical equations of motion are generalized to the case of excitation in a standing wave field, and an analytic solution for a special case is found, including ionization and spontaneous decay of the excited state.

In chapter 3, relevant non-relativistic matrix elements are presented in a unified formalism, i.e., transition matrix elements and dynamic polarizabilities, for a wide range of two-

photon transitions, supplementing the values in the literature. Being one of the most important systematic effects in high-precision two-photon spectroscopy, the dynamic Stark effect is considered closely and the conventional derivation is compared to a new, fully quantized description, which is valid also for nonclassical laser fields. Scaling relations for the nuclear charge and the reduced mass are derived, extending the applicability of the matrix elements to general two-body bound Coulomb systems. Angular prefactors for adjustment of the matrix elements to specific fine structure and hyperfine structure transitions are given.

Chapter 4 is dedicated to the calculation of leading order relativistic, radiative and non-dipole corrections to the non-relativistic transition matrix elements and the dynamic polarizabilities. As opposed to the static energies of the hydrogen atomic levels, that are known up to two-loop radiative corrections from QED calculations, radiative corrections to the dynamic polarizability have not yet been considered. Since for typical excitation intensities the dynamic Stark shift is a very small correction to the hydrogenic energy levels compared to the Lamb shift, the non-relativistic treatment of the dynamic Stark shift has been sufficient for experimental purposes up to now. Anticipating future increase in precision, a number of corrections to the dynamic Stark effect and to the transition matrix elements are evaluated.

In chapter 5, the general set of tools which is provided by the results of the preceding chapters, is applied to the specific problem of the hydrogen $1S$–$2S$ excitation, which is investigated experimentally by the MPQ group in Garching. A Monte Carlo simulation, relying on the quantum dynamics and the matrix elements of the earlier chapters, is implemented, and thanks to the close long-term cooperation with the MPQ group it is possible to compare the results from the simulation to the raw data recorded in 2003 [23] and to verify both the simulation and the matrix elements. The simulation additionally provides insight into systematic effects which are not under direct experimental control, and it can be used as a testing ground for evaluating the consequences of changes to the experimental setup.

In the first part of chapter 6, a number of specific details concerning the line shape model of the data analysis at the MPQ experiment is treated. In order to validate this numerical line shape model, an independent data analysis method was developed. Additional candidates for systematic effects previously unaccounted for are investigated and possible improvements to the experimental setup are proposed. In the second part of chapter 6, separate stringent limits to the drift of the finestructure constant and the cesium magnetic moment are derived by analyzing results of two independent high-precision spectroscopy experiments, namely the hydrogen $1S$–$2S$ absolute frequency measurement at the MPQ and the measurement of a quadrupole transition frequency in mercury, performed at the National Institute of Standards and Technology in Boulder, Colorado [24]. Complementary to astronomical [25] and geological [26] experiments, high-precision spectroscopy laboratory experiments can test the present drift of the constants with comparable sensitivity.

In chapter 7, conclusions and a brief outlook including proposals concerning future experiments are given.

Chapter 2

Two-Photon Excitation Dynamics

2.1 Introduction

Two-photon transitions involving the $1S$ and $2S$ states in hydrogen and hydrogenlike systems are of special interest in high-precision spectroscopy for two main reasons. First, direct transitions between two S states are forbidden by electric dipole selection rules and therefore the excited state in such a transition can have a very long natural lifetime. For the $2S$ state in hydrogen, the natural lifetime is about $1/8.2$ s, while the lifetime of the hydrogen $2P$ state is 10 ns. Consequently, the $1S$–$2S$ transition frequency can be measured with a much higher precision than the $1S$–$2P$ transition, because the corresponding width of the absorption line is so much smaller. Second, an experiment probing any two-photon transition can be designed in such a way that the two photons involved in the absorption process travel in opposite directions, which results in a cancellation of the both the Doppler shift and the absorption recoil shift to first order in v/c, for a moving atom. Also, for a trapped atom or hydrogenlike ion, the counter-propagating photon setup has the advantage of a very small mechanical recoil of the absorbing atom, minimizing the disturbing influence of the spectroscopic laser field on the confinement properties of the trap.

In many quantum optical processes in which one-photon resonant transitions are driven and strong spontaneous decay channels exist, the total interaction time is characterized by a short phase of fast transient dynamics, followed by a long period in which the atom is in the steady state, which means that the atomic state population does not change any more as a function of time. Accordingly, the quantum optical master equations, which are first-order differential equations, reduce to a set of ordinary equations, and can be solved, e.g., using Gaussian elimination. In these cases, several coupled levels can be taken into account and off-diagonal elements in the coefficient matrix, originating from spontaneous decay, do not complicate the situation dramatically.

In contrast, in all two-photon transitions in which the ground state is the $1S$ or the $2S$ state, the excited state can be ionized by absorption of one additional photon from the same laser field that drives the two-photon resonance, except for the case of the $2S$–$3S$ transition. As a consequence, the excitation of these spectroscopically interesting two-

photon transitions can only take place in the transient regime, because the system is not closed and the one-photon resonant ionization rate can be comparable with the two-photon Rabi frequency. In particular, it is impossible to describe the system using the steady-state of the master equations, it rather has to be treated with the fully time-dependent differential equations.

In this chapter the time-dependent excitation of a two-level system on two-photon resonance with a driving laser field is presented. In Sec. 2.2, an introduction to the well-known density matrix formalism is given, in which both the spontaneous decay and the ionization damping are included. The resulting excited state line shape as a function of interaction time is presented and an analytic solution excluding spontaneous decay is derived for the density matrix equations. This solution was also found in the literature. In Sec. 2.3, the basic master equations are generalized to the case of excitation in a standing wave field and time-dependent excitation intensity, which is used, e.g., in the setup at the Max–Planck–Institut für Quantenoptik (MPQ) in Garching, Germany [27, 28]. In Sec. 2.4, an analytic solution including both spontaneous decay and ionization damping is given. The inclusion of the spontaneous decay channel complicates the expression considerably, and since this solution has not been found in any publication, it is verified by means of a comparison with a numerical integration of the master equations.

2.2 Basic quantum dynamics

In this section, the basic model is introduced, which is used to describe the two-photon excitation and ionization of hydrogen, and, more generally, any hydrogenlike two-body Coulomb system. The main approximations which will be made, are to consider a driving laser field with vanishing spectral line width, and to neglect the direct three-photon ionization of the ground state.

For the systems which will be discussed in this thesis, an infinitely narrow laser is an adequate approximation, because the ionization of the excited state limits the total interaction time of the bound system with the laser field. As a consequence of the time-frequency uncertainty principle, the transient width of the excited state cannot be smaller than the inverse interaction time, and as long as the finite bandwidth of the laser is small compared to this transient width, a monochromatic laser is a good approximation. Note that for spectroscopic experiments probing a steady state, with an interaction time that is in principle infinitely large, one would have to compare the laser line width to the natural line width instead. As an example, one may consider the MPQ hydrogen $1S$–$2S$ experiment, where the excitation typically takes place on a sub-millisecond timescale. The spectral line width of the laser is on the order of 200 Hz at a wavelength of 121 nm, which is small compared to the typical inverse interaction time of some kHz, while the natural line width of the $2S$ state is only 1.31 Hz.

The standard approach [29, 30] is to solve the density matrix equations for a two-level system. One can restrict the Hilbert space of the atom to only two relevant states, an excited state $|e\rangle$ and a ground state $|g\rangle$, because close to the two-photon resonance, only that transition will be driven significantly by the laser field.

It will be assumed that the atoms are initially in $|g\rangle$ and are irradiated with the intensity $I(t)$, starting from time $t = 0$. For additional considerations concerning the intensity in a standing wave, see Sec. 2.3 below. The straightforward treatment of this interacting two-level system is extended by including decay channels accounting for spontaneous decay and ionization into the density matrix equations, which will later turn out to be crucial ingredients.

The starting point is the von Neumann equation [29] for the density operator ρ,

$$\mathrm{i}\hbar\frac{\partial}{\partial t}\,\rho = [\tilde{H}, \rho]\,, \tag{2.1}$$

with

$$\rho = \rho_{gg}|g\rangle\langle g| + \rho_{ee}|e\rangle\langle e| + \rho_{ge}|g\rangle\langle e| + \rho_{eg}|e\rangle\langle g| \tag{2.2}$$

$$\tilde{H} = E_g\,|g\rangle\langle g| + E_e\,|e\rangle\langle e| + \frac{\hbar\Omega}{2}\left[\exp(\mathrm{i}\omega_\mathrm{L}t) + \exp(-\mathrm{i}\omega_\mathrm{L}t)\right]^2\left(|e\rangle\langle g| + |g\rangle\langle e|\right)\,, \tag{2.3}$$

$$E_g = h\nu_g + h\Delta\nu_\mathrm{AC}(g)\,, \tag{2.4}$$

$$E_e = h\nu_e + h\Delta\nu_\mathrm{AC}(e)\,. \tag{2.5}$$

The tilde on $\tilde{H}$ signifies that the Hamiltonian is restricted to the two atomic states under consideration. The angular frequency of the laser is denoted by ω_L. The energies of the excited state E_e and ground state E_g are defined such that the dynamic (AC) Stark effect is already contained, expressed by the respective frequency shift $\Delta\nu_\mathrm{AC}$. As will be presented in detail in Sec. 3.5, these frequency shifts are proportional to the intensity $I(t)$ of the exciting laser field, and in accordance with [31], the AC Stark coefficient β_AC is defined as

$$\Delta\nu_\mathrm{AC}(g) = \beta_\mathrm{AC}(g)\,I(t)\,, \tag{2.6}$$

and likewise for the excited state. The AC Stark coefficients will be calculated in Sec. 3.5 and listed in SI units in Tabs. 3.3 and 3.4 in the next chapter. Further, the two-photon Rabi-frequency Ω is defined as

$$\Omega = 2\,(2\pi\beta_{ge})\,I(t)\,, \tag{2.7}$$

and due to the two-photon nature of the excitation process, Ω is also proportional to the light intensity, rather than to the electric field amplitude, as it is the case for one-photon dipole allowed transitions. Section 3.3 treats the calculation of the two-photon transition matrix elements β_{ge} and lists the results for a set of transitions in Tab. 3.1. Generally, both the symbols ω and Ω are be used for angular frequencies (measured in rad/s), appearing in the argument of exponential functions of the form $\exp(\mathrm{i}\omega t)$, and ν is used for frequencies as measured in Hz (compatible with the international unit system, SI).

For the description of the population dynamics of the system, it is useful to factor out a fast oscillating term of the off-diagonal elements of the density matrix in the equations

of motion (2.1). The transformed density matrix elements are denoted by a prime and defined by

$$\rho'_{gg} := \rho_{gg}\,, \qquad \rho'_{ge} := \rho_{ge}\,\exp(-\mathrm{i}\,2\omega_\mathrm{L} t)\,, \tag{2.8a}$$

$$\rho'_{ee} := \rho_{ee}\,, \qquad \rho'_{eg} := \rho_{eg}\,\exp(\mathrm{i}\,2\omega_\mathrm{L} t)\,. \tag{2.8b}$$

This corresponds to a transformation into the interaction picture, but with a phase factor of $\exp(-\mathrm{i}\,2\omega_\mathrm{L} t)$ instead of $\exp(-\mathrm{i}\omega_{eg} t)$ for the coherence ρ_{ge}. Note that the diagonal elements of the density matrix, representing the respective atomic state population, are invariant under this transformation. The resulting equations of motion for the matrix elements of the transformed density operator ρ' then contain both slowly varying terms, which determine the timescale of the population dynamics, and terms oscillating with $\pm 2\omega_\mathrm{L}$ and $\pm 4\omega_\mathrm{L}$. One can now employ the rotating wave approximation, dropping the terms oscillating at these optical frequencies, thereby neglecting the Bloch-Siegert shifts [32], which are on the order of 10^{-10} relative to the dynamic Stark shifts.

The spontaneous decay and the ionization of the excited state can be taken into account by adding

$$\rho'_\mathrm{relax} = -\left(\gamma_\mathrm{i} + \gamma_\mathrm{s}\right) \rho'_{ee}\,|e\rangle\langle e| + \gamma_\mathrm{s}\,\rho'_{ee}\,|g\rangle\langle g| - \frac{\gamma_\mathrm{i} + \gamma_\mathrm{s}}{2}\left(\rho'_{ge}\,|g\rangle\langle e| + \rho'_{eg}\,|e\rangle\langle g|\right) \tag{2.9}$$

to the right hand side of Eq. (2.1), after performing the transformation (2.8). The spontaneous decay rate is denoted by γ_s, while γ_i represents the rate with which the excited state is depopulated due to one-photon resonant ionization:

$$\gamma_\mathrm{i} = 2\pi\beta_\mathrm{ioni}(e)\,I(t)\,. \tag{2.10}$$

All transition rates in this thesis, denoted by γ with an appropriate index, are given in angular frequency units rad/s. In cases where a decay γ is the governing broadening mechanism this translates into a line width (Lorentzian full width at half maximum) of $\gamma/(2\pi)$.

The ionization coefficient β_ioni is closely connected to the dynamic Stark effect, which will be discussed in Sec. 3.5. Essentially, the dynamic Stark coefficient is a complex quantity, the real part yielding β_AC, and the imaginary part determining β_ioni. The ionization rate (2.10) is included into the equations of motion in analogy to the spontaneous decay rate, but with one important difference. In the particular case of the $1S$–$2S$ experiment, the atomic density is very low, in order to avoid collisional effects on the transition frequency. Therefore, the recombination probability for protons and electrons to form again a hydrogen atom in the ground state, is extremely small. Consequently, a recombination term is not included into ρ'_relax. For cases where recombination by radiative or three-body processes cannot be neglected, the recombination rates can be included by employing the principle of detailed balance (see e.g. pp. 102 and 151 of [33]).

In the cases where the lower level $|g\rangle$ is the $2S$ state, the excited state nS or nD, where n is the principal quantum number, can decay spontaneously into several levels, which in turn cascade (i) to the metastable $2S$ state, dominantly with an effective rate γ_s^{2S} and (ii) to the $1S$ ground state, with an effective rate γ_s^{1S}. If the decay cascade ends in $|1S\rangle$, the

population is lost for the dynamics of the considered two-level system, and can formally be treated as an additional intensity independent ionization rate: $\gamma_\mathrm{i} \to 2\pi\beta_\mathrm{ioni}(e)\, I + \gamma_\mathrm{s}^\mathrm{1S}$.

In this way, one arrives at the following master equations, sometimes referred to as the optical Bloch equations, which are the equations of motion (EOM) for the density matrix elements of the considered two-level system on two-photon resonance with the driving laser of angular frequency ω_L:

$$\frac{\partial}{\partial t}\rho'_{gg} = -\Omega\,\mathrm{Im}(\rho'_{ge}) + \gamma_\mathrm{s}\,\rho'_{ee}\,, \tag{2.11a}$$

$$\frac{\partial}{\partial t}\rho'_{ge} = -\mathrm{i}\,\Delta\omega\,\rho'_{ge} + \mathrm{i}\,\frac{\Omega}{2}\,(\rho'_{gg} - \rho'_{ee}) - \frac{\gamma_\mathrm{i}+\gamma_\mathrm{s}}{2}\,\rho'_{ge}\,, \tag{2.11b}$$

$$\frac{\partial}{\partial t}\rho'_{ee} = \Omega\,\mathrm{Im}(\rho'_{ge}) - (\gamma_\mathrm{i}+\gamma_\mathrm{s})\,\rho'_{ee}\,, \tag{2.11c}$$

with the definition for the excitation detuning,

$$\Delta\omega = 2\pi\Delta\nu = 2\,\omega_\mathrm{L} - 2\pi\nu_{eg} - 2\pi[\Delta\nu_\mathrm{AC}(e) - \Delta\nu_\mathrm{AC}(g)]\,. \tag{2.12}$$

Here, the absolute frequency of the unperturbed transition is denoted by $\nu_{eg} = \nu_e - \nu_g$. These equations are equivalent to, e.g., Eq. (8) of Ref. [34], in the case where $\gamma_\mathrm{s} = 0$.

Whereas the first-order Doppler shift is often canceled by using two counter-propagating beams, the second-order Doppler shift of an atom moving with velocity v, like any other single particle frequency shift, can be included into the excitation detuning by adding

$$\Delta\omega_\mathrm{D2} = (2\pi\nu_{eg})\,\frac{1}{2}\frac{v^2}{c^2} \tag{2.13}$$

to the right hand side of Eq. (2.12). At this point, it should be noted that the EOM (2.11) are similar to the case of a two-level system, coupled by a laser field driving a dipole allowed one-photon transition. In fact, the main conceptual difference lies in the calculation of the transition matrix elements entering into the Rabi frequency and the dynamic Stark coefficients. In particular, the dynamic Stark effect is fundamentally different for the two-photon case, where the time-dependent electric field is an off-resonant perturbation of second order, as opposed to the resonant one-photon case, where the level shift is linear in the electric field amplitude. Note also, that in contrast to one-photon transitions, the spontaneous decay rate is modified slightly in the presence of the laser field due to virtual intermediate P states, even for the $1S$–$2S$ transition, as detailed in Section 3.7.

The appropriate description of the excitation with a finite bandwidth laser field necessitates a treatment involving stochastic differential equations [35, 36], to model the phase and intensity fluctuations of the driving laser field as stochastic processes. This would result in a modification of the coherence terms in Eqs. (2.11), in the sense discussed in [37], resulting in further damping terms entering the right-hand side of Eq. (2.11b). For the short-time evolution of the density matrix, i.e., in the regime where the excited state population $\rho_{ee} \propto \Omega^2 t^2$, a simple averaging of ρ_{ee} over the power spectrum of the laser can be applied (see Eq. (2.74) of [38]), but this averaging is not applicable for longer excitation times.

2.2.1 Analytic solution for constant intensity

In the above form (2.11), for constant intensity $I(t) = I$, the EOM are a coupled set of first-order differential equations with constant coefficients and hence are solvable analytically for all times. The somewhat lengthy expression for the full solution is given in Sec. 2.4 below.

The analytic solution to Eqs. (2.11) without ionization ($\gamma_\mathrm{i} = 0$), taken in the limit of infinite interaction time, leads to the well-known steady state of the system with a Lorentzian line shape for the excited state population [29]. In this case, it is assumed that the population that decays out of the excited state reappears in full at the ground state. However, when discussing two-photon S–S and S–D transitions, this hardly ever happens. Even the two-photon dynamics of the $2S$–$3S$ transition, for which indeed $\gamma_\mathrm{i} = 0$, does not evolve to a steady state, because the population in the $3S$ state also spontaneously decays to the $1S$ state, mainly via $2P$, and does not reappear in the $2S$ state.

In this section, the focus will first be on the case of vanishing spontaneous decay, $\gamma_\mathrm{s} = 0$. This is often a good approximation when atoms or ions are excited in beams or gas cells, as opposed to trapped particles. In particular, it is a very good approximation for the hydrogen $1S$–$2S$ transition, because for typical intensities, the ionization rate dominates over the two-photon spontaneous decay rate. Later in this section, the general solution will be considered, for cases where the spontaneous decay rate is no longer negligible (e.g., for systems with nuclear charge number $Z > 1$).

Recall that the EOM describe an atom at rest or moving with a constant velocity, for which the Doppler shift can be included into the detuning $\Delta\omega$. The initial state is the ground state, so $\rho_{gg}(t = 0) = 1$ and $\rho_{ee}(0) = \rho_{ge}(0) = \rho_{eg}(0) = 0$. Starting from time $t = 0$, the system interacts with a monochromatic laser field of constant intensity I. The transient line shape, which is defined as the population in the excited $2S$ state as a function of detuning and time, $\rho'_{ee}(\Delta\omega, t)$, and the ground state population, $\rho'_{gg}(\Delta\omega, t)$, can then be expressed as

$$\rho'_{ee}(\Delta\omega, t) = \frac{4\,\Omega^2}{G} \exp\left(-\frac{\gamma_\mathrm{i}}{2}\,t\right) \left(\sin^2(\Omega_1 t) + \sinh^2(\Omega_2 t)\right), \tag{2.14a}$$

$$\begin{aligned}\rho'_{gg}(\Delta\omega, t) = {}& \rho'_{ee}(\Delta\omega, t) + \frac{1}{G\Omega_1\Omega_2} \exp\left(-\frac{\gamma_\mathrm{i}}{2}\,t\right) \times \\ & \big\{\Omega_2(4\Omega_1^2 - \Delta\omega^2)\big[4\Omega_1 \cos(2\Omega_1 t) + \gamma_\mathrm{i} \sin(2\Omega_1 t)\big] \\ & + \Omega_1(4\Omega_2^2 + \Delta\omega^2)\big[4\Omega_2 \cosh(2\Omega_2 t) + \gamma_\mathrm{i} \sinh(2\Omega_2 t)\big]\big\},\end{aligned} \tag{2.14b}$$

where

$$G = \sqrt{16\,\Delta\omega^2\gamma_\mathrm{i}^2 + \left(4\,\Delta\omega^2 + 4\,\Omega^2 - \gamma_\mathrm{i}^2\right)^2}, \tag{2.15a}$$

$$\Omega_1 = \frac{1}{4\sqrt{2}} \sqrt{G + 4\,\Delta\omega^2 + 4\,\Omega^2 - \gamma_\mathrm{i}^2}, \tag{2.15b}$$

$$\Omega_2 = \frac{1}{4\sqrt{2}} \sqrt{G - 4\,\Delta\omega^2 - 4\,\Omega^2 + \gamma_\mathrm{i}^2}. \tag{2.15c}$$

The angular frequencies Ω_1 and Ω_2 are always real. Reassuringly, this solution has been obtained in a rather different form in [36, 39], but agrees with the result presented here. Those works focus on resonant multiphoton ionization and it is not surprising that the same master equations are relevant for those studies.

For the case of vanishing ionization, $\beta_{\mathrm{ioni}} = 0$, one has $\Omega_2 = 0$ and one obtains the familiar Rabi oscillations with generalized Rabi frequency $\sqrt{\Delta\omega^2 + \Omega^2}$:

$$\rho'_{ee}(\Delta\omega, t) = \frac{1}{2}\frac{\Omega^2}{\Delta\omega^2 + \Omega^2}\left(1 - \cos\left(\sqrt{\Delta\omega^2 + \Omega^2}\, t\right)\right) , \tag{2.16}$$

as it should be. Note that the exponential decrease of the excited state population seems to take place with only half the expected rate in Eq. (2.14). However, as the result describes excitation starting from the ground state and subsequent ionization, the rate with which the population decreases is not simply γ_{i} for this particular solution. In comparison, the solution obtained with the same method, but with the excited state as the initial state and vanishing laser excitation ($\Omega = 0$) does in fact decrease with the rate γ_{i}, independent of the detuning.

In Figs. 2.1-2.4, the solution (2.14) for the transient line shape of the $2S$ population in the vicinity of the hydrogen $1S$–$2S$ two-photon resonance is illustrated, where an intensity of 2.3 MW/m^2 is used, which is a typical magnitude in the MPQ experiment. Specifically, in Figs. 2.1 and 2.2, one can investigate the influence of the ionization channel on the transient line shape for a typical interaction time of the $1S$–$2S$ experiment in Garching. The inclusion of the ionization channel mainly changes the excitation efficiency while having only little effect on the spectral line width or on coherence features. This is plausible, because on this timescale, which is much shorter than the Rabi oscillation time, the $2S$ state is only populated very little.

In Figs. 2.3 and 2.4, one can observe the strong influence of the ionization on the line shape for interaction times on the order of one Rabi oscillation and longer. With ionization taken into account (Fig. 2.4), the excitation of the $2S$ level is much less efficient, the coherence features (fringes) are washed out and spectral hole burning occurs, because close to zero detuning, excitation and subsequent ionization is enhanced. Also, the fact that the system does not evolve to a steady state is apparent.

As the EOM suggest, one obtains a symmetric line shape around $\Delta\omega = 0$. However, it should be pointed out that this is no longer true for a collective signal from a thermal atomic beam. In that case, different second-order Doppler shifts according to Eq. (2.13), which all have the same sign, asymmetrically distort the line shape, depending on the atomic beam parameters. The basic discussion here therefore only applies to a mono-energetic beam of atoms. In this case, the line center is simply shifted by the second-order Doppler shift and the dynamic Stark effect.

The discussion of the line width is more involved, because at each point in time, the line shape is different (see also Fig. 2.13) and therefore the width is not defined unambiguously in the transient regime. A possible measure for the line width is then the full width taken at the outermost half maximum values of the line. With this definition, the influence of ionization, excitation intensity and interaction time on the $\Delta\omega$-dependence of the line shape can be discussed at least qualitatively.

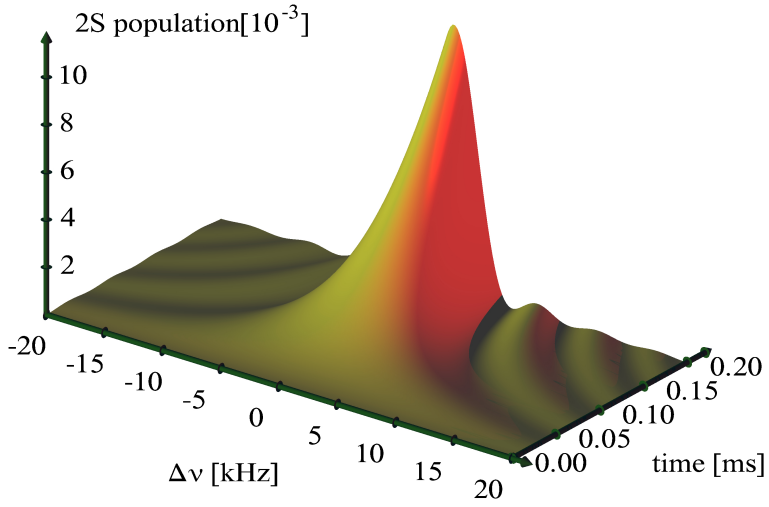

Figure 2.1: Atomic population in the $2S$ state of hydrogen (Z=1) as a function of interaction time t with the laser, and of detuning $\Delta\nu$ from the $1S$–$2S$ transition frequency, as defined in Eq. (2.12) with $\nu_{eg} \approx 2466$ THz. The laser intensity is $I = 2.3$ MW/m^2, corresponding to $\Omega = 2\pi \times 169$ Hz. The initial state at $t = 0$ is the $1S$ state. In the time evolution of the system, ionization from the $2S$ state into the continuum and spontaneous decay of the $2S$ state are neglected, i.e. ρ'_{ee} from Eq. (2.16) is plotted.

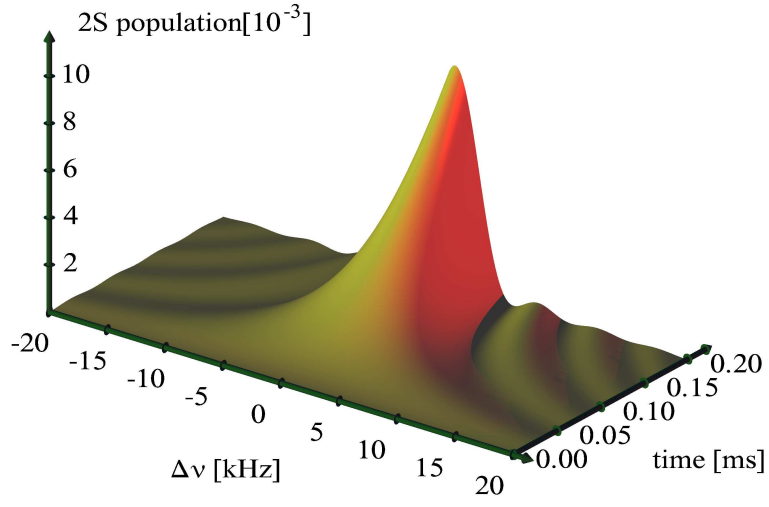

Figure 2.2: Same situation as in Fig. 2.1, except that in this plot, the effect of ionization is included, as in Eqs. (2.14,2.15). The ionization rate is $\gamma_i = 2\pi \times 276$ Hz. For the short times considered here, there is only a small difference to Fig. 2.1 in the total excitation efficiency, which is due to the ionization loss from the excited state.

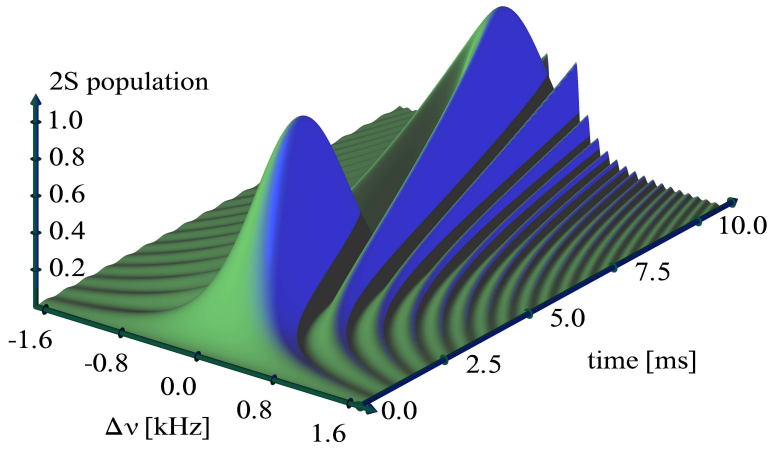

Figure 2.3: Same plot as in Fig. 2.1, but for interaction times comparable with the Rabi oscillation time of 5.9 ms. Ionization from the $2S$ state is not taken into account. At zero detuning, the $\sin^2$-shaped Rabi oscillations with full amplitude can be observed. All the other sections along constant detuning can also be understood as the well-known Rabi oscillations with diminished amplitude and generalized Rabi frequency $\Omega_R = \sqrt{\Delta\omega^2 + \Omega^2}$ in complete analogy with one-photon transitions, except that the two-photon Rabi frequency Ω as defined in Eq. (2.7) is proportional to the intensity, rather than to the electric field amplitude.

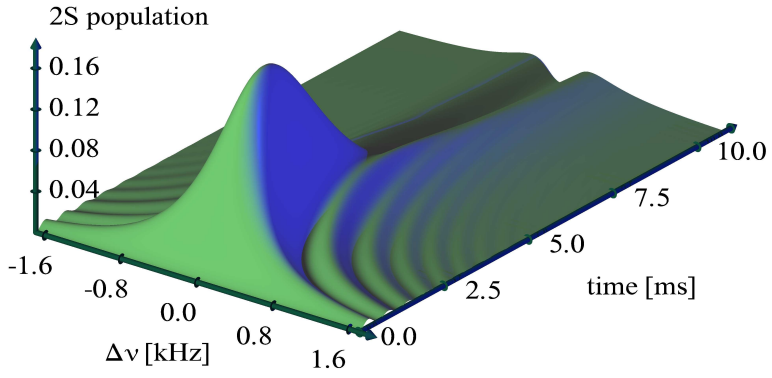

Figure 2.4: Same situation as in Fig. 2.3, except that here the ionization from the $2S$ state is properly included. The presence of the ionization channel leads to large differences compared to Fig. 2.3, because at times comparable to the Rabi oscillation time, the $2S$ state is significantly populated and consequently the ionization probability is not negligible. The decay of the $2S$ population, spectral hole burning and a loss of coherence can be observed in this image. The maximum population of the $2S$ state is 0.175, see Eq. (2.17), whereas without ionization the $2S$ population repeatedly reaches 100% on resonance ($\Delta\nu = 0$). Including the $2S$ spontaneous two-photon decay of $\gamma_s = 2\pi \times 1.31$ Hz does not change the plot discernibly.

Consider the $\Delta\omega$-dependent factors in the expression for the line shape (2.14a). The factor $1/G$ is time-independent and embodies two contributions to the width. For increasing detuning $\Delta\omega$, $1/G$ decreases more slowly if the intensity dependent Rabi frequency Ω is large. This results in a time-independent power broadening contribution. Likewise, the presence of an ionization channel, quantified by the ionization rate γ_i, adds to this width, which constitutes an ionization broadening of the line.

For the time-dependent factor, $\sin^2(\Omega_1 t) + \sinh^2(\Omega_2 t)$, first consider the case of vanishing ionization, $\Omega_2 = 0$ (see also Fig. 2.3). The remaining term $\sin^2(\Omega_1 t)$ produces fringes within the line shape that become arbitrarily narrow with increasing interaction time t in the absence of any damping. In Figs. 2.1 and 2.2, the $\sin^2(\Delta\omega)/\Delta\omega^2$-type of line shape, which is characteristic for the sudden turn-on of the excitation [38], can be recognized. However, the envelope of these fringes as well as any unfringed line shape always increase in width if ionization is taken into account by including the $\sinh^2$ term.

When one compares the detuning ranges of Figs. 2.1 and 2.2 with Figs. 2.3 and 2.4, one also observes that the width of the central peak decreases for increasing interaction time. Experimentally, this is observable as a time-of-flight dependent broadening contribution.

On two-photon resonance ($\Delta\nu = 0$) and for short interaction times, an expansion of the solution for ρ'_{ee} reveals that the $2S$ population initially grows proportional to t^2. The global maximum excited state population $\rho'^{(\mathrm{max})}_{ee}$, which occurs at zero detuning $\Delta\omega = 0$, can be obtained easily from Eq. (2.14a). It reads

$$\rho'^{(\mathrm{max})}_{ee} = \exp\left[-\frac{\beta_\mathrm{ioni} \arccos\left(\dfrac{\beta^2_\mathrm{ioni}}{8\beta^2_{ge}} - 1\right)}{\sqrt{16\beta^2_{ge} - \beta^2_\mathrm{ioni}}} \right], \tag{2.17}$$

and is independent of the intensity of the laser field. Note that for the strongly damped case where $\beta_\mathrm{ioni} > 4\beta_{ge}$, both the arccos and the square root are complex valued, but the result remains real. If spontaneous decay is included into the dynamics, as described below, the peak excited state population $\rho'^{(\mathrm{peak})}_{ee}$ is always less than given in Eq. (2.17), because the decay transfers population only from the excited state to the ground state. Expression (2.17) then gives the high-intensity limit for $\rho'^{(\mathrm{peak})}_{ee}$, where ionization dominates over the spontaneous decay.

2.2.2 Quantum dynamics including spontaneous decay

In the following, systems in which the spontaneous decay channel is no longer negligible will be considered. As specific examples, the $1S$–$2S$ and the $1S$–$3S$ transitions will be treated, in systems where the nuclear charge number is not restricted to $Z = 1$. Consider the Z-scaling of the spontaneous decay rates, listed in Tab. 2.1 (see, e.g., [40–42] and pp. 266-267 in [43]). One-photon spontaneous decay rates of dipole allowed transitions are denoted by $\gamma_\mathrm{s}^{1\gamma}$, for two-photon spontaneous decay rates, the symbol $\gamma_\mathrm{s}^{2\gamma}$ is used. The ionization rate coefficient β_ioni scales with Z^{-4} [see chapter 3, Eq. (3.37)], therefore the

Table 2.1: Spontaneous decay rates (angular frequency) relevant to the description of the quantum dynamics of the $1S$–$2S$ and $1S$–$3S$ transition in hydrogenlike systems with nuclear charge number Z.

$\gamma_{\rm s}^{1\gamma}(3S \to 2P)$	$6.32 \times 10^6\, Z^4\, \mathrm{rad/s}$
$\gamma_{\rm s}^{1\gamma}(2P \to 1S)$	$6.25 \times 10^8\, Z^4\, \mathrm{rad/s}$
$\gamma_{\rm s}^{2\gamma}(3S \to 1S)$	$2.08\, Z^6\, \mathrm{rad/s}$
$\gamma_{\rm s}^{2\gamma}(3S \to 2S)$	$6.45 \times 10^{-2}\, Z^6\, \mathrm{rad/s}$
$\gamma_{\rm s}^{2\gamma}(2S \to 1S)$	$8.23\, Z^6\, \mathrm{rad/s}$

ratio R of the spontaneous decay rate and the ionization rate $\gamma_{\rm i}$, as defined in (2.10), scales as

$$R^{1\gamma} = \frac{\gamma_{\rm s}^{1\gamma}}{\gamma_{\rm i}} \propto Z^8\,, \qquad R^{2\gamma} = \frac{\gamma_{\rm s}^{2\gamma}}{\gamma_{\rm i}} \propto Z^{10} \tag{2.18}$$

for a given laser intensity. Recall that in hydrogen $1S$–$2S$, for typical intensities, the spontaneous decay rate is small compared to the ionization rate, i.e. $R^{2\gamma} \ll 1$. In contrast, for the $1S$–$2S$ transition in hydrogenlike helium ($Z=2$) and the same intensity of 2.3 MW/m^2, both rates are of comparable magnitude, with $R^{2\gamma} \approx 1.6$. The simplified form of the analytic solution (2.14) is therefore no longer valid, and even qualitative discussions of the analytic form of the full solution for the line shape (see Sec. 2.4) are quite involved. Nevertheless, one can plot the full solution (2.35), and Figs. 2.5 and 2.6 show the transient line shape of the excited state of a He^+ ion, irradiated with a cw-laser of intensity 2.3 MW/m^2. This intensity is chosen to simplify the comparison with the hydrogen plots, although a cw-laser source with the required wavelength of 61 nm does not yet exist.

In Fig. 2.5 one can observe, that on a timescale comparable to the inverse spontaneous decay rate, the line shape evolves into a "quasi" steady state of approximate Lorentzian profile. Only on a longer timescale, ionization becomes important, and the excited state is significantly depopulated (see Fig. 2.6). The characteristic decay time of the excited $2S$ population is by far longer than the inverse ionization rate $2\pi/\gamma_{\rm i}$. The reason for this seemingly unintuitive behavior is, that the laser field continuously drives the system. While the excited state is depopulated by the ionization, new population from the ground state is transferred into the excited state, which acts like a reservoir for the population for the considered low-intensity regime.

For $\gamma_{\rm s} \neq 0$, the peak population of the excited state, $\rho_{ee}^{\prime(\mathrm{peak})}$, occurring in the transient dynamics, is a function of the intensity of the driving laser, when spontaneous decay is included in the EOM. For He^+, this dependence is shown in Fig. 2.7. For large intensities, the peak population approaches the maximum value given in Eq. (2.17).

In Fig. 2.8, the full solution of the EOM (2.11) for the $1S$–$2S$ transition in Li^{2+} is plotted, again for a laser intensity of 2.3 MW/m^2 as in Fig. 2.5, but with a wavelength of 27 nm.

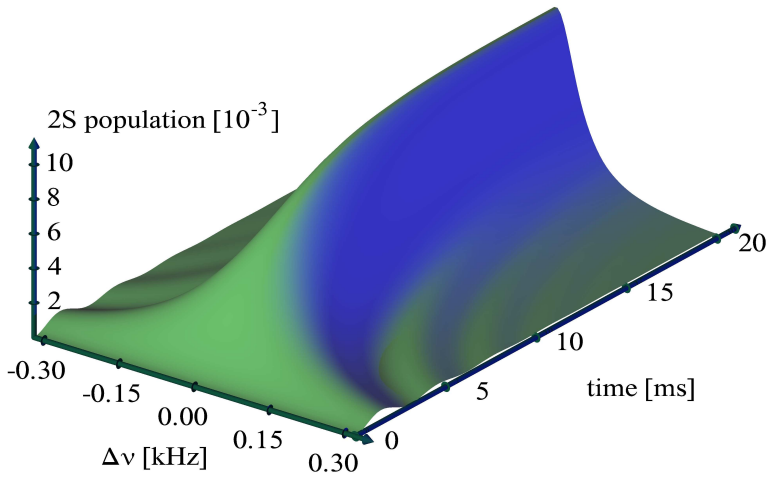

Figure 2.5: $2S$ population in a He^+ ion, as a function of detuning [defined in Eq. (2.12)] and interaction time with the laser, driving the $1S$–$2S$ transition. Ionization and spontaneous two-photon decay of the $2S$ state are taken into account. A constant intensity of 2.3 MW/m^2 is assumed and the ion is in the $1S$ ground state at time $t = 0$. On the timescale considered, the system evolves into a "quasi" steady state with approximate Lorentzian line shape.

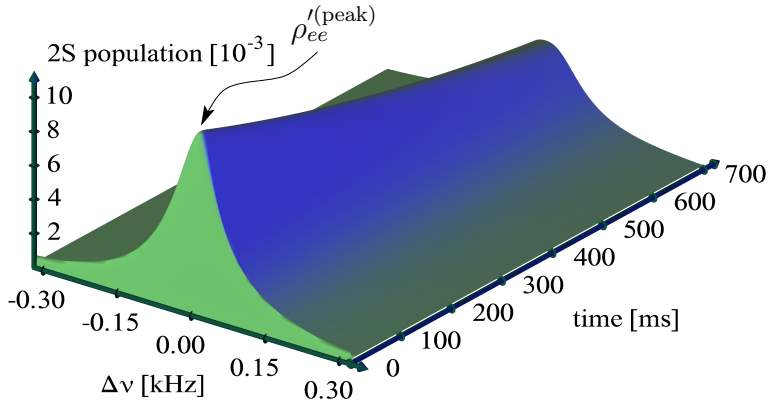

Figure 2.6: $2S$ population dynamics including two-photon spontaneous decay in a He^+ ion as in Fig. 2.5, but on a much longer timescale. Here the decrease of the population due to ionization is visible. Note that the effective population loss is by far smaller than the ionization rate $\gamma_i = 2\pi \times 17.3$ Hz (corresponding to a characteristic ionization time of 58 ms), because the "quasi" steady state population of the excited state is small. The peak population in the excited state is 10.6×10^{-3} for the considered intensity of 2.3 MW/m^2. The steep rise for $t < 20$ ms is shown in more detail in Fig. 2.5.

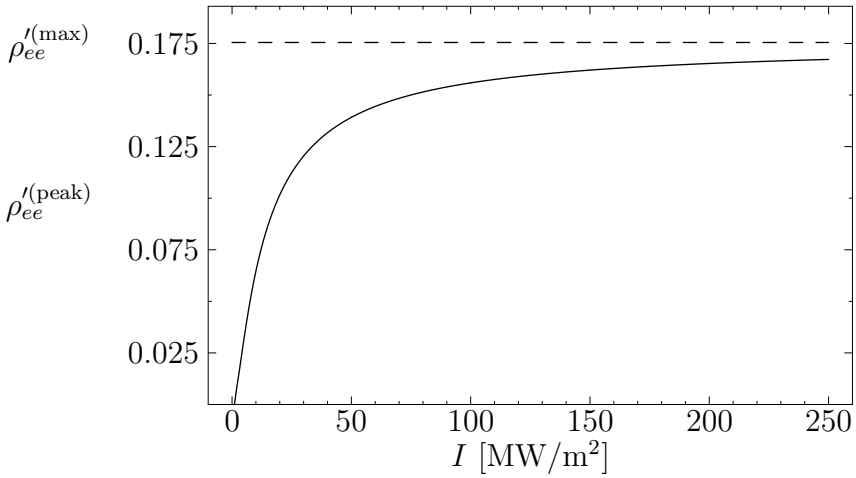

Figure 2.7: Peak $2S$ population in He^+ (see $\rho_{ee}^{\prime(\mathrm{peak})}$ in Fig. 2.6), as a function of intensity, including spontaneous decay (solid line) and without spontaneous decay (dashed line), which is equal to $\rho_{ee}^{\prime(\max)}$ in Eq. (2.17), evaluated for the $1S$–$2S$ transition. For increasing intensity, the ionization rate eventually becomes large compared to the spontaneous decay rate, and the peak population increases, approaching the maximum $\rho_{ee}^{\prime(\max)}$.

As $R^{2\gamma}$ is larger by a factor of 1000 as compared to hydrogen, spontaneous emission dominates the dynamics and the system evolves into a "quasi" steady state very fast.

By calculating the population in the continuum P state, $1 - \rho'_{gg}(\Delta\omega, t) - \rho'_{ee}(\Delta\omega, t)$, one obtains the probability of ionization via the two-photon resonant excited state as a function of detuning and time, if $|g\rangle$ is the $1S$ state. In Fig. 2.9, this ϵP population is plotted from the full solution (2.35) of the EOM (2.11) for the $1S$–$2S$ transition in hydrogen, and an intensity of 2.3 MW/m^2, as before.

Note that because of the ionization $\gamma_\mathrm{i} \neq 0$, the steady state of the system can be defined as the completely ionized atom, while for $\gamma_\mathrm{i} = 0$, a regular steady state with a certain population distribution between the excited and ground states exists. The limit $\gamma_\mathrm{i} \to 0$ is therefore non-uniform, in the sense that the steady state for $\gamma_\mathrm{i} \neq 0$ does not tend to the steady state of the case $\gamma_\mathrm{i} = 0$.

As a result, for increasing interaction time, the detuning range in which the atomic population is completely ionized, increases in width, as can be observed in Fig. 2.9. For a precision experiment relying on the detection of ionized particles, this means that the interaction time has to be chosen carefully in order to obtain a signal of minimal width. Using a detection scheme for charged particles instead of excited atoms has the advantage of a higher detection efficiency.

For the $1S$–$2S$ transition, the two-photon spontaneous decay rate $\gamma_\mathrm{s}^{2\gamma}$ is the only significant spontaneous decay channel (see also Sec. 3.7). For the $1S$–$3S$ transition, the dominating decay takes place via the real intermediate $2P$ state, as depicted in Fig. 2.10, because the one-photon rates are orders of magnitude larger than the two-photon rates (see Tab. 2.1).

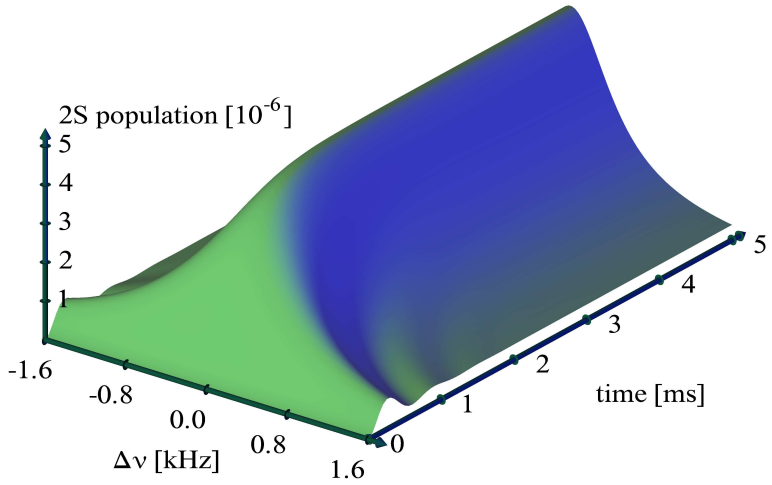

Figure 2.8: $2S$ population in Li^2+, as a function of detuning [defined in Eq. (2.12)] and interaction time with the laser, driving the $1S$–$2S$ transition. A constant intensity of 2.3 MW/m^2 is assumed and the ion is in the $1S$ ground state at t=0. The ratio of ionization rate to spontaneous decay rate is a thousand times smaller than for the hydrogen atom, and ionization is almost negligible.

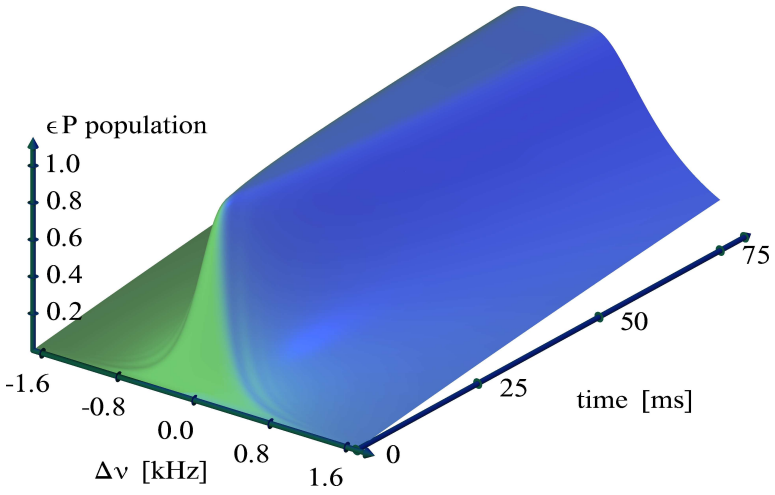

Figure 2.9: Ionized population in the continuum P state as a function of detuning [defined in Eq. (2.12)] and interaction time with the laser, driving the hydrogen $1S$–$2S$ transition, including spontaneous two-photon decay of the intermediate $2S$ state with $\gamma_s = 2\pi \times 1.31$ Hz. A constant intensity of 2.3 MW/m^2 is assumed and the atom is in the $1S$ ground state at $t = 0$.

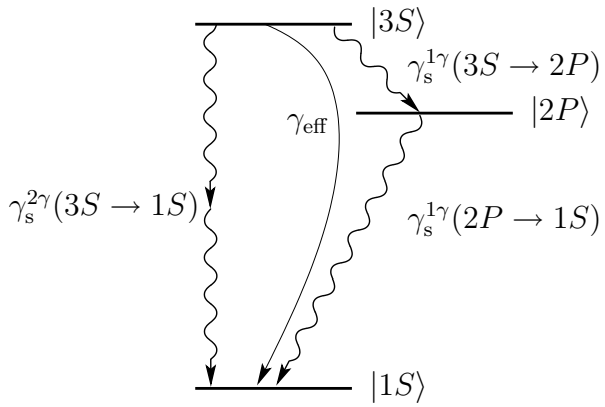

Figure 2.10: Level scheme of the $3S$–$1S$ spontaneous decay. The two-step one-photon channel with the rates $\gamma_s^{1\gamma}$ dominates over the direct two-photon decay, and can be expressed by a direct effective rate γ_{eff}. The two-step two-photon channel via the $2S$ state is omitted.

Strictly speaking, it would be necessary to introduce a new set of EOM including the real intermediate $2P$ level. However, the $2P$ state is not resonantly coupled to some other state by the laser field and is populated only by incoherent decay. In addition, the decay rate out of $2P$ is a hundred times larger than the decay rate into it. One can therefore approximate the quantum dynamics of a $1S$–$3S$ transition by the EOM (2.11), if one uses an effective decay rate from the $3S$ state to the $1S$ ground state, which equals $\gamma_{\text{eff}} = \gamma_s^{1\gamma}(3S \to 2P)$. The direct two-photon decay and the two-step process of two-photon decays via the $2S$ level are completely negligible in comparison.

2.3 Generalizations of the equations of motion

The basic interaction of an atom with a laser field of constant intensity as discussed above, is generalized to more realistic scenarios in this section. In particular, if one allows for the motion of an atom through the driving standing wave, the master equations (2.11) need to be modified. In addition, the light intensity in most experiments is not constant, e.g., the atom under consideration may move through an inhomogeneous laser profile. In this case, the laser intensity can be described in terms of the trajectory $\boldsymbol{r}(t)$ as $I(\boldsymbol{r}(t))$. The atom may also be excited with counter-propagating laser pulses, in which case one needs to consider the unequal, time-dependent intensities incident on the atom from opposite directions.

In general, an analytic solution including the varying AC Stark shift and varying Rabi frequency in these more general cases is either extremely difficult or impossible to find. Nonetheless, the equations of motion can still be integrated numerically with very little more computational requirements, if one includes a time dependent intensity $I(t)$, specific to the experimental setup, into the master equations, for example by using the Runge-Kutta routines from Ref. [44].

2.3.1 Motion in a standing wave and time-dependent intensity

When one uses the term "intensity" in the context of two-photon spectroscopy, one must be aware that in most experiments in an enhancement resonator on resonance, the intensity profile in longitudinal direction is spatially modulated as

$$I_s(x) = 2I\cos^2(k\,x)\,, \tag{2.19}$$

where I denotes the mean intensity averaged over an integer multiple of nodes, and where the cavity axis is taken as the x-axis, with k being the modulus of the wave vector. If the interacting atom is fixed in space, it is simply driven with the intensity at the respective position which ranges from 0 to $2I$. In this case the determination of the exact location of the atom in the resonator would be a difficult experimental task and could probably only be accomplished in a trap setup.

However, for moving atoms in a standing wave, the description of a laser electric field with one frequency ω_{L}, as used in the interaction Hamiltonian (2.3), is no longer appropriate, since in the rest frame of the atom, the electric field can only be described by a superposition of two oppositely running waves that are Doppler shifted with opposite signs. In the photon picture, this situation, as observed by the moving atom, is depicted in Fig. 2.11. As will be shown in the following, this leads to new master equations, which can only be reduced to the conventional EOM (2.11), if certain conditions are satisfied.

Since the electric field, experienced by a moving atom, cannot be described as a monochromatic, harmonic field, the electric field of a plane standing wave in the lab frame is reconsidered. The electric field strength $E(\boldsymbol{r},t)$ of the standing wave, which is taken to be polarized in the z direction, can be written as a superposition of two running waves,

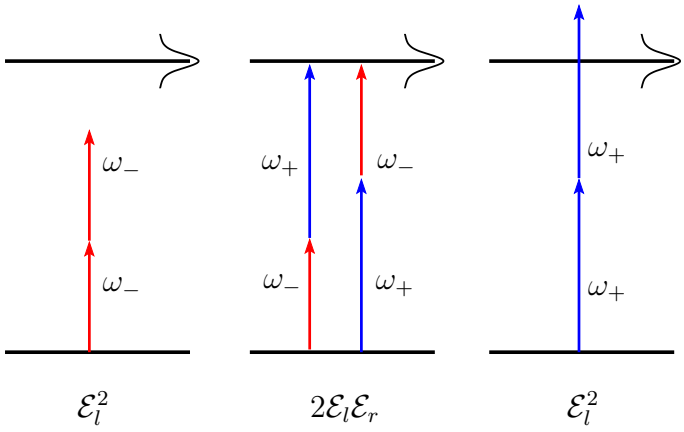

Figure 2.11: Excitation of a two-photon transition in a bichromatic field, which consists of a "left" beam with frequency ω_- and electric field amplitude $\mathcal{E}_l$ and a "right" beam with frequency ω_+ and electric field amplitude $\mathcal{E}_r$. The Rabi frequency with which the transition is driven, is proportional to the product of the electric field amplitudes, for the first-order Doppler free transition (middle).

propagating in the $+x$ and $-x$ directions, respectively:

$$E(\boldsymbol{r},t) = \mathcal{E}_l \cos[\omega_\mathrm{L}(t - x/c)] + \mathcal{E}_r \cos[\omega_\mathrm{L}(t + x/c)]\,. \tag{2.20}$$

Transformed into a frame moving along with an atom of velocity v relative to the lab frame, the field strength reads

$$E(\boldsymbol{r}',t') = \mathcal{E}_l \cos[\omega_-(t' - x'/c)] + \mathcal{E}_r \cos[\omega_+(t' + x'/c)]\,, \tag{2.21}$$

where $\beta = v/c$ and

$$\omega_+ = \omega_\mathrm{L}\frac{1+\beta}{\sqrt{1-\beta^2}}\,, \qquad \omega_- = \omega_\mathrm{L}\frac{1-\beta}{\sqrt{1-\beta^2}}\,. \tag{2.22}$$

At the location of the atom, set to be $x' = 0$, there is then a purely time-dependent field with field strength

$$E(t') = \mathcal{E}_l \cos(\omega_- t') + \mathcal{E}_r \cos(\omega_+ t')\,, \tag{2.23}$$

expressed in the proper time t' of the atom. In this field, the two-photon Rabi frequency Ω, the master equations, the dynamic Stark effect $\Delta\nu_\mathrm{AC}$ and the ionization rate γ_i receive modifications as compared to the monochromatic case. First, the effect on the quantum dynamics of the excitation process is considered.

To this end, the bichromatic field (2.23) is inserted into the interaction part of the Hamiltonian in the von Neumann equation (2.1), instead of the original $\cos(\omega_\mathrm{L}t)$ term. Then the transformation into the interaction picture is performed, with respect to the unshifted laser angular frequency ω_L, as defined in Eq. (2.8). Dropping all terms which oscillate with a frequency on the order of ω_L, one arrives at the set of equations:

$$\begin{aligned}
\frac{\partial}{\partial t}\rho'_{gg} =& -\Omega\,\mathrm{Im}(\rho'_{ge}) + \gamma_\mathrm{s}\,\rho'_{ee} \\
&+ \frac{\mathrm{i}}{2}\,\exp(-2\mathrm{i}\omega_\mathrm{D}t)\,\left(\Omega_\mathrm{r}\,\rho'_{ge} - \Omega_\mathrm{l}\,\rho'_{eg}\right) + \frac{\mathrm{i}}{2}\,\exp(2\mathrm{i}\omega_\mathrm{D}t)\,\left(\Omega_\mathrm{l}\,\rho'_{ge} - \Omega_\mathrm{r}\,\rho'_{eg}\right)\,, \qquad \text{(2.24a)} \\
\frac{\partial}{\partial t}\rho'_{ge} =& -\mathrm{i}\,\Delta\omega\,\rho'_{ge} + \mathrm{i}\,\frac{\Omega}{2}\,(\rho'_{gg} - \rho'_{ee}) - \frac{\gamma_\mathrm{i}+\gamma_\mathrm{s}}{2}\,\rho'_{ge} \\
&+ \frac{\mathrm{i}}{2}\,\exp(-2\mathrm{i}\omega_\mathrm{D}t)\,\Omega_\mathrm{l}\,\left(\rho'_{gg} - \rho'_{ee}\right) + \frac{\mathrm{i}}{2}\,\exp(2\mathrm{i}\omega_\mathrm{D}t)\,\Omega_\mathrm{r}\,\left(\rho'_{gg} - \rho'_{ee}\right)\,, \qquad \text{(2.24b)} \\
\frac{\partial}{\partial t}\rho'_{ee} =& \Omega\,\mathrm{Im}(\rho'_{ge}) - (\gamma_\mathrm{i}+\gamma_\mathrm{s})\,\rho'_{ee} \\
&+ \frac{\mathrm{i}}{2}\,\exp(-2\mathrm{i}\omega_\mathrm{D}t)\,\left(\Omega_\mathrm{l}\,\rho'_{eg} - \Omega_\mathrm{r}\,\rho'_{ge}\right) + \frac{\mathrm{i}}{2}\,\exp(2\mathrm{i}\omega_\mathrm{D}t)\,\left(\Omega_\mathrm{r}\,\rho'_{eg} - \Omega_\mathrm{l}\,\rho'_{ge}\right)\,, \qquad \text{(2.24c)}
\end{aligned}$$

where the first line of each subequation equals the expression obtained in the basic master equations (2.11), while the second line of each subequation represents the additional contribution which is due to the motion in the electric field of the standing wave. Here, the definitions

$$\Omega = 2(2\pi\beta_{ge}) \times 2\sqrt{I_l(t)I_r(t)}\,, \qquad \Omega_\mathrm{l} = 2(2\pi\beta_{ge})I_l(t)\,, \qquad \Omega_\mathrm{r} = 2(2\pi\beta_{ge})I_r(t) \tag{2.25}$$

were introduced, and the relation

$$I_l(t) = \frac{1}{2}\epsilon_0 c\, \mathcal{E}_l(t)^2 \qquad I_r(t) = \frac{1}{2}\epsilon_0 c\, \mathcal{E}_r(t)^2 \tag{2.26}$$

between the intensity and the electric field amplitude of a running plane wave was used. The time variation of the electric field amplitudes need to be slow as compared to the optical frequency, for the definition of the intensity to make sense. This condition is well fulfilled in all cases except for few-cycle pulses. Obviously, the Doppler shift of the two frequency components, which is denoted by $\omega_{\mathrm{D}} = \omega_+ - \omega_{\mathrm{L}} = \omega_{\mathrm{L}} - \omega_-$, determines the oscillation frequency of the additional terms in the differential equations (2.24). For the case that this frequency is much larger than all other frequencies occurring in these new master equations, the fast oscillations average out, in analogy with the high-frequency terms which are dropped in the rotating wave approximation.

Any other very-high frequency variation can be averaged in the sense as discussed above, but as soon as the characteristic time τ_I of the intensity variation does not fulfill the condition $1/\tau_I \gg \max\{\Omega, \gamma_{\mathrm{i}}, \gamma_{\mathrm{s}}\}$, $I(t)$ fully enters the equations of motion for the atomic density matrix. For example, in chapter 5 a numerical integration of the EOM is performed, where the laser field driving the hydrogen $1S$–$2S$ transition is a standing wave with a Gaussian beam profile. The radial intensity variations of this laser field, observed by the atoms along their trajectories passing the Gaussian beam, are included in the EOM and turn out to be the origin of an important broadening contribution to the experimental line width, namely the inhomogeneous AC Stark broadening.

In summary, an atom that moves with the velocity v through a superposition of counter-propagating lasers with equal frequency ω_{L} in the laboratory frame and with time-dependent intensities $I_l(t)$ and $I_r(t)$ at the location of the atom, can be described by the usual master equation (2.11), given that the condition

$$\omega_{\mathrm{L}}\left(\frac{1+\beta}{\sqrt{1-\beta^2}} - 1\right) \gg \max\{\Omega, \gamma_{\mathrm{i}}, \gamma_{\mathrm{s}}\} \tag{2.27}$$

is satisfied. In the case of unequal, time dependent intensities of the counter-propagating lasers, the following replacement for the two-photon Rabi frequency

$$\Omega = 2(2\pi\beta_{ge})I(t) \quad \rightarrow \quad \Omega = 2(2\pi\beta_{ge}) \times 2\sqrt{I_l(t) I_r(t)} \tag{2.28}$$

needs to be made in the master equation, if the first-order Doppler free transition is considered.

For the case of the hydrogen $1S$–$2S$ experiment, this is not a strong restriction as the required minimum velocity to satisfy condition (2.27) is very low for a typical thermal beam. For a driving laser intensity of some MW/m^2, this minimum velocity corresponds to a temperature of the atomic beam on the order of 10^{-14} K. From a laboratory frame point of view, condition (2.27) simply means that an atom passes through the intensity profile (2.19) quickly enough, such that it effectively averages over the nodes and antinodes of the field. Then the quantum dynamics of the atom can be treated as if it was driven by a constant intensity I.

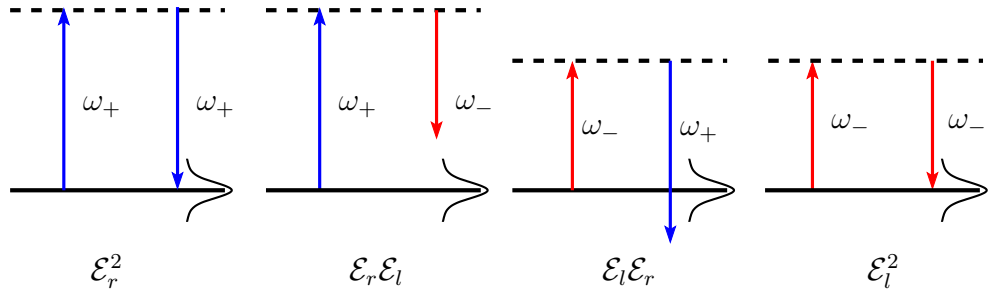

Figure 2.12: Illustration of contributions to the dynamic Stark effect in a bichromatic field (2.23). For sufficient frequency difference, only the processes involving photons of equal frequency can contribute.

Now the modification of the dynamic Stark effect in a bichromatic field is discussed. As will be shown in detail in chapter 3, the dynamic Stark shift of an atomic energy level is caused by an off-resonant interaction with the laser field. This interaction can loosely be interpreted as an absorption of a laser photon, bringing the atom to a virtual intermediate state, followed by the stimulated emission of the photon back to the laser mode. The opposite sequence of events can also take place. Here, only the fact that there are two laser fields of different frequency are present, will be briefly commented on. As is illustrated in Fig. 2.12, the situations in which two equal-frequency photons are involved, correspond to contributions to the dynamic Stark shift that are caused independently by the "left" and "right" laser beam. The processes in which one photon from each laser mode is involved, would lead to a nontrivial combined shift of the atomic energy, as well as to a net recoil and consequently to a large recoil shift. However, if condition (2.27) is satisfied, the frequency difference between the photons from each beam is much larger than the excited state width, therefore these processes, corresponding to the two sketches in the middle of Fig. 2.12, cannot take place.

This can also be explained, in a short anticipation of chapter 3, by considering the bichromatic interaction Hamiltonian

$$V(t) = -ez\left[\mathcal{E}_l\cos(\omega_- t) + \mathcal{E}_r\cos(\omega_+ t)\right] . \tag{2.29}$$

When one calculates the second-order perturbation to the energy in time-dependent perturbation theory (see Sec. 3.4.1), one encounters the time evolution operator

$$U_{\mathrm{I}}^{(2)}(0,t) = -\frac{1}{\hbar^2}\int_0^t dt' \int_0^{t'} dt'' V(t')V(t'') , \tag{2.30}$$

which splits into four summands upon insertion of (2.29). The integrals containing the unequal-frequency product $\cos(\omega_- t')\cos(\omega_+ t'')$ average to zero, precisely because the cosines oscillate with different frequencies, and the two conventional monochromatic contributions to the dynamic Stark shift remain.

Accordingly, if condition (2.27) is satisfied, in the master equations the replacements

$$\Delta\nu_{\mathrm{AC}} = \beta_{\mathrm{AC}}\, I(t) \quad \rightarrow \quad \Delta\nu_{\mathrm{AC}} = \beta_{\mathrm{AC}}[I_l(t) + I_r(t)] , \tag{2.31}$$

describe the dynamic Stark shift $\Delta\nu_{\mathrm{AC}}$ appropriately in the frame of the moving atom and for generally unequal beam intensities. Since the ionization rate γ_{i} is proportional to the imaginary part of the Stark effect, the analogous replacement reads

$$\gamma_{\mathrm{i}} = (2\pi\beta_{\mathrm{ioni}})\, I(t) \quad \rightarrow \quad \gamma_{\mathrm{i}} = (2\pi\beta_{\mathrm{ioni}})[I_l(t) + I_r(t)]\,. \tag{2.32}$$

The limits in the case of equal intensities $I_l(t) = I_r(t) =: I_{\text{per dir.}}(t)$ are intuitive, because then all replacements (2.28),(2.31), and (2.32) are equivalent to simply setting

$$I(t) \rightarrow 2I_{\text{per dir.}}(t)\,. \tag{2.33}$$

Taking the limit, e.g., $I_r \rightarrow 0$, leads to

$$\Omega \rightarrow 0\,, \qquad \Delta\nu_{\mathrm{AC}} \rightarrow \beta_{\mathrm{AC}} I_l(t)\,, \quad \gamma_{\mathrm{i}} = (2\pi\beta_{\mathrm{ioni}}) I_l(t) \tag{2.34}$$

for the Doppler free transition. The Rabi frequency vanishes because the Doppler free transition cannot be driven in a pure running wave, while the dynamic Stark effect, which is an off-resonant process, still remains to the extent that is expected from the interaction with the "left" laser.

2.3.2 Further generalizations

Any additional spontaneous decay channels can also be fully included in a numerical integration algorithm. In addition to the intensity dependent frequency shifts $\Delta\nu_{\mathrm{AC}}$, any other frequency shifting effect can be easily included into the numerical approach by adapting Eq. (2.12), as described already for the velocity dependent second-order Doppler shift in Eq. (2.13).

In most cases, instead of a single atom one considers an ensemble of atoms, all of which may experience different intensities, Doppler shifts and interaction times along different trajectories. The contribution of each single atom to the line shape can be calculated like described above, and the line shape observed for the atomic ensemble is then the sum of all single-atom contributions, given that the single atoms interact independently with the laser. In a dilute beam experiment this condition is very well fulfilled.

Together with the atomic constants presented in the following chapter, the set of equations (2.11) are thus a tool for a wide range of problems in spectroscopy. For the case of the MPQ $1S$–$2S$ experiment in hydrogen, a specific implementation is described in chapter 5.

Note that the transition matrix elements and Stark coefficients that enter into Eq. (2.11) vary slightly with the laser frequency. However, the detuning $\Delta\nu$ is typically a few kHz, whereas the optical resonance frequencies are on the order of 10^{15} Hz. For the $1S$–$2S$ transition, the resulting relative variation of β_{AC} is on the order of 10^{-12}, which is negligibly small.

2.4 Analytic solution including ionization and spontaneous decay

In this section, the time-dependent solution of the full master equation (2.11) including both ionization and spontaneous decay damping is given for the time-dependent line shapes describing the probability of an atom to be in the excited state, $\rho'_{ee}(\Delta\omega, t)$, and to be in the ground state, $\rho'_{gg}(\Delta\omega, t)$. The initial condition for which these solutions were evaluated, corresponds to the situation where the atom is in the ground state, i.e., $\rho'_{gg}(0) = 1$ and $\rho'_{ee}(0) = \rho'_{ge}(0) = \rho'_{eg}(0) = 0$.

The lineshape of ionization products, i.e., the ionization probability as a function of detuning and time, are obtained from these solutions by evaluating $1 - \rho'_{ee}(\Delta\omega, t) - \rho'_{gg}(\Delta\omega, t)$. This is useful for the modeling of the line shape in an experiment relying on the detection of the ionized particles, instead of atoms in the excited state. In the case of hydrogen, especially the protons emerging from the ionization are an attractive candidate for a detection scheme, since they are influenced less by small stray electric fields than the electrons, and therefore might be guided more reliably to a detector.

The fully time-dependent solution of (2.11) for the atomic state populations reads

$$\begin{aligned}\rho'_{ee}(\Delta\omega, t) =& C\,\Omega^2 \Big\{ e^{-\Omega_c t}\,\Omega_b \left[\Omega_a(\Omega_a^2 - \Omega_b^2)\cosh(\Omega_a t) + \Omega_c(3\Omega_a^2 + \Omega_b^2 - 4\Omega_c^2)\sinh(\Omega_a t)\right] \\ &+ e^{\Omega_c t}\,\Omega_a \left[\Omega_b(\Omega_b^2 - \Omega_a^2)\cosh(\Omega_b t) - \Omega_c(\Omega_a^2 + 3\Omega_b^2 - 4\Omega_c^2)\sinh(\Omega_b t)\right] \Big\},\end{aligned} \tag{2.35}$$

$$\begin{aligned}\rho'_{gg}(\Delta\omega, t) =& \rho'_{ee}(\Delta\omega, t) + C \times \Big\{ 2e^{-\Omega_c t}\Omega_b \Big[\Omega_a \Big(8\Omega_c^4 + (\Omega_a^2 - \Omega_b^2)(\Delta\omega^2 + \Omega_a^2) \\ &+ \Omega_c(\gamma_\mathrm{i} + \gamma_\mathrm{s})(2\Delta\omega^2 + \Omega_a^2 + \Omega_b^2 - 2\Omega_c^2) - \Omega_c^2(5\Omega_a^2 + 3\Omega_b^2)\Big)\cosh(\Omega_a t) \\ &+ \Big(\Omega_c\left(\Omega_a^2(\Omega_a^2 + 3\Omega_b^2) + \Omega_c^2(\Omega_b^2 - \Omega_a^2 - 4\Omega_c^2) + \Delta\omega^2(3\Omega_a^2 + \Omega_b^2 - 4\Omega_c^2)\right) \\ &+ \frac{\gamma_\mathrm{i} + \gamma_\mathrm{s}}{2}\left((\Omega_a^2 - \Omega_b^2 + 4\Omega_c^2)(\Delta\omega^2 + \Omega_a^2 + \Omega_c^2) - 8\Omega_a^2\Omega_c^2\right)\Big)\sinh(\Omega_a t)\Big] \\ &+ 2e^{\Omega_c t}\Omega_a \Big[\Omega_b \Big(8\Omega_c^4 + (\Omega_b^2 - \Omega_a^2)(\Delta\omega^2 + \Omega_b^2) \\ &- \Omega_c(\gamma_\mathrm{i} + \gamma_\mathrm{s})(2\Delta\omega^2 + \Omega_a^2 + \Omega_b^2 - 2\Omega_c^2) - \Omega_c^2(3\Omega_a^2 + 5\Omega_b^2)\Big)\cosh(\Omega_b t) \\ &- \Big(\Omega_c\left(\Omega_b^2(\Omega_b^2 + 3\Omega_a^2) + \Omega_c^2(\Omega_a^2 - \Omega_b^2 - 4\Omega_c^2) + \Delta\omega^2(\Omega_a^2 + 3\Omega_b^2 - 4\Omega_c^2)\right) \\ &- \frac{\gamma_\mathrm{i} + \gamma_\mathrm{s}}{2}\left((\Omega_b^2 - \Omega_a^2 + 4\Omega_c^2)(\Delta\omega^2 + \Omega_b^2 + \Omega_c^2) - 8\Omega_b^2\Omega_c^2\right)\Big)\sinh(\Omega_b t)\Big]\Big\},\end{aligned} \tag{2.36}$$

with

$$C = \frac{e^{-\frac{1}{2}(\gamma_\mathrm{i} + \gamma_\mathrm{s})t}}{2\Omega_a\Omega_b\left[(\Omega_a - \Omega_b)^2 - 4\Omega_c^2\right]\left[(\Omega_a + \Omega_b)^2 - 4\Omega_c^2\right]}\,, \tag{2.37}$$

$$\Omega_a = \frac{\sqrt{2(\gamma_\mathrm{i}+\gamma_\mathrm{s})^2 - 8\Delta\omega^2 - 8\Omega^2 - \frac{3\gamma_\mathrm{s}\Omega^2}{\Omega_c} - D - K}}{2\sqrt{6}}\,, \tag{2.38}$$

$$\Omega_b = \frac{\sqrt{2(\gamma_\mathrm{i}+\gamma_\mathrm{s})^2 - 8\Delta\omega^2 - 8\Omega^2 + \frac{3\gamma_\mathrm{s}\Omega^2}{\Omega_c} - D - K}}{2\sqrt{6}}\,, \tag{2.39}$$

$$\Omega_c = \frac{\sqrt{(\gamma_\mathrm{i}+\gamma_\mathrm{s})^2 - 4\Delta\omega^2 - 4\Omega^2 + D + K}}{2\sqrt{6}}\,, \tag{2.40}$$

$$K = \frac{16\Delta\omega^4 + \left((\gamma_\mathrm{i}+\gamma_\mathrm{s})^2 - 4\Omega^2\right)^2 + 8\Delta\omega^2\left(4\Omega^2 - 7(\gamma_\mathrm{i}+\gamma_\mathrm{s})^2\right)}{4D}\,, \tag{2.41}$$

$$\begin{aligned} D = 2^{2/3}\Bigg\{ & 27\gamma_\mathrm{i}\Omega^2(\gamma_\mathrm{i}+\gamma_\mathrm{s})^3 + 2\left(\frac{5}{4}(\gamma_\mathrm{i}+\gamma_\mathrm{s})^2 + \Delta\omega^2 + \Omega^2\right)^3 \\ & - \frac{9}{2}\gamma_\mathrm{i}\Omega^2(\gamma_\mathrm{i}+\gamma_\mathrm{s})\left(5(\gamma_\mathrm{i}+\gamma_\mathrm{s})^2 + 4\Delta\omega^2 + 4\Omega^2\right) \\ & - \frac{9}{8}(\gamma_\mathrm{i}+\gamma_\mathrm{s})\left(4\Delta\omega^2 + 5(\gamma_\mathrm{i}+\gamma_\mathrm{s})^2 + 4\Omega^2\right)\left(4\Delta\omega^2(\gamma_\mathrm{i}+\gamma_\mathrm{s}) + (\gamma_\mathrm{i}+\gamma_\mathrm{s})^3 + 2(2\gamma_\mathrm{i}+\gamma_\mathrm{s})\Omega^2\right) \\ & + \frac{27}{16}\left(4\Delta\omega^2(\gamma_\mathrm{i}+\gamma_\mathrm{s}) + (\gamma_\mathrm{i}+\gamma_\mathrm{s})^3 + 2\Omega^2(2\gamma_\mathrm{i}+\gamma_\mathrm{s})\right)^2 \\ & + \Bigg[-4\left(\Delta\omega^4 + \frac{1}{16}\left((\gamma_\mathrm{i}+\gamma_\mathrm{s})^2 - 4\Omega^2\right)^2 + \frac{1}{2}\Delta\omega^2\left(-7(\gamma_\mathrm{i}+\gamma_\mathrm{s})^2 + 4\Omega^2\right)\right)^3 \\ & \quad + \frac{1}{1024}\Big[(\gamma_\mathrm{i}+\gamma_\mathrm{s})^6 - 64\Delta\omega^6 - 64\Omega^6 - 12\Omega^2(\gamma_\mathrm{i}+\gamma_\mathrm{s})^4 \\ & \qquad + 24\Omega^4\left(2\gamma_\mathrm{i}^2 + 4\gamma_\mathrm{i}\gamma_\mathrm{s} - 7\gamma_\mathrm{s}^2\right) - 48\Delta\omega^4\left(11(\gamma_\mathrm{i}+\gamma_\mathrm{s})^2 + 4\Omega^2\right) \\ & \qquad + 12\Delta\omega^2\left(11(\gamma_\mathrm{i}+\gamma_\mathrm{s})^4 - 40\Omega^2(\gamma_\mathrm{i}+\gamma_\mathrm{s})^2 - 16\Omega^4\right)\Big]^2\Bigg]^{1/2}\Bigg\}^{1/3}. \end{aligned} \tag{2.42}$$

In this form, the auxiliary variables Ω_a, Ω_b, Ω_c, K and D are in general complex-valued, depending on the relative magnitude of the spontaneous decay rate γ_s, the ionization rate γ_i and the two-photon Rabi frequency Ω. Nevertheless, the resulting populations ρ_{ee} and ρ_{gg} are always real quantities.

In earlier works dealing with multiphoton ionization (see e.g. [45,46]), the above solution is obtained only in the limiting case $\gamma_\mathrm{s} = 0$, in which the expression reduces to a much simpler form [see Eqs. (2.14)]. Since in those papers the emphasis is on efficient ionization in strong fields, the spontaneous decay of the intermediate state is either neglected in comparison with the ionization rate or, if present in the master equations, it is treated numerically.

However, in experiments that detect the excited state line shape, and are therefore carried out in a relatively weak field, the spontaneous decay rate and the ionization rate can be of comparable magnitude, e.g., as discussed above for the case of He^+-spectroscopy (see also Figs. 2.5 and 2.6). Therefore only the above solution (2.35) describes the constant intensity case appropriately, as detailed in Sec. 2.2.2. Of course, a more compact expression would

be highly desirable, however a simpler expression could not yet be found. Quite generally, spontaneous decay channels complicate the exact solution of the dynamics, because they reduce the symmetry of the EOM, as has also been observed for a different set of master equations, considering autoionizing states in a laser field [47, 48].

In order to check the rather involved result (2.35), a numerical solution of the master equations for the hydrogen $1S$–$2S$ transition has been compared with the analytic result, see Fig. 2.13. In these plots, for different interaction times the $2S$ line shape is shown, where the green solid line represents the analytic solution and the blue dots mark the numerical results. With an intensity of $I = 2.3$ MW/m^2, the two-photon Rabi frequency $\Omega = 2\,(2\pi\beta_{ge})\,I = 1066$ rad/s, the ionization rate $\gamma_{\mathrm{i}} = 2\pi\beta_{\mathrm{ioni}}(2S)\,I = 1740$ rad/s and the two-photon spontaneous decay rate $\gamma_{\mathrm{s}} = 8.231$ rad/s are employed. The two solutions agree very well, as they must, and the maximum relative difference between the two solutions is 6×10^{-6} at very small values for the $2S$ population.

The *Mathematica* code of this numerical integration of the quantum dynamics also forms the basis of the Monte Carlo simulations presented in chapter 5. This comparison therefore also confirms the consistency of the simulation with the analytical solution for the case of constant intensity. In particular, one can infer that the numerical deviation is negligible even for large interaction times.

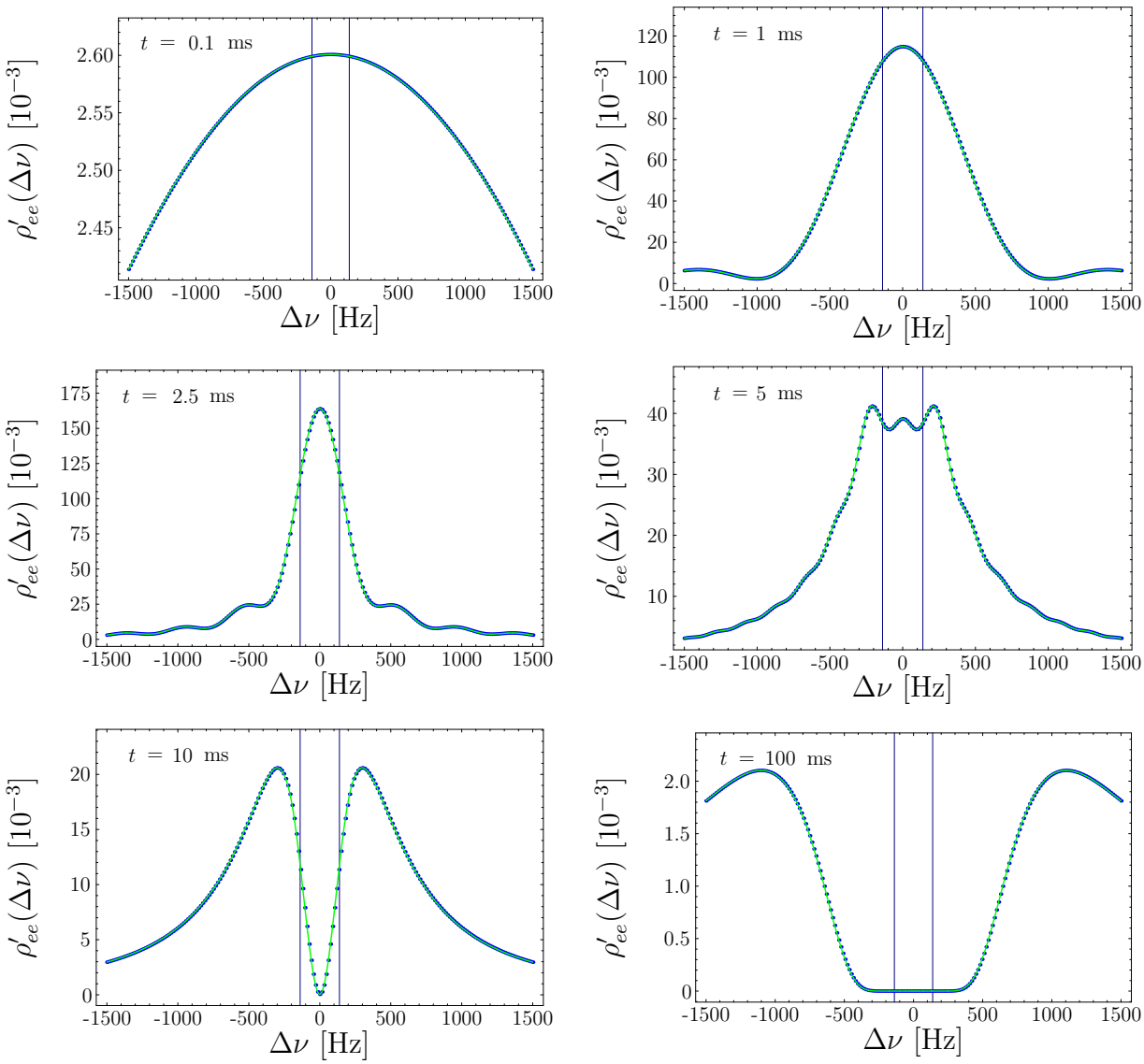

Figure 2.13: Line shape of the excited state population $\rho'_{ee}(\Delta\nu, t)$ of the $1S$–$2S$ quantum dynamics. Comparison of a numerical integration (dots) and the analytical solution (green line) of the master equations (2.11), for interaction times t as indicated on the respective plot. The parameters entering both approaches are: $\Omega = 1066$ rad/s, $\gamma_\mathrm{i} = 1740$ rad/s and $\gamma_\mathrm{s} = 8.231$ rad/s. The vertical lines in each plot are at detunings $\Delta\nu = \pm\frac{1}{2}\gamma_\mathrm{i}/(2\pi)$. One can observe that the full width at half maximum of the line shape is never smaller than the ionization width, as expected.

Chapter 3

Transition Matrix Elements and Dynamic Polarizability

3.1 Introduction

The dynamic Stark shift is one of the major systematic effects that shifts atomic energy levels in a high-precision two-photon spectroscopy experiment. As opposed to other shifting effects, e.g., the Zeeman effect or the static Stark effect, which can in principle be suppressed by an appropriate shielding of the interaction region, the dynamic Stark shift is caused by the probing laser field itself and therefore cannot be avoided. As such, it has received considerable attention in the literature [31, 49–53]. However, the results of some of these publications, also with respect to the two-photon transition matrix elements, have shown inconsistencies, which will be cleared up. A comparison was further complicated by the use of different definitions and unit systems.

In this chapter, the "atomic constants" β_{ge}, β_{AC} and β_{ioni} are calculated in a unified framework. These constants determine the matrix elements entering the Rabi frequency and the dynamic Stark shift, as they occur in the equations of motion for the population dynamics in the previous chapter and in chapter 5. A set of values including and extending the results available in the literature is derived and given in the SI unit system for convenient use in the experimental line shape model. The Z-scaling, the fine structure and hyperfine structure angular prefactors, and the dependence on the reduced mass of the system will be included, such that the results are applicable to any bound two-body Coulomb system, such as hydrogen, He^+, and muonium.

For the two-photon transitions which are of interest in the present thesis, the dynamic Stark shift is a one-photon off-resonant effect, and can be treated in the framework of perturbation theory. Although the high-precision experiments, for which these atomic constants are needed, aim for experimental tests of QED, it is presently sufficient to use the non-relativistic values as given in the tables below, because the dynamic Stark shift is only a small correction to the atomic eigenenergy. For example, for the hydrogen $2S$ state, the typical dynamic Stark shift in the MPQ $1S$–$2S$ experiment is on the order of kHz, calculated non-relativistically, while the $2S$ self-energy shift is on the order of

GHz. However, in chapter 4 the leading order relativistic and radiative corrections will be calculated quantitatively, which may well be needed in future experiments.

In the two-level approximation, in which the spectrum of the Hamiltonian is restricted to the ground state and the excited state of a transition of interest, the population dynamics of these two states as a function of time can be studied very well, as shown in the previous chapter. However, for the derivation of the transition matrix elements in hydrogen or hydrogenlike ions, quantifying the coupling strength between the levels interacting with a laser field, the full Hamiltonian of a two-body system needs to be considered. Especially for a two-photon transition matrix element, this is intuitively clear, as there is an intermediate virtual state involved. Also for the description of the dynamic Stark effect, which is a one-photon off-resonant effect, a virtual intermediate state is needed.

Two approaches to the derivation of the dynamic Stark effect will be presented, using a classical and a fully quantized description of the electric field of the laser. In the classical limit of high photon density, these approaches coincide, as is to be expected. In the course of this comparison, it will become apparent that the dynamic Stark shift can be used to illustrate a basic aspect of quantum electrodynamics, namely as being equivalent to the electron self-energy in a macroscopically populated monochromatic field, i.e., the dynamic Stark shift can be interpreted as a stimulated radiative correction [54].

In Sec. 3.2, an overview of the various perturbations of an atomic reference state by the laser field and the electromagnetic vacuum is given. Section 3.3 treats the calculation of two-photon transition matrix elements, listing the obtained results for a set of S–S and S–D transitions. The derivation of the dynamic Stark effect in two different frameworks is presented in Sec. 3.4, and results for the same set of transitions are given in Sec. 3.5. In Sec. 3.6, the well-known one-photon ionization cross-section is reconsidered and connected to the imaginary part of the dynamic Stark coefficients. Finally, Sec. 3.7 gives an account of a combined stimulated-spontaneous process representing an additional decay channel of excited states. In appendix A, reasons for the encountered inconsistencies in the literature are investigated and solutions are proposed.

3.2 Overview of the interactions of atom, laser mode and vacuum

In the following, the general framework of the interaction of a hydrogen atom or a hydrogenlike ion with a laser mode of angular frequency ω_{L} and the vacuum modes of the quantized electromagnetic field is described (see, e.g., textbooks [29, 55]). The Hamiltonian $H_0^{(\mathrm{s})}$ of the unperturbed system "atom+laser+vacuum" consists of the corresponding

three unperturbed parts

$$H_0^{(\mathrm{s})} = H_0 + H_\mathrm{L} + H_\mathrm{V}\,, \tag{3.1a}$$

$$H_0 = \frac{\boldsymbol{p}^2}{2\,m_\mathrm{e}} - \frac{Ze^2}{4\pi\epsilon_0\,r} = \sum_\phi E_\phi |\phi\rangle\langle\phi|\,, \tag{3.1b}$$

$$H_\mathrm{L} = \hbar\omega_\mathrm{L}\, a_\mathrm{L}^\dagger a_\mathrm{L}\,, \tag{3.1c}$$

$$H_\mathrm{V} = \sum_{\{\boldsymbol{k},\lambda\}\neq\mathrm{L}} \hbar\omega_k \left(a_\lambda^\dagger(\boldsymbol{k}) a_\lambda(\boldsymbol{k}) + \frac{1}{2}\right). \tag{3.1d}$$

Here, the non-relativistic atomic Hamiltonian H_0 is given both in the coordinate and momentum operator representation and in the spectral representation of its eigenfunctions ϕ, including both the discrete and continuum part of the spectrum. The photon creation and annihilation operators $a_\mathrm{L}^\dagger$ and a_L act only on the laser mode of the electromagnetic field with angular frequency ω_L and the polarization given by the laser. The Hamiltonian for the laser field H_L is therefore expressed in terms of the number operator acting on a Fock state of the electromagnetic field. The operators $a_\lambda^\dagger(\boldsymbol{k})$ and $a_\lambda(\boldsymbol{k})$ create and annihilate a photon with wavevector $\boldsymbol{k}$, angular frequency ω_k, and polarization λ in a quantization volume $\mathcal{V}$, with the exception of the laser mode, such that H_V describes all modes of the electromagnetic field other than the laser mode. Note that the laser field Hamiltonian does not contain the term $1/2\,\hbar\omega_\mathrm{L}$, by definition. A finite constant energy shift does not affect the physics described by the Hamiltonian. The nuclear charge number is denoted by Z, the electron mass by m_e, and ϵ_0 denotes the vacuum permittivity.

The unperturbed state vector and its eigenvalue are written as

$$|\phi_0\rangle = |\phi, n_\mathrm{L}, 0\rangle \tag{3.2}$$

$$E_0 = H_0^{(\mathrm{s})}|\phi_0\rangle = E_\phi + n_\mathrm{L}\hbar\omega_\mathrm{L} + 0\,, \tag{3.3}$$

where n_L is the number of photons in the laser mode, and the vacuum energy is defined to be zero, if all other electromagnetic modes are unoccupied. The eigenenergy of a bound atomic state ϕ with principal quantum number n in the framework of Schödinger theory is defined by

$$E_\phi = -\frac{(Z\alpha)^2\, m_\mathrm{e}\, c^2}{2\,n^2}\,, \tag{3.4}$$

where α denotes the fine-structure constant. The interaction of the atom with the quantized electromagnetic field is described in the length gauge and dipole approximation (see Sec. 4.6.1 for quantitative corrections to the atomic constants beyond the dipole approximation). The interaction Hamiltonian reads

$$H_\mathrm{I} = H_\mathrm{LI} + H_\mathrm{VI}\,, \tag{3.5a}$$

$$H_\mathrm{LI} = -e\,z\sqrt{\frac{\hbar\omega_\mathrm{L}}{2\epsilon_0\mathcal{V}}}\big(a_\mathrm{L}^\dagger + a_\mathrm{L}\big)\,, \tag{3.5b}$$

$$H_\mathrm{VI} = -e \sum_{\{\boldsymbol{k},\lambda\}\neq\mathrm{L}} \boldsymbol{r}\cdot\boldsymbol{\epsilon}_\lambda(\boldsymbol{k})\sqrt{\frac{\hbar\omega_k}{2\epsilon_0\mathcal{V}}}\big(a_\lambda^\dagger(\boldsymbol{k}) + a_\lambda(\boldsymbol{k})\big)\,, \tag{3.5c}$$

where H_{LI} describes the interaction of the atom with the laser field and H_{VI} the interaction with the vacuum modes. Here, without loss of generality, the laser field is taken to be linearly polarized along the z-direction, and the discrete form of the creation and annihilation operators is used, defined in a quantization volume $\mathcal{V}$, which will later be extended to infinity in order to translate the results to the classical field. Note that all operators are given in the Schrödinger picture and carry no time-dependence. In Sec. 3.4, it will be demonstrated with the example of the dynamic Stark effect, that in a second-quantized formalism, also dynamic processes can be treated in time-independent perturbation theory.

3.2.1 Second-order perturbation

Now the second-order perturbations to an atomic energy eigenstate, caused by the interaction with the laser mode and the vacuum modes will be briefly summarized. Since in the following sections two-photon transitions involving $1S$ and $2S$ states are treated, the laser mode is not on resonance with any one-photon transition of the atom, so the perturbation theory approach is valid in all these cases. In contrast, a laser field driving the $3S$–$5S$ two-photon transition, is also on one-photon resonance with the $5S$–$15P$ transition, as given by the Schrödinger energy (3.4). In the one-photon resonant case, the atomic level shifts resulting from the laser-atom interaction would have to be evaluated in the laser dressed state picture, which is briefly discussed in the context of radiative corrections in Sec. 4.7.

Since both H_{LI} and H_{VI} are operators with odd parity, acting on the atomic state wavefunction, the first-order correction to the atomic state energy vanishes:

$$\Delta E^{(1)}_{\mathrm{LV}}(\phi_0) = \langle \phi_0 | H_{\mathrm{I}} | \phi_0 \rangle = 0\,, \tag{3.6}$$

and the second order reads

$$\Delta E^{(2)}_{\mathrm{LV}}(\phi_0) = \left\langle \phi_0 \left| H_{\mathrm{I}} \left(\frac{1}{E_0 - H_0^{(\mathrm{s})}} \right)' H_{\mathrm{I}} \right| \phi_0 \right\rangle . \tag{3.7}$$

The reduced Green's function, denoted by a prime, excludes the reference state $|\phi_0\rangle$ from the intermediate states, but can be replaced by the full Green's function (denoted without the prime), because application of H_{I} to $|\phi_0\rangle$ leads to a superposition of states excluding $|\phi_0\rangle$ anyway, as can be seen from Eq. (3.6).

It should be mentioned that the above notation of the second order energy perturbation, is equivalent to another common notation involving the sum over $H_0^{(\mathrm{s})}$-eigenstates ψ_0:

$$\left\langle \phi_0 \left| H_I \underbrace{\frac{1}{E_0 - H_0^{(\mathrm{s})}} H_I}_{\propto |\delta\phi_0\rangle} \right| \phi_0 \right\rangle = \left\langle \phi_0 \left| H_I \frac{1}{E_0 - H_0^{(\mathrm{s})}} \mathbb{1}\, H_I \right| \phi_0 \right\rangle = \sum_{\psi_0} \frac{\langle \phi_0 | H_I | \psi_0 \rangle \langle \psi_0 | H_I | \phi_0 \rangle}{E_0 - E_{\psi_0}}\,, \tag{3.8}$$

with a complete set of $H_0^{(\mathrm{s})}$-eigenstates denoted by

$$\mathbb{1} = \sum_{\psi_0} |\psi_0\rangle\langle\psi_0| \,. \tag{3.9}$$

The explicit sum over intermediate states on the right hand side of Eq. (3.8) is widely used throughout the experimental laser spectroscopy literature, while the left hand side notation is used mainly in publications with a more field-theoretic formalism (e.g., Refs. [56, 57]). In this thesis, the notation on the left hand side of (3.8) is used.

The second-order expression (3.7) consists of four terms, since $H_\mathrm{I} = H_\mathrm{LI} + H_\mathrm{VI}$. The first contribution, including only the laser field, reads

$$\Delta E^{(2)}_\mathrm{AC}(\phi_0) = \left\langle \phi_0 \left| H_\mathrm{LI} \frac{1}{E_0 - H_0^{(\mathrm{s})}} H_\mathrm{LI} \right| \phi_0 \right\rangle \,. \tag{3.10}$$

This perturbation will be discussed in detail in Secs. 3.4 and 3.5. The real part of $\Delta E^{(2)}_\mathrm{AC}(\phi_0)$ is the dynamic Stark shift of the atomic state $|\phi\rangle$, while the imaginary part yields the ionization rate of $|\phi\rangle$ to the continuum.

The contribution which is purely due to the vacuum mode reads

$$\Delta E^{(2)}_\mathrm{SE}(\phi_0) = \left\langle \phi_0 \left| H_\mathrm{VI} \frac{1}{E_0 - H_0^{(\mathrm{s})}} H_\mathrm{VI} \right| \phi_0 \right\rangle \,. \tag{3.11}$$

The real part of $\Delta E^{(2)}_\mathrm{SE}(\phi_0)$ is the one-loop self-energy part of the Lamb shift of the atomic state $|\phi\rangle$, and from the imaginary part one obtains the one-photon decay rate of $|\phi\rangle$ [58]. From the analogy to expression (3.10), the Lamb shift can be interpreted as the dynamic Stark shift caused by all empty vacuum modes, or vice versa, the dynamic Stark shift can be viewed as the self-energy of a bound electron in an electromagnetic field with a single macroscopically populated mode, the laser mode [54].

The remaining two terms of $\Delta E^{(2)}_\mathrm{LV}(\phi_0)$, containing one laser interaction and one vacuum interaction each, vanish, as can be seen by explicitly writing out the intermediate states:

$$\begin{aligned} &\left\langle \phi, n_\mathrm{L}, 0 \left| H_\mathrm{LI} \frac{1}{E_0 - H_0^{(\mathrm{s})}} H_\mathrm{VI} \right| \phi, n_\mathrm{L}, 0 \right\rangle \propto \\ &\sum_{\psi,\pm} \frac{\langle \phi, n_\mathrm{L}, 0 | z | \psi, n_\mathrm{L} \pm 1, 0 \rangle \langle \psi, n_\mathrm{L} \pm 1, 0 | H_\mathrm{VI} | \phi, n_\mathrm{L}, 0 \rangle}{E_\phi - (E_\psi \pm \hbar\omega_\mathrm{L})} = 0 \,, \end{aligned} \tag{3.12}$$

because H_VI acts on all modes except the laser mode, and therefore all matrix elements

$$\langle \psi, n_\mathrm{L} \pm 1, 0 | H_\mathrm{VI} | \phi, n_\mathrm{L}, 0 \rangle \propto \langle n_\mathrm{L} \pm 1 | n_\mathrm{L} \rangle = 0 \,, \tag{3.13}$$

as a consequence of the orthogonality of the Fock states. The same argument applies to the term with $H_\mathrm{LI} \leftrightarrow H_\mathrm{VI}$. The leading-order correction to the energy of the atomic reference state containing both vacuum and laser perturbation is therefore of fourth order.

3.2.2 Fourth order perturbation

As a consequence of the odd parity of the perturbation operators (3.5), the third order perturbation to the atomic state energy vanishes, and the fourth order reads

$$\Delta E^{(4)}_{\mathrm{LV}}(\phi_0) = \langle\phi_0|H_{\mathrm{I}}\frac{1}{E_0-H_0^{(\mathrm{s})}}H_{\mathrm{I}}\frac{1}{E_0-H_0^{(\mathrm{s})}}H_{\mathrm{I}}\frac{1}{E_0-H_0^{(\mathrm{s})}}H_{\mathrm{I}}|\phi_0\rangle\,. \tag{3.14}$$

As H_{I} consists of two parts, one obtains sixteen terms in total. One term is entirely due to the influence of the laser field

$$\Delta E^{(4)}_{\mathrm{AC}}(\phi_0) = \langle\phi_0|H_{\mathrm{LI}}\frac{1}{E_0-H_0^{(\mathrm{s})}}H_{\mathrm{LI}}\frac{1}{E_0-H_0^{(\mathrm{s})}}H_{\mathrm{LI}}\frac{1}{E_0-H_0^{(\mathrm{s})}}H_{\mathrm{LI}}|\phi_0\rangle \tag{3.15}$$

and describes the fourth-order dynamic Stark shift, whereas the real part of the fourth-order term in the vacuum perturbation operator

$$\Delta E^{(4)}_{\mathrm{SE}}(\phi_0) = \langle\phi_0|H_{\mathrm{VI}}\frac{1}{E_0-H_0^{(\mathrm{s})}}H_{\mathrm{VI}}\frac{1}{E_0-H_0^{(\mathrm{s})}}H_{\mathrm{VI}}\frac{1}{E_0-H_0^{(\mathrm{s})}}H_{\mathrm{VI}}|\phi_0\rangle \tag{3.16}$$

yields the two-loop self-energy contribution to the Lamb shift [59, 60], and the imaginary part relates to the two-photon decay rate of the atomic state $|\phi\rangle$ [40]. Then there are eight terms which contain an odd number of operators H_{LI} and consequently also an odd number of H_{VI}. These terms vanish for the same reason as given in Eq. (3.12): An odd number of creation and annihilation processes never lead back to the original Fock state.

The remaining six terms read

$$\Delta E^{(4)}_{6}(\phi_0) = \langle\phi_0|(LLVV + LVLV + LVVL + VLLV + VLVL + VVLL)|\phi_0\rangle\,, \tag{3.17}$$

where the interaction Hamiltonians are represented by their subscript only and the propagators are omitted for brevity. These terms give rise to an energy shift caused by the interaction of the atom with both the laser field and the vacuum modes. This effect is treated in chapter 4, in a somewhat different formalism, as radiative corrections to the second-order energy shift induced by the laser field.

The imaginary part of the shift (3.17) again describes a decay process and can be examined further, if a specific final state of the decay is fixed. In particular, if one considers the excited state of a two-photon transition, one is interested in the decay to the ground state via emission or absorption of one laser photon and spontaneous emission of a second photon. This combined induced-spontaneous two-photon decay rate is described by the imaginary part of the resonances of $\Delta E^{(4)}_{6}(|e, n_{\mathrm{L}}, 0\rangle)$, caused by the two possible final states $|g, n_{\mathrm{L}}+1, 1_z(\boldsymbol{k}_-)\rangle$ and $|g, n_{\mathrm{L}}-1, 1_z(\boldsymbol{k}_+)\rangle$. Section 3.7 is dedicated to a quantitative analysis of this process.

3.2.3 Transition matrix elements

For two-photon transitions, the transition matrix elements can be treated in an analogous formalism as the matrix elements above describing the perturbation of an atomic state

energy. Therefore, only a short definition, excluding the interaction with the vacuum, will be given here.

Since the laser field, interacting with the two-photon transitions of interest, is one-photon off-resonant, the two-photon transition matrix element between the atomic states ϕ (excited state) and ψ (ground state) can be written as

$$M_{\omega_\mathrm{L}} = \left\langle \phi, n_\mathrm{L} - 2 \left| H_\mathrm{LI} \frac{1}{E_0 - H_0^{(\mathrm{s})}} H_\mathrm{LI} \right| \psi, n_\mathrm{L} \right\rangle \tag{3.18}$$

$$\propto \sqrt{n_\mathrm{L}(n_\mathrm{L}-1)} \left\langle \phi \left| z \frac{1}{E_\phi + \hbar\omega_\mathrm{L} - H_0} z \right| \psi \right\rangle \underbrace{\langle n_\mathrm{L} | n_\mathrm{L} \rangle}_{=1} \tag{3.19}$$

and reduced to an integral involving only the atomic Hamiltonian H_0. The twofold action of the laser photon creation or annihilation operators only results in a prefactor proportional to the laser photon number, and for large photon numbers n_L per quantization volume $\mathcal{V}$, the photon number can be related to the macroscopic intensity via

$$I = c \frac{n_\mathrm{L} \hbar \omega_\mathrm{L}}{\mathcal{V}} \,. \tag{3.20}$$

In the following section, the atomic integration needed to obtain the transition matrix element will be described, using a classical description of the electric field of the laser, which corresponds to the limit $n_\mathrm{L}/\mathcal{V} \gg 1$, and a set of results will be listed for S–S and S-D transitions.

In Sec. 3.4, the differences of a classical and a quantized treatment of the dynamic Stark shift will be discussed in detail, and the main conclusion concerning the large photon number limit also applies to the case of the transition matrix element.

The corrections received by the transition matrix elements from taking into account the interaction of the atom with the vacuum will be discussed in detail in chapter 4.

3.3 Calculation of two-photon transition matrix elements

3.3.1 Calculational method

In this section, the calculation of the two-photon transition matrix elements will be presented, which are used in the quantum dynamics of the two-level system of chapter 2. In that chapter, the interacting system of atom and laser field has been described by an effective two-level Hamiltonian, focusing on the time-dependent atomic population of these levels. In order to describe transition matrix elements and dynamic Stark coefficients, involving virtual intermediate states, one has to consider the full, time-dependent Hamiltonian

$$H(t) = H_0 + V(t) \,, \tag{3.21}$$

where H_0 is defined in Eq. (3.1b) and

$$V(t) = V\,\frac{1}{2}\left[\exp(\mathrm{i}\,\omega_\mathrm{L}\,t) + \exp(-\mathrm{i}\,\omega_\mathrm{L}\,t)\right]\,, \tag{3.22a}$$

$$V = -e\,z\,\mathcal{E}_\mathrm{L}\,, \tag{3.22b}$$

describing a one-electron system with nuclear charge number Z in a harmonic laser field of angular frequency ω_L and classical electric field amplitude $\mathcal{E}_\mathrm{L}$, linearly polarized in the z-direction. The interaction potential $V(t)$ is chosen to be in the length gauge, which has some advantages in the description of time-dependent problems (for a detailed discussion see for e.g. [61]), and the dipole approximation is made. The time-dependent two-photon transition matrix element connecting the ground state $|g\rangle$ and excited state $|e\rangle$, then reads

$$\left\langle e \left| V(t) \frac{1}{(E_g + \hbar\omega_\mathrm{L}) - H_0} V(t) \right| g \right\rangle\,, \tag{3.23}$$

where E_ϕ is the Schrödinger energy of any eigenstate $|\phi\rangle$ of H_0, depending only on its principal quantum number n and is defined in Eq. (3.4). Now one can establish the connection with the off-diagonal element of the two-level Hamiltonian $\tilde{H}$ from Sec. 2.2, Eq. (2.3), by equating

$$-\left\langle e \left| V(t) \frac{1}{H_0 - (E_g + \hbar\omega_\mathrm{L})} V(t) \right| g \right\rangle = \frac{\hbar\Omega}{2}\left[\,\exp(\mathrm{i}\omega_\mathrm{L}t) + \exp(-\mathrm{i}\omega_\mathrm{L}t)\,\right]^2\,. \tag{3.24}$$

Observe that a minus sign is explicitly pulled out with respect to Eq. (3.23) in order to write the Green's function in the familiar form $1/[H_0 - E]$, with intermediate state energy E. With the definition of the two-photon Rabi-frequency from Eq. (2.7)

$$\Omega = 2\,(2\pi\beta_{ge})\,I\,, \tag{3.25}$$

and the intensity of an electromagnetic plane wave

$$I = \frac{1}{2}\epsilon_0\,c\,\mathcal{E}_\mathrm{L}^2\,, \tag{3.26}$$

one obtains for the time-independent two-photon transition matrix element

$$\beta_{ge} = -\frac{e^2}{2\,h\,c\,\epsilon_0}\left\langle e \left| z \frac{1}{H_0 - (E_g + \hbar\omega_\mathrm{L})} z \right| g \right\rangle\,. \tag{3.27}$$

There are a number of different approaches to the evaluation of matrix elements involving the non-relativistic hydrogen Green's function as in Eq. (3.27) [62, 63]. In this thesis, a fully analytic evaluation is used, which is based on the Sturmian representation of the radial Green's function for the hydrogen atom. The basic formalism of such an evaluation has been laid out in [64–66], and the non-relativistic hydrogen Green's function reads, in coordinate representation,

$$G(\boldsymbol{r}_1, \boldsymbol{r}_2; \eta) = \left\langle \boldsymbol{r}_1 \left| \frac{1}{H_0 - E(\eta)} \right| \boldsymbol{r}_2 \right\rangle = \sum_{l,m} g_l(r_1, r_2; \eta)\, Y_{lm}(\theta_1, \varphi_1)\, Y^*_{lm}(\theta_2, \varphi_2)\,, \tag{3.28}$$

with a radial part

$$g_l(r_1, r_2; \eta) = \frac{2\, m_\mathrm{e}}{\hbar^2} \left(\frac{2}{a_0 \eta}\right)^{2l+1} (r_1 r_2)^l \, \mathrm{e}^{-(r_1+r_2)/a_0\eta} \sum_{k=0}^{\infty} \frac{L_k^{2l+1}\left(\frac{2r_1}{a_0\eta}\right) L_k^{2l+1}\left(\frac{2r_2}{a_0\eta}\right)}{(k+1)_{2l+1}\,(l+1+k-\eta)} \,, \quad (3.29)$$

where the usual spherical coordinates $\boldsymbol{r}_i = \{r_i, \theta_i, \phi_i\}$ are used, and $(x)_n \equiv \Gamma(x+n)/\Gamma(x)$ is the Pochhammer symbol. The Bohr radius is denoted by a_0, the symbols L_k^{2l+1} designate the associated Laguerre polynomials, and the invertible energy parameterization

$$\eta \equiv \eta(E) = \frac{Z\,\hbar}{a_0} \sqrt{-\frac{1}{2\, m_\mathrm{e}\, E}} \quad (3.30)$$

is used for conciseness of notation, converting any energy E into the dimensionless parameter η, chosen such that for eigenstates $|\phi\rangle$ of H_0 with principal quantum number n, one obtains $\eta(E_\phi) = n$. For the calculation of the transition matrix elements, one has to consider a virtual intermediate P state in the propagator, with energy $E_g + \hbar\omega_\mathrm{L}$, where ω_L is fixed by the two-photon resonance condition. Since the intermediate state lies in between two bound states, its energy is always negative, and therefore η and the transition matrix elements are real. In the process of calculating the dynamic Stark coefficients in Sec. 3.5, also intermediate states in the continuum will occur, and consequently the Stark coefficients will acquire an imaginary part.

Up to now, the states $|g\rangle$ and $|e\rangle$ have been characterized by the principal quantum number n and orbital angular momentum quantum number l only. Evaluated for any S–S transition, the two-photon transition operator, with which the transition matrix element can also be written as $\langle e|T|g\rangle$, reads

$$T^{ij} = r^i \frac{1}{H_0 - (E_g + \hbar\omega_\mathrm{L})} r^j \quad (3.31)$$

and has isotropic symmetry: $\langle e|T^{xx}|g\rangle = \langle e|T^{yy}|g\rangle = \langle e|T^{zz}|g\rangle$, $\langle e|T^{ij}|g\rangle = 0$ for $i \neq j$ and therefore transforms like a scalar under rotation. As a consequence, the two-photon transition matrix element for each individual allowed transition between fine structure (FS) and hyperfine structure (HFS) substates can be obtained from β_{ge} of the gross structure transition without any angular prefactors. In the following, the transitions among states with different principal quantum number will be referred to as the "gross structure" of the atom. For S–D transitions, the rotational symmetry is broken by the D state, and $\sum_i \langle e|T^{ii}|g\rangle = 0$. Therefore, the reduced matrix elements of the rank two component, $\beta_{ge}^{(2)}$ must be calculated for orbital angular momentum eigenstates

$$\beta_{ge}^{(2)} = -\frac{e^2}{2\, h\, c\, \epsilon_0} \langle n' D \,||\boldsymbol{T}(2)||\, nS\rangle \,, \quad (3.32)$$

from which the transition matrix elements for specific magnetic sublevels can be obtained via the Wigner-Eckhart theorem. For the gross structure S–D transition, the only transition which can be driven by linearly polarized light is the $m_l = 0 \to m_l' = 0$ transition. For transitions between FS sublevels of angular momentum $J = L + S$ and $J' = L' + S$,

where S is the spin of the orbiting particle, the angular momenta have to be recoupled via the $6j$-symbols [67]

$$\langle n'\,(L'S)J'||\boldsymbol{T}(2)||n\,(LS)J\rangle = \sqrt{(2J+1)(2J'+1)}\times$$
$$(-1)^{L'+S+J+2}\left\{\begin{array}{ccc} L' & J' & S \\ J & L & 2 \end{array}\right\}\langle n'\,L'||\boldsymbol{T}(2)||n\,L\rangle\,, \tag{3.33}$$

because the two-photon transition operator only acts on the orbital angular momentum part of the wavefunction. If HFS sublevels are resolved, also the nuclear spin I has to be taken into account in the same way. Denoting the total angular momenta by $F = J + I$ and $F' = J' + I$, one obtains:

$$\langle n'\,(J'I)F'||\boldsymbol{T}(2)||n\,(JI)F\rangle = \sqrt{(2F+1)(2F'+1)}\times$$
$$(-1)^{J'+I+F+2}\left\{\begin{array}{ccc} J' & F' & I \\ F & J & 2 \end{array}\right\}\langle n'\,(L'S)J'||\boldsymbol{T}(2)||n\,(LS)J\rangle\,. \tag{3.34}$$

Finally, via the Wigner-Eckhart theorem, the transition matrix element between hyperfine magnetic sublevels $|g\rangle = |nS,(JI)Fm_F\rangle$ and $|e\rangle = |n'D,(J'I)F'm'_F\rangle$ in a linearly z-polarized laser reads

$$\beta_{ge} = (-1)^{F'-m'_F}\begin{pmatrix} F' & 2 & F \\ -m'_F & 0 & m_F \end{pmatrix}\left\{-\frac{e^2}{2\,h\,c\,\epsilon_0}\langle n'\,(J'I)F'||\boldsymbol{T}(2)||n\,(JI)F\rangle\right\}\,, \tag{3.35}$$

where the $3j$-symbol is defined as in Ref. [67]. In summary, to arrive at β_{ge} for a specific S–D HFS transition, one starts with the value for $\beta_{ge}^{(2)}$ of the gross structure transition from Tab. 3.2, solves Eq. (3.32) for the reduced matrix element and sequentially inserts the results into Eqs. (3.33)-(3.35). For FS transitions, the step implied by Eq. (3.34) is skipped and in Eq. (3.35), one substitutes $F \to J$, $m_F \to m_J$ and $F' \to J'$, $m'_F \to m'_J$.

3.3.2 Results for two-photon transitions

Results for the two-photon transition matrix elements β_{ge} for the transitions $1S \Leftrightarrow nS$ $(2 \le n \le 20)$ and $2S \Leftrightarrow nS$ $(3 \le n \le 20)$ are given in Tab. 3.1. For the transitions $1S \Leftrightarrow nD$ and $2S \Leftrightarrow nD$ $(3 \le n \le 20)$, the reduced matrix elements for orbital angular momentum eigenstates are given in Tab. 3.2. Appendix A is devoted to the comparison with other literature sources, where some of these results are also obtained, clarifying the prefactors and discussing some occasional inconsistencies, which were encountered in the literature search related to the problem. These non-relativistic results are relevant for the given transitions in any bound two-body Coulomb system with nuclear charge number Z, where $1 \le Z \lesssim 10$. Generally, one of the particles involved will be referred to as "the nucleus", although it does not need to be made up of baryons. Because the values, as listed in the tables, have been obtained for $Z = 1$ and infinite nuclear mass, the scaling with Z and the dependence on the reduced mass of the system remain to be clarified. One needs to use the scaling relations for the position operator as a function of Z [43], and for the propagator denominators in (3.27). Note that the relevant laser

Table 3.1: Two-photon transition matrix elements β_{ge} in units Hz $(\mathrm{W/m^2})^{-1}$ for $1S \Leftrightarrow nS$ and $2S \Leftrightarrow nS$ transitions, as defined in Eq. (3.27), evaluated for atomic hydrogen ($Z = 1$), in the non-relativistic dipole approximation. The electron mass is employed in the calculation; reduced-mass effects and the dependence of the results on the nuclear charge number Z is given in Eq. (3.37). For transitions between $F = F' = 0$ and $F = F' = 1$ HFS sublevels, these values are valid with an angular prefactor of unity and directly give the coefficient β_{ge} defined in Eq. (3.35).

n	$1S \Leftrightarrow nS$ β_{ge} $[\mathrm{Hz(W/m^2)^{-1}}]$	$2S \Leftrightarrow nS$ β_{ge} $[\mathrm{Hz(W/m^2)^{-1}}]$
2	3.68111×10^{-5}	–
3	1.00333×10^{-5}	1.23306×10^{-3}
4	5.13409×10^{-6}	7.79393×10^{-5}
5	3.28555×10^{-6}	-4.39666×10^{-5}
6	2.35088×10^{-6}	-6.89568×10^{-5}
7	1.79744×10^{-6}	-7.26216×10^{-5}
8	1.43591×10^{-6}	-6.99362×10^{-5}
9	1.18344×10^{-6}	-6.52683×10^{-5}
10	9.98415×10^{-7}	-6.01620×10^{-5}
11	8.57763×10^{-7}	-5.52069×10^{-5}
12	7.47736×10^{-7}	-5.06214×10^{-5}
13	6.59655×10^{-7}	-4.64686×10^{-5}
14	5.87791×10^{-7}	-4.27450×10^{-5}
15	5.28215×10^{-7}	-3.94201×10^{-5}
16	4.78153×10^{-7}	-3.64542×10^{-5}
17	4.35589×10^{-7}	-3.38061×10^{-5}
18	3.99031×10^{-7}	-3.14375×10^{-5}
19	3.67348×10^{-7}	-2.93136×10^{-5}
20	3.39672×10^{-7}	-2.74039×10^{-5}

frequency $\omega_{\mathrm{L}}(Z) = Z^2\,\omega_{\mathrm{L}}(Z = 1)$ has to be scaled by a factor of Z^2 as compared to the corresponding frequency in hydrogen. Thus, one finds that

$$\beta_{ge}(Z) = \frac{1}{Z^4}\,\beta_{ge}(Z = 1)\,. \tag{3.36}$$

If one considers a bound two-body system, consisting of particles with respective masses m_{N} for the nucleus and m_{S} for the other particle, this system is equivalent to a system with infinite nuclear mass and an orbiting particle with reduced mass μ. It is therefore sufficient to replace the electron mass with the reduced mass in the previous calculations, bearing in mind, that also the Bohr radius $a_0 = 4\pi\,\epsilon_0\hbar^2/m_{\mathrm{e}}e^2$ has to be replaced. Therefore, to obtain the transition matrix elements β_{ge} for a two-body Coulomb system of nuclear charge number Z and reduced mass μ (even for hydrogen itself), the values from Tabs. 3.1

Table 3.2: Two-photon reduced transition matrix elements $\beta^{(2)}_{ge}$ in units [Hz $(\mathrm{W/m^2})^{-1}$] for $1S \Leftrightarrow nS$ and $2S \Leftrightarrow nS$ transitions, as defined in Eq. (3.32), evaluated for atomic hydrogen ($Z = 1$), in the non-relativistic dipole approximation. The electron mass is employed in the calculation; reduced-mass effects and the dependence of the results on the nuclear charge number Z is given in Eq. (3.37). For specific transitions in FS and HFS sublevels, the angular prefactors in Eqs. (3.33)-(3.35) must be taken into account, as applicable.

n	$1S \Leftrightarrow nD$ $\beta^{(2)}_{ge}$ [Hz$(\mathrm{W/m^2})^{-1}$]	$2S \Leftrightarrow nD$ $\beta^{(2)}_{ge}$ [Hz$(\mathrm{W/m^2})^{-1}$]
3	-6.16579×10^{-5}	4.23147×10^{-4}
4	-3.89301×10^{-5}	-2.23806×10^{-3}
5	-2.72644×10^{-5}	-1.75124×10^{-3}
6	-2.04728×10^{-5}	-1.39563×10^{-3}
7	-1.61138×10^{-5}	-1.15144×10^{-3}
8	-1.31174×10^{-5}	-9.74048×10^{-4}
9	-1.09516×10^{-5}	-8.39046×10^{-4}
10	-9.32523×10^{-6}	-7.32816×10^{-4}
11	-8.06659×10^{-6}	-6.47159×10^{-4}
12	-7.06862×10^{-6}	-5.76793×10^{-4}
13	-6.26133×10^{-6}	-5.18119×10^{-4}
14	-5.59721×10^{-6}	-4.68586×10^{-4}
15	-5.04300×10^{-6}	-4.26327×10^{-4}
16	-4.57477×10^{-6}	-3.89943×10^{-4}
17	-4.17491×10^{-6}	-3.58362×10^{-4}
18	-3.83018×10^{-6}	-3.30751×10^{-4}
19	-3.53048×10^{-6}	-3.06453×10^{-4}
20	-3.26799×10^{-6}	-2.84944×10^{-4}

and 3.2 must be multiplied by a factor

$$\frac{1}{Z^4}\left(\frac{m_\mathrm{e}}{\mu}\right)^3 = \frac{1}{Z^4}\left(\frac{m_\mathrm{e}(m_\mathrm{N}+m_\mathrm{S})}{m_\mathrm{N}\,m_\mathrm{S}}\right)^3 . \tag{3.37}$$

This scaling law equally applies for the Stark coefficients β_AC and β_ioni discussed below. Note that for atomic nuclei, one also obtains isotope shifts to the transition matrix elements via the dependence on the nuclear mass m_N.

3.4 Dynamic Stark effect

In this section, the classical derivation of the dynamic Stark effect, in the usual framework of time-dependent perturbation theory, is contrasted with a second-quantized approach. In this approach, in which the laser field is quantized, a time-independent treatment is possible, because the light field is characterized by a Fock state representation, in which the photons are stationary excitations of the field.

In addition, by comparing the two approaches, it will be shown that the quantized and the classical descriptions agree for the case that the laser field tends towards a classical field, i.e., when the laser photon number per quantization volume is large, as is to be expected.

3.4.1 Classical field approach

The usual derivation of the dynamic Stark shift, as it is found in several textbooks, using a classical electric field, is presented in the following. The argument goes along the lines of chapter 5 of Ref. [68], but in the general notation of this chapter. Consider the time-dependent Hamiltonian

$$H = H_0 + V(\epsilon, t)\,, \tag{3.38a}$$
$$V(\epsilon, t) = V \exp(-\epsilon|t|)\cos(\omega_{\mathrm{L}} t)\,, \tag{3.38b}$$
$$V = -e\, z\, \mathcal{E}_{\mathrm{L}}\,, \tag{3.38c}$$

where H_0 is the unperturbed atomic Hamiltonian, as defined in (3.1b), describing a one-electron system of nuclear charge number Z in a plane-wave monochromatic laser field, polarized along the z-direction. The classical electric field amplitude is denoted by $\mathcal{E}_{\mathrm{L}}$. The dipole, length gauge interaction Hamiltonian $V(t, \epsilon)$ describes a harmonic perturbation with magnitude V which is adiabatically damped in the distant past ($t \to -\infty$) and the distant future ($t \to \infty$) by means of the damping parameter $\epsilon > 0$. This damping parameter is introduced to avoid a sudden turn-on of the perturbation, and in the limit $\epsilon \to 0$, which will be carried out towards the end of the derivation, one obtains the constant intensity result. The introduction of an adiabatic damping parameter is also a key element of time-dependent perturbation theory in QED [69]. In QED, the interaction Hamiltonian is usually expressed in the interaction picture and a time-dependence is incurred for the field operators (see appendix A of Ref. [70]).

Now the effect of the off-resonant perturbation by the time-dependent electric field on a reference state $|\phi\rangle$ of the unperturbed atom will be considered. In the interaction picture (denoted by the subscript I), $V(\epsilon, t)$ is represented by

$$V_{\mathrm{I}}(\epsilon, t) = \exp\left(\frac{\mathrm{i}}{\hbar} H_0 t\right) V(\epsilon, t) \exp\left(-\frac{\mathrm{i}}{\hbar} H_0 t\right)\,. \tag{3.39}$$

From the Dyson series, one can calculate the time evolution operator $U_{\mathrm{I}}(\epsilon, t)$ up to second

order in V_I:

$$U_\mathrm{I}(\epsilon,t) = 1 - \frac{\mathrm{i}}{\hbar}\int_{-\infty}^{t} dt' V_\mathrm{I}(\epsilon,t') + \left(-\frac{\mathrm{i}}{\hbar}\right)^2 \int_{-\infty}^{t} dt' \int_{-\infty}^{t'} dt'' V_\mathrm{I}(\epsilon,t') V_\mathrm{I}(\epsilon,t'')\,. \tag{3.40}$$

Now consider the time-dependent atomic state, $|\psi_\mathrm{I}(t)\rangle$ in the interaction picture, subject to the initial condition $|\psi_\mathrm{I}(t{=}-\infty)\rangle = |\phi\rangle$, where the reference state $|\phi\rangle$ is an eigenstate of the unperturbed Hamiltonian H_0. One can expand $|\psi_\mathrm{I}(t)\rangle$ in a complete set $\{|m\rangle\}$ of eigenstates of H_0 as

$$|\psi_\mathrm{I}(t)\rangle = U_\mathrm{I}(\epsilon,t)|\psi_\mathrm{I}(-\infty)\rangle = \sum_m c_m(t)|m\rangle\,, \tag{3.41}$$

where $c_m(t) = \langle m|\psi_I(t)\rangle$. The initial condition is thus $c_\phi(-\infty) = 1$ for the reference state $|\phi\rangle$ with all other $c_m(-\infty)$ equal to zero. The amplitude of interest is obtained by the projection

$$c_\phi(t) = \langle\phi|\psi_\mathrm{I}(t)\rangle = \langle\phi|U_\mathrm{I}(\epsilon,t)|\phi\rangle\,. \tag{3.42}$$

Substituting $U_\mathrm{I}(\epsilon,t)$ from Eq. (3.40), and because $\langle\phi|z|\phi\rangle$ vanishes for parity eigenstates $|\phi\rangle$, the leading order is V^2 and the problem reduces to calculating the matrix element

$$M = \int_{-\infty}^{t} dt' \int_{-\infty}^{t'} dt'' \langle\phi|V_\mathrm{I}(\epsilon,t')V_\mathrm{I}(\epsilon,t'')|\phi\rangle \tag{3.43a}$$

$$= \sum_m \int_{-\infty}^{t} dt' \int_{-\infty}^{t'} dt'' \langle\phi|V_\mathrm{I}(\epsilon,t')|m\rangle\langle m|V_\mathrm{I}(\epsilon,t'')|\phi\rangle\,, \tag{3.43b}$$

where the multi-index m counts all bound and continuum states of the unperturbed hydrogen atom. Because the perturbation is harmonic, the time integrals can be done without much difficulty, convergence being ensured by the adiabatic damping. One obtains

$$M = -\frac{\hbar}{\mathrm{i}}\frac{1}{4}\sum_{m,\pm}\frac{\langle\phi|V|m\rangle\langle m|V|\phi\rangle\exp(2\epsilon t)}{2\epsilon(E_\phi - E_m \pm \hbar\omega_\mathrm{L} + \mathrm{i}\hbar\epsilon)}\,, \tag{3.44}$$

with V as defined in Eq. (3.38c), and E_ϕ representing the energy of the unperturbed atomic state $|\phi\rangle$. The $\pm$ summation index indicates that the two terms differing only in the sign of $\hbar\omega_\mathrm{L}$ in the denominator have to be added. This sum and the factor of $1/4$ originate from the definition of the cosine in terms of exponential functions. Combining Eqs. (3.40), (3.42), and (3.44), one obtains in second-order time-dependent perturbation theory

$$c_\phi(t) = 1 - \frac{\mathrm{i}}{4\hbar}\sum_{m,\pm}\frac{\langle\phi|V|m\rangle\langle m|V|\phi\rangle\exp(2\epsilon t)}{2\epsilon(E_\phi - E_m \pm \hbar\omega_\mathrm{L} + \mathrm{i}\hbar\epsilon)} + \ldots\,, \tag{3.45}$$

where higher-order terms have been neglected. Now consider

$$\frac{\partial}{\partial t}\ln(c_\phi(t)) = -\frac{\mathrm{i}}{4\hbar}\sum_{m,\pm}\frac{\langle\phi|V|m\rangle\langle m|V|\phi\rangle}{E_\phi - E_m \pm \hbar\omega_\mathrm{L} + \mathrm{i}\hbar\epsilon}. \tag{3.46}$$

Here the logarithm has been expanded up to second order in V and, in the limit $\epsilon \to 0$, $\exp(2\epsilon t)$ has been replaced by unity. The solution of Eq. (3.46) implies that

$$c_\phi(t) = \exp\left(-\frac{\mathrm{i}}{\hbar}\Delta E_{\mathrm{AC}}(\phi)t\right), \tag{3.47}$$

where the dynamic Stark shift $\Delta E_{\mathrm{AC}}(\phi)$ of the reference state $|\phi\rangle$ has been defined as

$$\Delta E_{\mathrm{AC}}(\phi) = \frac{1}{4}\sum_{m,\pm}\frac{\langle\phi|V|m\rangle\langle m|V|\phi\rangle}{E_\phi - E_m \pm \hbar\omega_{\mathrm{L}}}. \tag{3.48}$$

In view of Eq. (3.41), one then has

$$|\psi_{\mathrm{I}}(t)\rangle = U_{\mathrm{I}}(\epsilon, t)|\psi_{\mathrm{I}}(-\infty)\rangle = c_\phi(t)|\phi\rangle + \ldots, \tag{3.49}$$

where the ellipsis denotes the projections onto the non-reference atomic states. Because the Schrödinger picture wave function is related to its interaction-picture counterpart via $|\psi(t)\rangle = \exp(-\mathrm{i}H_0 t)|\psi_{\mathrm{I}}(t)\rangle$, one obtains

$$\langle\phi|\psi(t)\rangle = \exp\left(-\frac{\mathrm{i}}{\hbar}(E_\phi + \Delta E_{\mathrm{AC}}(\phi))t\right). \tag{3.50}$$

The non-reference states from Eq. (3.49) give no contribution because they are orthogonal to $|\phi\rangle$. The projection (3.50) yields the influence of the perturbation on the reference state $|\phi\rangle$ by projecting the time-evolved perturbed state onto the reference state such that the perturbation to the eigenenergy E_ϕ can be directly seen.

Note that $\Delta E_{\mathrm{AC}}(\phi)$ can in general be complex, rather than purely real. The imaginary part is accommodated in the definition

$$\gamma_\phi = -\frac{2}{\hbar}\mathrm{Im}[\Delta E_{\mathrm{AC}}(\phi)], \tag{3.51}$$

$$\Delta E_\phi = \mathrm{Re}[\Delta E_{\mathrm{AC}}(\phi)]. \tag{3.52}$$

The real part of the AC Stark effect describes the energy shift of the unperturbed energy E_ϕ, and the imaginary part, if present, can be interpreted as the ionization rate γ_ϕ. The dynamic Stark shift of $|\phi\rangle$ can now be expressed as

$$\Delta E_{\mathrm{AC}}(\phi) = \frac{1}{4}\sum_{\pm}\left\langle\phi\left|V\frac{1}{E_\phi - H_0 \pm \hbar\omega_{\mathrm{L}}}V\right|\phi\right\rangle, \tag{3.53}$$

where the closure relation for the spectrum is employed. This expression can be written as a product of a prefactor and a sum of two matrix elements, where $E_\phi \mp \hbar\omega_{\mathrm{L}}$ is the energy of the respective intermediate state:

$$P_{\omega_{\mathrm{L}}}(\phi) = \sum_{\pm}\left\langle\phi\left|z\frac{1}{H_0 - E_\phi \pm \hbar\omega_{\mathrm{L}}}z\right|\phi\right\rangle, \tag{3.54a}$$

$$\Delta E_{\mathrm{AC}}(\phi) = -\frac{e^2\mathcal{E}_{\mathrm{L}}^2}{4}P_{\omega_{\mathrm{L}}}(\phi) = -\frac{e^2}{2c\epsilon_0}IP_{\omega_{\mathrm{L}}}(\phi), \tag{3.54b}$$

where $P_{\omega_{\mathrm{L}}}(\phi)$ is the dynamic polarizability of the atom in the reference state for angular frequency ω_{L} of the driving laser field and relation (3.26) was used.

3.4.2 Second-quantized approach

In second quantization the Hamiltonian for the coupled system, "atom+radiation field" (see also Sec. 3.2), reads

$$H = \sum_n E_n |n\rangle\langle n| + \hbar\omega_{\mathrm{L}} a_{\mathrm{L}}^\dagger a_{\mathrm{L}} + H_{\mathrm{LI}}. \tag{3.55}$$

Electron-positron pair creation is not considered, since in two-photon precision spectroscopy experiments one operates in the low-energy regime, and therefore the fermion field does not need to be quantized. The laser field is described as a quantized photon field with creation and annihilation operators $a_{\mathrm{L}}^\dagger$ and a_{L}, respectively. Recall the length gauge dipole interaction Hamiltonian H_{LI} (3.5b) in a z-polarized laser field:

$$H_{\mathrm{LI}} = -ez\hat{E}_{\mathrm{L}} = -ez\sqrt{\frac{\hbar\omega_{\mathrm{L}}}{2\epsilon_0\mathcal{V}}}\left(a_{\mathrm{L}}^\dagger + a_{\mathrm{L}}\right), \tag{3.56}$$

defined in the normalization volume $\mathcal{V}$, which is chosen so that the energy density of a one-photon Fock state, when integrated over $\mathcal{V}$, yields $\hbar\omega_{\mathrm{L}}$. It might be argued that a coherent state of the photon field is a much better description than a Fock state with n_{L} photons in the laser mode, which is assumed here. However, in the limit of a large photon number, the relative fluctuation of the photon number $\delta n_{\mathrm{L}}/n_{\mathrm{L}}$ goes to zero for a coherent state, and one may therefore resort to the Fock-state approximation [29].

Although the dynamic Stark effect should intuitively be treated by time-dependent perturbation theory, as described in the previous section, it is not so well known that it is possible to formulate time-independent operators for the quantized radiation field and to carry out meaningful calculations with these Schrödinger picture operators. This concept is introduced in a few textbooks such as Ref. [55] and has also been used for quantum electrodynamic calculations (see for example, Eq. (5) of Ref. [71]).

Explicitly writing out the states of the total system, this approach leads from the second-order perturbation (3.10) to the result of time-independent perturbation theory for the energy shift of the unperturbed eigenstate $|\phi, n_{\mathrm{L}}\rangle$,

$$\begin{aligned}
\Delta E_{\mathrm{AC}}(\phi) &= \sum_m \left[\frac{\langle \phi, n_{\mathrm{L}} | H_{\mathrm{LI}} | m, n_{\mathrm{L}} - 1\rangle\langle m, n_{\mathrm{L}} - 1 | H_{\mathrm{LI}} | \phi, n_{\mathrm{L}}\rangle}{E_\phi + n_{\mathrm{L}}\hbar\omega_{\mathrm{L}} - (E_m + (n_{\mathrm{L}} - 1)\hbar\omega_{\mathrm{L}})} \right. \\
&\qquad \left. + \frac{\langle \phi, n_{\mathrm{L}} | H_{\mathrm{LI}} | m, n_{\mathrm{L}} + 1\rangle\langle m, n_{\mathrm{L}} + 1 | H_{\mathrm{LI}} | \phi, n_{\mathrm{L}}\rangle}{E_\phi + n_{\mathrm{L}}\hbar\omega_{\mathrm{L}} - (E_m + (n_{\mathrm{L}} + 1)\hbar\omega_{\mathrm{L}})} \right] \\
&= \frac{e^2\hbar\omega_{\mathrm{L}}}{2\epsilon_0\mathcal{V}} \sum_m \left[\frac{\langle\phi|z|m\rangle\langle m|z|\phi\rangle}{E_\phi - E_m + \hbar\omega_{\mathrm{L}}} n_{\mathrm{L}} + \frac{\langle\phi|z|m\rangle\langle m|z|\phi\rangle}{E_\phi - E_m - \hbar\omega_{\mathrm{L}}} (n_{\mathrm{L}} + 1) \right].
\end{aligned} \tag{3.57}$$

The sum over virtual intermediate atomic states $|m\rangle$, including bound and continuum states, has been split into two parts depending on the number of photons in the field. Considering this expression, the AC Stark shift receives an interpretation as being mediated by transitions to virtual intermediate states of the combined system "atom+laser field", due to virtual creation and annihilation of laser photons. When this perturbation is

evaluated using an empty Fock space as the unperturbed state, and when a sum is formed over all possible virtual excitations, i.e., evaluating expression (3.11), the self-energy is obtained [70, 72].

In the classical limit, $n_{\mathrm{L}} \to \infty$, $\mathcal{V} \to \infty$, $n_{\mathrm{L}}/\mathcal{V} =$ constant, and Eq. (3.57) can be simplified to

$$\Delta E_{\mathrm{AC}}(\phi) = -\frac{e^2 \hbar n_{\mathrm{L}} \omega_{\mathrm{L}}}{2\epsilon_0 \mathcal{V}} P_{\omega_{\mathrm{L}}}(\phi), \tag{3.58}$$

with $P_{\omega_{\mathrm{L}}}(\phi)$ as already defined in Eq. (3.54a). This result can now be matched to the classical result in Eq. (3.54). In the quantized formalism the term

$$w = \frac{n_{\mathrm{L}} \hbar \omega_{\mathrm{L}}}{\mathcal{V}} \tag{3.59}$$

gives the energy density in which the atom is immersed, which is related to the intensity via

$$I = wc\,. \tag{3.60}$$

Using Eqs. (3.58)–(3.60) one obtains

$$\Delta E_{\mathrm{AC}}(\phi) = -\frac{e^2}{2\epsilon_0 c} I P_{\omega_{\mathrm{L}}}(\phi), \tag{3.61}$$

in agreement with Eq. (3.54). Thus the classical-field and the quantized-field approach give consistent results in the classical limit, and Eq (3.57) quantifies, how the classical predictions should be modified in an environment where the photon number is not large. Using (3.61), in the next section a number of dynamic polarizabilities relevant for two-photon transitions will be evaluated.

3.5 Calculation of the AC Stark shift

This section treats the dynamic Stark shift of atomic energy levels in the spectroscopically relevant case where an atom or hydrogenlike ion interacts with a laser field which is on two-photon resonance with an S–S or S–D transition. Both the lower state ($1S$ or $2S$) and the excited state of the respective transition are shifted as a consequence of the interaction with the very laser field that is used to probe the atomic transition. This shift cannot be suppressed experimentally and constitutes a major systematic effect in many precision spectroscopy experiments.

Both the classical time-dependent theory, and the time-independent fully quantized treatment, in the limit of macroscopic photon number, yield the same physical result for the dynamic Stark shift, as presented above in Sec. 3.4.

3.5.1 Matrix elements

As has been demonstrated in Sec. 3.4, the calculation of the dynamic Stark shift of any reference state $|\phi\rangle$ in a z-polarized laser field

$$\Delta E_{\mathrm{AC}}(\phi) = \frac{e^2\mathcal{E}_{\mathrm{L}}^2}{4} \sum_{\pm} \left\langle \phi \left| z \, \frac{1}{E_\phi - H_0 \pm \hbar\omega_{\mathrm{L}}} \, z \right| \phi \right\rangle \tag{3.62}$$

reduces to calculating the matrix element of the dynamic polarizability (3.54a), where the same analytic technique as for the two-photon transition matrix elements is used [see Eqs. (3.28)-(3.30)].

Note that the contributions of two intermediate states, with energies $E_\phi + \hbar\omega_{\mathrm{L}}$ and $E_\phi - \hbar\omega_{\mathrm{L}}$, have to be summed. These energies are determined by the choice of angular frequency of the laser field $\omega_{\mathrm{L}} = (E_e - E_g)/2\hbar$ in the two-photon resonant spectroscopy of the transition $g \Leftrightarrow e$. For laser detunings which drive the transition appreciably, the matrix elements are constant to a good approximation (see also end of Sec. 2.3).

If the upper intermediate state is a continuum state, the energy parameter $\eta(E_\phi + \hbar\omega_{\mathrm{L}} > 0)$ [see Eq. (3.30)] is complex, and the dynamic polarizability acquires an imaginary part, describing the population loss rate due to ionization. As given in Eq. (3.52), the real part of the AC Stark shift determines the frequency shift of the atomic level $|\phi\rangle$ in Hz via the relation

$$\Delta\nu_{\mathrm{AC}}(\phi) = \frac{1}{h} \, \mathrm{Re}[\Delta E_{\mathrm{AC}}(\phi)] = \beta_{\mathrm{AC}}(\phi) \, I \,, \tag{3.63}$$

defining the dynamic Stark coefficient β_{AC} [see also Eq. (2.6)]. The imaginary part of the AC Stark shift, if present, yields the decay constant of the probability amplitude of the atom to be in the reference state $|\phi\rangle$ as indicated in Eq. (3.51). The atomic state population, as described by the diagonal elements of the density matrix in (2.11), is equal to the modulus squared of this probability amplitude, therefore the ionization rate of the population in $|\phi\rangle$ reads

$$\gamma_{\mathrm{i}} = -\frac{2}{\hbar} \, \mathrm{Im}[\Delta E_{\mathrm{AC}}(\phi)] = 2\pi\beta_{\mathrm{ioni}}(\phi) \, I \,, \tag{3.64}$$

proportional to the double of the imaginary part of the AC Stark shift. This defines the ionization coefficient $\beta_{\mathrm{ioni}}(\phi)$, which is intensity-independent like $\beta_{\mathrm{AC}}(\phi)$. For this reason, in this thesis, these are called "atomic constants", along with the transition matrix elements β_{ge}. Note that the ionization rate is given in units of angular frequency.

As the laser is assumed to be linearly polarized in z-direction, the sum over the magnetic quantum number m of the intermediate states in the propagator (3.28) can be restricted to the $m = 0$ term. This choice of polarization does not restrict the generality of the discussion, because the initial S states of the investigated transitions are spherically symmetric.

Some explicit polarizability matrix elements are given in appendix B. They involve the hypergeometric function ${}_2F_1$, which originates from the infinite sum over Laguerre polynomials, involved in the non-relativistic hydrogen Green's function (3.29). In general, after

the radial integrations, one obtains a sum involving several hypergeometric functions, which can be reduced to a single one, using the contiguous relations for the hypergeometric functions (see e.g. [73]). In Sec. 3.6, the connection of $\beta_{\rm ioni}$ to the usual ionization cross section will be used for an independent verification of the present calculations.

To calculate the Stark shift coefficient $\beta_{\rm AC}$ and ionization coefficient $\beta_{\rm ioni}$ for FS and HFS states, the same considerations as for the transition operator (3.31) as given in Sec. 3.3 apply. For S states, the coefficients for the Schrödinger states are also applicable to each individual FS and HFS sublevel without modification. For an nD state, consider the light shift operator

$$Q^{ij} = \sum_{\pm} r^i \frac{1}{H_0 - E_n \pm \hbar\omega_{\rm L}} r^j \,. \tag{3.65}$$

It consists of both a nonzero scalar component $\boldsymbol{Q}(0)$ and a rank two traceless component $\boldsymbol{Q}(2)$. To obtain the dynamic Stark shift coefficient $\beta_{\rm AC}(nD)$ in a linearly z-polarized laser field, the reduced matrix elements $\beta^{(0)}_{\rm AC}$ and $\beta^{(2)}_{\rm AC}$ have to be added after applying the appropriate angular prefactors.

In particular, the reduced matrix element $\beta^{(0)}_{\rm AC}$ needs no modification for FS and HFS sublevels, while $\beta^{(2)}_{\rm AC}$ must be multiplied by

$$(-1)^{L+S+J}(2J+1)\left\{ \begin{array}{ccc} L & J & S \\ J & L & 2 \end{array} \right\} \tag{3.66}$$

for a FS level with angular momentum $J = L + S$, where $L = 2$, and additionally by

$$(-1)^{J+I+F}(2F+1)\left\{ \begin{array}{ccc} J & F & I \\ F & J & 2 \end{array} \right\} \tag{3.67}$$

if the state under consideration is a HFS level with angular momentum $F = J + I$. The Wigner-Eckhart theorem yields the dependence on the magnetic quantum number, such that, e.g., for a HFS state $|\phi\rangle = |nD, (JI)Fm_F\rangle$ in a linearly z-polarized laser field, one obtains

$$\begin{aligned} \beta_{\rm AC}(\phi) =& \frac{1}{\sqrt{2L+1}}\,\beta^{(0)}_{\rm AC}(nD) + (-1)^{L+S+2J+I+2F-m_F}(2J+1)(2F+1)\times \\ & \left(\begin{array}{ccc} F & 2 & F \\ -m_F & 0 & m_F \end{array} \right) \left\{ \begin{array}{ccc} L & J & S \\ J & L & 2 \end{array} \right\} \left\{ \begin{array}{ccc} J & F & I \\ F & J & 2 \end{array} \right\} \beta^{(2)}_{\rm AC}(nD)\,, \end{aligned} \tag{3.68}$$

where $L = 2$ for D states. The ionization coefficient $\beta_{\rm ioni}$ of an nD state is calculated in exactly the same way.

3.5.2 Results for two-photon transitions

The non-relativistic results for the dynamic Stark coefficients $\beta_{\rm AC}$ and the ionization coefficient $\beta_{\rm ioni}$, as defined in Eqs. (3.63) and (3.64), are given in the following Tabs. 3.3-3.6, for laser frequencies on two-photon resonance with S–S and S–D transitions. The analytic results, evaluated in the tables, are obtained in the dipole approximation and

Table 3.3: Dynamic Stark shift coefficients $\beta_{\rm AC}$ and ionization coefficients $\beta_{\rm ioni}$ for $1S \Leftrightarrow nS$ transitions (on two-photon resonance), as defined in Eqs. (2.6), (2.10), (3.63) and (3.64), in the non-relativistic dipole approximation, evaluated for nuclear charge number $Z = 1$ and infinite nuclear mass. Reduced mass effects and the dependence of the results on Z can be included by multiplication with the scaling factor (3.37). For all S states, the values are also applicable to all FS and HFS sublevels. The non-relativistic treatment implies that about 3 decimals of the results in this table are relevant for a comparison of theory and experiment. Relativistic corrections to the $\beta_{\rm AC}$ and $\beta_{\rm ioni}$ listed here, can be obtained from (4.54) and (4.55) in chapter 4, for radiative corrections see (4.57) and (4.58). Leading order non-dipole effects are summarized in (4.73) and (4.74).

$1S \Leftrightarrow nS$	$\beta_{\rm AC}(1S)$ [Hz $(\mathrm{W/m^2})^{-1}$]	$\beta_{\rm AC}(nS)$ [Hz $(\mathrm{W/m^2})^{-1}$]	$\beta_{\rm ioni}(nS)$ [Hz $(\mathrm{W/m^2})^{-1}$]
$1S$–$2S$	-2.67827×10^{-5}	1.39927×10^{-4}	1.20208×10^{-4}
$1S$–$3S$	-3.02104×10^{-5}	9.80847×10^{-5}	2.02241×10^{-5}
$1S$–$4S$	-3.18301×10^{-5}	8.66487×10^{-5}	7.10785×10^{-6}
$1S$–$5S$	-3.26801×10^{-5}	8.20398×10^{-5}	3.35245×10^{-6}
$1S$–$6S$	-3.31724×10^{-5}	7.97219×10^{-5}	1.85663×10^{-6}
$1S$–$7S$	-3.34805×10^{-5}	7.83897×10^{-5}	1.13885×10^{-6}
$1S$–$8S$	-3.36851×10^{-5}	7.75526×10^{-5}	7.50088×10^{-7}
$1S$–$9S$	-3.38277×10^{-5}	7.69918×10^{-5}	5.20731×10^{-7}
$1S$–$10S$	-3.39307×10^{-5}	7.65976×10^{-5}	3.76481×10^{-7}
$1S$–$11S$	-3.40076×10^{-5}	7.63098×10^{-5}	2.81130×10^{-7}
$1S$–$12S$	-3.40664×10^{-5}	7.60932×10^{-5}	2.15538×10^{-7}
$1S$–$13S$	-3.41124×10^{-5}	7.59261×10^{-5}	1.68914×10^{-7}
$1S$–$14S$	-3.41490×10^{-5}	7.57945×10^{-5}	1.34855×10^{-7}
$1S$–$15S$	-3.41786×10^{-5}	7.56889×10^{-5}	1.09389×10^{-7}
$1S$–$16S$	-3.42029×10^{-5}	7.56030×10^{-5}	8.99638×10^{-8}
$1S$–$17S$	-3.42231×10^{-5}	7.55321×10^{-5}	7.48861×10^{-8}
$1S$–$18S$	-3.42400×10^{-5}	7.54729×10^{-5}	6.30029×10^{-8}
$1S$–$19S$	-3.42544×10^{-5}	7.54229×10^{-5}	5.35100×10^{-8}
$1S$–$20S$	-3.42667×10^{-5}	7.53804×10^{-5}	4.58347×10^{-8}

with the approximation of retaining only the second-order in perturbation theory [see Eq. (3.62)]. In this case, both the frequency shift $\Delta\nu_{\rm AC}$ and the angular ionization rate $\gamma_{\rm i}$ are proportional to the light intensity. Corrections beyond the non-relativistic dipole approach are discussed in the following chapter.

Some of the results listed in the tables have appeared in the literature before (e.g. Ref. [31]). An overview of the previous results is provided in appendix A. The results presented here are in full agreement with those given in Refs. [31, 74–76] and more transitions are added to the analysis. In the comparison with results given in atomic units,

as in [31], the conversion

$$\beta_{\mathrm{AC}}(\phi)\,[\mathrm{at.u.}] = \beta_{\mathrm{AC}}(\phi)\,[\mathrm{SI}]\,\frac{\hbar^2}{m_{\mathrm{e}}\,a_0^4\,\alpha} \tag{3.69}$$

has to be used, and analogously for β_{ioni} (see also Eq. (A.2) in appendix A).

It is perhaps interesting to observe that the transition $2S$–$3S$ is special in that the dynamic Stark shift of the $3S$ state has no imaginary part (see Tab. 3.4). The reason is, that the energy of one photon with half the $2S$–$3S$ transition energy is too small for one-photon ionization. Note also that the $|1S\rangle$ state as the ground state of the unperturbed atom-field Hamiltonian is always shifted downwards in energy, as it must be for any second-order perturbation theory effect.

Concerning the dependence of the results on the nuclear charge number Z and the reduced mass μ of the system, the same considerations apply as for the transition matrix elements in Sec. 3.3. In particular, the values from Tabs. 3.3-3.6 must be multiplied with the scaling factor (3.37), for a specific two-body Coulomb system.

The $1/Z^4$ dependence of the dynamic Stark coefficients, and especially the 16-fold reduction of the ionization coefficient, might be important in the context of planned measurements on trapped hydrogenlike helium. For spectroscopic experiments on systems with $Z > 1$, the required light sources with ultra-stable frequencies and sufficient intensity have recently been demonstrated to be within reach in the near future [77].

The analytic calculations of the matrix elements for the highly excited states have been performed with the computer algebra system *Mathematica* [78], without which the results would not have been obtained in a reasonable time. The reason that the calculations are carried out up to these high quantum numbers is that they facilitate the evaluation of the asymptotics of the light shifts for $n \to \infty$. If theoretical predictions for higher n than those included in the tables are required, these can be obtained by fitting inverse powers of the principal quantum number to the real and to the imaginary parts of the data in Tabs. 3.3 and 3.4, see also Tab. Ic in [31]. One then obtains the following estimates of the asymptotic limits, valid for $n \to \infty$, for $1S \Leftrightarrow nS$ transitions:

$$\beta_{\mathrm{AC}}(1S) \approx \left[-3.44(1)\times 10^{-5} + \mathcal{O}\left(\frac{1}{n}\right)\right]\,\frac{\mathrm{Hz}}{\mathrm{W/m^2}}\,, \tag{3.70a}$$

$$\beta_{\mathrm{AC}}(nS) \approx \left[7.49(2)\times 10^{-5} + \mathcal{O}\left(\frac{1}{n}\right)\right]\,\frac{\mathrm{Hz}}{\mathrm{W/m^2}}\,, \tag{3.70b}$$

$$\beta_{\mathrm{ioni}}(nS) \approx \left[\frac{3.63(1)\times 10^{-4}}{n^3} + \mathcal{O}\left(\frac{1}{n^4}\right)\right]\,\frac{\mathrm{Hz}}{\mathrm{W/m^2}}\,, \tag{3.70c}$$

Table 3.4: Dynamic Stark shift coefficients and ionization coefficients (on two-photon resonance) as in Tab. 3.3, but for $2S \Leftrightarrow nS$ transitions.

$2S \Leftrightarrow nS$	$\beta_{\mathrm{AC}}(2S)$ [Hz $(\mathrm{W/m^2})^{-1}$]	$\beta_{\mathrm{AC}}(nS)$ [Hz $(\mathrm{W/m^2})^{-1}$]	$\beta_{\mathrm{ioni}}(nS)$ [Hz $(\mathrm{W/m^2})^{-1}$]
$2S$–$3S$	-7.18795×10^{-4}	-6.99895×10^{-3}	0
$2S$–$4S$	-9.47799×10^{-4}	2.11716×10^{-3}	1.25626×10^{-3}
$2S$–$5S$	-1.16885×10^{-3}	1.70310×10^{-3}	4.65485×10^{-4}
$2S$–$6S$	-1.36379×10^{-3}	1.52064×10^{-3}	2.28478×10^{-4}
$2S$–$7S$	-1.52869×10^{-3}	1.42368×10^{-3}	1.30721×10^{-4}
$2S$–$8S$	-1.66537×10^{-3}	1.36562×10^{-3}	8.23925×10^{-5}
$2S$–$9S$	-1.77773×10^{-3}	1.32791×10^{-3}	5.55288×10^{-5}
$2S$–$10S$	-1.86994×10^{-3}	1.30194×10^{-3}	3.93145×10^{-5}
$2S$–$11S$	-1.94583×10^{-3}	1.28325×10^{-3}	2.89099×10^{-5}
$2S$–$12S$	-2.00858×10^{-3}	1.26932×10^{-3}	2.19090×10^{-5}
$2S$–$13S$	-2.06078×10^{-3}	1.25865×10^{-3}	1.70162×10^{-5}
$2S$–$14S$	-2.10451×10^{-3}	1.25029×10^{-3}	1.34890×10^{-5}
$2S$–$15S$	-2.14138×10^{-3}	1.24361×10^{-3}	1.08794×10^{-5}
$2S$–$16S$	-2.17269×10^{-3}	1.23819×10^{-3}	8.90578×10^{-6}
$2S$–$17S$	-2.19945×10^{-3}	1.23372×10^{-3}	7.38465×10^{-6}
$2S$–$18S$	-2.22247×10^{-3}	1.23000×10^{-3}	6.19281×10^{-6}
$2S$–$19S$	-2.24238×10^{-3}	1.22687×10^{-3}	5.24540×10^{-6}
$2S$–$20S$	-2.25971×10^{-3}	1.22420×10^{-3}	4.48258×10^{-6}

and for $2S \Leftrightarrow nS$ transitions:

$$\beta_{\mathrm{AC}}(2S) \approx \left[-2.37(7) \times 10^{-3} + \mathcal{O}\left(\frac{1}{n}\right)\right] \frac{\mathrm{Hz}}{\mathrm{W/m^2}}\,, \tag{3.71a}$$

$$\beta_{\mathrm{AC}}(nS) \approx \left[1.19(2) \times 10^{-3} + \mathcal{O}\left(\frac{1}{n}\right)\right] \frac{\mathrm{Hz}}{\mathrm{W/m^2}}\,, \tag{3.71b}$$

$$\beta_{\mathrm{ioni}}(nS) \approx \left[\frac{3.47(5) \times 10^{-2}}{n^3} + \mathcal{O}\left(\frac{1}{n^4}\right)\right] \frac{\mathrm{Hz}}{\mathrm{W/m^2}}\,. \tag{3.71c}$$

The limit $n \to \infty$ is interesting because highly excited Rydberg S states have a long lifetime, allowing for a high spectral resolution [79]. The asymptotic behavior in the limit of high quantum numbers is analogous to the one which has recently been observed for Bethe logarithms of highly excited Rydberg states [80].

Table 3.5: Dynamic Stark coefficients as in Tab. 3.3, but for $1S \Leftrightarrow nD$ transitions. The respective coefficients for the $1S$ state, $\beta_{\rm AC}(1S)$, are identical with those from Tab. 3.3, and are therefore not listed again. For FS and HFS sublevels of an nD state, the appropriate angular prefactors from Eqs. (3.66)-(3.68) must be taken into account.

$1S \Leftrightarrow nD$	$\beta^{(0)}_{\rm AC}(nD)$ [Hz $(\mathrm{W/m^2})^{-1}$]	$\beta^{(2)}_{\rm AC}(nD)$ [Hz $(\mathrm{W/m^2})^{-1}$]	$\beta^{(0)}_{\rm ioni}(nD)$ [Hz $(\mathrm{W/m^2})^{-1}$]	$\beta^{(2)}_{\rm ioni}(nD)$ [Hz $(\mathrm{W/m^2})^{-1}$]
$1S$–$3D$	2.11378×10^{-4}	1.30662×10^{-5}	3.67432×10^{-6}	-2.11508×10^{-6}
$1S$–$4D$	1.90315×10^{-4}	4.70825×10^{-6}	1.39210×10^{-6}	-8.11183×10^{-7}
$1S$–$5D$	1.81694×10^{-4}	2.24738×10^{-6}	6.70000×10^{-7}	-3.92504×10^{-7}
$1S$–$6D$	1.77255×10^{-4}	1.25298×10^{-6}	3.74221×10^{-7}	-2.19848×10^{-7}
$1S$–$7D$	1.74652×10^{-4}	7.71734×10^{-7}	2.30562×10^{-7}	-1.35678×10^{-7}
$1S$–$8D$	1.72990×10^{-4}	5.09668×10^{-7}	1.52256×10^{-7}	-8.96938×10^{-8}
$1S$–$9D$	1.71863×10^{-4}	3.54487×10^{-7}	1.05879×10^{-7}	-6.24189×10^{-8}
$1S$–$10D$	1.71062×10^{-4}	2.56634×10^{-7}	7.66377×10^{-8}	-4.52039×10^{-8}
$1S$–$11D$	1.70472×10^{-4}	1.91828×10^{-7}	5.72754×10^{-8}	-3.37962×10^{-8}
$1S$–$12D$	1.70025×10^{-4}	1.47183×10^{-7}	4.39391×10^{-8}	-2.59345×10^{-8}
$1S$–$13D$	1.69678×10^{-4}	1.15414×10^{-7}	3.44509×10^{-8}	-2.03388×10^{-8}
$1S$–$14D$	1.69403×10^{-4}	9.21865×10^{-8}	2.75145×10^{-8}	-1.62467×10^{-8}
$1S$–$15D$	1.69182×10^{-4}	7.48066×10^{-8}	2.23252×10^{-8}	-1.31844×10^{-8}
$1S$–$16D$	1.69001×10^{-4}	6.15416×10^{-8}	1.83651×10^{-8}	-1.08470×10^{-8}
$1S$–$17D$	1.68851×10^{-4}	5.12407×10^{-8}	1.52901×10^{-8}	-9.03172×10^{-9}
$1S$–$18D$	1.68726×10^{-4}	4.31191×10^{-8}	1.28659×10^{-8}	-7.60040×10^{-9}
$1S$–$19D$	1.68620×10^{-4}	3.66289×10^{-8}	1.09289×10^{-8}	-6.45656×10^{-9}
$1S$–$20D$	1.68529×10^{-4}	3.13799×10^{-8}	9.36238×10^{-9}	-5.53143×10^{-9}

3.6 Calculation of the photoionization cross section

In this section, the cross-section for the one-photon resonant ionization of the $2S$ state in a low-intensity field of arbitrary frequency, but minimum photon energy of $(Z^2 \times 13.6\,\mathrm{eV})/4$, is presented. The theory for this process is very well understood since the 1930s [81], including the Z-scaling, but a comparison of the results constitutes an independent verification of the ionization rate coefficients $\beta_{\rm ioni}$ obtained in Sec. 3.5.

In analogy to bound states (3.4), one can assign to a continuum state a generalized principal quantum number n', which is real and positive. The energy of an electron in the continuum can then be written as

$$E_{n'} = -\frac{(Z\alpha)^2\, m_{\rm e}\, c^2}{2(\mathrm{i}\, n')^2} > 0\,. \tag{3.72}$$

Here, the continuum threshold is taken to be the zero point of the energy scale, such that bound states extend into the negative energy region. This is different from the conventions used in an early article [81] on this subject.

Table 3.6: Dynamic Stark coefficients as in Tab. 3.5, but for $2S \Leftrightarrow nD$ transitions. The respective coefficients for the $2S$ state, $\beta_{\rm AC}(2S)$, are identical with those from Tab. 3.4.

$2S \Leftrightarrow nD$	$\beta^{(0)}_{\rm AC}(nD)$ [Hz $(\mathrm{W/m^2})^{-1}$]	$\beta^{(2)}_{\rm AC}(nD)$ [Hz $(\mathrm{W/m^2})^{-1}$]	$\beta^{(0)}_{\rm ioni}(nD)$ [Hz $(\mathrm{W/m^2})^{-1}$]	$\beta^{(2)}_{\rm ioni}(nD)$ [Hz $(\mathrm{W/m^2})^{-1}$]
$2S$–$3D$	-1.17698×10^{-2}	4.99866×10^{-3}	0	0
$2S$–$4D$	5.47527×10^{-3}	-1.64045×10^{-4}	1.91609×10^{-3}	-1.10511×10^{-3}
$2S$–$5D$	3.91342×10^{-3}	1.89977×10^{-4}	5.84726×10^{-4}	-3.43343×10^{-4}
$2S$–$6D$	3.40856×10^{-3}	1.64090×10^{-4}	2.62740×10^{-4}	-1.55670×10^{-4}
$2S$–$7D$	3.17241×10^{-3}	1.21898×10^{-4}	1.43176×10^{-4}	-8.52682×10^{-5}
$2S$–$8D$	3.03968×10^{-3}	8.99553×10^{-5}	8.75750×10^{-5}	-5.23245×10^{-5}
$2S$–$9D$	2.95642×10^{-3}	6.74381×10^{-5}	5.78591×10^{-5}	-3.46451×10^{-5}
$2S$–$10D$	2.90022×10^{-3}	5.15428×10^{-5}	4.03987×10^{-5}	-2.42271×10^{-5}
$2S$–$11D$	2.86026×10^{-3}	4.01348×10^{-5}	2.94079×10^{-5}	-1.76557×10^{-5}
$2S$–$12D$	2.83068×10^{-3}	3.17867×10^{-5}	2.21175×10^{-5}	-1.32900×10^{-5}
$2S$–$13D$	2.80812×10^{-3}	2.55609×10^{-5}	1.70777×10^{-5}	-1.02684×10^{-5}
$2S$–$14D$	2.79046×10^{-3}	2.08355×10^{-5}	1.34753×10^{-5}	-8.10656×10^{-6}
$2S$–$15D$	2.77637×10^{-3}	1.71910×10^{-5}	1.08282×10^{-5}	-6.51678×10^{-6}
$2S$–$16D$	2.76493×10^{-3}	1.43390×10^{-5}	8.83715×10^{-6}	-5.32030×10^{-6}
$2S$–$17D$	2.75549×10^{-3}	1.20777×10^{-5}	7.30950×10^{-6}	-4.40183×10^{-6}
$2S$–$18D$	2.74762×10^{-3}	1.02634×10^{-5}	6.11704×10^{-6}	-3.68459×10^{-6}
$2S$–$19D$	2.74098×10^{-3}	8.79168×10^{-6}	5.17212×10^{-6}	-3.11603×10^{-6}
$2S$–$20D$	2.73533×10^{-3}	7.58614×10^{-6}	4.41334×10^{-6}	-2.65934×10^{-6}

If one considers a dipole transition from the bound $2S$ state to the continuum εP state, with the wavefunction

$$\varepsilon P(r,\theta,\phi) = R_{n'P}(r)\, Y_{10}(\theta,\phi)\,, \tag{3.73}$$

$$R_{n'P}(r) = \frac{\sqrt{m_e}}{\hbar}\left(\frac{Z}{a_0}\right)^{3/2} \frac{\sqrt{1+n'^2}}{\sqrt{1-e^{-2\pi n'}}}\,\frac{2\,r}{3\,n'}\exp\left(-\frac{\mathrm{i}Zr}{n'a_0}\right){}_1F_1\left[\mathrm{i}n'+2,4,2\,\frac{\mathrm{i}\,Z\,r}{n'a_0}\right], \tag{3.74}$$

the one-photon ionization cross section of a single atom for linearly polarized light is proportional to the square of the transition matrix element and reads

$$\sigma_{2\mathrm{S}} = \frac{\pi\, e^2\, \omega_{\mathrm{L}}}{\epsilon_0\, c}\,|\langle 2S|z|\varepsilon P\rangle|^2\,, \tag{3.75}$$

where ω_{L} is the angular frequency of the incident laser radiation, and e is the electron charge. The radial integrals encountered have be calculated in two different ways: (i) direct integration of terms generated by the series representation of the ${}_1F_1$ hypergeometric function and (ii) contour integration using an integral representation of the hypergeometric function (see e.g. [43]) and evaluation of the residues. Both (i) and (ii) lead to the

Table 3.7: Ionization cross sections for hydrogen atoms (Z=1) in the excited state nS, at an incident laser frequency on two-photon resonance with the respective $1S \Leftrightarrow nS$ or $2S \Leftrightarrow nS$ transition, as obtained via Eq. (3.78) from the dynamic Stark coefficient β_{ioni}. This table is provided for convenient comparison with other cross section calculations. Therefore, the values are here given in the usual units cm^2 instead of SI units.

n	$1S \Leftrightarrow nS$ $\sigma_{\text{ioni}}(nS)$ [cm^2]	$2S \Leftrightarrow nS$ $\sigma_{\text{ioni}}(nS)$ [cm^2]
2	6.174×10^{-18}	–
3	1.231×10^{-18}	0
4	4.563×10^{-19}	1.613×10^{-17}
5	2.204×10^{-19}	6.694×10^{-18}
6	1.236×10^{-19}	3.477×10^{-18}
7	7.640×10^{-20}	2.055×10^{-18}
8	5.057×10^{-20}	1.322×10^{-18}
9	3.522×10^{-20}	9.037×10^{-19}
10	2.552×10^{-20}	6.462×10^{-19}
11	1.909×10^{-20}	4.786×10^{-19}
12	1.466×10^{-20}	3.647×10^{-19}
13	1.150×10^{-20}	2.844×10^{-19}
14	9.188×10^{-21}	2.262×10^{-19}
15	7.458×10^{-21}	1.830×10^{-19}
16	6.137×10^{-21}	1.501×10^{-19}
17	5.111×10^{-21}	1.247×10^{-19}
18	4.301×10^{-21}	1.047×10^{-19}
19	3.654×10^{-21}	8.881×10^{-20}
20	3.131×10^{-21}	7.598×10^{-20}

same result

$$|\langle 2S|z|\varepsilon P\rangle|^2 = \frac{2^{17}\, a_0^4\, m_{\text{e}}}{3Z^4\, \hbar^2} \frac{\exp[-4n' \operatorname{arccot}(n'/2)]}{1-\exp(-2\pi\, n')} \frac{n'^{10}\,(1+n'^2)}{(4+n'^2)^6}\,. \tag{3.76}$$

Observe that this expression is proportional to $1/Z^4$ because the matrix element contains one continuum state. For two bound states, the transition matrix element squared would scale as $1/Z^2$. In [82], one can find a result differing by a factor of 3/2 from Eq. (3.76). The analysis of that work has shown that there has been an error in the conversion of expressions taken from [81], where a rather peculiar choice of the zero point of the energy scale is used.

For the case of an incident laser angular frequency of one half of the $1S$–$2S$ transition frequency, the generalized quantum number of the continuum state is $n' = 2\sqrt{2}$, and one obtains the result

$$\sigma_{2S} = \frac{1}{Z^2}\, 6.174 \times 10^{-18}\, \text{cm}^2\,. \tag{3.77}$$

One can compare the ionization rate coefficient $\beta_{\rm ioni}$ from Sec. 3.5 directly with the $2S$ cross section calculated above using the relation

$$\sigma_{\rm ioni} = 2\,\pi\,\beta_{\rm ioni}\,\hbar\omega_{\rm L} = \frac{1}{Z^2}\,6.174\times 10^{-18}\,{\rm cm}^2\,, \tag{3.78}$$

which agrees with (3.77), i.e., $\sigma_{2S} = \sigma_{\rm ioni}$. Here, the Z-scaling of the ionization cross section is the result of a factor Z^{-4} for the ionization coefficient $\beta_{\rm ioni}$ and the Z^2-scaling of the photon energy $\hbar\omega_{\rm L}$, required for maintaining two-photon resonance with a given transition. In Tab. 3.7 the ionization cross sections in cm^2 for a set of excited nS levels is given, as obtained from the imaginary part of the dynamic Stark coefficient $\beta_{\rm ioni}$. All considerations concerning the relativistic and radiative corrections to $\beta_{\rm ioni}$ given in chapter 4 also apply to the ionization cross section through relation (3.78). Their magnitude is small and below the current precision of measurement, decreasing even more for larger nuclear charge. This behavior is different than in most radiative corrections of non-dynamic processes [70].

3.7 Combined induced-spontaneous two-photon decay

In the context of laser driven two-photon S–S transitions and two-photon spontaneous emission, one also has to consider the two-step process of combined induced-spontaneous two-photon decay of the excited level. In this process, the interaction of the excited atom with the laser field and the vacuum modes leads to a final state of the system, where the atom is in the ground state, the laser mode photon number is increased or decreased by one, and one photon is spontaneously emitted into an empty mode of the electromagnetic field. One contribution is depicted Fig. 3.1, where the interaction with the laser field takes place before the spontaneous emission.

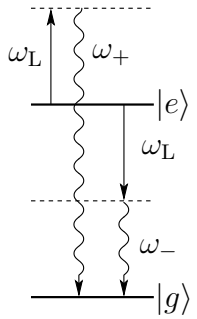

Figure 3.1: Combined induced-spontaneous decay process leading to a depopulation of the excited state $|e\rangle$. Absorption or stimulated emission of one laser photon with energy $\hbar\omega_{\rm L}$ and subsequent spontaneous decay of the virtual intermediate states (dashed) to the ground state can take place, via emission of a photon of energy $\hbar\omega_+$ or $\hbar\omega_-$, respectively.

Table 3.8: Combined induced-spontaneous two-photon decay coefficients $\beta_{\rm is}$ between two S states interacting with a laser field on two-photon resonance, as defined in Eq. (3.81). The coefficients $\beta_{\rm is}$ scale with the nuclear charge number as Z^{-2}.

n	$1S \Leftrightarrow nS$ $\beta_{\rm is}$ [Hz/(W/m^2)]	$2S \Leftrightarrow nS$ $\beta_{\rm is}$ [Hz/(W/m^2)]
2	8.05160×10^{-11}	–
3	1.11235×10^{-11}	1.00370×10^{-8}
4	3.70994×10^{-12}	1.60542×10^{-10}
5	1.71123×10^{-12}	5.39512×10^{-11}
6	9.36717×10^{-13}	2.56181×10^{-11}
7	5.70630×10^{-13}	1.45368×10^{-11}
8	3.74182×10^{-13}	9.18434×10^{-12}
9	2.58988×10^{-13}	6.23200×10^{-12}
10	1.86845×10^{-13}	4.44898×10^{-12}
11	1.39303×10^{-13}	3.29922×10^{-12}
12	1.06674×10^{-13}	2.52023×10^{-12}
13	8.35218×10^{-14}	1.97163×10^{-12}
14	6.66319×10^{-14}	1.57309×10^{-12}
15	5.40172×10^{-14}	1.27606×10^{-12}
16	4.44032×10^{-14}	1.04988×10^{-12}
17	3.69465×10^{-14}	8.74445×10^{-13}
18	3.10733×10^{-14}	7.36203×10^{-13}
19	2.63839×10^{-14}	6.25741×10^{-13}
20	2.25940×10^{-14}	5.36386×10^{-13}

In the following, the interaction of the atom with the laser mode is described with the second-quantized electric dipole interaction Hamiltonian $H_{\rm LI}$, as defined in Eq. (3.5b). The interaction with the vacuum modes is described by the interaction Hamiltonian $H_{\rm VI}$, as given in Eq. (3.5c).

The initial state is denoted by $|\phi_0\rangle = |e, n_{\rm L}, 0\rangle$, with $n_{\rm L}$ photons in the laser mode and no photons in any other mode. To evaluate the transition rate of the combined induced-spontaneous decay, one needs to evaluate the imaginary part of the principal term of the fourth-order energy perturbation

$$\Delta E^{(4)}_{\rm LV}(\phi_0) = \langle\phi_0| H_{\rm LV} \frac{1}{E_0 - H_0^{(\rm s)}} H_{\rm LV} \frac{1}{E_0 - H_0^{(\rm s)}} H_{\rm LV} \frac{1}{E_0 - H_0^{(\rm s)}} H_{\rm LV} |\phi_0\rangle \,, \tag{3.79}$$

where $H_{\rm LV} = H_{\rm LI} + H_{\rm VI}$, taking into account only those terms, which contain both the laser interaction and the vacuum interaction in second order. Here, the unperturbed Hamiltonian $H_0^{(\rm s)}$ includes the atomic spectrum as well as the field modes as defined in Eq. (3.1).

From the resonances caused by the possible final states of the system, $|g, n_\mathrm{L}+1, 1_z(\boldsymbol{k}_-)\rangle$ and $|g, n_\mathrm{L}-1, 1_z(\boldsymbol{k}_+)\rangle$, the induced-spontaneous decay rate γ_is is obtained:

$$\gamma_\mathrm{is} = (2\pi\beta_\mathrm{is})\, I\,, \tag{3.80}$$

$$\beta_\mathrm{is} = \frac{4e^4}{6\pi c^4 \epsilon_0^2 h} \left\{ \omega_-^3 \left| \left\langle e \left| z \frac{1}{H_0 - (E_e - \hbar\omega_\mathrm{L})} z \right| g \right\rangle \right|^2 + \omega_+^3 \left| \left\langle e \left| z \frac{1}{H_0 - (E_e + \hbar\omega_\mathrm{L})} z \right| g \right\rangle \right|^2 \right\}, \tag{3.81}$$

where the same limit $n_\mathrm{L}/\mathcal{V} \gg 1$ as in Sec. 3.4.2 leads to the classic intensity I. In this limit, the Fock states factor out, and again only H_0, the atomic part of the unperturbed Hamiltonian as defined in (3.1b), enters in the matrix elements. The angular frequencies of the spontaneously emitted photons (see Fig. 3.1), read

$$\omega_\pm = c|\boldsymbol{k}_\pm| = \omega_{eg} \pm \omega_\mathrm{L}\,. \tag{3.82}$$

For a set of two-photon transitions, the decay coefficients β_is are listed in Tab. 3.8. It is obvious that for typical intensities of several MW/m^2, as considered in chapter 2, the contribution of this process to the width of the excited state is small, when compared to ionization and spontaneous decay.

3.8 Conclusion

In this chapter, the non-relativistic interaction of a hydrogen atom or hydrogenlike ion with a one-photon off-resonant monochromatic driving laser field was examined. In a unified framework of perturbation theory, the transition matrix elements and the dynamic polarizabilities have been obtained. In particular, a large set of values for transitions relevant for high-precision spectroscopy were calculated, involving the stable $1S$ and the metastable $2S$ state as the ground state. The results are given in SI units such that they are directly usable in the equations for the quantum dynamics (2.11) of chapter 2. A comparison with some values which have appeared in the literature before, and the resolution of several inconsistencies encountered, is given in appendix A.

All angular prefactors relevant for the application to transitions between fine structure and hyperfine structure states were presented. The Z-scaling and the reduced mass scaling have been derived to extend the validity of the results to any bound two-body Coulomb system, e.g., positronium, muonium or anti-hydrogen.

Two ways of deriving analytic expressions for the dynamic Stark shift of a hydrogenic energy level have been contrasted. One is based on an adiabatically damped length-gauge interaction, using a classical description of the laser field. The second, using a quantized description of the electromagnetic field, leads to a more general expression, which was found to agree with the classical result in the limit of a large occupation number of the laser mode.

By calculating the one-photon ionization cross-section of the $2S$ state in two independent ways, the result obtained for the ionization coefficient as the imaginary part of the dynamic Stark matrix element has been verified.

The decay channel of combined induced-spontaneous decay, which is due to the interaction of the atomic system with both the laser field and the vacuum, has been examined and the corresponding decay coefficients for the S–S transitions have been obtained.

Chapter 4

Relativistic and Radiative Corrections to Dynamic Processes

This chapter is dedicated to corrections to the atomic constants which have been treated in the previous chapter, namely the dynamic polarizability, determining β_{AC} and β_{ioni}, and the two-photon transition matrix element β_{ge}. These constants have been calculated using a number of approximations, each of which is well justified for the current experimental use, but will probably break down at some point for future measurements with increased precision. The approximations used and the corresponding leading order corrections which are calculated in this chapter, are the following:

First of all, to go beyond the framework of nonrelativistic Schrödinger theory, corrections due to relativistic effects are considered. Second, the interaction of the system "atom+laser field" with the QED vacuum, has not yet been fully considered and is taken into account by leading logarithmic order (LLO) radiative corrections. Finally, there is the dipole approximation for the harmonic electric field of the laser, which is supplemented by leading order geometric corrections, which in fact depend on the electric field configuration in a specific experimental setup. Therefore, the most common excitation scheme, consisting of a standing wave, is considered. If these corrections become important for the hydrogen $1S$–$2S$ measurement, they will become even more important for planned experiments with systems where $Z>1$, as is obvious from the Z scaling of the results.

Connected with the precise knowledge of the atomic constants is the experimental problem of accurately determining the excitation intensity, by which the constants are multiplied in order to obtain the observable shift and transition frequencies. As will be discussed in the next chapter, the intensity measurement in the MPQ setup amounts to a power measurement, the precision of which is quite hard to improve. An alternative non-invasive measurement procedure is proposed in chapter 6.

One could argue, that at least the relativistic effects could be included non-perturbatively using Dirac theory [63]. However, by using the effective Hamiltonian approach of Nonrelativistic Quantum Electrodynamics (NRQED) [83], relativistic effects can be treated in a unified formalism with the radiative corrections, simply as perturbation effects to the nonrelativistic expression, which is appropriate for the low-Z systems which are used in

high-precision spectroscopy.

The results obtained in the following constitute corrections to dynamic processes induced by the laser field, as opposed to the static Lamb shift of energy levels. Therefore, the corrections depend on the frequency of the laser, as do the atomic constants themselves. For a set of two-photon transitions, the corrections are therefore evaluated for the appropriate frequencies used to drive the respective transitions. As the atomic constants are expressions of second-order perturbation theory, one could view the following considerations as calculating "corrections to corrections".

4.1 Perturbation to the dynamic polarizability

The general treatment of a perturbation δV to the dynamic polarizability and the corresponding definitions are the subject of this section, to set the scene for the remainder of the chapter, in which specific expressions for δV are considered, accommodating relativistic and radiative effects.

Consider the dynamic polarizability P_{ω_L} of a reference state, ϕ, which is an atomic energy eigenstate of the Schrödinger theory,

$$P_{\omega_\mathrm{L}}(\phi) = \sum_{\pm} \left\langle \phi \left| z \, \frac{1}{H_0 - E_\phi \pm \omega_\mathrm{L}} \, z \right| \phi \right\rangle , \tag{4.1}$$

where the harmonic electric field of angular frequency ω_L is taken to be polarized in z-direction. In this chapter, only S states are considered, the results are therefore invariant under this choice of polarization. Here, H_0 is the unperturbed Hamiltonian of the hydrogen atom,

$$H_0 = \frac{\boldsymbol{p}^2}{2m_\mathrm{e}} - \frac{Z\alpha\hbar c}{r} , \tag{4.2}$$

where m_e is the electron mass and α the fine structure constant. Any perturbation δV, which is added to H_0, also generates a shift of the eigenenergy and a perturbation to the corresponding wavefunction:

$$H_0 \to H_0 + \lambda\, \delta V , \qquad E_\phi \to E_\phi + \lambda \, \langle \phi | \delta V | \phi \rangle , \qquad |\phi\rangle \to |\phi\rangle + \lambda \, |\delta\phi\rangle , \tag{4.3}$$

where

$$|\delta\phi\rangle = \left(\frac{1}{E_\phi - H_0} \right)' \, \delta V \, |\phi\rangle . \tag{4.4}$$

Inserted into the dynamic polarizability (4.1), and retaining only the leading order in λ, these replacements generate three separate corrections to the dynamic polarizability, giving the contribution from the change of the Hamiltonian (H), its eigenenergies (E)

and the wavefunction (W), respectively:

$$\delta P^H_{\omega_\mathrm{L}}(\phi) = -\sum_{\pm} \left\langle \phi \left| z \, \frac{1}{H_0 - E_\phi \pm \omega_\mathrm{L}} \, \delta V \, \frac{1}{H_0 - E_\phi \pm \omega_\mathrm{L}} \, z \right| \phi \right\rangle , \tag{4.5}$$

$$\delta P^E_{\omega_\mathrm{L}}(\phi) = \sum_{\pm} \left\langle \phi \left| z \left(\frac{1}{H_0 - E_\phi \pm \omega_\mathrm{L}} \right)^2 z \right| \phi \right\rangle \langle \phi | \delta V | \phi \rangle , \tag{4.6}$$

$$\delta P^W_{\omega_\mathrm{L}}(\phi) = \sum_{\pm} \left(\left\langle \delta\phi \left| z \, \frac{1}{H_0 - E_\phi \pm \omega_\mathrm{L}} \, z \right| \phi \right\rangle + \left\langle \phi \left| z \, \frac{1}{H_0 - E_\phi \pm \omega_\mathrm{L}} \, z \right| \delta\phi \right\rangle \right) . \tag{4.7}$$

The derivation of the Hamiltonian contribution $\delta P^H_{\omega_\mathrm{L}}(\phi)$ does not require the expansion of the denominator or the exchange of the operators H_0 and δV, which in general do not commute. For any number x, trivially

$$\frac{1}{H_0 + \delta V - x} = \underbrace{\frac{1}{H_0 - x}}_{=0^{\mathrm{th}}\ \mathrm{order}} + \underbrace{\frac{1}{H_0 + \delta V - x} - \frac{1}{H_0 - x}}_{\mathrm{higher\ orders}} \tag{4.8}$$

$$=: \mathcal{P}_0 + \mathcal{P}_{1,\infty} , \tag{4.9}$$

and elementary transformations lead to:

$$\mathcal{P}_{1,\infty} = -\frac{1}{H_0 + \delta V - x} \, \delta V \, \frac{1}{H_0 - x} . \tag{4.10}$$

Inserting the zeroth order propagator for the first fraction, the first order propagator is therefore:

$$\mathcal{P}_1 = -\frac{1}{H_0 - x} \, \delta V \, \frac{1}{H_0 - x} . \tag{4.11}$$

The results for the real and imaginary part of the contributions (4.5)-(4.7) which will be obtained below, are given separately, and related to the unperturbed polarizability $P_{\omega_\mathrm{L}}(\phi)$, by

$$\xi \, R_H(\phi) = \frac{\mathrm{Re}[\delta P^H_{\omega_\mathrm{L}}(\phi)]}{\mathrm{Re}[P_{\omega_\mathrm{L}}(\phi)]} , \qquad \xi \, I_H(\phi) = \frac{\mathrm{Im}[\delta P^H_{\omega_\mathrm{L}}(\phi)]}{\mathrm{Im}[P_{\omega_\mathrm{L}}(\phi)]} , \tag{4.12}$$

and likewise for R_E, I_E, R_W and I_W. Here, ξ stands for a scale parameter which is characteristic for the perturbation and is defined in the respective cases below. It also contains the Z scaling such that the values for R and I are purely numeric. The total correction to the dynamic polarizability, caused by the action of the perturbation, is then the sum of the three contributions:

$$\mathrm{Re}[\delta P_{\omega_\mathrm{L}}(\phi)] = \mathrm{Re}[P_{\omega_\mathrm{L}}(\phi)] \times \xi \left[R_H(\phi) + R_E(\phi) + R_W(\phi) \right] , \tag{4.13}$$

$$\mathrm{Im}[\delta P_{\omega_\mathrm{L}}(\phi)] = \mathrm{Im}[P_{\omega_\mathrm{L}}(\phi)] \times \xi \left[I_H(\phi) + I_E(\phi) + I_W(\phi) \right] . \tag{4.14}$$

4.2 Perturbation to the transition matrix element

For the two-photon transition matrix element M between two S states with principal quantum numbers n and n',

$$M_{\omega_{\rm L}} = \left\langle n'S \left| z \, \frac{1}{H_0 - E_{\rm int}} \, z \right| nS \right\rangle , \tag{4.15}$$

the reasoning in determining the corrections δM is similar to the previous section. However, there is an additional aspect to be aware of, because both the energies of the ground state and the excited state are shifted, generally by a different amount. The energy of the intermediate state, in the unperturbed case, satisfies $E_{\rm int} = E_n + \omega_{\rm L} = E_{n'} - \omega_{\rm L}$, and one can define the leading order contribution from the change of the Hamiltonian and the wavefunctions in analogy to the corrections to the dynamic polarizability:

$$\delta M^H_{\omega_{\rm L}} = - \left\langle n'S \left| z \, \frac{1}{H_0 - E_{\rm int}} \delta V \frac{1}{H_0 - E_{\rm int}} \, z \right| nS \right\rangle , \tag{4.16}$$

$$\delta M^W_{\omega_{\rm L}} = \left\langle \delta n'S \left| z \, \frac{1}{H_0 - E_{\rm int}} \, z \right| nS \right\rangle + \left\langle n'S \left| z \, \frac{1}{H_0 - E_{\rm int}} \, z \right| \delta nS \right\rangle . \tag{4.17}$$

Note that there is a contribution from both the upper state wave function correction $|\delta n'S\rangle$ and the lower state wave function correction $|\delta nS\rangle$, for $\delta M^W_{\omega_{\rm L}}$. For $\delta M^E_{\omega_{\rm L}}$, the energy of the intermediate state needs to be written in a symmetrical way,

$$E_{\rm int} = \frac{E_n + E_{n'}}{2} , \tag{4.18}$$

because in general, $\langle n'|\delta V|n'\rangle \neq \langle n|\delta V|n\rangle$. The correction to the transition matrix element due to the shift of the energies then reads

$$\begin{aligned} \delta M^E_{\omega_{\rm L}} &= \left\langle n'S \left| z \frac{1}{H_0 - [\,(E_n + \langle n|\delta V|n\rangle + E_{n'} + \langle n'|\delta V|n'\rangle)/2\,]} z \right| nS \right\rangle \\ &= \left\langle n'S \left| z \left(\frac{1}{H_0 - [\,(E_n + E_{n'})/2)]} \right)^2 z \right| nS \right\rangle \left(\frac{\langle n'|\delta V|n'\rangle}{2} + \frac{\langle n|\delta V|n\rangle}{2} \right) . \end{aligned} \tag{4.19}$$

In analogy with Eq. (4.12), the normalized contribution due to the Hamiltonian contribution reads

$$\xi \, R_H = \frac{\delta M^H_{\omega_{\rm L}}}{M_{\omega_{\rm L}}} , \tag{4.20}$$

and analogously for R_E and R_W. The corrections to the transition matrix elements are purely real, just as the matrix elements themselves, because the intermediate bound state energy is always negative. The total correction to the transition matrix element is finally given by

$$\delta M^H_{\omega_{\rm L}} = M_{\omega_{\rm L}} \times \xi \, [R_H + R_E + R_W] . \tag{4.21}$$

4.3 Potential for relativistic corrections

In order to find the effective perturbation potential δV, describing the leading order relativistic energy corrections, one needs to consider the nonrelativistic limit of the Dirac equation passing over into the Pauli-Schrödinger theory of spin-1/2 particles. As opposed to nonrelativistic theory, in the direct nonrelativistic limit of the Dirac theory, the components of the velocity operator do not commute, while the components of the momentum operator do. These difficulties have first been solved by Foldy and Wouthuysen [84], and based on a transformation of the Dirac Hamiltonian, an effective Hamiltonian

$$\delta V_{\rm FW} = \underbrace{-\frac{\boldsymbol{p}^4}{8m_{\rm e}^3c^2}}_{\rm kinetic} + \underbrace{\frac{\pi(Z\alpha)\hbar^3}{2m_{\rm e}^2c}\delta^{(3)}(\boldsymbol{r})}_{\rm zitterbewegung} + \underbrace{\frac{Z\alpha}{4m_{\rm e}^2r^3}(\boldsymbol{L}\cdot\boldsymbol{S})}_{\rm spin-orbit}, \tag{4.22}$$

describing the desired leading order effects was obtained. Here, contributions due to the interaction of the magnetic field with the electron are neglected. The first term ("kinetic term"), can be motivated by considering the expansion in $\beta = v/c$ of the relativistic energy-momentum relation

$$E = \sqrt{m_{\rm e}^2c^4 + \boldsymbol{p}^2c^2} = m_{\rm e}c^2 + \frac{\boldsymbol{p}^2}{2m_{\rm e}} - \frac{\boldsymbol{p}^4}{8m_{\rm e}^3c^2} + \mathcal{O}(\beta^6), \tag{4.23}$$

while the second term in (4.22) is the potential generating the Darwin term [85], which appears in the low-energy approximation of the Dirac equation. In Dirac theory, negative-energy plane wave components necessarily arise for the description of localized wavepackets, and the interference between the negative-energy and positive-energy components induces a very fast oscillatory behavior of the expectation values of the position and velocity operators. This behavior, called "zitterbewegung" of the electron, was proposed by Schrödinger, and is still a subject of current interest [86]. In the Schrödinger theory, the zitterbewegung appears as an effective potential, and for bound states, this is nonzero only for S states due to the $\delta^{(3)}(\boldsymbol{r})$ dependence.

The third term in the perturbation (4.22) is the spin-orbit coupling energy, which generally gives rise to the fine structure. For S states, with which we are concerned in this chapter, the orbital angular momentum is zero, so there is no fine structure splitting. Therefore, the total angular momentum is identical with the electron spin and the atomic state wave function is a simple tensor product of a Schrödinger wave function and a spin-1/2 state

$$|\phi\rangle = \left|n, l=0, m_l=0\,;\, s=\frac{1}{2}, m_s=\pm\frac{1}{2}\right\rangle. \tag{4.24}$$

In the expressions for $\delta P^E_{\omega_{\rm L}}$ and $\delta P^W_{\omega_{\rm L}}$ [see (4.6-4.7)], the contribution due to the spin-orbit coupling vanishes, as $\boldsymbol{L}\cdot\boldsymbol{S}$ acts only on $l=0$ eigenstates. The $\boldsymbol{L}$-$\boldsymbol{S}$ energy is also zero for the remaining Hamiltonian correction, where the operator acts on the intermediate P state, because for the ket

$$(L_xS_x + L_yS_y + L_zS_z)\left|n, 1, 0\,;\frac{1}{2}, \pm\frac{1}{2}\right\rangle, \tag{4.25}$$

which appears in the expression for $P^H_{\omega_L}(\phi)$, one has

$$L_z\,|n,1,0\rangle = S_x\left|\frac{1}{2},\pm\frac{1}{2}\right\rangle = S_y\left|\frac{1}{2},\pm\frac{1}{2}\right\rangle = 0\,. \tag{4.26}$$

In short, the spin-orbit coupling has no effect on the leading order relativistic correction of S states, which leaves the kinetic term and the zitterbewegung term to be evaluated.

4.4 Potential for radiative corrections

The interaction of a bound electron with the vacuum modes of the electromagnetic field is treated in bound state QED [70], and the resulting energy shift of an atomic energy eigenstate ϕ is called the self-energy of the electron in that state. This shift of the atomic levels is the largest contribution to the Lamb shift, was observed for the first time as lifting the degeneracy of the $2S_{1/2}$ and $2P_{1/2}$ states, as predicted by Dirac theory. Other contributions to the Lamb shift include the vacuum polarization and the finite charge radius of the proton, as well as higher-order loop corrections [59, 60].

The second-order expression of time-independent perturbation theory for the electron self-energy reads

$$\Delta E_{\rm SE} = \left\langle \phi,0 \left| H_I \left(\frac{1}{E_{\phi,0}-H_0}\right)' H_I \right| \phi,0 \right\rangle\,, \tag{4.27}$$

$$H_0 = \sum\!\!\!\!\!\!\int_n E_n|n\rangle\langle n| + \sum_{\boldsymbol{k},\lambda} \hbar\omega_k\, a^\dagger_\lambda(\boldsymbol{k}) a_\lambda(\boldsymbol{k})\,, \quad H_I = -e\,\boldsymbol{r}\cdot\boldsymbol{E}\,, \tag{4.28}$$

where $|\phi,0\rangle$ denotes an eigenstate of the unperturbed Hamiltonian H_0, in which the atom is in the state ϕ and the electromagnetic field is empty. Here, the unperturbed Hamiltonian H_0 in spectral representation contains all bound and continuum states $|n\rangle$ and all modes of the quantized electromagnetic field with wave vector $\boldsymbol{k}$ and polarization λ, which satisfy periodic boundary conditions in some quantization volume $\mathcal{V}$. The operators $a^\dagger_\lambda(\boldsymbol{k})$ and $a_\lambda(\boldsymbol{k})$ are the creation and annihilation operators for a photon with the specified wave vector and polarization and the angular frequency $\omega_k = c|\boldsymbol{k}|$. The electric dipole interaction Hamiltonian H_I is given in the length gauge, using the electric field operator

$$\boldsymbol{E} = \sum_{\boldsymbol{k},\lambda} \mathrm{i}\sqrt{\frac{\hbar\omega_k}{2\epsilon_0\mathcal{V}}}\,\boldsymbol{\epsilon}_\lambda(\boldsymbol{k})\left[a_\lambda(\boldsymbol{k}) - a^\dagger_\lambda(\boldsymbol{k})\right]\,, \tag{4.29}$$

where the polarization direction is denoted by $\boldsymbol{\epsilon}_\lambda(\boldsymbol{k})$. At first glance, the evaluation of the integral (4.27) seems not difficult, and the continuum limit

$$\frac{1}{\mathcal{V}}\sum_{\boldsymbol{k}} \to \int_0^K \frac{d^3k}{(2\pi)^3} \tag{4.30}$$

must be taken. However, the result diverges as $K\to\infty$ as a consequence of the unlimited energy contributions of high frequency modes. The first step to remove this divergence is

to renormalize the self-energy by subtracting the mass counterterm, which constitutes the self-energy of a free electron. As a result, the parts which diverge at least linearly with K vanish. Still, the remainder consists of a logarithmically divergent term and the Bethe logarithm, which is of utmost importance for the calculation of high-precision values of the Lamb shift of hydrogenic states in higher orders [87, 88]. The logarithmic divergence, ultimately, cancels with the infrared divergence in the electron form factor correction to the electron-nucleus interaction [58]. To leading logarithmic order, the self-energy shift of a bound state in a hydrogenic system with nuclear charge number Z can then be described by the effective Lamb shift potential

$$\delta V_{\mathrm{SE}} = \frac{4}{3}\,\alpha(Z\alpha)\ln[(Z\alpha)^{-2}]\frac{\hbar^3}{m_{\mathrm{e}}^2 c}\,\delta^{(3)}(\boldsymbol{r})\,, \tag{4.31}$$

with vanishing expectation value for states of angular momentum $l \neq 0$. For the evaluation of high-precision Lamb shifts, this is just the leading order term, but it is perfectly suitable for the evaluation of the leading order corrections to the dynamic polarizability which already describes a small correction of the energy of an atomic level. It should be noted that in spherical coordinates, the three-dimensional Dirac δ-distribution, normalized to unity, reads

$$\delta^{(3)}(\boldsymbol{r}) = \frac{1}{2\pi r^2}\,\delta^{(1)}(r)\,, \tag{4.32}$$

rather than with a denominator of $4\pi r^2$. This is the consequence of the radial coordinate r running from zero to infinity, yielding $1/2$ for the radial integral over the one-dimensional Dirac distribution.

4.5 Calculation of relativistic and radiative corrections

For an efficient approach to the calculation of the relativistic and radiative corrections, it should first be noted, that both potentials δV_{FW} and δV_{SE} contain a $\delta^{(3)}$-term, so that for evaluation purposes, the distinction "δ-correction" and "$\boldsymbol{p}^4$-correction" was made, rather than the actual physical discrimination. The evaluation of these corrections has been performed in a mixture of analytical and numerical techniques.

4.5.1 Wavefunction contributions

First, the perturbations to the hydrogen wave functions will be described, which give analytical results. Consider the defining equation (4.4) for the correction $|\delta\phi\rangle$ to the wavefunction. Acting on this equation with $(E_\phi - H_0)$ from the left and writing the result in position space, the problem is separable into a radial and an angular part in spherical coordinates, because both the δ-potential and the $\boldsymbol{p}^4$-potential are isotropic. The angular

differential equation is therefore the same as for the unperturbed case and as solutions one obtains the spherical harmonics. The radial differential equation, for S states, reads

$$\left[2r\frac{\partial}{\partial r}+r^2\frac{\partial^2}{\partial r^2}+\frac{2m_\mathrm{e}cZ\alpha}{\hbar}\,r+\frac{2m_\mathrm{e}}{\hbar^2}\,r^2E_\phi\right]\delta\phi(r)=\frac{2m_\mathrm{e}}{\hbar^2}\,r^2\big[\delta V-\langle\phi|\delta V|\phi\rangle\big]\phi(r)\,, \quad (4.33)$$

where $\phi(r)$ are the radial hydrogen wavefunctions, E_n are the Schrödinger energies [see Eq. (3.4)], and the perturbation potential matrix elements for a hydrogenic S state with principal quantum number n read

$$\langle\phi|\delta V|\phi\rangle=\frac{\kappa Z^3}{\pi n^3a_0^3} \qquad \text{for} \qquad \delta V=\kappa\delta^{(3)}(\boldsymbol{r})\,, \quad (4.34)$$

$$\langle\phi|\delta V|\phi\rangle=\frac{(3-8n)(Z\alpha)^4m_\mathrm{e}c^2}{8n^4} \qquad \text{for} \qquad \delta V=-\frac{\boldsymbol{p}^4}{8m_\mathrm{e}^3c^2}\,, \quad (4.35)$$

where a_0 is the Bohr radius and κ is an arbitrary constant. The solutions of (4.33) for fixed n were obtained analytically, where the boundary condition $\lim_{r\to\infty}\delta\phi(r)=0$ excludes those parts of the solution which increase exponentially with r. Another integration constant is fixed by the requirement

$$\langle\phi|\delta\phi\rangle\stackrel{!}{=}0\,, \quad (4.36)$$

which is clear from the definition (4.4), where the reduced Green's function explicitly excludes the ϕ component from the propagator. The first two corrections, for the perturbation $\delta V=\kappa\delta^{(3)}(\boldsymbol{r})$, read

$$\delta1S(r)=\kappa\frac{Z^{3/2}m_\mathrm{e}}{\pi a_0^{7/2}\hbar^2}\frac{e^{-\frac{Zr}{a_0}}}{r}\left[2Z^2r^2+(2\gamma-5)Zra_0-a_0^2+2Zra_0\ln\left(\frac{2Zr}{a_0}\right)\right], \quad (4.37)$$

$$\delta2S(r)=-\kappa\frac{Z^{3/2}m_\mathrm{e}}{8\sqrt{2}\pi a_0^{9/2}\hbar^2}\frac{e^{-\frac{Zr}{2a_0}}}{r}\Bigg[Z^3r^3+(4\gamma-13)Z^2r^2a_0+2(3-4\gamma)Zra_0^2 + 4a_0^3+4Zra_0(Zr-2a_0)\ln\left(\frac{Zr}{a_0}\right)\Bigg], \quad (4.38)$$

where γ is Euler's constant

$$\gamma=\lim_{N\to\infty}\sum_{k=1}^{N}\frac{1}{k}-\ln(N)\approx0.5772\,. \quad (4.39)$$

For the potential $\delta V=-\boldsymbol{p}^4/(8m_\mathrm{e}^3c^2)$, the corrections to the $1S$ and $2S$ wavefunctions read

$$\delta1S(r)=-\frac{Z^{5/2}\hbar^2}{2a_0^{9/2}m_\mathrm{e}^2c^2}\frac{e^{-\frac{Zr}{a_0}}}{r}\left[2Z^2r^2+(4\gamma-7)Zra_0-2a_0^2+4Zra_0\ln\left(\frac{2Zr}{a_0}\right)\right], \quad (4.40)$$

$$\delta2S(r)=\frac{Z^{5/2}\hbar^2}{32\sqrt{2}a_0^{11/2}m_\mathrm{e}^2c^2}\frac{e^{-\frac{Zr}{2a_0}}}{r}\Bigg[3r^3Z^3+(16\gamma-47)Z^2r^2a_0+2(15-16\gamma)Zra_0^2 + 16a_0^3+16Zra_0(Zr-2a_0)\ln\left(\frac{rZ}{a_0}\right)\Bigg]. \quad (4.41)$$

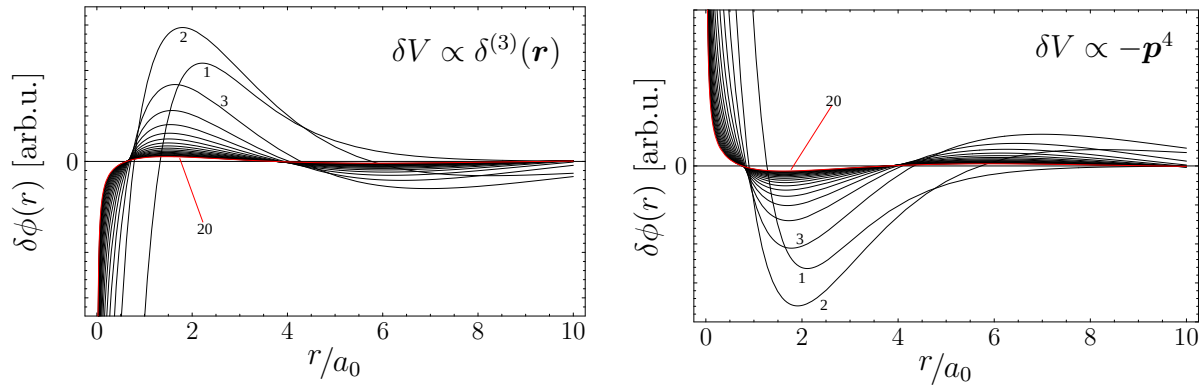

Figure 4.1: Corrections $\delta\phi(r)$ to the radial hydrogen wavefunctions $\phi(r)$, as defined in Eq. (4.33), for principal quantum numbers $n = 1 \ldots 20$, as indicated close to the respective graph, and for Z=1. The wave function corrections are caused by a perturbation potential δV with $\delta^{(3)}(\boldsymbol{r})$-characteristic (left), and by a $\boldsymbol{p}^4$-potential (right). The Bohr radius is denoted by a_0. Both types of wavefunction corrections enter into the calculation of the relativistic corrections, whereas for the radiative corrections, only the $\delta^{(3)}(\boldsymbol{r})$ wavefunctions are of relevance.

A plot of all calculated corrections for n up to 20 is given in Fig. 4.1. With the wave function corrections $\delta\phi(\boldsymbol{r}) = \delta\phi(r)Y_{00}(\theta,\phi)$ at hand, the calculation of the $\delta P^W_{\omega_\mathrm{L}}$ proceeds by considering the integral

$$\iint d^3r_1 d^3r_2 \; \phi(\boldsymbol{r}_1)\, r_1 \cos(\theta_1)\; G(\boldsymbol{r}_1, \boldsymbol{r}_2; \eta)\; r_2 \cos(\theta_2)\, \delta\phi(\boldsymbol{r}_2)\,, \tag{4.42}$$

where for the propagator, the Schrödinger-Coulomb Green's function (3.28) is used, in which only the $l = 1$ intermediate states with energies $E_\phi \pm \hbar\omega_\mathrm{L}$ contribute. The laser frequency ω_L is determined by the two-photon resonance condition of the considered transition. The angular integral is trivial, yielding $1/3$, while for the radial integral, involving generalized Laguerre polynomials, the integral rule [89]

$$\int_0^\infty dr\, e^{-\lambda r} r^\xi\, L_k^\mu(r) = \frac{\lambda^{-1-\xi}\,\Gamma(\xi+1)}{k!\,\Gamma(\mu+1)} \Gamma(\mu+k+1)\, {}_2F_1(-k, \xi+1; \mu+1; 1/\lambda) \tag{4.43}$$

is employed, and an analytical result is obtained for a given intermediate state index k [see Eq. (3.29)]. The generalized hypergeometric functions are defined by

$${}_pF_q(a_1, \ldots, a_p; b_1, \ldots, b_q; z) = \sum_{n=0}^{\infty} \frac{(a_1)_n \ldots (a_p)_n}{(b_1)_n \ldots (b_q)_n} \frac{z^n}{n!} \tag{4.44}$$

with the Pochhammer symbols $(a)_n = \Gamma(a+n)/\Gamma(a)$. The final k-summation of the Green's function in Eq. (4.42), which could not be done analytically, was performed

numerically up to $k = 200$, with very good convergence properties. For the case of the correction to the excited state polarizability and where the intermediate state is in the continuum, i.e. $E(\eta) = E_\phi + \hbar\omega_\mathrm{L}$, the series of partial sums diverges, but with both negative and positive signs, such that the expression is accessible to a Padé resummation, which showed very good convergence behavior for this particular problem.

4.5.2 Eigenenergy contributions

For the calculation of the eigenenergy perturbations to the dynamic polarizability, $\delta P^E_{\omega_\mathrm{L}}(\phi)$, it is useful to observe that they are proportional to the expectation values of the respective potential [see Eq. (4.6)], which are known in closed form (4.34), (4.35). The remaining two-propagator matrix element

$$\left\langle \phi \left| z \left(\frac{1}{H_0 - E(\eta)} \right)^2 z \right| \phi \right\rangle = \iiint d^3r_1\, d^3r_2\, d^3r_3\, \phi(\boldsymbol{r}_1)\, z_1\, G(\boldsymbol{r}_1, \boldsymbol{r}_2; \eta)\, G(\boldsymbol{r}_2, \boldsymbol{r}_3; \eta)\, z_3\, \phi(\boldsymbol{r}_3) \tag{4.45}$$

can also be calculated in closed form, as described in the following, such that the $\delta P^E_{\omega_\mathrm{L}}(\phi)$ can be given analytically. The $\boldsymbol{r}_1$ and $\boldsymbol{r}_3$ integrations are again carried out using relation (4.43), leaving the $\boldsymbol{r}_2$ integral over $l = 1$ intermediate states to be done. In the radial part, the integrand contains an r_2-dependent factor of the form

$$e^{-r_2}\, r_2^4\, L^3_{k_1}(r_2)\, L^3_{k_2}(r_2) \tag{4.46}$$

where the independent summation indices k_1 and k_2 originate from the two Green's functions and $\mu = 2l + 1 = 3$ for the intermediate state Laguerre polynomials. Using the identity

$$L^\mu_m(r_2) = L^{\mu+1}_m(r_2) - L^{\mu+1}_{m-1}(r_2)\,, \tag{4.47}$$

expression (4.46) is brought into a form where $\mu = 4$ matches the r_2 exponent, such that the orthogonality relation for the generalized Laguerre polynomials [89]

$$\int_0^\infty dr\, e^{-r} r^\mu L^\mu_m(r) L^\mu_n(r) = \frac{(\mu+n)!}{n!} \delta_{m,n} \tag{4.48}$$

can be used to perform the desired r_2 integration. Using this procedure, the final result for the matrix elements (4.45) are analytic expressions. For the $1S$ reference state, the

result reads: [1]

$$\left\langle 1S \left| z \left(\frac{1}{H_0 - E(\eta)} \right)^2 z \right| 1S \right\rangle = \frac{4\, m_\mathrm{e}^2 a_0^6}{3\, Z^6 \hbar^4} \times \tag{4.49}$$
$$\left\{ \frac{\eta^4}{(\eta-1)^6(\eta+1)^7} \Big(64\eta^{11} + 288\eta^{10} - 75\eta^9 - 523\eta^8 - 470\eta^7 - 118\eta^6 \right.$$
$$\left. + 48\eta^5 + 48\eta^4 - 18\eta^3 - 18\eta^2 + 3\eta + 3 \Big) \right.$$
$$+ \frac{128\,\eta^{11}\,(5-2\eta^2)\;{}_2F_1\left(1, -\eta; 1-\eta; \frac{(\eta-1)^2}{(\eta+1)^2}\right)}{(\eta^2-1)^6}$$
$$\left. + \frac{64\,\eta^{13}\,{}_3F_2\left(1, 2-\eta, 2-\eta; 3-\eta, 3-\eta; \frac{(\eta-1)^2}{(\eta+1)^2}\right)}{(\eta-2)^2(\eta-1)(\eta+1)^9} \right\}.$$

The appropriate energy parameters for the intermediate state energies $\eta(E_{1S} \pm \hbar\omega_\mathrm{L})$ are again fixed by the two-photon resonance condition for the angular frequency ω_L of the laser, driving any two-photon transition involving the $1S$ state.

4.5.3 Hamiltonian contributions

Finally, the corrections $\delta P^H_{\omega_\mathrm{L}}(\phi)$ [see Eq. (4.5)] are considered. Here, the fact that the perturbation potential operator δV acts onto the $l = 1$ intermediate state, immediately yields

$$\delta P^H_{\omega_\mathrm{L}}(nS) = 0 \qquad \text{for} \qquad \delta V = \kappa \delta^{(3)}(\boldsymbol{r})\,, \tag{4.50}$$

because the intermediate P state wavefunction vanishes at the origin.

For the $\boldsymbol{p}^4$-correction, using the coordinate representation $\boldsymbol{p} = -\mathrm{i}\hbar\boldsymbol{\nabla}$, the matrix element in (4.5) can be written as a double sum of summands of the form

$$\sigma(k_1, k_2) = -\frac{\hbar^4}{8\, m_\mathrm{e}^3\, c^2} \int d^3r\, [\Delta\tilde{\phi}_{k_1}(\boldsymbol{r};\eta)]^\dagger [\Delta\tilde{\phi}_{k_2}(\boldsymbol{r};\eta)]\,, \tag{4.51}$$

because the Laplacian Δ is a Hermitian operator. Here, $\tilde{\phi}_k(\boldsymbol{r};\eta)$ represents the intermediate state with index $k = n-l-1$ and energy parameter η, given by carrying out the integration over the "outer" Green's function coordinate $\boldsymbol{r}_1$:

$$\sum_k \tilde{\phi}_k(\boldsymbol{r};\eta) = \int d^3r_1\, G(\boldsymbol{r}, \boldsymbol{r}_1; \eta)\, z_1\, \phi(\boldsymbol{r}_1)\,. \tag{4.52}$$

For given k and η, $\tilde{\phi}_k(\boldsymbol{r})$ can again be obtained by invoking Eq. (4.43). The following application of the Laplacian and the remaining $\boldsymbol{r}$-integration result in an analytical

[1] Any reader who finds this thesis rather unentertaining, but has made it up to here, should be recompensated by having a look at [90]. No, seriously!

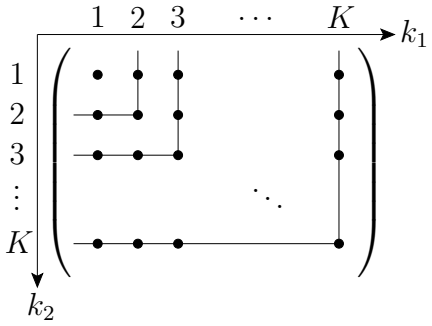

Figure 4.2: Composition of the partial sums in the numerical evaluation of the Hamiltonian contribution. The partial sum of order $i+1$ is obtained by adding a "shell" of one row and one column to the partial sum of order i.

expression for the summand $\sigma(k_1, k_2)$. The remaining double sum

$$\lim_{K\to\infty} \sum_{k_1,k_2=0}^{K} \sigma(k_1, k_2) \tag{4.53}$$

could not be expressed in closed form, so the summation was performed numerically as depicted in Fig. 4.2, the partial sums of order K involving a square section of the infinite matrix of summands. Making use of the symmetry of this matrix, the series of partial sums was evaluated with an adaptive summation algorithm, checking for convergence of the series, in order to save computation time, when the desired precision of about 20 digits had been reached. Again, for the case of a positive intermediate state energy, a Padé resummation was applied to the series of partial sums, obtaining a finite result.

The calculation of the corrections to the transition matrix elements, $\delta M^H_{\omega_L}$, $\delta M^E_{\omega_L}$ and $\delta M^W_{\omega_L}$ proceeds analogously to the evaluation of the corrections to the polarizability, therefore the details are omitted. Because the intermediate state energy occurring in the propagator of the matrix elements (4.16,4.17,4.19) is always negative, there is even no need to invoke a Padé resummation, and all k-sums can be carried out straightforwardly.

4.5.4 Results for S–S transitions

The results of the relativistic and radiative corrections to the dynamic polarizability are compiled in Tabs. 4.1-4.6, and the corrections to the transition matrix elements are given in Tabs. 4.7 and 4.8. All these corrections, as well as the uncorrected matrix elements, are evaluated for the relevant frequency, where the laser field is on two-photon resonance with the respective S–S transition.

The corrections to the matrix elements β_{AC}, β_{ioni}, and β_{ge}, as considered in the previous chapter, can now be obtained using the following scheme.

The leading order relativistic corrections, with $\xi_{\rm rel} = (Z\alpha)^2$, are given by

$$\frac{\delta\beta_{\rm AC}(\phi)}{\beta_{\rm AC}(\phi)} = R_{\rm rel}(\phi)\,\xi_{\rm rel} \qquad \text{Tabs. 4.1, 4.2}\,, \tag{4.54}$$

$$\frac{\delta\beta_{\rm ioni}(\phi)}{\beta_{\rm ioni}(\phi)} = I_{\rm rel}(\phi)\,\xi_{\rm rel} \qquad \text{Tab. 4.3}\,, \tag{4.55}$$

$$\frac{\delta\beta_{ge}}{\beta_{ge}} = R_{\rm rel}\,\xi_{\rm rel} \qquad \text{Tab. 4.7}\,. \tag{4.56}$$

The radiative corrections of leading logarithmic order to the SI matrix elements, with $\xi_{\rm rad} = \alpha(Z\alpha)^2\ln[(Z\alpha)^{-2}]$, follow from

$$\frac{\delta\beta_{\rm AC}(\phi)}{\beta_{\rm AC}(\phi)} = R_{\rm rad}(\phi)\,\xi_{\rm rad} \qquad \text{Tabs. 4.4, 4.5}\,, \tag{4.57}$$

$$\frac{\delta\beta_{\rm ioni}(\phi)}{\beta_{\rm ioni}(\phi)} = I_{\rm rad}(\phi)\,\xi_{\rm rad} \qquad \text{Tab. 4.6}\,, \tag{4.58}$$

$$\frac{\delta\beta_{ge}}{\beta_{ge}} = R_{\rm rad}\,\xi_{\rm rad} \qquad \text{Tab. 4.8}\,. \tag{4.59}$$

Table 4.1: Relativistic corrections to the dynamic polarizability of the ground state $|g\rangle$ [see Eqs. (4.12) and (4.54)], for a laser frequency $\omega_{\rm L}$ on two-photon resonance with the transition $|g\rangle \Leftrightarrow |e\rangle$.

rel. $\delta P_{\omega_{\rm L}}(g)$ $\lvert g\rangle \Leftrightarrow \lvert e\rangle$	$R_{\rm H}(g)$	$R_{\rm E}(g)$	$R_{\rm W}(g)$	$\Sigma = R_{\rm rel}(g)$
$1S$–$2S$	2.93618×10^{-1}	-4.79719×10^{-1}	-9.99134×10^{-1}	-1.18523×10^{0}
$1S$–$3S$	3.26556×10^{-1}	-5.94216×10^{-1}	-1.01221×10^{0}	-1.27987×10^{0}
$1S$–$4S$	3.41534×10^{-1}	-6.49617×10^{-1}	-1.01776×10^{0}	-1.32584×10^{0}
$1S$–$5S$	3.49266×10^{-1}	-6.79009×10^{-1}	-1.02052×10^{0}	-1.35027×10^{0}
$1S$–$6S$	3.53707×10^{-1}	-6.96129×10^{-1}	-1.02208×10^{0}	-1.36451×10^{0}
$1S$–$7S$	3.56473×10^{-1}	-7.06877×10^{-1}	-1.02305×10^{0}	-1.37345×10^{0}
$1S$–$8S$	3.58304×10^{-1}	-7.14033×10^{-1}	-1.02368×10^{0}	-1.37941×10^{0}
$1S$–$9S$	3.59577×10^{-1}	-7.19023×10^{-1}	-1.02412×10^{0}	-1.38356×10^{0}
$1S$–$10S$	3.60497×10^{-1}	-7.22635×10^{-1}	-1.02443×10^{0}	-1.38657×10^{0}
$1S$–$11S$	3.61181×10^{-1}	-7.25331×10^{-1}	-1.02467×10^{0}	-1.38881×10^{0}
$1S$–$12S$	3.61705×10^{-1}	-7.27395×10^{-1}	-1.02484×10^{0}	-1.39053×10^{0}
$2S$–$3S$	2.80456×10^{0}	-4.63104×10^{0}	-2.00465×10^{0}	-3.83114×10^{0}
$2S$–$4S$	1.89809×10^{0}	-2.91011×10^{0}	-2.05234×10^{0}	-3.06437×10^{0}
$2S$–$5S$	1.75859×10^{0}	-2.85737×10^{0}	-2.08474×10^{0}	-3.18352×10^{0}
$2S$–$6S$	1.75225×10^{0}	-3.07862×10^{0}	-2.10636×10^{0}	-3.43273×10^{0}
$2S$–$7S$	1.78092×10^{0}	-3.34811×10^{0}	-2.12113×10^{0}	-3.68833×10^{0}
$2S$–$8S$	1.81769×10^{0}	-3.60447×10^{0}	-2.13154×10^{0}	-3.91832×10^{0}
$2S$–$9S$	1.85375×10^{0}	-3.83054×10^{0}	-2.13908×10^{0}	-4.11587×10^{0}
$2S$–$10S$	1.88626×10^{0}	-4.02397×10^{0}	-2.14470×10^{0}	-4.28242×10^{0}
$2S$–$11S$	1.91458×10^{0}	-4.18751×10^{0}	-2.14899×10^{0}	-4.42192×10^{0}
$2S$–$12S$	1.93889×10^{0}	-4.32528×10^{0}	-2.15232×10^{0}	-4.53870×10^{0}

Table 4.2: Relativistic corrections to the real part of the dynamic polarizability of the excited state $|e\rangle$ [see Eqs. (4.12) and (4.54)], for a laser frequency $\omega_{\rm L}$ on two-photon resonance with the transition $|g\rangle \Leftrightarrow |e\rangle$.

rel. $\delta P_{\omega_{\rm L}}(e)$ $\lvert g\rangle \Leftrightarrow \lvert e\rangle$	$R_{\rm H}(e)$	$R_{\rm E}(e)$	$R_{\rm W}(e)$	$\Sigma = R_{\rm rel}(e)$
$1S$–$2S$	3.26248×10^{-1}	1.23196×10^{0}	-1.74852×10^{0}	-1.90310×10^{-1}
$1S$–$3S$	2.70412×10^{-2}	1.89466×10^{0}	-1.99580×10^{0}	-7.41008×10^{-2}
$1S$–$4S$	-2.58957×10^{-2}	2.71122×10^{0}	-2.73013×10^{0}	-4.48016×10^{-2}
$1S$–$5S$	-3.92665×10^{-2}	3.54485×10^{0}	-3.53559×10^{0}	-3.00097×10^{-2}
$1S$–$6S$	-4.32467×10^{-2}	4.37988×10^{0}	-4.35805×10^{0}	-2.14186×10^{-2}
$1S$–$7S$	-4.44260×10^{-2}	5.21446×10^{0}	-5.18605×10^{0}	-1.60133×10^{-2}
$1S$–$8S$	-4.46568×10^{-2}	6.04854×10^{0}	-6.01628×10^{0}	-1.24057×10^{-2}
$1S$–$9S$	-4.45512×10^{-2}	6.88225×10^{0}	-6.84758×10^{0}	-9.88441×10^{-3}
$1S$–$10S$	-4.43332×10^{-2}	7.71573×10^{0}	-7.67946×10^{0}	-8.05592×10^{-3}
$1S$–$11S$	-4.40895×10^{-2}	8.54907×10^{0}	-8.51167×10^{0}	-6.68911×10^{-3}
$1S$–$12S$	-4.38537×10^{-2}	9.38232×10^{0}	-9.34411×10^{0}	-5.64139×10^{-3}
$2S$–$3S$	4.65348×10^{0}	-2.46975×10^{1}	-1.29337×10^{0}	-2.13374×10^{1}
$2S$–$4S$	2.04258×10^{-1}	2.91749×10^{0}	-3.28041×10^{0}	-1.58665×10^{-1}
$2S$–$5S$	8.26178×10^{-2}	3.62378×10^{0}	-3.79857×10^{0}	-9.21700×10^{-2}
$2S$–$6S$	2.74300×10^{-2}	4.41907×10^{0}	-4.50703×10^{0}	-6.05343×10^{-2}
$2S$–$7S$	-1.49147×10^{-4}	5.23839×10^{0}	-5.28082×10^{0}	-4.25868×10^{-2}
$2S$–$8S$	-1.52026×10^{-2}	6.06537×10^{0}	-6.08154×10^{0}	-3.13707×10^{-2}
$2S$–$9S$	-2.40131×10^{-2}	6.89520×10^{0}	-6.89509×10^{0}	-2.39078×10^{-2}
$2S$–$10S$	-2.94621×10^{-2}	7.72625×10^{0}	-7.71550×10^{0}	-1.87136×10^{-2}
$2S$–$11S$	-3.29851×10^{-2}	8.55790×10^{0}	-8.53988×10^{0}	-1.49712×10^{-2}
$2S$–$12S$	-3.53471×10^{-2}	9.38990×10^{0}	-9.36675×10^{0}	-1.21986×10^{-2}

Table 4.3: Relativistic corrections to the imaginary part of the dynamic polarizability of the excited state $|e\rangle$ [see Eqs. (4.12) and (4.55)], for a laser frequency $\omega_{\rm L}$ on two-photon resonance with the transition $|g\rangle \Leftrightarrow |e\rangle$.

rel. $\delta P_{\omega_{\rm L}}(e)$ $\lvert g\rangle \Leftrightarrow \lvert e\rangle$	$I_{\rm H}(e)$	$I_{\rm E}(e)$	$I_{\rm W}(e)$	$\Sigma = I_{\rm rel}(e)$
$1S$–$2S$	-3.85775×10^{-1}	6.71173×10^{-1}	-8.06825×10^{-2}	2.04715×10^{-1}
$1S$–$3S$	-1.11018×10^{0}	2.08108×10^{-1}	1.02199×10^{0}	1.19922×10^{-1}
$1S$–$4S$	-1.38322×10^{0}	9.09461×10^{-2}	1.33496×10^{0}	4.26893×10^{-2}
$1S$–$5S$	-1.51224×10^{0}	4.77390×10^{-2}	1.45316×10^{0}	-1.13407×10^{-2}
$1S$–$6S$	-1.58295×10^{0}	2.81326×10^{-2}	1.50463×10^{0}	-5.01900×10^{-2}
$1S$–$7S$	-1.62580×10^{0}	1.79607×10^{-2}	1.52859×10^{0}	-7.92495×10^{-2}
$1S$–$8S$	-1.65369×10^{0}	1.21617×10^{-2}	1.53979×10^{0}	-1.01740×10^{-1}
$1S$–$9S$	-1.67284×10^{0}	8.61496×10^{-3}	1.54459×10^{0}	-1.19637×10^{-1}
$1S$–$10S$	-1.68656×10^{0}	6.32444×10^{-3}	1.54603×10^{0}	-1.34208×10^{-1}
$1S$–$11S$	-1.69673×10^{0}	4.77943×10^{-3}	1.54565×10^{0}	-1.46295×10^{-1}
$1S$–$12S$	-1.70446×10^{0}	3.69958×10^{-3}	1.54428×10^{0}	-1.56481×10^{-1}
$2S$–$3S$	–	–	–	–
$2S$–$4S$	1.08417×10^{-1}	4.19162×10^{-1}	-5.04330×10^{-1}	2.32492×10^{-2}
$2S$–$5S$	-1.00610×10^{-1}	2.04015×10^{-1}	-6.83207×10^{-2}	3.50840×10^{-2}
$2S$–$6S$	-2.11683×10^{-1}	1.15772×10^{-1}	1.20557×10^{-1}	2.46455×10^{-2}
$2S$–$7S$	-2.77983×10^{-1}	7.23210×10^{-2}	2.16360×10^{-1}	1.06974×10^{-2}
$2S$–$8S$	-3.20773×10^{-1}	4.83017×10^{-2}	2.69753×10^{-1}	-2.71788×10^{-3}
$2S$–$9S$	-3.50007×10^{-1}	3.39002×10^{-2}	3.01396×10^{-1}	-1.47106×10^{-2}
$2S$–$10S$	-3.70868×10^{-1}	2.47246×10^{-2}	3.20932×10^{-1}	-2.52121×10^{-2}
$2S$–$11S$	-3.86278×10^{-1}	1.85952×10^{-2}	3.33312×10^{-1}	-3.43712×10^{-2}
$2S$–$12S$	-3.97984×10^{-1}	1.43417×10^{-2}	3.41265×10^{-1}	-4.23775×10^{-2}

Table 4.4: Radiative corrections to the dynamic polarizability of the ground state $|g\rangle$ [see Eqs. (4.12) and (4.57)], for a laser frequency $\omega_{\rm L}$ on two-photon resonance with the transition $|g\rangle \Leftrightarrow |e\rangle$.

rad. $\delta P_{\omega_{\rm L}}(g)$ $\lvert g\rangle \Leftrightarrow \lvert e\rangle$	$R_{\rm H}(g)$	$R_{\rm E}(g)$	$R_{\rm W}(g)$	$\Sigma = R_{\rm rad}(g)$
$1S$–$2S$	0	1.62879×10^{0}	1.98835×10^{0}	3.61714×10^{0}
$1S$–$3S$	0	2.01754×10^{0}	2.02703×10^{0}	4.04457×10^{0}
$1S$–$4S$	0	2.20565×10^{0}	2.04354×10^{0}	4.24919×10^{0}
$1S$–$5S$	0	2.30544×10^{0}	2.05180×10^{0}	4.35724×10^{0}
$1S$–$6S$	0	2.36357×10^{0}	2.05647×10^{0}	4.42004×10^{0}
$1S$–$7S$	0	2.40006×10^{0}	2.05935×10^{0}	4.45941×10^{0}
$1S$–$8S$	0	2.42436×10^{0}	2.06124×10^{0}	4.48560×10^{0}
$1S$–$9S$	0	2.44130×10^{0}	2.06255×10^{0}	4.50385×10^{0}
$1S$–$10S$	0	2.45357×10^{0}	2.06349×10^{0}	4.51706×10^{0}
$1S$–$11S$	0	2.46272×10^{0}	2.06419×10^{0}	4.52691×10^{0}
$1S$–$12S$	0	2.46973×10^{0}	2.06473×10^{0}	4.53446×10^{0}
$2S$–$3S$	0	6.28952×10^{0}	2.57188×10^{0}	8.86140×10^{0}
$2S$–$4S$	0	3.95228×10^{0}	2.63463×10^{0}	6.58692×10^{0}
$2S$–$5S$	0	3.88066×10^{0}	2.67736×10^{0}	6.55802×10^{0}
$2S$–$6S$	0	4.18114×10^{0}	2.70592×10^{0}	6.88706×10^{0}
$2S$–$7S$	0	4.54714×10^{0}	2.72545×10^{0}	7.27260×10^{0}
$2S$–$8S$	0	4.89532×10^{0}	2.73922×10^{0}	7.63453×10^{0}
$2S$–$9S$	0	5.20234×10^{0}	2.74921×10^{0}	7.95155×10^{0}
$2S$–$10S$	0	5.46505×10^{0}	2.75665×10^{0}	8.22169×10^{0}
$2S$–$11S$	0	5.68715×10^{0}	2.76232×10^{0}	8.44946×10^{0}
$2S$–$12S$	0	5.87426×10^{0}	2.76673×10^{0}	8.64099×10^{0}

Table 4.5: Radiative corrections to the real part of the dynamic polarizability of the excited state $|e\rangle$ [see Eqs. (4.12) and (4.57)], for a laser frequency $\omega_{\rm L}$ on two-photon resonance with the transition $|g\rangle \Leftrightarrow |e\rangle$.

rad. $\delta P_{\omega_{\rm L}}(e)$ $\lvert g\rangle \Leftrightarrow \lvert e\rangle$	$R_{\rm H}(e)$	$R_{\rm E}(e)$	$R_{\rm W}(e)$	$\Sigma = R_{\rm rad}(e)$
$1S$–$2S$	0	-1.67316×10^{0}	2.20122×10^{0}	5.28060×10^{-1}
$1S$–$3S$	0	-2.14432×10^{0}	2.24850×10^{0}	1.04181×10^{-1}
$1S$–$4S$	0	-2.83244×10^{0}	2.87246×10^{0}	4.00186×10^{-2}
$1S$–$5S$	0	-3.53995×10^{0}	3.55981×10^{0}	1.98509×10^{-2}
$1S$–$6S$	0	-4.24887×10^{0}	4.26021×10^{0}	1.13476×10^{-2}
$1S$–$7S$	0	-4.95731×10^{0}	4.96443×10^{0}	7.11165×10^{-3}
$1S$–$8S$	0	-5.66528×10^{0}	5.67003×10^{0}	4.75675×10^{-3}
$1S$–$9S$	0	-6.37291×10^{0}	6.37625×10^{0}	3.34060×10^{-3}
$1S$–$10S$	0	-7.08034×10^{0}	7.08278×10^{0}	2.43690×10^{-3}
$1S$–$11S$	0	-7.78765×10^{0}	7.78949×10^{0}	1.83270×10^{-3}
$1S$–$12S$	0	-8.49489×10^{0}	8.49631×10^{0}	1.41327×10^{-3}
$2S$–$3S$	0	2.79519×10^{1}	1.41593×10^{0}	2.93678×10^{1}
$2S$–$4S$	0	-3.04793×10^{0}	3.41132×10^{0}	3.63393×10^{-1}
$2S$–$5S$	0	-3.61878×10^{0}	3.80876×10^{0}	1.89980×10^{-1}
$2S$–$6S$	0	-4.28688×10^{0}	4.39959×10^{0}	1.12710×10^{-1}
$2S$–$7S$	0	-4.98006×10^{0}	5.05273×10^{0}	7.26680×10^{-2}
$2S$–$8S$	0	-5.68104×10^{0}	5.73073×10^{0}	4.96832×10^{-2}
$2S$–$9S$	0	-6.38490×10^{0}	6.42039×10^{0}	3.54923×10^{-2}
$2S$–$10S$	0	-7.08999×10^{0}	7.11623×10^{0}	2.62388×10^{-2}
$2S$–$11S$	0	-7.79569×10^{0}	7.81564×10^{0}	1.99416×10^{-2}
$2S$–$12S$	0	-8.50175×10^{0}	8.51726×10^{0}	1.55063×10^{-2}

Table 4.6: Radiative corrections to the imaginary part of the dynamic polarizability of the excited state $|e\rangle$ [see Eqs. (4.12) and (4.58)], for a laser frequency $\omega_{\rm L}$ on two-photon resonance with the transition $|g\rangle \Leftrightarrow |e\rangle$.

rad. $\delta P_{\omega_{\rm L}}(e)$ $\lvert g\rangle \Leftrightarrow \lvert e\rangle$	$I_{\rm H}(e)$	$I_{\rm E}(e)$	$I_{\rm W}(e)$	$\Sigma = I_{\rm rad}(e)$
$1S$–$2S$	0	-9.11535×10^{-1}	1.03853×10^{-1}	-8.07681×10^{-1}
$1S$–$3S$	0	-2.35530×10^{-1}	-8.67492×10^{-1}	-1.10302×10^{0}
$1S$–$4S$	0	-9.50122×10^{-2}	-1.04636×10^{0}	-1.14138×10^{0}
$1S$–$5S$	0	-4.76730×10^{-2}	-1.09290×10^{0}	-1.14058×10^{0}
$1S$–$6S$	0	-2.72911×10^{-2}	-1.10408×10^{0}	-1.13137×10^{0}
$1S$–$7S$	0	-1.70750×10^{-2}	-1.10373×10^{0}	-1.12081×10^{0}
$1S$–$8S$	0	-1.13910×10^{-2}	-1.09939×10^{0}	-1.11078×10^{0}
$1S$–$9S$	0	-7.97739×10^{-3}	-1.09379×10^{0}	-1.10177×10^{0}
$1S$–$10S$	0	-5.80362×10^{-3}	-1.08800×10^{0}	-1.09380×10^{0}
$1S$–$11S$	0	-4.35376×10^{-3}	-1.08243×10^{0}	-1.08678×10^{0}
$1S$–$12S$	0	-3.34965×10^{-3}	-1.07725×10^{0}	-1.08060×10^{0}
$2S$–$3S$	–	–	–	–
$2S$–$4S$	0	-4.37903×10^{-1}	5.94061×10^{-1}	1.56158×10^{-1}
$2S$–$5S$	0	-2.03733×10^{-1}	2.02743×10^{-1}	-9.89750×10^{-4}
$2S$–$6S$	0	-1.12309×10^{-1}	5.16890×10^{-2}	-6.06197×10^{-2}
$2S$–$7S$	0	-6.87545×10^{-2}	-1.82596×10^{-2}	-8.70141×10^{-2}
$2S$–$8S$	0	-4.52411×10^{-2}	-5.41148×10^{-2}	-9.93559×10^{-2}
$2S$–$9S$	0	-3.13913×10^{-2}	-7.35961×10^{-2}	-1.04987×10^{-1}
$2S$–$10S$	0	-2.26886×10^{-2}	-8.44776×10^{-2}	-1.07166×10^{-1}
$2S$–$11S$	0	-1.69390×10^{-2}	-9.05475×10^{-2}	-1.07487×10^{-1}
$2S$–$12S$	0	-1.29852×10^{-2}	-9.37998×10^{-2}	-1.06785×10^{-1}

Table 4.7: Relativistic corrections to the two-photon transition matrix element of the transition $|g\rangle \Leftrightarrow |e\rangle$ [see Eqs. (4.20) and (4.56)], for a laser frequency $\omega_{\rm L}$ on two-photon resonance.

rel. $\delta M_{\omega_{\rm L}}$ $\lvert g\rangle \Leftrightarrow \lvert e\rangle$	$R_{\rm H}$	$R_{\rm E}$	$R_{\rm W}$	$\Sigma = R_{\rm rel}$
$1S$–$2S$	7.45176×10^{-2}	-5.17652×10^{-1}	-4.15130×10^{-1}	-8.58265×10^{-1}
$1S$–$3S$	1.85772×10^{-1}	-2.70751×10^{-1}	-1.31733×10^{0}	-1.40231×10^{0}
$1S$–$4S$	2.62542×10^{-1}	-1.87263×10^{-1}	-1.72343×10^{0}	-1.64815×10^{0}
$1S$–$5S$	3.06941×10^{-1}	-1.46968×10^{-1}	-1.93955×10^{0}	-1.77958×10^{0}
$1S$–$6S$	3.33842×10^{-1}	-1.24224×10^{-1}	-2.06773×10^{0}	-1.85811×10^{0}
$1S$–$7S$	3.51106×10^{-1}	-1.10117×10^{-1}	-2.15000×10^{0}	-1.90901×10^{0}
$1S$–$8S$	3.62758×10^{-1}	-1.00776×10^{-1}	-2.20607×10^{0}	-1.94409×10^{0}
$1S$–$9S$	3.70959×10^{-1}	-9.42768×10^{-2}	-2.24613×10^{0}	-1.96945×10^{0}
$1S$–$10S$	3.76933×10^{-1}	-8.95782×10^{-2}	-2.27584×10^{0}	-1.98849×10^{0}
$1S$–$11S$	3.81412×10^{-1}	-8.60736×10^{-2}	-2.29856×10^{0}	-2.00322×10^{0}
$1S$–$12S$	3.84854×10^{-1}	-8.33916×10^{-2}	-2.31638×10^{0}	-2.01491×10^{0}
$2S$–$3S$	9.94167×10^{-1}	-1.12406×10^{0}	-1.61217×10^{0}	-1.74206×10^{0}
$2S$–$4S$	4.53014×10^{0}	1.58377×10^{0}	-1.10554×10^{1}	-4.94146×10^{0}
$2S$–$5S$	-3.97965×10^{0}	-4.98650×10^{0}	1.14531×10^{1}	2.48699×10^{0}
$2S$–$6S$	-1.45324×10^{0}	-3.36532×10^{0}	5.03772×10^{0}	2.19162×10^{-1}
$2S$–$7S$	-8.31092×10^{-1}	-3.14160×10^{0}	3.60318×10^{0}	-3.69518×10^{-1}
$2S$–$8S$	-5.25480×10^{-1}	-3.12073×10^{0}	2.97143×10^{0}	-6.74781×10^{-1}
$2S$–$9S$	-3.36904×10^{-1}	-3.15420×10^{0}	2.61897×10^{0}	-8.72130×10^{-1}
$2S$–$10S$	-2.07134×10^{-1}	-3.20247×10^{0}	2.39640×10^{0}	-1.01320×10^{0}
$2S$–$11S$	-1.12101×10^{-1}	-3.25222×10^{0}	2.24457×10^{0}	-1.11975×10^{0}
$2S$–$12S$	-3.96592×10^{-2}	-3.29872×10^{0}	2.13533×10^{0}	-1.20305×10^{0}

Table 4.8: Radiative corrections to the two-photon transition matrix element of the transition $|g\rangle \Leftrightarrow |e\rangle$ [see Eqs. (4.20) and (4.59)], for a laser frequency $\omega_{\rm L}$ on two-photon resonance.

rad. $\delta M_{\omega_{\rm L}}$ $\lvert g\rangle \Leftrightarrow \lvert e\rangle$	$R_{\rm H}$	$R_{\rm E}$	$R_{\rm W}$	$\Sigma = R_{\rm rad}$
$1S$–$2S$	0	1.50650×10^{0}	1.19976×10^{0}	2.70626×10^{0}
$1S$–$3S$	0	8.57997×10^{-1}	1.84243×10^{0}	2.70042×10^{0}
$1S$–$4S$	0	6.14542×10^{-1}	2.08532×10^{0}	2.69987×10^{0}
$1S$–$5S$	0	4.89674×10^{-1}	2.21053×10^{0}	2.70020×10^{0}
$1S$–$6S$	0	4.16974×10^{-1}	2.28446×10^{0}	2.70143×10^{0}
$1S$–$7S$	0	3.71108×10^{-1}	2.33209×10^{0}	2.70320×10^{0}
$1S$–$8S$	0	3.40422×10^{-1}	2.36479×10^{0}	2.70522×10^{0}
$1S$–$9S$	0	3.18933×10^{-1}	2.38835×10^{0}	2.70728×10^{0}
$1S$–$10S$	0	3.03327×10^{-1}	2.40598×10^{0}	2.70931×10^{0}
$1S$–$11S$	0	2.91649×10^{-1}	2.41959×10^{0}	2.71124×10^{0}
$1S$–$12S$	0	2.82690×10^{-1}	2.43036×10^{0}	2.71305×10^{0}
$2S$–$3S$	0	1.45987×10^{0}	2.06135×10^{0}	3.52123×10^{0}
$2S$–$4S$	0	-2.08157×10^{0}	1.15924×10^{1}	9.51079×10^{0}
$2S$–$5S$	0	6.62873×10^{0}	-1.10445×10^{1}	-4.41580×10^{0}
$2S$–$6S$	0	4.50614×10^{0}	-4.62009×10^{0}	-1.13951×10^{-1}
$2S$–$7S$	0	4.22541×10^{0}	-3.19418×10^{0}	1.03123×10^{0}
$2S$–$8S$	0	4.20919×10^{0}	-2.57055×10^{0}	1.63864×10^{0}
$2S$–$9S$	0	4.26220×10^{0}	-2.22460×10^{0}	2.03760×10^{0}
$2S$–$10S$	0	4.33284×10^{0}	-2.00712×10^{0}	2.32571×10^{0}
$2S$–$11S$	0	4.40399×10^{0}	-1.85931×10^{0}	2.54468×10^{0}
$2S$–$12S$	0	4.46977×10^{0}	-1.75330×10^{0}	2.71647×10^{0}

4.6 Beyond the dipole approximation

4.6.1 Field-configuration dependent corrections

In this section, the leading field-configuration correction to the dynamic polarizability is considered, which is due to the fact that the laser field, interacting with an atom of finite extension, is not strictly a dipole field, but also varies in space at a fixed time t. The case of a plane standing wave will be discussed, which approximates the situation in the MPQ hydrogen $1S$–$2S$ experiment well enough for the evaluation of this correction. For other field configurations like e.g. tight foci, the results of this section are not applicable, but must be re-evaluated to suit the respective geometry.

As is illustrated in Fig. 4.3, the electric field of a plane standing wave deviates appreciably from the field in dipole approximation, when one compares the two in a region around the nucleus which corresponds to the characteristic size of e.g. the $20S$ wavefunction.

This deviation becomes smaller as the principal quantum number decreases, and this trend is additionally supported by the fact that also the wavelength of the standing wave increases, when two-photon resonance condition is maintained. However, for the polarizability of highly excited states this non-dipole effect is important.

In the treatment of chapter 3, all results were obtained in the electric dipole approxima-

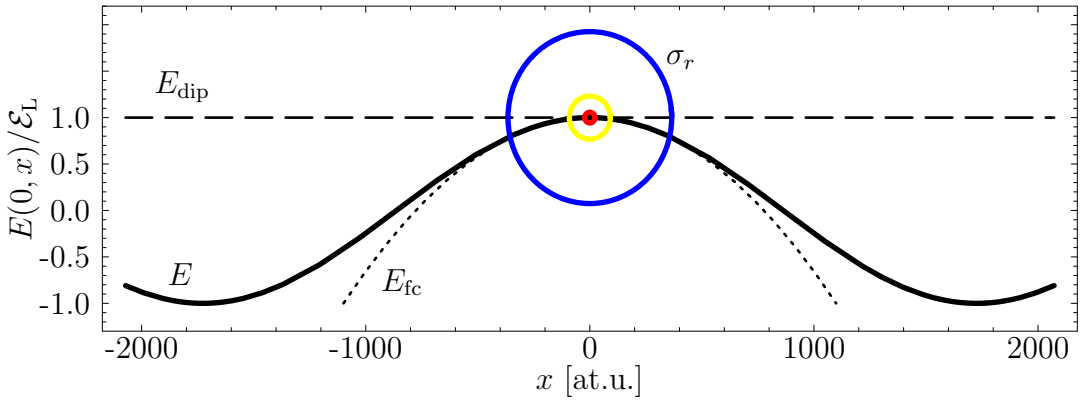

Figure 4.3: Comparison of the electric field of a plane standing wave $E(t=0,x)$ on two-photon resonance with the $1S$–$20S$ transition in hydrogen (solid line), the electric field in dipole approximation $E_{\rm dip}$ (dashed line), and the electric field taken into account by the field configuration corrections considered in this section ($E_{\rm fc}$, dotted line). The spatial extent of some wavefunctions, drawn to scale and characterized by $\sigma_r = \sqrt{\langle\psi|r^2|\psi\rangle}$, is indicated at the antinode of the standing wave for $\psi = 5S$ (red), $\psi = 10S$ (yellow), $\psi = 20S$ (blue). This illustration shows that the dipole approximation is no longer a good approximation for highly excited states, but that the calculated leading order corrections take into account very well the extended character of the wavefunction.

tion, where the interaction part of the Hamiltonian was expressed as

$$V_{\mathrm{dip}}(t) = -e\,\boldsymbol{r}\cdot\boldsymbol{E}(t)\,. \tag{4.60}$$

Expanding the electric field, varying both in space and time, around $\boldsymbol{r}=0$, the atom-field interaction Hamiltonian can be written as (see also [57] and Eq. (3.59) of [91])

$$V_{\mathrm{LW}}(t,\boldsymbol{r}) = -e\,\boldsymbol{r}\cdot\boldsymbol{E}(t,\boldsymbol{0}) - \frac{e}{2}\,r^i\,r^j\,\frac{\partial E^i(t,\boldsymbol{r})}{\partial r^j}\bigg|_{\boldsymbol{r}=\boldsymbol{0}} - \frac{e}{6}\,r^i\,r^j\,r^k\,\frac{\partial^2 E^i(t,\boldsymbol{r})}{\partial r^j\partial r^k}\bigg|_{\boldsymbol{r}=\boldsymbol{0}}\,, \tag{4.61}$$

up to second order, for the case that the wavelength of the laser field is large compared to the characteristic extent of the atomic wavefunction (long-wavelength limit). For a plane standing wave of linearly z-polarized light with wave vector $\boldsymbol{k}$, aligned along the x-direction, the electric field is

$$\boldsymbol{E}(t,x) = \hat{\boldsymbol{e}}_z\,\mathcal{E}_{\mathrm{L}}\,\cos(\omega t)\,\cos(kx)\,. \tag{4.62}$$

For the last term in (4.61) one simply obtains

$$V^{(2)}_{\mathrm{LW}} = \frac{e}{6}\,z\,k^2\,x^2\,\mathcal{E}_{\mathrm{L}}\,\cos(\omega t)\,. \tag{4.63}$$

The leading order correction to the dynamic polarizability of a state $|\phi\rangle$ of an atom at the antinode of a standing wave therefore reads

$$\delta P_{\omega_{\mathrm{L}}}(\phi) = -\frac{k^2}{3}\sum_{\pm}\left\langle\phi\,\middle|\,z\,\frac{1}{H_0-E_\phi\pm\hbar\omega_{\mathrm{L}}}\,x^2 z\,\middle|\,\phi\right\rangle\,, \tag{4.64}$$

from the two contributions containing one $V^{(2)}_{\mathrm{LW}}$ and one V_{dip} each. The lower order contributions in k

$$-\frac{k}{2}\left\langle\phi\,\middle|\,z\,\frac{1}{H_0-E}\,xz\,\middle|\,\phi\right\rangle = 0\,, \tag{4.65}$$

$$\frac{k^2}{4}\left\langle\phi\,\middle|\,zx\,\frac{1}{H_0-E}\,xz\,\middle|\,\phi\right\rangle = 0\,, \tag{4.66}$$

vanish for symmetry reasons. The modulus of the wave vector k of the standing wave is determined by the two-photon resonance condition, where one obtains e.g.

$$k = \frac{3}{16}(Z\alpha)^2\,\frac{c\,m_{\mathrm{e}}}{\hbar} = \frac{\omega_{\mathrm{L}}}{c} \tag{4.67}$$

for the $1S$–$2S$ transition. This condition also determines the frequency ω_{L} at which the polarizability itself is evaluated. With these parameters fixed, the leading order field configuration correction, relative to the polarizability in dipole approximation, reads

$$\xi_{\mathrm{fc}}\,R_{\mathrm{fc}}(\phi) = \frac{\mathrm{Re}(\delta P_{\omega_{\mathrm{L}}}(\phi))}{\mathrm{Re}(P_{\omega_{\mathrm{L}}}(\phi))}\,, \tag{4.68}$$

$$\xi_{\mathrm{fc}}\,I_{\mathrm{fc}}(\phi) = \frac{\mathrm{Im}(\delta P_{\omega_{\mathrm{L}}}(\phi))}{\mathrm{Im}(P_{\omega_{\mathrm{L}}}(\phi))}\,, \tag{4.69}$$

where again the correction to the real part R_{fc} and to the imaginary part I_{fc} are considered separately, and the characteristic scale factor

$$\xi_{\mathrm{fc}} = (Z\alpha)^2 \tag{4.70}$$

is identified. The correction $\delta P_{\omega_{\mathrm{L}}}(\phi)$ is proportional to k^2, consequently four powers of $(Z\alpha)$ are obtained from Eq. (4.67), while the matrix element in Eq. (4.64) contributes two negative powers of $(Z\alpha)$ from the energy denominator, and four negative powers from the four components x and z of the position operator, resulting in a $(Z\alpha)^{-2}$ scaling of $\delta P_{\omega_{\mathrm{L}}}(\phi)$. Because the polarizability $P_{\omega_{\mathrm{L}}}(\phi)$ is of the order $(Z\alpha)^{-4}$, the relative scaling is of the given order ξ_{fc}. Therefore one observes that the field configuration dependent corrections are of the same order in $(Z\alpha)$ as the relativistic corrections.

For the two-photon transition matrix element of the transition $|g\rangle \leftrightarrow |e\rangle$, the leading order field configuration correction reads

$$\delta M_{\omega_{\mathrm{L}}} = -\frac{k^2}{6}\left(\left\langle e\left|\, z\,\frac{1}{H_0-(E_g+\hbar\omega_{\mathrm{L}})}\,x^2 z\,\right|g\right\rangle + \left\langle e\left|\, x^2 z\,\frac{1}{H_0-(E_g+\hbar\omega_{\mathrm{L}})}\,z\,\right|g\right\rangle\right), \tag{4.71}$$

and the definition of the relative magnitude of the correction, R_{fc}, reads

$$\xi_{\mathrm{fc}}\,R_{\mathrm{fc}} \;=\; \frac{\delta M_{\omega_{\mathrm{L}}}(\phi)}{M_{\omega_{\mathrm{L}}}(\phi)}\,. \tag{4.72}$$

4.6.2 Results for two-photon transitions

In the following tables, the results of the field configuration corrections to the dynamic polarizability (Tab. 4.9 and 4.10) and to the transition matrix elements (Tab. 4.11) are listed. The results are valid for a scenario, where an atom is situated at an antinode, e.g. $x = 0$, of a plane standing wave of the form (4.62), and is driven on two-photon resonance on the respective S–S transition. For different locations along the axis of the standing wave, the corrections vary like $\cos^2(kx)$, vanishing (to second order) at the nodes of the field.

The corrections to the constants β_{AC}, β_{ioni}, and β_{ge}, as derived in the previous chapter, are obtained using the following relations. With $\xi_{\mathrm{fc}} = (Z\alpha)^2$,

$$\frac{\delta\beta_{\mathrm{AC}}(\phi)}{\beta_{\mathrm{AC}}(\phi)} = R_{\mathrm{fc}}(\phi)\,\xi_{\mathrm{fc}} \qquad \text{Tabs. 4.9, 4.10}\,, \tag{4.73}$$

$$\frac{\delta\beta_{\mathrm{ioni}}(\phi)}{\beta_{\mathrm{ioni}}(\phi)} = I_{\mathrm{fc}}(\phi)\,\xi_{\mathrm{fc}} \qquad \text{Tabs. 4.9, 4.10}\,, \tag{4.74}$$

$$\frac{\delta\beta_{ge}}{\beta_{ge}} = R_{\mathrm{fc}}\,\xi_{\mathrm{fc}} \qquad \text{Tab. 4.11}\,. \tag{4.75}$$

As was already suggested in Fig. 4.3, the corrections for the polarizability of the excited state become very large as the principal quantum number n increases (see $R_{\mathrm{fc}}(e)$ in Tabs. 4.9 and 4.10). This is clear, because the polarizability of an atom whose electronic

wavefunction is extended far into an inhomogeneous field is sensitive to the variation of this field.

It may be surprising that the corrections to the transition matrix elements do not show this behavior (see Tab. 4.11), rather they vary only little, converging for large principal quantum numbers. However, this can be explained by the observation that the transition matrix element is essentially determined in the region where the ground state wave function and the excited state wave function overlap. Because the considered $1S$ and $2S$ ground states are very well localized on the scale of the laser wavelength, the dipole approximation is still a good approximation for the transition matrix elements.

Table 4.9: Field configuration corrections to the dynamic polarizabilities of the states $|1S\rangle$ and $|e\rangle$ [see Eqs. (4.68) and (4.73),(4.74)], as occurring at the antinode of a standing wave laser field on two-photon resonance with the transition $|1S\rangle \Leftrightarrow |e\rangle$.

fc. δP_{ω_L} $\lvert g\rangle \Leftrightarrow \lvert e\rangle$	$R_{\rm fc}(g)$	$R_{\rm fc}(e)$	$I_{\rm fc}(e)$
$1S$–$2S$	-2.25564×10^{-2}	-1.98832×10^{-1}	3.75000×10^{-2}
$1S$–$3S$	-3.24442×10^{-2}	-1.10505×10^{0}	1.18519×10^{-1}
$1S$–$4S$	-3.64547×10^{-2}	-3.89523×10^{0}	1.46875×10^{-1}
$1S$–$5S$	-3.84178×10^{-2}	-9.99755×10^{0}	1.60000×10^{-1}
$1S$–$6S$	-3.95140×10^{-2}	-2.12824×10^{1}	1.67130×10^{-1}
$1S$–$7S$	-4.01853×10^{-2}	-4.00403×10^{1}	1.71429×10^{-1}
$1S$–$8S$	-4.06252×10^{-2}	-6.89792×10^{1}	1.74219×10^{-1}
$1S$–$9S$	-4.09288×10^{-2}	-1.11224×10^{2}	1.76132×10^{-1}
$1S$–$10S$	-4.11469×10^{-2}	-1.70316×10^{2}	1.77500×10^{-1}
$1S$–$11S$	-4.13088×10^{-2}	-2.50214×10^{2}	1.78512×10^{-1}
$1S$–$12S$	-4.14323×10^{-2}	-3.55292×10^{2}	1.79282×10^{-1}
$1S$–$13S$	-4.15285×10^{-2}	-4.90343×10^{2}	1.79882×10^{-1}
$1S$–$14S$	-4.16050×10^{-2}	-6.60574×10^{2}	1.80357×10^{-1}
$1S$–$15S$	-4.16668×10^{-2}	-8.71611×10^{2}	1.80740×10^{-1}
$1S$–$16S$	-4.17174×10^{-2}	-1.12949×10^{3}	1.81055×10^{-1}
$1S$–$17S$	-4.17594×10^{-2}	-1.44068×10^{3}	1.81315×10^{-1}
$1S$–$18S$	-4.17946×10^{-2}	-1.81205×10^{3}	1.81534×10^{-1}
$1S$–$19S$	-4.18244×10^{-2}	-2.25090×10^{3}	1.81716×10^{-1}
$1S$–$20S$	-4.18498×10^{-2}	-2.76492×10^{3}	1.81879×10^{-1}

Table 4.10: Field configuration corrections to the dynamic polarizabilities of the states $|2S\rangle$ and $|e\rangle$ [see Eqs. (4.68) and (4.73),(4.74)], as occurring at the antinode of a standing wave laser field on two-photon resonance with the transition $|2S\rangle \Leftrightarrow |e\rangle$.

fc. δP_{ω_L} $\|g\rangle \Leftrightarrow \|e\rangle$	$R_{\rm fc}(g)$	$R_{\rm fc}(e)$	$I_{\rm fc}(e)$
$2S$–$3S$	-1.00779×10^{-2}	3.77122×10^{-3}	–
$2S$–$4S$	-1.90455×10^{-2}	-1.69675×10^{-1}	9.37500×10^{-3}
$2S$–$5S$	-2.44802×10^{-2}	-4.85438×10^{-1}	2.25000×10^{-2}
$2S$–$6S$	-2.78586×10^{-2}	-1.11734×10^{0}	2.96296×10^{-2}
$2S$–$7S$	-3.00648×10^{-2}	-2.20531×10^{0}	3.39286×10^{-2}
$2S$–$8S$	-3.15723×10^{-2}	-3.91750×10^{0}	3.67188×10^{-2}
$2S$–$9S$	-3.26429×10^{-2}	-6.44876×10^{0}	3.86317×10^{-2}
$2S$–$10S$	-3.34282×10^{-2}	-1.00202×10^{1}	4.00000×10^{-2}
$2S$–$11S$	-3.40201×10^{-2}	-1.48791×10^{1}	4.10124×10^{-2}
$2S$–$12S$	-3.44767×10^{-2}	-2.12989×10^{1}	4.17824×10^{-2}
$2S$–$13S$	-3.48360×10^{-2}	-2.95789×10^{1}	4.23817×10^{-2}
$2S$–$14S$	-3.51235×10^{-2}	-4.00447×10^{1}	4.28571×10^{-2}
$2S$–$15S$	-3.53571×10^{-2}	-5.30479×10^{1}	4.32407×10^{-2}
$2S$–$16S$	-3.55494×10^{-2}	-6.89659×10^{1}	4.35547×10^{-2}
$2S$–$17S$	-3.57095×10^{-2}	-8.82026×10^{1}	4.38149×10^{-2}
$2S$–$18S$	-3.58442×10^{-2}	-1.11187×10^{2}	4.40329×10^{-2}
$2S$–$19S$	-3.59585×10^{-2}	-1.38376×10^{2}	4.42175×10^{-2}
$2S$–$20S$	-3.60565×10^{-2}	-1.70251×10^{2}	4.43750×10^{-2}

Table 4.11: Field configuration corrections to the two-photon transition matrix element of the transition $|g\rangle \Leftrightarrow |e\rangle$ [see Eqs. (4.72) and (4.75)], as occurring at the antinode of a standing wave laser field on two-photon resonance.

fc. δM_{ω_L} $\|g\rangle \Leftrightarrow \|e\rangle$	$R_{\rm fc}$	$\|g\rangle \Leftrightarrow \|e\rangle$	$R_{\rm fc}$
$1S$–$2S$	-6.02958×10^{-2}	-	–
$1S$–$3S$	3.37934×10^{-2}	$2S$–$3S$	-1.53814×10^{-2}
$1S$–$4S$	7.46868×10^{-2}	$2S$–$4S$	2.29524×10^{-1}
$1S$–$5S$	9.58743×10^{-2}	$2S$–$5S$	-3.42709×10^{-1}
$1S$–$6S$	1.08137×10^{-1}	$2S$–$6S$	-1.76620×10^{-1}
$1S$–$7S$	1.15822×10^{-1}	$2S$–$7S$	-1.38632×10^{-1}
$1S$–$8S$	1.20936×10^{-1}	$2S$–$8S$	-1.21615×10^{-1}
$1S$–$9S$	1.24503×10^{-1}	$2S$–$9S$	-1.12013×10^{-1}
$1S$–$10S$	1.27085×10^{-1}	$2S$–$10S$	-1.05906×10^{-1}
$1S$–$11S$	1.29013×10^{-1}	$2S$–$11S$	-1.01723×10^{-1}
$1S$–$12S$	1.30489×10^{-1}	$2S$–$12S$	-9.87082×10^{-2}
$1S$–$13S$	1.31644×10^{-1}	$2S$–$13S$	-9.64521×10^{-2}
$1S$–$14S$	1.32564×10^{-1}	$2S$–$14S$	-9.47140×10^{-2}
$1S$–$15S$	1.33308×10^{-1}	$2S$–$15S$	-9.33434×10^{-2}
$1S$–$16S$	1.33920×10^{-1}	$2S$–$16S$	-9.22417×10^{-2}
$1S$–$17S$	1.34427×10^{-1}	$2S$–$17S$	-9.13418×10^{-2}
$1S$–$18S$	1.34853×10^{-1}	$2S$–$18S$	-9.05965×10^{-2}
$1S$–$19S$	1.35215×10^{-1}	$2S$–$19S$	-8.99720×10^{-2}
$1S$–$20S$	1.35524×10^{-1}	$2S$–$20S$	-8.94432×10^{-2}

4.7 Lamb shift of laser dressed states [1]

In this section, radiative corrections to another dynamic process are considered, namely the inelastic resonance fluorescence of a driven two-level atom. In contrast to the discussion above, here the system is driven strongly on a dipole-allowed one-photon resonance. A perturbative treatment of the energies of the bare atomic states due to the interaction with the laser field is therefore not possible and new eigenstates of the Hamiltonian of the system "atom+laser field" need to be considered. The transitions among these so-called laser-dressed states [92], can readily explain the well-known Mollow spectrum [93] of the resonance fluorescence light emitted by the system.

The problem under consideration now is, whether radiative corrections to the strongly driven system of atom and laser field result in a Lamb shift of the observable Mollow sidebands, which is different from the shift that is expected from the Lamb shift of the bare states. In a nutshell, the question is, how real are the laser-dressed states, as judged by the electromagnetic vacuum?

In the following, only the main results will be briefly presented, a detailed account of the calculations is beyond the scope of this thesis and can be found in Refs. [70, 94].

The dressed states $|(\pm, n)\rangle$ of a strongly driven two-level system can be written in terms of product states of bare states $|g\rangle$ and $|e\rangle$, and laser Fock states $|n\rangle$, and in the rotating wave approximation, as

$$|(+, n)\rangle = \cos\theta_n |e, n\rangle + \sin\theta_n |g, n+1\rangle \,, \tag{4.76a}$$

$$|(-, n)\rangle = -\sin\theta_n |e, n\rangle + \cos\theta_n |g, n+1\rangle \,, \tag{4.76b}$$

where $\tan(2\theta_n) = \Omega_n/\Delta$, and Ω_n is the Rabi frequency of the interacting atom and the laser field in a Fock state with n photons. The detuning of the driving laser field from the bare state atomic resonance frequency ω_{eg} is denoted by Δ. The eigenenergies of these states, without taking into account radiative corrections, read

$$E_{(\pm,n)} = \left(n + \frac{1}{2}\right)\omega_{\mathrm{L}} + \frac{1}{2}\omega_{eg} \pm \frac{1}{2}\Omega_n \,. \tag{4.77}$$

Since the energy spacing of the dressed state transitions $|(+, n)\rangle \Leftrightarrow |(+, n \pm 1)\rangle$ and $|(-, n)\rangle \Leftrightarrow |(-, n \pm 1)\rangle$ is equal to one laser photon energy, transitions among these states lead to a central peak around the driving laser frequency ω_{L} in the incoherent resonance fluorescence spectrum $S_{\mathrm{inc}}(\omega)$, which is plotted in Fig. 4.4. Transitions between the dressed states $|(+, n+1)\rangle \Leftrightarrow |(-, n)\rangle$ and $|(-, n+1)\rangle \Leftrightarrow |(+, n)\rangle$ give rise to the sidebands, which are shifted by one generalized Rabi frequency

$$\Omega_{\mathrm{R}} = \sqrt{\Omega_n^2 + \Delta^2} \tag{4.78}$$

to higher or lower frequency, respectively. If one takes into account the usual interaction of

[1] The results of this section have been obtained in close collaboration with seminal contributions from Drs. U. Jentschura and J. Evers, Max-Planck-Institut für Kernphysik, Heidelberg.

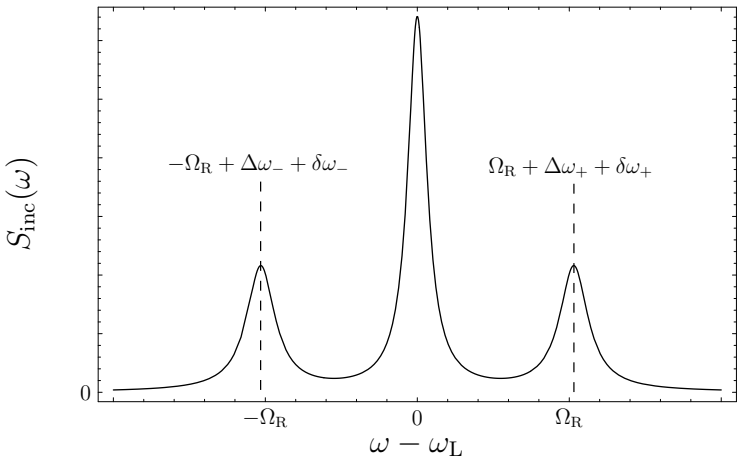

Figure 4.4: The Mollow spectrum of inelastic resonance fluorescence of a strongly driven two-level system. The sidebands are shifted by $\pm\Omega_{\rm R}$, the generalized Rabi frequency (4.78), from the center frequency $\omega = \omega_{\rm L}$, if no radiative corrections are taken into account. Radiative corrections to the bare state energies (usual Lamb shift), shift the Mollow sidebands by $\Delta\omega_\pm$, while radiative corrections to the Rabi frequency contribute an additional shift, $\delta\omega_\pm$, resulting in the fully dressed Lamb shift (4.82). The width of the peaks is connected with the spontaneous decay rate Γ, which for this plot is $\Gamma = 0.15\,\Omega_{\rm R}$.

the bare states with the vacuum, the bare states acquire a Lamb shift, which is transformed via the relation (4.76) into a shift of the Mollow sidebands of

$$\Delta\omega_\pm = \mp\,\frac{\Delta}{\hbar\,\sqrt{\Omega^2+\Delta^2}}L_{\rm bare}\,, \tag{4.79}$$

where $L_{\rm bare} = \langle e|\delta V_{\rm SE}|e\rangle - \langle g|\delta V_{\rm SE}|g\rangle$ is the Lamb shift of the bare transition frequency, with $\delta V_{\rm SE}$ as defined in Eq. (4.31). By first performing the transformation to the dressed states, and then calculating the self-energy for the dressed states, one obtains an additional shift of the Mollow sidebands of [94]

$$\delta\omega_\pm = \mp\,C\frac{\Omega^2}{\sqrt{\Omega^2+\Delta^2}}\,, \tag{4.80}$$

where

$$C = \frac{\alpha\ln[(Z\alpha)^{-2}]}{\pi}\,\frac{\langle g|\boldsymbol{p}^2|g\rangle + \langle e|\boldsymbol{p}^2|e\rangle}{m^2\,c^2} \tag{4.81}$$

is a dimensionless constant. These two contributions to the shift of the Mollow sidebands can be unified in one expression for the fully dressed Lamb shift

$$\Delta\mathcal{L}_\pm = \pm\left(\sqrt{\Omega^2(1-C)^2+(\Delta-L_{\rm bare})^2} - \sqrt{\Omega^2+\Delta^2}\right) \approx \Delta\omega_\pm + \delta\omega_\pm\,, \tag{4.82}$$

from which, to first order in $L_{\rm bare}$, the bare Lamb shift contribution $\Delta\omega_\pm$ can be recovered, and equally, to first order in C, the additional shift $\delta\omega_\pm$ is obtained. Expression (4.82)

allows for an interpretation of the C-term as being a radiative correction to the Rabi frequency, in much the same way as L_{bare} is a radiative correction to the detuning Δ, expressed in the Lamb shift of of the bare states.

If the above results are considered in the limit of a very strong driving field, i.e., $\Omega \gg \Gamma$, where Γ is the spontaneous decay rate from $|e\rangle \to |g\rangle$, the Mollow triplet splits into three distinct peaks, with well-defined line centers (secular approximation). For an experimental verification of the results, this is the scenario of choice, because very small line shifts can be best measured in a symmetric line shape. Assuming that a shift-to-width ratio of about

$$\frac{\delta\omega_{\pm}}{\Gamma} = \mathcal{O}\left(10^{-3}\right) \tag{4.83}$$

is in principle observable experimentally, an estimation of the lower limit of the Rabi frequency Ω needed for the experimental verification can be obtained. From Eq. (4.80) follows

$$|\delta\omega_{\pm}| \approx \Omega\, C\,, \tag{4.84}$$

in the case where $\Omega \gg \Delta$. Evaluated for the $1S$-$2P$ transition, the result for C is on the order of 10^{-6}, and consequently the ratio of Rabi frequency and spontaneous decay rate needs to be on the order of $\Omega/\Gamma = \mathcal{O}(10^3)$ or larger. For a tightly focused cw-source of Lyman-α radiation, this requires a minimum power of about $340\,\mu$W. Such a light source is being developed in the group of J. Walz [95], using a four-wave mixing scheme in a Mercury gas cell. The presently available power is yet a factor of 1000 below the required $340\,\mu$W to observe and distinguish the fully dressed Lamb shift from the usual Lamb shift in the Mollow spectrum. However, promising improvements are in progress, such that maybe in the near future, an experiment will be able to observe whether or not dressed states are shifted by a nontrivially different amount than atomic bare states.

Chapter 5

Monte Carlo Investigations and Lineshape

5.1 Introduction

The analysis of the two-photon excitation process, and the calculation of the atomic constants, as treated in the previous chapters, has provided a detailed insight into the interaction of a single atom moving in a laser field which, up to now, has been characterized by a standing plane wave. This general scenario is common to many high-precision spectroscopy experiments and the special case of a trapped atom or hydrogenlike ion is naturally also contained in this description.

In this chapter, the missing link between the single atom response and the signal which is actually observed in an experiment is established. For this reason, it is now necessary to focus the discussion onto a specific experimental setup, the atomic hydrogen $1S$–$2S$ spectrometer of Theodor Hänsch's group at the Max–Planck–Institut für Quantenoptik in Garching, which is depicted in a simplified sketch in Fig. 5.1.

The main steps which need to be performed are the following. First of all, the total observed line shape is made up from contributions of an ensemble of atoms in a cold effusive beam with certain parameters characterizing the velocity distribution and the atomic trajectories. Second, the laser field in the excitation resonator is a standing Gaussian wave, dominantly in the TEM_{00} mode, which gives rise to a radial intensity distribution which has to be taken into account in the modeling of the excitation process. Moreover, the MPQ detection method employs a time resolved scheme, in order to reduce the influence of fast atoms with large Doppler systematics. The different interaction times resulting from this procedure also need to be taken into account. Finally, the systematic effects affecting the collective signal, like the shift and the broadening of the line, mainly originate in the dynamic Stark shift, ionization and the second-order Doppler shift of the single atoms, but in a quite involved and nonlinear fashion, depending on the characteristics of both the atomic and the laser beams. This is particularly important for the extraction of the unperturbed, single-atom $1S$–$2S$ transition frequency, which is the primary goal of the experiment and the subject of the next chapter.

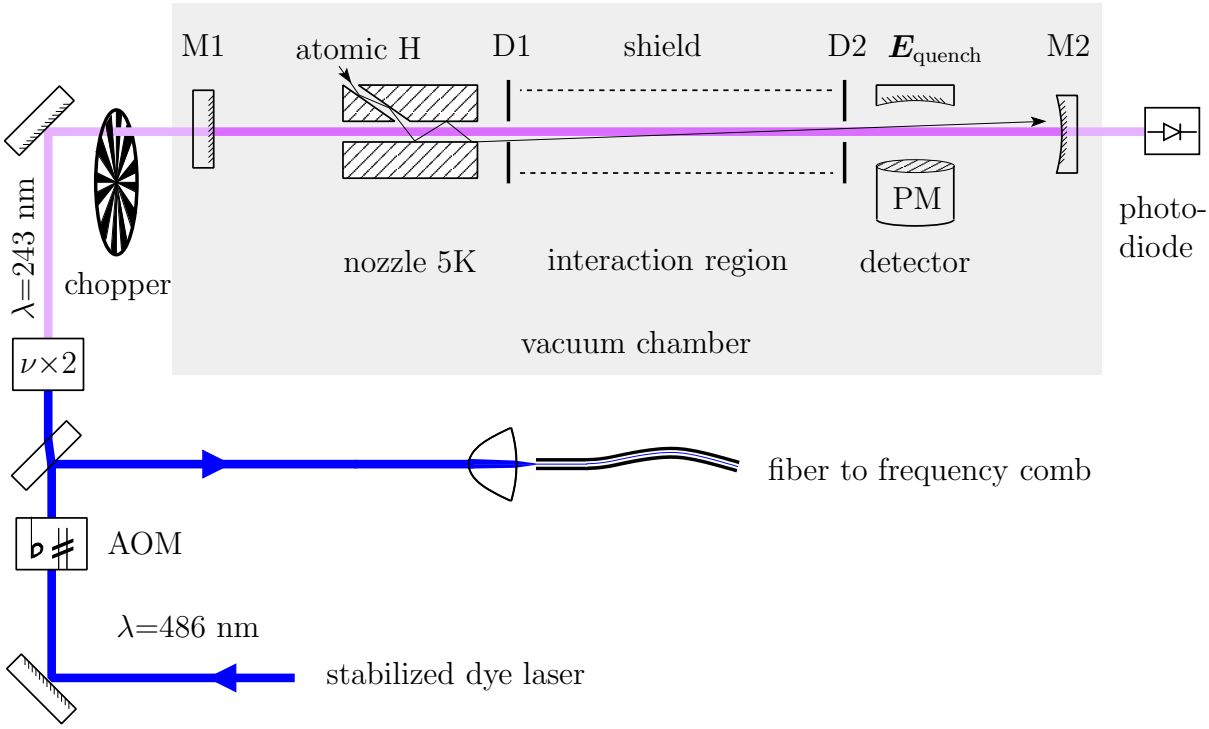

Figure 5.1: Schematic of the MPQ hydrogen $1S$–$2S$ spectrometer. The output from a stabilized dye laser at 486 nm is frequency doubled in a β-barium borate crystal and coupled into the enhancement resonator consisting of a plane in-coupling mirror (M1) and a concave out-coupling mirror (M2). The atomic hydrogen is cooled and effused by a copper nozzle, which is connected to a 5 K liquid helium cryostat. The interaction zone is confined by two diaphragms, D1 and D2, and shielded from electric fields by a Faraday cage. In this region the coherent two-photon excitation of the $1S$–$2S$ transition takes place. In the detector a weak electric field $\boldsymbol{E}_{\text{quench}}$ triggers the emission of Lyman-α photons, which are detected in a photomultiplier (PM). The acousto-optic modulator (AOM) detunes the driving laser, scanning it over the $1S$–$2S$ resonance. A small part of the fundamental beam is transferred via an optical fiber to the frequency comb, which is stabilized to a cesium fountain clock. This links the frequency of the driving laser phase-coherently to the primary frequency standard. The PM counts are recorded as a function of AOM detuning and delay with respect to the beginning of the dark phase, generated by the chopper.

As the trajectory and the velocity of an individual atom that contributes to the signal are unobservable in the experiment, and therefore constitute random parameters, the generation of the total line shape relies on a Monte Carlo simulation of the trajectories and velocities with a appropriate probability distributions. Comparing the output of this simulation of the excitation process with the data recorded by the MPQ group allows one to test to a certain degree the validity of the model, and the constants which have been used in it. In Sec. 5.4 such a test is performed for two observables, k_{shift} and k_{broad}, which

describe the power-dependence of the observed line center and line width, respectively, and which depend on the dynamic Stark coefficient β_{AC}, the ionization coefficient β_{ioni}, and the two-photon transition matrix element β_{ge}.

In addition, after a reasonable agreement of simulation and experiment is established, one can study the effect of different experimental conditions on various observables of interest. This is especially useful for systematic effects, that cannot be controlled or quantified in the laboratory. In Secs. 5.5 and 5.6 two such effects are investigated and are found to contribute to the systematic scatter in the line center of the single spectra. The results of these investigations can then be used to improve the design of the experimental setup accordingly.

5.2 Experimental setup

This section gives a short general overview of the setup and a more specific account of the experimental details which are relevant for the theoretical modeling of the excitation process and the interpretation of the observed signal. For an in-depth description of the complete setup and the frequency comb technique, see e.g. Refs. [18, 23, 96].

The experimental setup consists of three main parts: (i) the hydrogen spectrometer, (ii) the laser system, and (iii) the frequency comb.

In the hydrogen spectrometer, see Fig. 5.1, atomic hydrogen in a cold beam interacts with a standing wave of 243 nm laser light, driving the two-photon $1S$–$2S$ transition. The standing wave is the fundamental mode of the optical cavity, made up of the mirrors M1 and M2, and passes right through the nozzle through which the hydrogen is flowing after being dissociated by an electric discharge. In the interaction zone adjacent to the nozzle, the excitation and partially also ionization of the hydrogen atoms takes place, properly shielded from stray electric fields which would quench atoms in the metastable $2S$ state. In the detector, this effect is exploited, where a static electric field $\boldsymbol{E}_{\mathrm{quench}}$ couples the $2S$ and $2P$ states of the unperturbed atom, triggering the fast decay $2P \to 1S$. The emitted 121 nm photon is detected in a photomultiplier and is an unambiguous signature of the excited $2S$ hydrogen atom, because the photons from the laser mode have the double wavelength. This is one of the reasons why the signal is practically noise-free.

The optical cavity provides a standing wave for the first-order Doppler free excitation. Also, it enhances the power available for the excitation of atoms by a factor of about 40, resulting in a maximum power of 800 mW per direction. Behind the cavity, a photodiode records the power which is transmitted by the out-coupling mirror, giving a measure for the circulating power if one assumes a constant transmittivity of the mirror.

The laser system is designed to provide a primary beam with extremely high frequency stability at a wavelength of 486 nm. This is achieved by locking a dye laser to a special optical cavity which has been developed and continuously refined at the MPQ. The cavity which was used for the 2003 measurements has been built by Marc Fischer and shows a drift of less than 1 Hz/s with a spectral line width of less than 100 Hz during an observation time of 2 s [23]. This cavity is suspended in vacuum and elaborately decou-

pled from vibrations in the laboratory. The temperature is actively stabilized at around 300 K, where the expansion coefficient of the spacer material is very small. This ultra low expansion (ULE) substrate, which carries the cavity mirrors, also has the advantage that crystallization processes are absent, which caused length changes in the previous cavity made from Zerodur.

The frequency comb [18] is situated in the neighboring laboratory and a part of the primary laser beam is therefore directed there via an optical fiber. By measuring the beat note between the hydrogen laser and one specific mode of the frequency comb, the absolute frequency of the hydrogen laser can be determined, because the comb is stabilized to the primary frequency standard. The angular frequency of the n^{th} mode of the frequency comb is related via

$$\omega_n = n\,\omega_\text{r} + \omega_0 \tag{5.1}$$

to two radio frequencies: ω_r, the repetition rate of a femtosecond laser and ω_0 the frequency offset of the zeroth mode, which can be obtained by measuring the beat note between two modes of the comb which are an octave apart. Both ω_r and ω_0 can be measured with the precision of the SI second, which in this experiment was realized by a cesium fountain clock (FOM) from the Bureau National de Métrologie, Observatoire de Paris [13,97]. The relative accuracy of this clock, which is on the order of 10^{-15}, therefore directly determines the accuracy with which the frequency of the primary hydrogen driving laser is known.

The measurement cycle is synchronized to a chopper wheel that interrupts the frequency doubled primary laser beam in front of the vacuum chamber. The light is admitted to the chamber during an interval of about 3.1 ms, driving the $1S$–$2S$ transition in the atomic beam, followed by a dark phase of equal length. The start of this dark phase defines the zero point for an important time delay, τ, which is used for time-resolved detection of excited $2S$ atoms at the detector. The larger τ is selected, the smaller is the maximum velocity v_max of excited atoms contributing to the signal, since excited atoms faster than v_max have already passed the detector during that delay time. A larger τ results in less Doppler systematics but also in a lower $2S$ count rate. In the actual data taking, a set of delays is recorded simultaneously, by sorting the detector counts in time bins corresponding to $\tau = 10\,\mu\text{s}, 210\,\mu\text{s}, \ldots, 2210\,\mu\text{s}$, where e.g. the time bin $1210\,\mu\text{s}$ accumulates the counts starting $1210\,\mu\text{s}$ from the beginning of the dark phase up to its end.

Finally, the acousto-optic modulator (AOM) is used to detune the frequency of the driving laser field in order to record a frequency dependent $2S$ line shape. In the simulation, this is implemented by integrating the equations of motion (2.11) numerically in a loop, stepping the frequency of the laser by 150 Hz in a range of $\pm$ 7.5 kHz. It is a remarkable fact that the resolution of the experiment is so high, that the detuning range through which the AOM is scanned during the recording of one spectrum spans only some kHz. This frequency interval is so small that it could be perceived by the human ear, while being added to a frequency that is twelve orders of magnitude higher - an optical frequency at the upper end of the visible range.

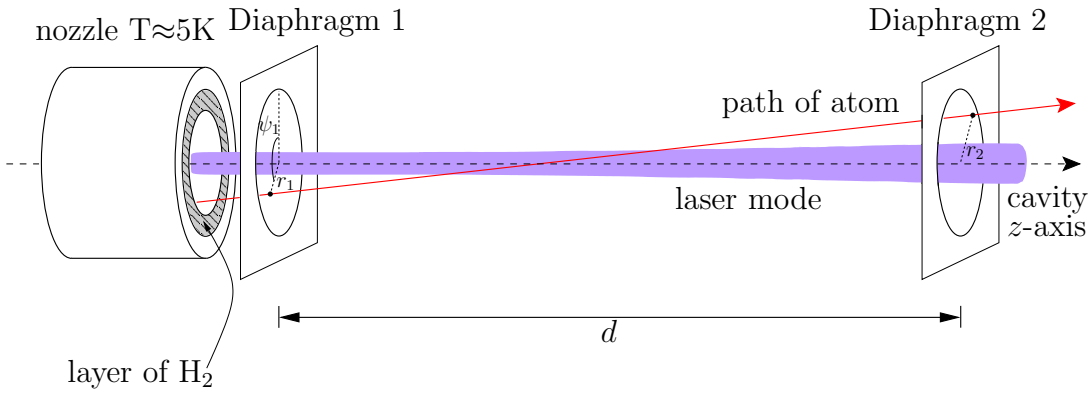

Figure 5.2: Illustration of the interaction region. The straight trajectories of the atoms leaving the cold nozzle are confined by two diaphragms and characterized by (r, ψ) at each diaphragm. The trajectories overlap with the radially symmetric Gaussian laser mode. Molecular hydrogen adhering to the nozzle walls may additionally confine r_1 of the atomic trajectories (see Sec. 5.5 below).

5.3 Implementation of the simulation

In Fig. 5.2, the interaction zone is shown in more detail. Hydrogen atoms are effusing from the cooled nozzle and follow randomly distributed straight trajectories in the vacuum setup. From these trajectories, only those that are very close to the cavity axis are selected by means of two diaphragms and can reach the detector. To model this atomic beam, the following Monte Carlo generation of trajectories is invoked. Each trajectory is characterized by its coordinates on the entrance diaphragm, (r_1, ψ_1) and on the exit diaphragm, (r_2, ψ_2). These pairs of coordinates are generated randomly and independently, with a constant area density on both diaphragms, and subject to the conditions $r_1 < r_{D1} = 650\,\mu$m and $r_2 < r_{D2} = 700\,\mu$m. Further, the speed of a specific atom on its trajectory is chosen at random with the probability distribution [98]

$$f(v) \propto (v/v_0)^3 \exp[(v/v_0)^2]\,, \tag{5.2}$$

which is valid for a one dimensional beam effusing from a thermalized volume, in which the modulus of the velocity v is distributed according to a Maxwell-Boltzmann distribution, and where $v_0 = \sqrt{2k_B T/m_H}$, T is the temperature and m_H is the mass of a hydrogen atom. Finally, the "dark point" of the atom, which is the location along its trajectory at the time when the dark phase starts, is chosen at random uniformly in the interval $[0,d]$, where d is the length of the interaction region. With these parameters fixed, it is easy to determine, whether the atom will have passed the detector before the given time delay τ for which the simulation is run. If this is the case, the atom is rejected from the ensemble. If, on the other hand, the atom will still be in the interaction region after τ, its parameters are appended to a list of valid trajectories. This process continues until an ensemble of typically 10 000 atoms, which contribute to the signal, have been found.

For each of the atoms contained in the list, the individual interaction time with the laser

field is calculated and then the probability of being in the $2S$ state, when the dark phase starts is obtained by numerically integrating the master equations (2.11). Each atom observes an individual, time dependent intensity $I(t)$, which results in a time dependent Rabi frequency $\Omega(t)$, a time dependent AC Stark shift $\Delta\nu_{\mathrm{AC}}(t)$ and a time dependent ionization rate $\gamma_{\mathrm{i}}(t)$. To obtain $I(t)$ for each atom, the location along the trajectory $\boldsymbol{r}(t)$ of each atom is inserted into the Gaussian beam profile

$$I(r,z) = \frac{4P}{\pi w(z)^2}\, e^{-2\, r^2/w(z)^2}\,, \tag{5.3}$$

where the beam waist w slightly varies along the cavity axis as $w(z)^2 = w_0^2(1+(z\lambda/\pi w_0^2)^2)$, with $w_0 = 283\,\mu$m and P being the power per direction, stored in the cavity. Also the second-order Doppler shift is calculated from the atomic velocity and taken into account in the quantum dynamics.

By integrating the master equations for a set of detunings, typically in the range of [-7500,7500] Hz, the single atom response line shapes are obtained and added to obtain the collective signal. Because of the different interaction parameters of each atom, each contributing single-atom line shape is shifted and broadened by a different amount, depending on the atomic velocity, interaction time and the geometry of its trajectory.

The simulation is implemented in *Mathematica* [78], and several program switches are introduced in order to separately investigate the influence of ionization, dynamic Stark shift and spontaneous decay on the total line shape. As expected, the influence of spontaneous two-photon emission turns out to be negligible for hydrogen. The different effects from ionization and the dynamic Stark effect on the line center shift and the line width however are significant and are discussed in the following section.

5.4 Photoionization broadening of the $1S$–$2S$ transition line shape[1]

5.4.1 Introduction

As has been demonstrated in chapter 2, the inclusion of ionization of the $2S$ state into the excitation dynamics can change the single atom line shape dramatically (cf. Figs. 2.3 and 2.4). However, for typical interaction times occurring in the MPQ hydrogen experiment, this influence is only very small (cf. Figs. 2.1 and 2.2), which is one reason why in the analysis of the experimental data up to date, ionization has not been considered as a line broadening factor. However, as will be demonstrated in this section, the collective line shape does show a substantial sensitivity to the presence of ionization of $2S$ atoms. This can be understood qualitatively by considering the fact that the slowest atoms, which would give the strongest and narrowest contributions, also run the highest risk of being ionized and therefore do not contribute much to the observable line. In fact, this influence

[1] The results of this section have been obtained in cooperation with Dr. N. Kolachevsky, MPQ Garching and P. N. Lebedev Physics Institute, Moscow and M. Herrmann, MPQ Garching.

of ionization on the velocity distribution of atoms contributing to the signal needs to be taken into account in the future, since only the collective line shape is observable in an atomic beam experiment.

5.4.2 Experimentally observed broadening and shift coefficients

The experimental data presented in this section have been recorded in February 2003 during the absolute frequency measurement of the $1S$–$2S$ transition in hydrogen at the MPQ in Garching, by Marc Fischer [23] and Nikolai Kolachevsky. The analysis of the raw data was performed by the present author with a Lorentzian data analysis approach, which will be described and compared to the full line shape model in the next chapter.

The atomic constants β_{AC}, β_{ioni} and β_{ge} which govern the excitation dynamics of the $1S$–$2S$ transition are not directly observable, because of the complex superposition of single-atom contributions in the collective line shape. The comparison between the predictions of theory and experimental observations can therefore only take place on the level of the collective line shape. The measured collective line shape for a detection time delay $\tau = 1210\,\mu$s was fitted with a Lorentzian line profile

$$f(A, \nu_{\mathrm{c}}, \Gamma_{\mathrm{fwhm}}; \nu) = A\,\frac{(\Gamma_{\mathrm{fwhm}}/2)^2}{(\nu-\nu_{\mathrm{c}})^2 + (\Gamma_{\mathrm{fwhm}}/2)^2}\,, \tag{5.4}$$

where A is the overall amplitude, ν_{c} is the line center and Γ_{fwhm} is the full width at half maximum. A Lorentzian has turned out to be a very good approximation to the experimental data of the chosen time delay. The Doppler systematics for the slow atoms which contribute are small, while the count rate is still large enough to achieve a good signal-to-noise ratio for the fit.

Figure 5.3 shows the results of the Lorentzian fit to a number of spectra recorded on one of 12 days of measurement, plotted as a function of excitation power per direction in the enhancement cavity. The left plot shows the shift of the fitted line center ν_{c} with respect to an offset frequency which is measured via the frequency comb, including a constant offset at the AOM. In the data analysis leading to the $1S$–$2S$ frequency (see also chapter 6) the line centers are routinely extrapolated with a linear model to zero excitation power:

$$\nu_{\mathrm{c}}(P) = \nu_0 + k_{\mathrm{shift}} P\,. \tag{5.5}$$

In the next section, it will be demonstrated that this procedure is compatible with the theoretical predictions following from the Monte Carlo simulation, albeit only in the low-power regime.

The plot on the right hand side of Fig. 5.3 shows the fitted line widths Γ_{fwhm} as a function of excitation power, which has not been examined systematically in the hydrogen analysis before. Here, also a linear dependence on the power of the driving laser field is observed, and modeled by

$$\Gamma_{\mathrm{fwhm}}(P) = \Gamma_0 + k_{\mathrm{broad}} P\,. \tag{5.6}$$

The extrapolation of this model to zero laser power yields the total intensity-independent width Γ_0, which is due to the spectral laser line width and time-of-flight broadening.

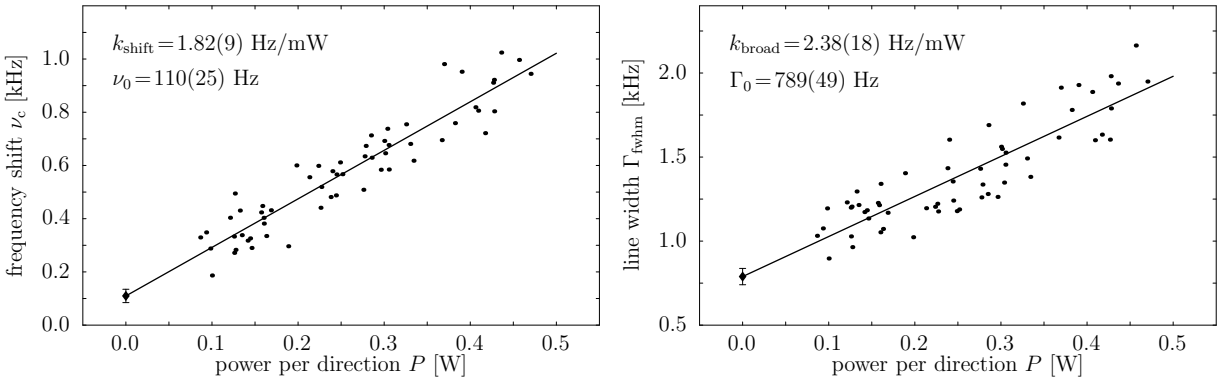

Figure 5.3: Results from a Lorentzian fit (dots) to the experimental raw data, for $\tau = 1210\,\mu$s, of one day of measurement (Feb. 13$^{\mathrm{th}}$ 2003). The frequency shift ν_{c} of the fitted line center (left) and the full width at half maximum Γ_{fwhm} of the fitted Lorentzian (right) are plotted as a function of laser power per direction in the interaction zone. Unweighted least squares fits with a linear model [see Eqs. (5.5) and (5.6)] are indicated by the solid lines.

It should be noted that the uncertainties of the Lorentzian fit are small compared to the scatter of the results of both the line center and the line width around the respective linear models. This scatter is not due to the Lorentzian approximation to the line shape, rather the Lorentzian data analysis has been introduced originally to test whether this scatter, which is also obtained when the full line shape model is invoked, is caused by the more comprehensive model (see Sec. 6.1.3). As will also be discussed in Sec. 6.1.4, the weighting of the individual data points does not make sense in this case, because the reduced χ^2_{r} of the fits would be much too large. For this reason, an unweighted fit of the data points is performed, and the small error bars are omitted.

The amount of scatter of the line centers observed in the data is the most important limiting factor for the precision with which the $1S$–$2S$ absolute frequency can be determined. Therefore, in Secs. 5.5 and 5.6, two possible contributions to this scatter are considered.

The values for k_{shift} and k_{broad} for the other days of measurement are obtained in the same fashion and plotted in Fig. 5.5 below. In the following, a Monte Carlo simulation of the measurement will yield theoretical values for these coefficients, which can then be compared with the values obtained from the experiment.

5.4.3 Simulated broadening and shift coefficients

In this section, the results from a Monte Carlo simulation of the $1S$–$2S$ spectroscopy experiment are discussed, which has been performed for a set of different excitation powers and for a time delay $\tau = 1210\,\mu$s, in order to be compatible with the experimental results described above. The simulation was done with an ensemble of 10 000 atoms in a detuning range of ± 7500 Hz with a beam temperature of 5 K. The geometry of the interaction

region, as given by the MPQ experimental setup is characterized by an interaction region length of 136 mm, a diameter of the entrance diaphragm of 1.3 mm, a diameter of the exit diaphragm of 1.4 mm and a Gaussian beam waist of 283 μm.

In analogy with the experimental data, the line shape obtained by the simulation was fitted with a Lorentzian line profile (5.4), and the obtained line centers and line widths are plotted as a function of simulated laser power in Fig. 5.4. In addition to the physical case, in which both the dynamic Stark effect and ionization from the excited $2S$ state are taken into account, these two processes have been artificially switched off one at a time, and both at the same time, in three additional runs of the simulation.

The results of the simulation show, that the line center shift (left hand side of Fig. 5.4) is caused dominantly by the dynamic Stark effect, which is to be expected. However, if ionization from the excited $2S$ state is taken into account, the line center shift is not quite as large as without ionization. This behavior can be understood by contrasting the contributions of atoms passing along different paths in the interaction region. Those atoms which give the contributions with the largest line shift have passed through regions with high laser intensity. In the case where ionization is switched off, these contributions are included in the collective signal, whereas with ionization switched on, the "highly shifting" atoms are also preferably ionized and therefore lost to the $2S$ signal. This results in a smaller line center shift for the collective signal.

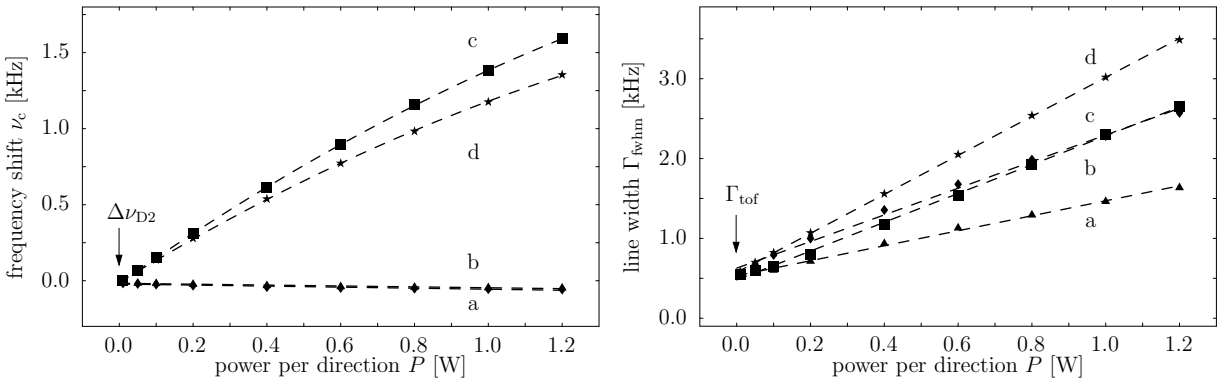

Figure 5.4: Results of Lorentzian fits to the $\tau = 1210\,\mu$s line shapes of a Monte Carlo simulation of one day of measurement: Frequency shift of the line center (left) and full width at half maximum (right) of a fitted Lorentzian, as a function of laser power per direction. The following scenarios with and without ionization and dynamic Stark effect are shown: (a), triangles: $\gamma_i = 0, \beta_{AC} = 0$; (b), diamonds: $\gamma_i \neq 0, \beta_{AC} = 0$; (c), squares: $\gamma_i = 0, \beta_{AC} \neq 0$; (d), stars, physical case: $\gamma_i \neq 0, \beta_{AC} \neq 0$. Because of the finite interaction time, the line width Γ_{tof} at $P = 0$ is also finite. The average of four simulated days of measurement, with a linear extrapolation to zero power is $\Gamma_{tof} = 555(9)$ Hz (including only the physical case). The residual line shift at zero excitation power, caused by the second-order Doppler shift, is $\Delta\nu_{D2} = -14(1)$ Hz. The dashed lines indicate a linear/quadratic fit of the power-dependence of ν_c and Γ_{fwhm}.

The discussion of the simulated line width (right hand side of Fig. 5.4) is a little more complicated. Obviously, even without taking into account ionization or the dynamic Stark effect, the line width of the simulated spectra depends on the excitation power (triangles). This is the power-broadening contribution to the total width. If the ionization channel from the $2S$ state is switched on in the simulation, the power dependence of the line width increases (diamonds). This can only partially be explained by the reduction of the lifetime of the $2S$ state in the single-atom response, in addition there is again a collective effect. The class of atoms in the cold beam with a short total interaction time make broader contributions to the line shape (time-of-flight broadening), and are less affected by ionization because of the short interaction with the field. Vice versa, those atoms which interact longer with the laser field, contribute strong and narrow lines to the signal, but are also preferentially removed by the ionization process. Via this effect, ionization has a much larger impact on the line width than expected from the usual ionization broadening in the single-atom case (cf. Figs. 2.1 and 2.2).

By switching off ionization while including the dynamic Stark effect in the quantum dynamics (squares), the observed line width of the collective $2S$ signal is also additionally broadened as compared to the pure power-broadening case. This contribution to the width originates in the fact that the atoms pass through an inhomogeneous intensity profile during the excitation process. The resulting inhomogeneous dynamic Stark shift broadens the single-atom line shape and correspondingly also the width of the collective signal is increased. Finally, the simulation of the physical case, with both the dynamic Stark effect and the ionization process properly included (stars), results in an excitation power dependent line width, which unites all the mentioned processes. In view of the rather involved interplay between the single-atom responses, interaction times, velocity distribution effects and excitation in an inhomogeneous intensity profile, it is not surprising that the contributions from the power broadening, ionization broadening and inhomogeneous Stark broadening cannot simply be added.

In order to obtain a valid comparison with the experimentally obtained values for k_{shift} and k_{broad}, the same linear models, (5.5) and (5.6), have been fitted to the simulated data. Since for the physical case a nonlinear power-dependence of the line center shift is observed at high excitation powers in the simulation, the determination of the Monte Carlo value for k_{shift} has been obtained from a linear fit restricted to the experimental range of excitation powers.

5.4.4 Comparison

In Fig. 5.5, a comparison is shown of the experimentally observed coefficients k_{shift} and k_{broad} with the corresponding values from the Monte Carlo simulations. The values obtained from the different days of measurement are shown on the left hand side of the respective plot, and the unweighted average and the standard error of the mean value are indicated by the solid line and the turquoise bar, respectively. On the right hand side of each plot, the averaged results from four Monte Carlo simulated days of measurement are shown. The statistical uncertainties of these values are on the order of the symbol size, therefore no error bars are indicated.

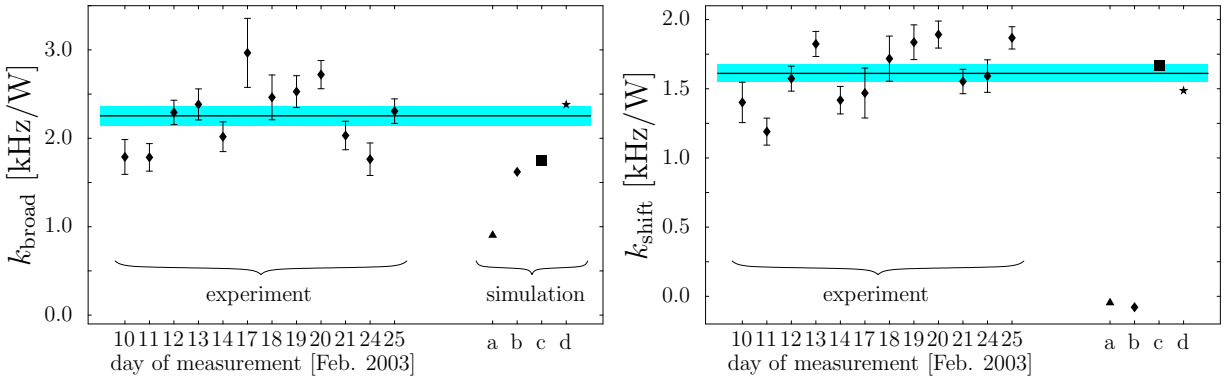

Figure 5.5: Comparison of measured coefficients k_{broad} (left) and k_{shift} (right), with values obtained from the Monte Carlo simulation, where the following scenarios were distinguished, by means of program switches: (a), triangles: $\gamma_{\mathrm{i}}=0, \beta_{\mathrm{AC}}=0$; (b), diamonds: $\gamma_{\mathrm{i}}\neq 0, \beta_{\mathrm{AC}}=0$; (c), squares: $\gamma_{\mathrm{i}}=0, \beta_{\mathrm{AC}}\neq 0$; (d), stars, physical case: $\gamma_{\mathrm{i}}\neq 0, \beta_{\mathrm{AC}}\neq 0$.

Four different scenarios have been simulated, as already depicted in Fig. 5.4, taking into account the dynamic Stark effect and the ionization channel from the $2S$ state in different combinations. By comparing the experimental average of k_{shift} with the simulated results, it is obvious that both simulations omitting the dynamic Stark effect [cases (a) and (b)] do not agree with the experimental observation. However, it is not possible to make an unambiguous distinction between the scenarios where the dynamic Stark shift is taken into account, but ionization is included (d) or neglected (c), given the scatter of the experimental values.

In the comparison of the broadening coefficients k_{broad} from the observation and the simulation, clearly only the scenario in which both the ionization channel and the dynamic Stark effect are taken into account in the quantum dynamics, agrees with the observed line broadening coefficient. This result is an important argument for taking ionization seriously in future line shape models to be used in the analysis of the $1S$–$2S$ transition in hydrogen.

5.4.5 Laser line width

Apart from comparing the intensity-dependent broadening contributions, it is also interesting to consider the residual line width at zero excitation power. In the Monte Carlo simulation, a monochromatic laser with vanishing spectral line width is assumed, while a beat note measurement of the dye laser by the MPQ group resulted in a spectral linewidth of 60 Hz at the fundamental wavelength of 486 nm [99].

If one assumes that the contributions at zero excitation power have a Lorentzian line shape, the line widths can be added, and the total experimental line width Γ_0 reads

$$\Gamma_0 = \Gamma_{\mathrm{tof}} + 4\,\Gamma_{\mathrm{laser}}\,, \tag{5.7}$$

where no involved intensity-dependent broadening contributions need to be considered. The spectral line width of the laser enters with a factor of four, because line widths of the $2S$ spectra are given at a wavelength of 121 nm, while the spectral width of the laser has been characterized at 486 nm. It is not self-evident that a frequency doubling stage also doubles the spectral width of the laser, but for the dye laser used at the MPQ this property has been confirmed experimentally [1].

For the intensity-independent width of the $2S$ spectra at a delay of $\tau = 1210\,\mu$s, one obtains, by averaging the Γ_0 of each day of measurement (see Fig. 5.3):

$$\Gamma_0 = 776(21)\,\text{Hz}\,. \tag{5.8}$$

From a set of four Monte Carlo simulations, a zero power extrapolation of the physical case (d) results in $\Gamma_{\text{tof}} = 555(9)$ Hz (see Fig. 5.4), which is exclusively due to the finite interaction time of the atom and the laser field (time-of-flight width). Solving Eq. (5.7) for the spectral laser line width leads to

$$\Gamma_{\text{laser}} = 55(6)\text{Hz} \tag{5.9}$$

from the indirect analysis of the experimental spectra, which is in good agreement with the independent and more direct measurement, resulting in $\Gamma_{\text{laser}} = 60$ Hz, as mentioned above.

5.5 Effects of nozzle freezing

In the course of the hydrogen $1S$–$2S$ measurements, the MPQ group observed a decrease of the hydrogen flow over time, which could be restored by interrupting the measurement and "heating" the hydrogen nozzle to above 10 K. Because this temperature is close to the melting point of molecular hydrogen in vacuum, this drop of nozzle throughput could be retraced to a film of molecular hydrogen, freezing to the 5 K copper surface and reducing the diameter of the nozzle. In Fig. 5.2, this layer of hydrogen frost is illustrated at the orifice of the nozzle. If the only effect of this nozzle congestion would be the lower flow of atomic hydrogen, only the signal amplitude would be affected. However, also the atomic trajectories are influenced, because they are additionally confined at the entrance of the interaction zone.

Since the exact thickness of the layer cannot be controlled and is very difficult to quantify in the experiment, a Monte Carlo simulation has been performed to study the effect of the nozzle freezing on the final $2S$ line shape, and in particular its effect on a possible shift of the line center. The implementation of this aspect was achieved by modifying the seeding of the trajectory starting points (r_1, ψ_1). A cylindrically symmetric layer of hydrogen was assumed, changing the boundary condition for r_1 during the generation of the trajectories. In the experiment, the excitation power was varied in a random pattern, while the layer of hydrogen is assumed to increase gradually. Therefore, in the simulation, the radius of the entrance diaphragm, r_1, was varied at random in the interval $[w_0 = 283\,\mu\text{m}, r_{\text{D1}} = 650\,\mu\text{m}]$

[1] Nikolai Kolachevsky, private communication.

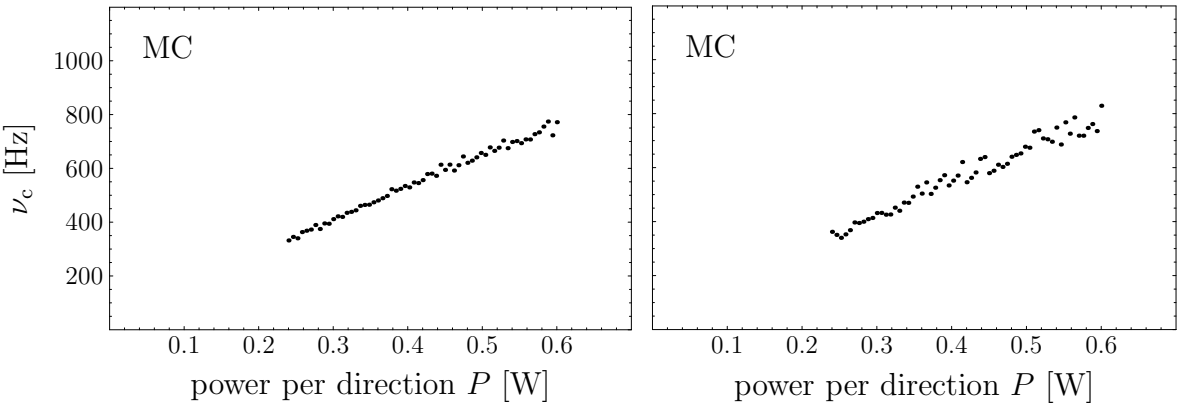

Figure 5.6: Comparison of two sets of Monte Carlo simulations of the line centers of $2S$ spectra at a delay of $1210\,\mu$s, with a sample of 10 000 atoms for each spectrum. On the left, the trajectories are unrestricted at the entrance diaphragm, simulating a free nozzle. On the right, the starting points of the atomic trajectories are radially confined at the entrance diaphragm to one random value in the range [$283\,\mu$m, $650\,\mu$m] per spectrum. This simulates in a simple fashion a freezing of the nozzle.

(see also Sec. 5.3), while stepping gradually through the excitation powers, which results in the same random relation between excitation power and nozzle radius. The lower limit for the radius of the entrance diaphragm has been chosen to be the laser beam waist, since a further congestion of the nozzle would significantly affect the laser mode and correspondingly would have led to an observable loss of excitation power during the measurement.

The results of the line centers as a function of excitation power, obtained in the simulation of spectra with delay $\tau = 1210\,\mu$s in a 5 K atomic beam, are shown in Fig. 5.6. On the left hand side, the nozzle was unobstructed, while on the right hand side, the nozzle freezing was modeled as described above. As can be observed in the figure, the nozzle freezing does have an effect on the line centers causing a scatter on the order of at least 50 Hz. The scatter in the plot on the left hand side is due to the finite sample size of Monte Carlo trajectories. The smaller the radius of the entrance diaphragm, the higher the resulting central frequency of the $2S$ line shape. This correlation can be explained by the action of the dynamic Stark effect. Since the starting points of the contributing atoms have been confined closer to the cavity axis, the average intensity observed by the atoms is higher than for a free nozzle, resulting in a somewhat larger shift of the line center.

However, the scatter which is observed in a set of data from one given day of measurement (see Fig. 5.7, right) is much larger and the noise caused by the nozzle freezing cannot account for the observed frequency variation. In Fig. 5.7 (left), an additional 10% of noise has been added to the excitation power of each simulated data point from Fig. 5.6 (right). This is a more or less realistic estimate of the accuracy with which the excitation power in the enhancement cavity is known. The calibration of the photodiode measuring the power leaking from the out-coupling mirror (see Fig. 5.1) is much better than that, but

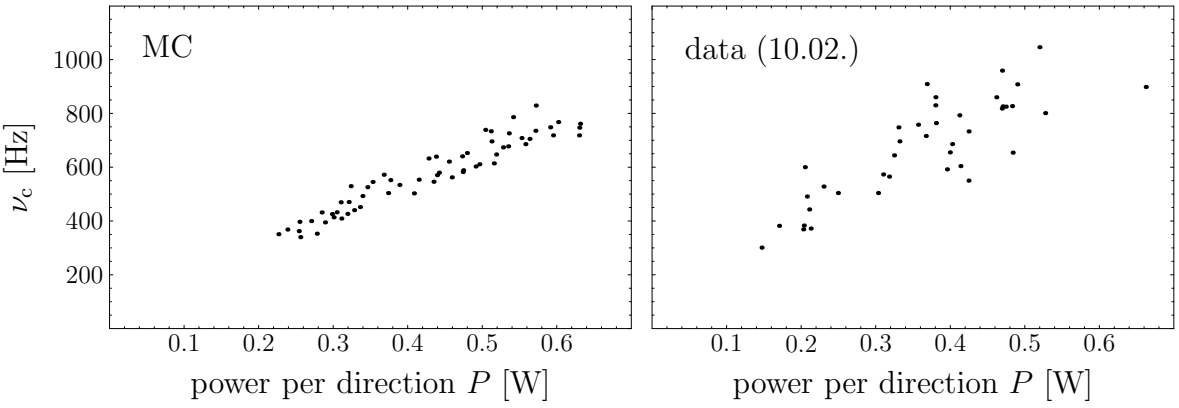

Figure 5.7: Left: Monte Carlo simulation like in Fig. 5.6, with an added intensity uncertainty of 10%. Right: Line centers of experimental spectra from one day of measurement, recorded at a delay of 1210 μs, as in the simulation.

suspicion has come up concerning the variability of the transmittivity of this mirror while being exposed to molecular hydrogen.

From the above comparison, it is clear that both the nozzle freezing and a possible uncertainty in the determination of the excitation power significantly contribute to the scatter of the center frequency of the spectra, but that these effects alone, even when exerted to the maximum, cannot fully explain the source of the frequency noise. However, the order of magnitude and especially the systematic upwards shift in frequency of the nozzle freezing, need to be taken seriously and amended in future experiments. For example, by using a nozzle with a radius which is larger than the radius of the entrance diaphragm, one would avoid the restriction of the trajectories in the interaction zone, as long as the film of hydrogen is not allowed to grow excessively (see Sec. 6.1.6).

5.6 Effect of laser beam misalignment

Up to now, the two-photon excitation in the optical resonator has been considered to take place in a laser with Gaussian beam characteristics [100]. In this section, the effect of a possible misalignment of the cavity axis and the direction of the in-coupling laser beam is investigated, giving rise to a deviation from the pure Gaussian light profile. The reason why one expects an influence on the observed spectra from such a misalignment is clarified in the following consideration: For an atom moving in the enhancement cavity with a velocity v and absorbing two counter-propagating photons, the Doppler shift cancels to first order in $\beta = v/c$ and the remaining second order shift is small and can be corrected reliably in the line shape model. The condition for this cancellation is, that the absorbed photons have exactly opposite propagation directions, which is the case if both photons are quanta from the fundamental cavity mode. These photons will be referred to as "cavity photons". However, it is also possible, that an atom absorbs one cavity photon and one photon from the incoming laser beam, which is partially transmitted through

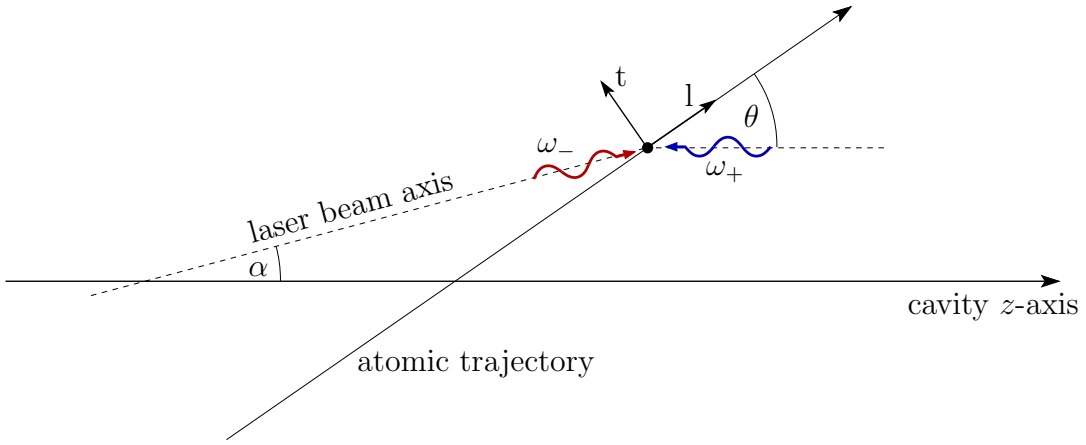

Figure 5.8: Geometry of a situation in which the wavevectors of the two absorbed photons are not perfectly antiparallel. The angles are on the order of mrad and not drawn to scale. In the reference frame of the moving atom before the absorption, the cavity photon is blue-shifted to the angular frequency ω_+ and encloses an angle θ with the longitudinal (l) coordinate of the atom, while the photon from the in-coupling beam is red-shifted to ω_- and observed under the angle $\theta - \alpha$. The absorption of these photons results in a residual first-order Doppler shift (5.14) and a small recoil which also has a component transversal (t) to the original trajectory.

the in-coupling mirror M1 (see Fig. 5.1). If the axis of the cavity and the laser beam axis enclose a small angle α, the Doppler shift no longer cancels and a residual first order effect remains. This scenario is depicted in Fig. 5.8, where the blue photon illustrates a cavity photon and the red photon a "stray photon" from the in-coupling laser beam.

The evaluation of the Doppler shift in the given situation is done in the rest frame of the moving atom, before the absorption process has taken place. In this frame, initially the atom has no momentum, no kinetic energy and is in the electronic ground state. The frequency of the photons is given by the well-known Doppler formula

$$\omega_+ = \omega_\mathrm{L} \frac{1+\beta\cos(\theta)}{\sqrt{1-\beta^2}}\,, \qquad \omega_- = \omega_\mathrm{L} \frac{1-\beta\cos(\theta-\alpha)}{\sqrt{1-\beta^2}}\,, \tag{5.10}$$

where $\beta = v/c$ and v is the velocity of the atom along the l-axis, as measured in the laboratory frame, where both photons are observed with the laser frequency ω_L. The angle α quantifies the misalignment of the laser beam with respect to the cavity axis, while θ is the angle which the atomic trajectory encloses with the cavity axis. For simplicity, all three axes are considered to be in one plane. Also, the angles α and θ strictly would have to be transformed into the frame of the moving atom, but for $v \ll c$ and in the small angle approximation, one obtains

$$\phi_\mathrm{at.frame} \approx \phi_\mathrm{lab.frame} \left(1 - \frac{v}{c}\right) \approx \phi_\mathrm{lab.frame} \tag{5.11}$$

and the aberration is on a level of less than 10^{-5} for the MPQ setup and is neglected in the following. For the case of vanishing misalignment, $\alpha = 0$, the terms of order β in the numerators of Eq. (5.10) cancel, if the photon frequencies are summed, and only the second-order time dilation contribution to the Doppler shift remains. This is the situation every time an atom absorbs two cavity photons. In the case of absorption of one stray photon and one cavity photon, energy and momentum conservation require

$$\hbar\omega_0 + mv'^2/2 = \hbar\omega_+ + \hbar\omega_- \,, \tag{5.12a}$$

$$mv'_l = -\hbar k_+ \cos(\theta) + \hbar k_- \cos(\theta - \alpha) \,, \tag{5.12b}$$

$$mv'_t = \hbar k_+ \sin(\theta) - \hbar k_- \sin(\theta - \alpha) \,, \tag{5.12c}$$

for the case of two-photon resonance. Here, m is the rest mass of the absorbing atom, $k_\pm = \omega_\pm/c$ and $\boldsymbol{v}' = (v'_l, v'_t)$ is the velocity of the atom after the absorption. Solving for ω_L and expanding to first order in β, one obtains

$$\begin{aligned}\hbar\omega_\mathrm{L} = {} & \frac{\sqrt{m^2c^4 + mc^2\hbar\omega_0[\cos(\alpha) - 1]} - mc^2}{[\cos(\alpha) - 1]} \\ & + \beta \, \frac{\sin\left(\alpha/2 - \theta\right)}{2\sin\left(\alpha/2\right)} \left(\sqrt{m^2c^4 + mc^2\hbar\omega_0[\cos(\alpha) - 1]} - mc^2 \right) .\end{aligned} \tag{5.13}$$

The laser detuning, which is needed to fulfill the $1S$–$2S$ resonance in the atomic frame, therefore reads

$$2\pi\,\Delta\nu_\mathrm{D1} = 2\omega_\mathrm{L} - \omega_0 = \frac{1}{2}\omega_0\beta\alpha\theta - \frac{1}{4}\omega_0\beta\alpha^2 + \frac{1}{8}\omega_0\beta\alpha^2\theta^2 + \frac{\hbar\omega_0^2\alpha^2}{8mc^2} \,, \tag{5.14}$$

to second order in the angles θ and α. With a set of realistic parameters, $\alpha = \theta = 1$ mrad and $\beta = 10^{-6}$, one obtains, in frequency units Hz,

$$\frac{1}{2}\nu_0\beta\alpha\theta = 1233\mathrm{Hz} \,, \qquad -\frac{1}{4}\nu_0\beta\alpha^2 = -617\mathrm{Hz} \,, \tag{5.15}$$

$$\frac{1}{8}\nu_0\beta\alpha^2\theta^2 = 3.08 \times 10^{-4}\mathrm{Hz} \,, \qquad \frac{h\nu_0^2\alpha^2}{8mc^2} = 3.35\mathrm{Hz} \,. \tag{5.16}$$

Especially the contributions from the $\alpha\theta$-term and the α^2-term are worth being discussed in more detail. Since the former is linear in θ, and the signal consists of contributions of atoms with both positive and negative angles θ, this residual first-order Doppler contribution is expected to average out, if $\langle\theta\rangle = 0$. However, in an asymmetric hydrogen beam, this term could produce a systematic shift, as detailed in Sec. 5.6.1 below.

In contrast, the shift due to the α^2 term, although smaller in magnitude, does not average, and occurs also in a symmetric beam of hydrogen (see Sec. 5.6.2). The reason why the shift of the observed line center does not reach the large values as given in the estimation above is, that only a small fraction of the total absorption processes is affected by the shift. In the MPQ cavity, where a power enhancement of 40 with respect to the in-coupling beam power is achieved, the assumption of a level 1/40 of stray photons is a reasonable upper bound. In the following sections, the misalignment effect on the collective signal is investigated. It should be mentioned, that the results depend sensitively on the ratio of stray photons and cavity photons, and that a cavity with a higher power enhancement factor would suppress these systematics.

5.6.1 The $\alpha\theta$-term

In the following, the shift of the observed $2S$ spectra is examined, which is due to the term $^1/_2\,\omega_0\beta\alpha\theta$ in Eq. (5.14). By separating the contributions to the total Doppler effect $\Delta\nu_{\mathrm{D1}}$, it is easier to physically interpret the results obtained in the Monte Carlo simulation. In order to maximize the visibility of the effect caused by the $\alpha\theta$-term, the trajectories of the hydrogen atoms were generated in such a way that only positive angles θ occur, lying in the range [0,10] mrad, as permitted by the experimental geometry. This represents an asymmetric situation for the hydrogen beam in which, e.g., the upper half of the nozzle is frozen and the atoms pass the entrance diaphragm only on the lower half, while passing the exit diaphragm on the upper half. As a function of the misalignment angle, the Monte Carlo simulation of the spectra at 1210 μs delay and the usual beam temperature of 5 K, results in a line center shift as depicted in Fig. 5.9.

First of all, it is important to observe that the magnitude of the shift of the collective signal is in the range of ± 10 Hz, for a maximum asymmetry, and thus far smaller than the single-atom estimate in Eq. (5.15), because only in a small fraction of the absorption processes a stray photon is involved. In addition, although for small angles α, the line shift depends linearly on α as expected, for large misalignment angles, the shift of the line center disappears. This effect is also caused by the low level of stray photons, and can be interpreted as follows (see Fig. 5.10): The total line shape (black line) is the sum of the contribution of atoms which have absorbed only cavity photons (blue line) and of atoms which have absorbed one cavity photon and one stray photon (red line). The red contribution is shifted linearly in α by a large amount, on the order of kHz, while the blue contribution is unaffected by the misalignment. Because the "stray contribution" is

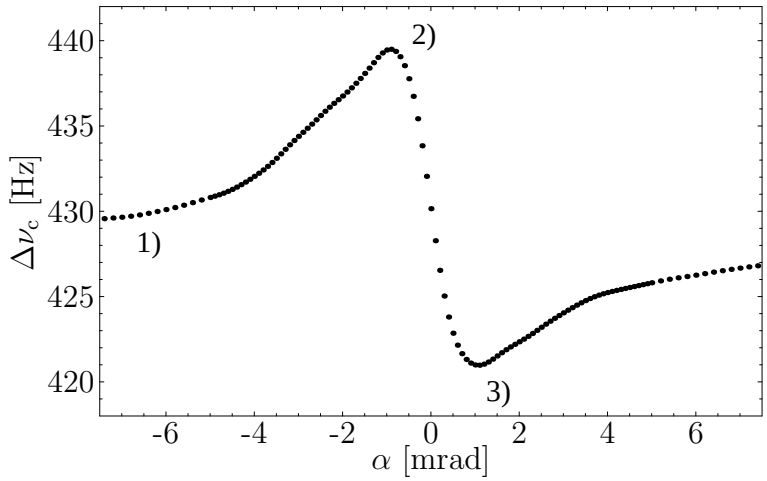

Figure 5.9: Monte Carlo results of the residual first-order Doppler shift in an asymmetric hydrogen beam, interacting partially with stray photons from the in-coupling laser beam. The angle of misalignment is denoted by α. The offset of the line center $\Delta\nu_c$ of about 428 Hz is due to the dynamic Stark shift and the second-order Doppler shift.

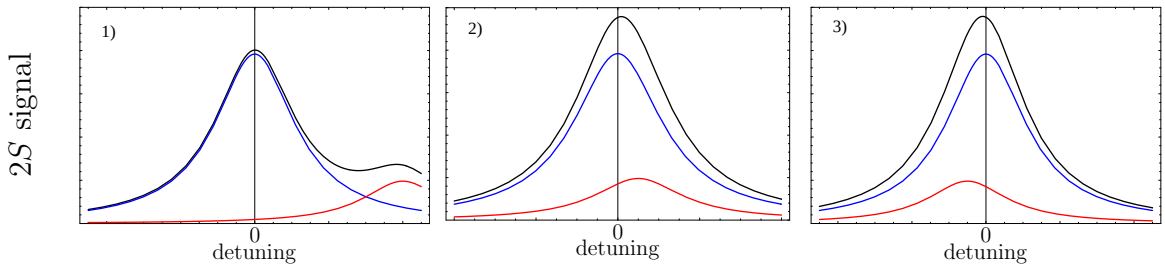

Figure 5.10: Interpretation of the Monte Carlo results in Fig. 5.9. The total line shape of the $2S$ signal (black line) is composed of a large unshifted contribution (blue line) and a small contribution (red line), subject to a residual first-order Doppler shift. The center of the total line shape is only shifted discernibly, if the red contribution is close to zero detuning (small misalignment α). For illustrational purposes, the amplitude of the red contribution is exaggerated.

small in amplitude, the center of the total line shape is only significantly affected for the case that the red contribution is close to this center [cases (2) and (3)]. For large shifts of the red contribution [case (1)], the center of a fit to the collective signal (Lorentzian fit or line shape model fit), is not influenced by the small disturbance on the wings of the signal. For even larger misalignments, the stray contribution is not even in the recorded frequency range.

For the current $1S$–$2S$ experiment at the MPQ, one can conclude that the contribution from the $\alpha\theta$-term is bounded by ± 10 Hz, but realistically it is smaller, since the asymmetry in the atomic beam, as assumed here, is quite large. In addition, if one assumes small vibrations of α around zero, or repeated readjustments of the optics, resulting in an average value of zero for α, the Doppler effect due to the $\alpha\theta$-term averages out during a day of measurement. However, for small angles, this effect very sensitively depends on α, so when the precision of the line center fits reaches the 10 Hz level, the large slope of the $\Delta\nu(\alpha)$ dependence will impose a tight upper limit on the misalignment of the in-coupling laser beam, if a certain asymmetry of the hydrogen beam cannot be ruled out.

5.6.2 The α^2-term

The second important contribution to the residual first-order Doppler shift (5.14) is the term $-{}^1\!/_4\,\omega_0\beta\alpha^2$. Since it is independent of θ, it is also independent of the symmetry properties of the atomic beam, therefore the α^2 contribution is also present under perfect hydrogen beam conditions. A simulation with a symmetric beam of 10 000 atoms at 5 K and a 1210 μs time delay has been performed. The line centers of the collective spectra for each run with a different misalignment angle α are plotted in Fig. 5.11.

For small misalignment angles α, the collective signal again behaves like expected from the single atom shift, being shifted proportional to α^2. The amplitude of the shift is reduced, as above, due to the fact that the largest contribution to the signal is unshifted, originating in the exclusive absorption of cavity photons. A very similar picture like Fig. 5.10 can

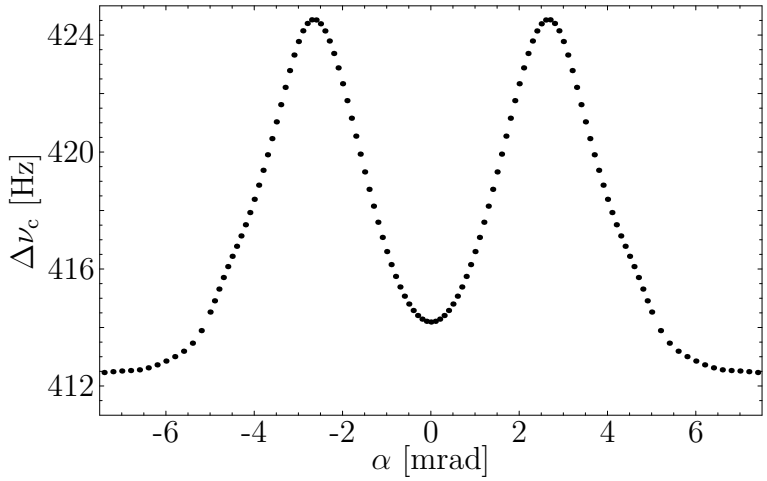

Figure 5.11: Systematic line shift of the collective $2S$ signal, as occurring in a cavity with a power enhancement factor of 40 and an in-coupling beam misalignment angle α with respect to the cavity axis. The offset of about 414 Hz is due to the collective AC Stark shift and the second-order Doppler effect.

be drawn for the interpretation of the fall-off of the collective line center shift for large misalignment angles, and the characteristic of the α^2 contribution to the total line shape can be explained with the same argument. The only difference is, that here, the red contribution to the total line shape is always shifted towards positive detunings.

The reason that the two curves in Figs. 5.9 and 5.11 are not centered around the same offset is, that different hydrogen beam geometries were considered. The integrated dynamic Stark effect along these trajectories is therefore a little different.

The consequence of this result for the MPQ experiment is, that the α^2-contribution can have an important influence, again when the line center precision is at about 10 Hz. The most important observation is, that this effect shifts the line upwards systematically, and therefore does not average out. However, at small angles a deviation from $\alpha = 0$ is not as critical as for the $\alpha\theta$-term, because $\partial\nu_c/\partial\alpha|_{\alpha=0} = 0$.

5.7 Conclusion

The Monte Carlo simulation presented in this chapter has been shown to be able to model the two-photon excitation process in the MPQ setup to full extent. The simulated line broadening coefficient, line shift coefficient and laser line width inferred from the simulation, agree well with the experimentally observed values. This also constitutes an indirect verification of the $1S$–$2S$ transition matrix element, β_{ge}, and the dynamic polarizabilities β_{AC} and β_{ioni} of the involved states.

The simulation also provides a strong contribution in identifying an important broadening contribution, namely the ionization broadening of the collective $2S$ line shape observed

in the experiment, which goes beyond the single-atom ionization broadening.

In addition, the simulation has been shown to be a valuable tool to investigate systematic effects which are difficult to assess or quantify experimentally. In this way, the importance of nozzle freezing and cavity beam misalignment could be clarified in contributing to the observed scatter.

For future experiments, this simulation can provide a testing ground for changes of the setup and for a quantitative evaluation of relative count rates and line shapes for different setups or detection schemes. In particular, the detection of the ionization fragments instead of the $2S$ signal is a promising perspective to increase the signal amplitude. The generation of the corresponding ionization line shape is already implemented in the Monte Carlo program.

Chapter 6

$1S$–$2S$ Spectroscopy and Possible Drift of Fundamental Constants

This chapter consists of two main parts. In the first part, the data analysis procedure of the hydrogen $1S$–$2S$ absolute frequency measurement used at the Max–Planck–Institut für Quantenoptik (MPQ) is examined. This investigation of the existing line shape model is aimed at the question, whether the very intricate fitting algorithm might be responsible for the residual scatter which is observed in the results of the line shape fits during one day of measurement and also among the results for the absolute frequency of different days. On the basis of direct scrutiny and by comparison with an own independent data analysis, it an be concluded that the line shape model can be ruled out as the main source of scatter. This conclusion however leads to the question of which physical processes could explain the remaining uncontrolled systematics instead. Different candidates for these processes are examined and specific improvements to the experimental setup are proposed.

The second part of this chapter is dedicated to one of the most exciting insights which present-day high-precision spectroscopy laboratory experiments are able to provide. The question of whether the coupling strengths of fundamental interactions in physics are really constant, or whether they are subject to a temporal change, is addressed. This question is especially interesting in the context of the search for unified theories, some of which predict a tiny drift of the observable fundamental constants due to the cosmological evolution of compact extra spatial dimensions. As a consequence of the very high absolute precision on the order of 10^{-14}, the considered laboratory experiments reach the same level of sensitivity to a drift of fundamental constants, within an interval of some years, as do astronomical and geological investigations, which rely on very long time scales separating the probing of the constants' values. Stringent limits on the relative order of 10^{-15}/yr are derived for the drift of the fine structure constant and the cesium nuclear magnetic moment, based on the repeated MPQ $1S$–$2S$ measurements and an experiment probing the mercury clock transition in the group of J. Bergquist at NIST.

6.1 Data analysis and systematic effects

The physical model of the two-photon excitation process, discussed in chapter 2 and the calculation of experimental observables from this model, as performed by means of a Monte Carlo simulation in chapter 5, constitute a so-called forward problem. That is, a set of physical and experimental parameters, e.g., the $1S$–$2S$ absolute frequency, is used as input, and an observable, e.g., the collective $2S$ spectrum, is obtained as the output. The data analysis, where one aims to obtain the $1S$–$2S$ absolute frequency from the observed spectra, constitutes the corresponding inverse problem. For the $1S$–$2S$ experiment, the data analysis is routinely carried out at the MPQ by a numerical fitting program, *FitAll* [101], which is a commercial product, and which has been extensively adapted to the $1S$–$2S$ experiment by A. Huber [102], M. Niering [96] and M. Fischer [23]. This program, referred to as the line shape model (LSM) below, is essentially based on a Levenberg-Marquardt nonlinear fitting algorithm. In an iterative process, a set of parameters is varied, in each step solving the forward problem and minimizing a least squares figure of merit. After a brief description of this data analysis method in Sec. 6.1.1, the aspect of specific velocity distributions that enter the LSM is discussed in Sec. 6.1.2. Section 6.1.3 is dedicated to the independent verification of the LSM by means of a transparent data analysis method relying on spectra with low Doppler systematics. In Sec. 6.1.4 a statistical argument is given to support the observation that some unaccounted systematic effects exist, and the weighted fitting of the data is briefly addressed. In Secs. 6.1.5-6.1.6, possible candidates for these systematic effects are examined and improvements to the experimental setup and to the LSM are proposed.

6.1.1 MPQ data analysis procedure

The analysis of the hydrogen $1S$–$2S$ data recorded at the MPQ takes place in three major stages. First, the time resolved spectra are simultaneously fitted with the LSM, which contains all the physical modeling of the excitation process, the laser geometry and the hydrogen beam characteristics. For an example of a LSM fit to a time resolved experimental spectrum see Fig. 6.1. This is by far the most involved step and is described in more detail below. From the LSM fit, a frequency value $\Delta\mathrm{det}$ is obtained for each spectrum, representing the $1S$–$2S$ resonance frequency, already corrected for the second-order Doppler effect. Since in the LSM the excitation power is fixed to 450 mW, the dynamic Stark shift is not taken into account correctly for other excitation powers and therefore has to be corrected for.

For this purpose, in the second stage all results $\Delta\mathrm{det}$ from the LSM fits are plotted versus the excitation power (Fig. 6.2, left), which varies in a range of about 100 mW ... 500 mW during one day of measurement. A linear extrapolation to zero excitation power yields the absolute frequency associated with that day of measurement.

Finally, in the third stage, a constant is fitted to all day values, i.e., all days of measurement are averaged (Fig. 6.2, right), resulting in the value for the absolute frequency ν_F of the $1S(F=1, m_F=\pm1) \Leftrightarrow 2S(F'=1, m'_F=\pm1)$ transition. To obtain the centroid $1S$–$2S$

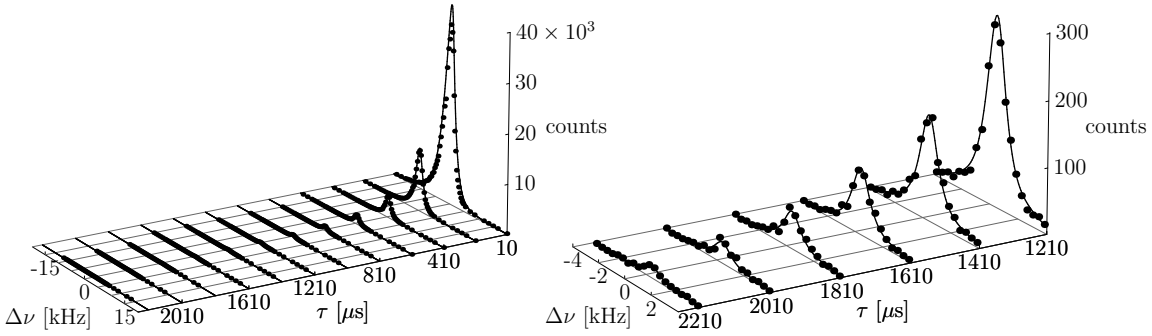

Figure 6.1: Fit of the line shape model (solid line) to time-resolved experimental spectra (dots) of the hydrogen $1S$–$2S$ transition. All delays are taken into account simultaneously, as shown on the left hand side. The right hand side plot shows a close-up for the delays $\tau \geq 1210\,\mu$s, where the signal amplitude is about two orders of magnitude lower.

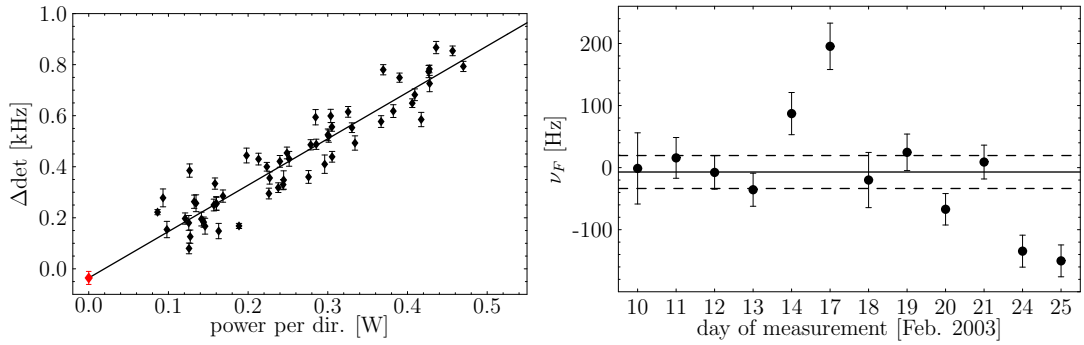

Figure 6.2: Left: Extrapolation to zero excitation power of the line shape model results of the line center Δdet, for the data of Feb. 13$^{\text{th}}$. The scatter of the Δdet values, exceeding their respective statistical uncertainty is a strong indication for remaining systematic effects as investigated in chapter 5 and in this chapter. Right: Final averaging over the results of all days of measurement.

absolute frequency, the hyperfine splitting $\nu^{\text{HFS}}(1S)$ of the ground state and the hyperfine splitting $\nu^{\text{HFS}}(2S)$ of the excited state have to be taken into account:

$$\nu^{\text{cent.}}(1S{-}2S) = \nu_F + \frac{1}{4}\nu^{\text{HFS}}(1S) - \frac{1}{4}\nu^{\text{HFS}}(2S)\,. \tag{6.1}$$

In the first stage, the LSM fit, a set of seven free parameters is used to fit the experimental data. These parameters are used to calculate the theoretical line shape of the collective signal from a set of signal contributions obtained for ensembles of atoms with a constant velocity and at a constant detuning. This method is described in a little more detail in Sec. 6.1.7 and in full detail in [102]. In this section, the focus is put on the LSM parameters, in particular on those which describe the velocity distribution.

An overall amplitude parameter, A, scales the theoretical line shape to fit the experimental signal height. The second parameter, Δdet, corresponds to the second-order Doppler corrected line center shift with respect to a fixed frequency which is determined with the frequency comb (see Fig 5.1). Four parameters, T, v_{s}, v_{exp} and K_{nL}, are used to model the velocity distribution as described in more detail in Sec. 6.1.2. The $2S$ signal contributions for constant velocity are weighted with this velocity distribution to obtain the theoretical line shape corresponding to a thermal ensemble in the atomic beam. Finally, a normalized Lorentzian, with a width parameter $\mathrm{FWHM}_{\mathrm{Lor}}$ is convoluted with the this line shape in order to account for broadening effects.

These parameters are obviously not the only parameters determining the line shape, as it also depends on the geometry of the interaction region, as presented in detail in chapter 5. However, the geometric parameters are taken into account, via the modeling of trajectories, during the numerical integration of the master equations (2.11), and the seven parameters mentioned above represent the free parameters which are not included into the integration of the quantum dynamics. The nonlinear fitting of the seven-parameter model to the data is a time consuming process and it is therefore desirable to reduce the number of free parameters by improving the physical model, which would result in a faster fit. Since only a certain probability to represent the true values can be assigned to a given set of fitted parameter values, any such estimate of parameters is in general ambiguous, and the true values might be located closer to a different local minimum of the figure of merit of the fit. The reduction of the number of free parameters would therefore also improve the stability of the fitting procedure.

Currently the LSM does not include the ionization channel γ_{i} in the integration of the master equations (2.11). This might have been motivated by the observation that ionization does not change the excitation line shape of a single-atom contribution. However, in view of the results of chapter 5, where a significant ionization broadening was identified as an effect on the collective signal, one could argue that the $\mathrm{FWHM}_{\mathrm{Lor}}$ parameter could be removed, or at least its importance be reduced, by including the ionization broadening into the LSM. This would probably leave only the laser line width to be accounted for by this free parameter. As will be argued in Sec. 6.1.2, the phenomenological parameters v_{s} and v_{exp} might also be dispensable by inclusion of the ionization damping, because the modification to the velocity distribution which is described by those parameters can also be partly explained by ionization losses.

The most striking feature of the data analysis is the scatter of LSM fit results Δdet around the expected linear power dependence, as depicted in Fig. 6.2 (left). Since the seven-parameter regression is a quite involved process, the MPQ group decided to have the LSM checked by an independent group. For this purpose of direct examination of the program, *FitAll* was ported to a *Linux* environment by the present author. After a thorough examination of the source code, the sensitivity to initial conditions, and many detailed cross-checks, it could be concluded that Δdet is an exceptionally stable fit parameter, especially when the fit takes into account only delays $\tau \geq 1210\,\mu$s. From this analysis, the LSM could rather confidently be ruled out as the major source of the scatter. A stronger and quantitative argument is provided by the comparison of the LSM with an own independent data analysis, described in Sec. 6.1.3.

In the course of the investigation, a number of different models for the velocity distribution were tried out and one interesting result is given in the next section. Also, the LSM was extended with a scripting mode, such that the data analysis can now be run without manual input.

6.1.2 Models for the velocity distribution

In the MPQ experimental setup, the excitation of atomic hydrogen takes place in a cold beam which is aligned parallel to the standing wave laser field. For a brief description of the experimental setup, see chapter 5, and Figs. 5.1 and 5.2. In Sec. 5.5, the implications of different perturbations on the trajectories are discussed. In this section, the aspect of the atomic velocity distribution, i.e., the distribution of the absolute value of the velocities $f(|\boldsymbol{v}|) = f(v)$, will be addressed, as it enters the data analysis by means of the MPQ line shape model.

For an ideal gas in thermal equilibrium, the velocity distribution is a Maxwell-Boltzmann distribution, which is uniquely defined by one parameter, the temperature T. For an effusive beam flowing from a thermalized volume through a diaphragm into a small solid angle, the normalized Maxwell-Boltzmann distribution of atoms, passing the diaphragm in a given time interval, reads [98]

$$f_{\mathrm{M}}(v) = \frac{2}{v_0}\left(\frac{v}{v_0}\right)^3 \exp[(v/v_0)^2]\,, \qquad v_0 = \sqrt{\frac{2k_BT}{m}}\,. \tag{6.2}$$

Note that this expression for the velocity distribution of the one-dimensional flow differs from the velocity distribution in a stationary gas cell, where $f(v) \propto v^2$ for small velocities. Individual atoms in the effused dilute beam are assumed to no longer interact. This is also implied in the Monte Carlo simulations, where only straight trajectories are taken into account. It has been observed by the MPQ group [102] that a better agreement of the LSM and the experimental spectra is achieved, if the velocity distribution $f(v)$ is suppressed for low velocities by means of the model

$$f_{\mathrm{s}}(v) = \begin{cases} f_{\mathrm{M}}(v)\left(\dfrac{v}{v_{\mathrm{s}}}\right)^{v_{\mathrm{exp}}-3} & v < v_{\mathrm{s}}\,, \\ f_{\mathrm{M}}(v) & v \geq v_{\mathrm{s}}\,. \end{cases} \tag{6.3}$$

For velocities below the suppression threshold v_{s}, the v^3-dependence is replaced by a $v^{v_{\mathrm{exp}}}$ dependence. In addition to the temperature, this model introduces two free parameters v_{s} and v_{exp} into the LSM. In order to give a physical interpretation to this phenomenological approach, the new loss model

$$f_{\mathrm{l}}(v) = f_{\mathrm{M}}(v)\,\exp[-a(v/v0)^{-b}]\,, \tag{6.4}$$

was introduced into the LSM. It avoids the unphysical threshold velocity and the associated discontinuity in the first derivative of the velocity distribution. The exponential damping for small velocities is motivated by the fact that atoms which are ionized during the interaction do not contribute to the signal. The lower an atom's velocity, the longer

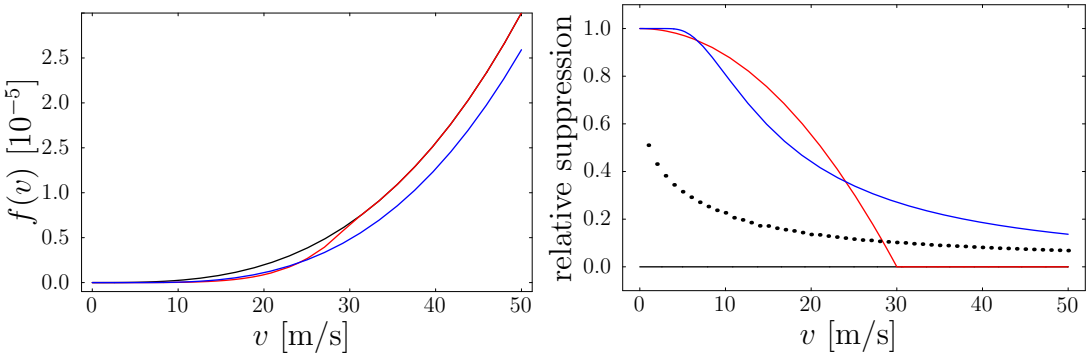

Figure 6.3: Comparison of the low-velocity tails of different velocity distributions $f(v)$ in a beam of atomic hydrogen, corresponding to a temperature of 5 K. The Maxwellian velocity distribution of an effusive beam (6.2) is plotted as a black solid line, the v_s-model (6.3) with $v_s = 30\,\mathrm{m/s}$ and $v_{exp} = 5$ is plotted in red. The loss model (6.4), with parameters $a = 0.01$ and $b = 1.5$, is shown in blue. Left: direct comparison of the velocity distributions. Right: suppression of atoms with low velocities relative to a Maxwellian distribution. The relative loss of atoms from an initial Maxwellian distribution due to ionization, obtained from a Monte Carlo simulation, is denoted by the black dots. The Monte Carlo results can be represented in terms of the loss model with parameters $a = 0.02$ and $b = 0.75$.

is the mean interaction time and the higher is the probability of being ionized. The loss model also introduces two parameters and shows comparable success in fitting the observed lines. However, the parameter a turns out not to be a very stable fit parameter and displays a large fitting uncertainty. In Fig. 6.3, the three models are compared for typical parameters, with the focus on the relevant low-velocity regime. On the left hand side, the different modifications to the Maxwellian velocity distribution by the v_s-model and the loss model are displayed. Since the modification is in general a very small effect, the suppression of atoms relative to the Maxwellian distribution is depicted on the right hand side of the figure.

The comparison shows, that both the v_s-model and the loss model effectively suppress the slow atoms, but in a quite different fashion. The loss model also removes atoms above the threshold velocity v_s, approaching zero suppression for large velocities. The fact that the loss model is quite successful in the fitting of the experimental spectra is a hint that ionization losses might actually be responsible for the suspected suppression of slow atoms. To support this argument, a Monte Carlo simulation of the excitation process at very small velocities was performed and the ionization loss to the initial Maxwellian velocity distribution was was evaluated. The result is plotted in Fig. 6.3 (right). The magnitude of the ionization loss is not on the same level as represented by the v_s-model and the loss model, indicating that there are additional processes removing of slow atoms in the beam, e.g., collisions with the background gas or intra-beam collisions, scattering out very slow atoms.

It should be mentioned that the LSM takes into account an additional modification of

the velocity distribution, the Zacharias effect [98, 102]. This effect is caused by the finite length of the nozzle and is parameterized by the Knudsen number $K_{nL} = \bar{\lambda}/L_{\text{nozzle}}$, which is the ratio of the mean free path of atoms in the nozzle and the nozzle length. This effect shifts the distribution in the whole range of velocities. For a discussion of the relative suppression of the very slow atoms, this effect is therefore negligible.

6.1.3 Full line shape model and Lorentz data analysis

The analysis of the absolute frequency measurement by means of the line shape model discussed above, is an involved nonlinear fitting procedure in a seven parameter space, which is computationally demanding. On a 2.4 GHz Opteron machine, the automated evaluation of one day of measurement as implemented by the present author takes about 10 hours. A faster data analysis routine would therefore be desirable for online evaluation or neartime evaluation in the lab on the same day. Ultimately, for a feedback loop stabilizing an all-optical clock, a sub-second analysis of the line shape would be desirable.

However, any model which is simpler than the full line shape model must also prove that it does not sacrifice precision for speed. In this section, a fast data analysis method is presented, which relies on fitting a Lorentz line shape to the raw data. As is to be expected, this method only works for spectra with long delay τ, where the data display a symmetric line shape. For these data, the systematic Doppler shift is small, but still has to be accounted for.

In addition, the Lorentz approach provides a LSM-independent evaluation of the hydrogen $1S$–$2S$ absolute frequency, taking into account all recorded data corresponding to a specific delay, and as such constitutes an independent verification of the LSM. It should be stressed that it has become possible to reliably fit selected single delays from the whole data set, because of a number of experimental improvements achieved by the MPQ group as compared to the 1999 setup. A substantially higher stability of the primary laser beam, improvements of the vacuum, enlargement of the detection solid angle, a hydrogen chopper and an improved shielding of the interaction region, contributed to an excellent signal-to-noise ratio and high count rates even for the longest delays. The counts in the time bins with long delays originate from an atomic ensemble from a narrow, low-velocity interval of the velocity distribution of the atomic beam, and therefore are not very sensitive to the overall distortions of the velocity distribution. Therefore, the high-τ spectra resemble very closely a Lorentzian lineshape of an atom at rest.

The Lorentz data analysis has been performed as follows. The MPQ raw data files (e.g., `10_02_02.dat`) which contain the count rates of the time-resolved spectra as a function of AOM frequency, have been automatically split into 12 separate files, each containing one spectrum of delay $\tau = (10, 210, \ldots, 2210)\,\mu$s. In order to ensure the comparability with the LSM, the manual line cuttings as recorded in the respective `inf` files have also been applied. This line cutting removes extensive stretches of zero count rate far off resonance, as a function of τ.

For a specific delay, the generated set of files corresponding to each day of measurement were loaded into a *Mathematica* notebook in which a Lorentzian (5.4) was fitted to the

line and the resulting line centers and line widths were recorded as a function of excitation power. The excitation power was obtained from the UVN-2 voltage value at the photodiode detector as recorded in the `dat` files, and converted by means of the power-voltage calibration curves provided by the MPQ group.

An exemplary set of results obtained from the Lorentz analysis is presented in Fig. 5.3 (left) for spectra with delay $\tau = 1210$. At this stage, the only difference to corresponding LSM results is that the second-order Doppler shift still has to be accounted for. Note that in the analysis of the power shift coefficient k_{shift}, a constant frequency offset was irrelevant. As has already been discussed above [see e.g. Eq. (2.13)], in order to obtain the true resonance frequency of an atom at rest, the second-order Doppler shift of

$$\delta\nu(v) = \nu_{\text{L}} \left(\frac{v}{c}\right)^2 \tag{6.5}$$

has to be added to the measured resonance frequency, because the frequency in the moving atom frame is blue shifted with respect to the laboratory laser frequency. Here, ν_{L} is the laser frequency in Hz and v denotes the speed of the atom. In the model-independent Lorentz analysis, the Doppler shift correction is calculated starting from a Maxwellian velocity distribution (6.2) for the atomic beam. The frequency correction of the Lorentzian fits of a given delay τ is calculated as the mean second-order Doppler shift $\langle\delta\nu\rangle$ in an effective atom velocity distribution $f_\tau(v)$:

$$\langle\delta\nu\rangle = \frac{\int_0^{v_{\max}} dv\, f_\tau(v)\, \delta\nu(v)}{\int_0^{v_{\max}} dv\, f_\tau(v)}\,, \tag{6.6}$$

where $v_{\max}$ is the maximal velocity of excited atoms reaching the detector, and is given by the length of the interaction region divided by the respective delay time τ. The effective velocity distribution

$$f_\tau(v) = f_{\text{M}}(v) \left(1 - \frac{v}{v_{\max}}\right) \tag{6.7}$$

takes into account the fact that the Maxwellian velocity distribution $f_{\text{M}}(v)$ of atoms in the beam and the velocity distribution of atoms contributing to the signal $f_\tau(v)$ are different. Atoms from the original velocity distribution, although being excited to the $2S$ state, can pass the detector during the time τ after the beginning of the dark phase. Because at the start of the dark phase, all atoms with a specific velocity are evenly distributed along the longitudinal coordinate in the interaction zone, the higher the velocity of a class of atoms, the larger is the fraction of atoms which pass the detector unnoticed. This can be illustrated best by considering the class of atoms with $v = v_{\max}$. By the time the detector starts binning the counts for the considered delay τ, all these atoms have passed the detector and do not contribute to the signal, and consequently, $f_\tau(v_{\max}) = 0$. The following table lists the mean frequency shift $\langle\delta\nu\rangle$ as a function of delay for a 5 K atomic beam of the MPQ setup.

τ	610μs	810μ	1010μs	1210μs	1410μs	1610μs	1810μs	2010μs	2210μs
$\langle\delta\nu\rangle$	211 Hz	122 Hz	79 Hz	55 Hz	41 Hz	31 Hz	25 Hz	20 Hz	17 Hz

If one approximates the velocity distribution in the relevant low-velocity regime to be of the form $f(v) = a\, v^b$, one obtains

$$\langle\delta\nu\rangle = \frac{(1+b)(2+b)}{(3+b)(4+b)}\,\delta\nu(v_{\max})\,, \tag{6.8}$$

which can be used as an approximation on the 1 Hz level for delays of about $\tau = 1210\,\mu$s and longer.

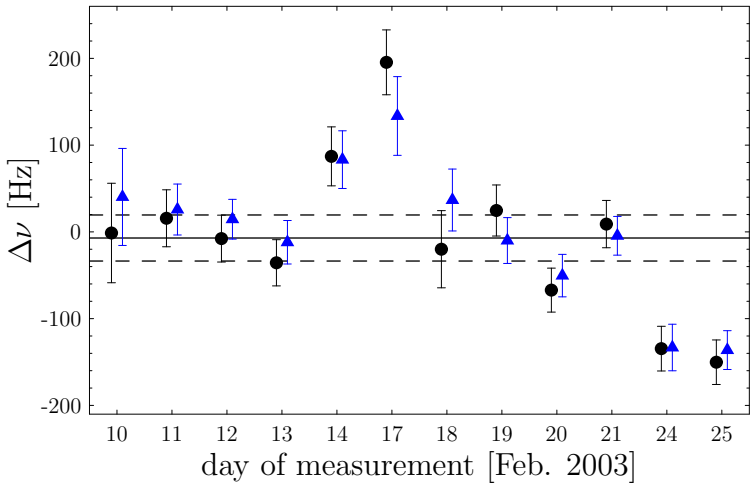

Figure 6.4: Comparison of $1S$–$2S$ absolute frequency results obtained from the LSM analysis (black circles) and the independent Lorentz analysis (blue triangles) as a function of day of measurement. The LSM fit was performed using the basic MPQ model $(T, v_s, v_{exp}, K_{nL})$ for the velocity distribution, including the delays $\tau = 1210, 1410, \ldots, 2210\,\mu$s. An unweighted mean and the standard error of the mean are indicated by solid and dashed lines, respectively. The Lorentz analysis is shown for the delay $\tau = 1210\,\mu$s, corrected for the second-order Doppler shift according to Eq. (6.6) with a Maxwellian velocity distribution corresponding to a temperature of 5 K. The error bars indicate the standard error of the linear extrapolation to zero excitation power. The frequency detuning $\Delta\nu$ denotes the $1S$–$2S$ absolute frequency relative to the 1999 result [6]. In the fitting of the spectra, in both the LSM and the Lorentz analysis, a $\sigma(n)$-weighting was performed (see Eq. 6.17) below, while the zero-power extrapolation and the averaging of the day results was performed without weighting (see Sec. 6.1.4). The systematic trend that, e.g., the day value of Feb 17$^{\text{th}}$ is far above average, and the day values of Feb 24$^{\text{th}}$ and 25$^{\text{th}}$ are below the average, is equally observable in the Lorentzian analysis of the delays other than 1210μs, as well as the LSM analysis with different models for the velocity distribution.

The Doppler corrected values of the line centers were then extrapolated to zero excitation power, as shown in Fig. 5.3 (left), with a linear model. The final results for the 1210 μs Lorentz analysis of all days of measurement are shown in Fig. 6.4, together with a LSM analysis using the MPQ model for the velocity distribution. For comparability, the LSM analysis was performed taking into account only the delays $\tau = 1210\,\mu$s and longer, for which the Lorentz analysis is self-consistent (see Fig. 6.5).

From this comparison, some important conclusions can be drawn. First of all, the results of the two independent data analysis methods are in mutual agreement. This is a strong indication that both methods do not contain substantial errors in evaluating the raw data. Second, the deviations from the mean value of each day of measurement show the same trend in both evaluations, e.g., the final result of February 17$^{\text{th}}$ is significantly higher than the final result of February 24$^{\text{th}}$. This suggests that the scatter of the values around the mean is not caused by a statistical uncertainty but that rather a systematic effect is responsible for the observed scatter. Some possible candidates for this systematic effect have already been encountered in chapter 5, and more are discussed below. As the standard errors of both the LSM results and the Lorentz results are of comparable magnitude, statistics is obviously not a limiting factor for the Lorentzian analysis, although it is based only on a single delay of the 12-delay data set. This is a direct benefit of experimental improvements and therefore should be put to use at least for a preliminary evaluation during future measurements. Finally, the observed agreement is also an indication that the simplified second-order Doppler correction (6.6) works well for the spectra with long delays.

In Fig. 6.5, the final day averaged results of the Lorentz analysis are shown as a function of delay under consideration. The 1210 μs value corresponds to the unweighted mean of the Lorentz results shown in Fig. 6.4. For the delays 1210 μs and longer, the Lorentz analysis yields self-consistent results, while for shorter delays, this is no longer the case. As is to be expected, the Lorentzian approximation to the line shape gets worse for shorter time delays, where the recorded spectra show significant asymmetries.

6.1.4 Weighting and χ^2_{r} in the data regression

One special aspect of the data analysis will now be considered closer, namely the weighting of individual data points at the different stages of fitting: (i) LSM fit to the time-resolved spectra (Fig. 6.1), (ii) linear fit to the ν_c-power plot (Fig. 6.2, left) and (iii) averaging of the day values (Fig. 6.2, right). In the MPQ data analysis, weighting is not used in any of these steps. It will be argued that weighting makes sense for the analysis of the raw data in the LSM and the Lorentz analysis for delays $\tau \geq 1210\,\mu$s, but that it is justified not to weight the individual data points for the fits at stages (ii) and (iii). In the Lorentz analysis in Sec. 6.1.3, the proposed weighting procedure has been applied.

Performing a fit of a model to data points amounts to minimizing a figure of merit, which normally is the sum of squared deviations of the model from the data points, where in a weighted fit, each deviation in the sum is multiplied by a weighting factor. The results of such a fit have to be interpreted in probabilistic terms. How probable is it to find

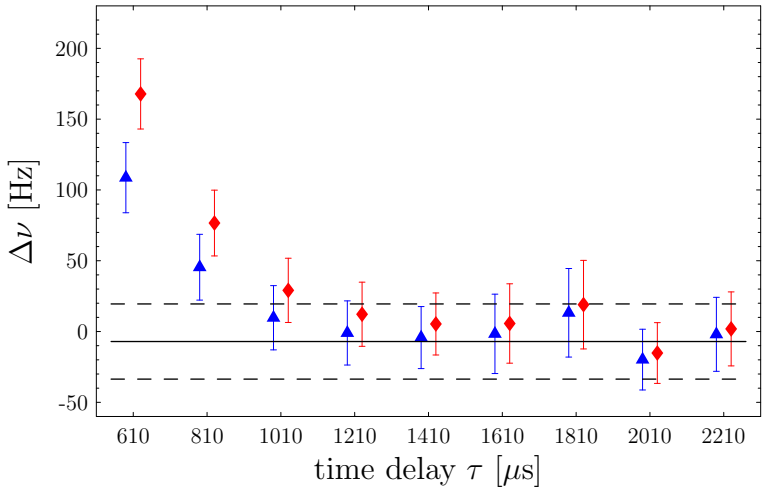

Figure 6.5: Comparison of the day-averaged result obtained with the lineshape model (solid line; dashed lines indicate 1σ uncertainty) with independent day-averaged results from a Lorentz analysis of spectra with a specific delay τ (symbols). The dynamic Stark shift is taken into account in both cases by a linear extrapolation to zero excitation power. In the Lorentz analysis, the second-order Doppler effect is corrected for by Eq. (6.6), with a 5 K Maxwellian velocity distribution (blue triangles) and with a v^5-distribution (red diamonds). The Lorentzian analysis agrees well with the line shape model result for long delays, but is limited by line shape asymmetries at delays $\tau \lesssim 1210\mu$s.

the true values in a given interval about the parameters resulting from the fit? Is the model appropriate? These questions can be answered by considering the reduced χ^2_{r} of a fit, which provides valuable additional information. To recall the reduced chi-square χ^2_{r}-distribution (see, e.g., [103]), consider the random variable

$$S = \frac{1}{n}\sum_{i=1}^{n} X_i^2 \,, \tag{6.9}$$

as a function of mutually independent random variables X_i that are assumed to be standard normally distributed, i.e., with zero mean and a standard deviation of unity. The corresponding Gaussian probability densities of the X_i will be denoted by $\rho_{X_i}(x_i)$. Then the probability density for the realization $\{x_1, \ldots, x_n\}$ of the $\{X_1, \ldots, X_n\}$ is the product

$$\rho_{X_1,\ldots,X_n}(x_1, \ldots, x_n) = \prod_{i=1}^{n} \rho_{X_i}(x_i) \,, \tag{6.10}$$

and the probability density for S is [103]

$$\rho_S(s) = \int dx_1 \ldots dx_n \; \delta(s - x_1^2/n \ldots - x_n^2/n) \; \rho_{X_1,\ldots,X_n}(x_1, \ldots, x_n) \,. \tag{6.11}$$

Inserting a standard normal distribution for the ρ_{X_i}, one obtains:

$$\rho_S(s) = \int dx_1 \ldots dx_n \, \delta(s - x_1^2/n \ldots - x_n^2/n) \, (2\pi)^{-\frac{n}{2}} e^{-\frac{1}{2}(x_1^2+\ldots+x_n^2)} \tag{6.12a}$$

$$= n\frac{(ns)^{\frac{n}{2}-1} \, e^{-\frac{ns}{2}}}{2^{\frac{n}{2}} \, \Gamma\left(\frac{n}{2}\right)} =: \rho_{\chi^2_{\rm r}}(s) \, . \tag{6.12b}$$

This probability density is called the $\chi^2_{\rm r}$-distribution with n degrees of freedom. Its expectation value and variance are

$$\langle \chi^2_{\rm r} \rangle = \int_0^\infty ds \, s \, \rho_{\chi^2_{\rm r}}(s) = 1 \, , \qquad {\rm var}(\chi^2_{\rm r}) = \int_0^\infty ds \, (s - \langle \chi^2_{\rm r} \rangle)^2 \, \rho_{\chi^2_{\rm r}}(s) = \frac{2}{n} \, . \tag{6.13}$$

This means that for a random realization $\{x_1, \ldots, x_n\}$, the value of $s = (x_1^2 + \cdots + x_n^2)/n$ falls into the interval $\mathcal{I}$=[1-$\sqrt{2/n}$, 1+$\sqrt{2/n}$] with a certain probability, given by the integral of (6.12b) over $\mathcal{I}$, which tends to 68.3 % for large n. The important point this implies is that if the sum of squares s is far outside of the interval $\mathcal{I}$, the corresponding x_i represent an extremely unlikely realization from a statistical point of view. To apply this formalism to the data analysis, consider the case where

$$X_i = \left(\frac{f(i) - Y_i}{\sigma_i} \right) \, , \tag{6.14}$$

where $f(i)$ is a physical model that gives a prediction for the $i^{\rm th}$ data point Y_i. The statistical uncertainty of the data point, which is assumed to obey Gaussian statistics for a repeated measurement, is denoted by σ_i. If, and only if, (i) the physical model is appropriate, giving the correct mean of the Y_i and (ii) the uncertainty of the data is only given by the statistical uncertainty σ_i and is not in fact larger, then the X_i are standard normally distributed. For a given realization $\{y_1, \ldots, y_n\}$ of the Y_i in Eq. (6.14), and a best-fit physical model with m parameters, the reduced $\chi^2_{\rm r}$ is given by

$$\chi^2_{\rm r} = \frac{1}{dof} \sum_{i=1}^{n} x_i^2 \, , \tag{6.15}$$

and is a measure of the mean squared deviation of the model in terms of the individual standard uncertainty of each data point. Here, $dof = n$–m denotes the adjusted number of degrees of freedom. For the resulting value of $\chi^2_{\rm r}$, the confidence level of the fit is defined as the integral over "worse" realizations

$${\rm CL}(\chi^2_{\rm r}) = \int_{\chi^2_{\rm r}}^\infty ds \, \rho_{\chi^2_{\rm r}}(s) \, . \tag{6.16}$$

This is the basis for the so-called chi-square test for the goodness of a fit. A low confidence level, corresponding to a value of $\chi^2_{\rm r}$ far above $\mathcal{I}$, indicates either an extremely unlikely set of data or the violation of assumptions (i) or (ii). If the experiment is repeated and

the fit results in the same low confidence level, one therefore can conclude that either the physical model is not appropriate or that the uncertainties of the data have been underestimated.

In the first fitting stage of the MPQ data, the LSM fit to the time resolved spectra, an experimentally determined σ_i is used. By varying the excitation power and keeping all other parameters fixed, the MPQ group has experimentally characterized the count rate statistics in the $1S$–$2S$ excitation process. For a mean count rate n, the standard deviation is best described by the non-Poissonian model

$$\sigma(n) = \sqrt{n} + 0.025\, n\,. \tag{6.17}$$

The Poissonian $\sqrt{n}$-behavior for a statistical count rate is dominated by a linear noise term for larger count rates, suggesting an explanation in terms of laser power fluctuations. Using this uncertainty for each data point, the χ^2_{r}-test of the LSM fits taking into account all delays $\tau \geq 1210\,\mu$s yields satisfactory confidence levels.

At the second stage, which is the linear fit to the excitation-power dependence (see Fig. 6.2, left), one obtains $\chi^2_r = 6.5$ with $\mathcal{I} =$[0.8, 1.2] and consequently a confidence level of close to zero for the data of Feb. 13^{th} shown in the figure, and similar values for the other days of measurement. At this stage, there is not much doubt about the linear model, even though it has been observed in the Monte Carlo simulations in Sec. 5.4.3, that a small nonlinearity exists for high excitation powers. One must therefore conclude that the true uncertainty of the data is not purely statistical, and unaccounted systematic effects exist. The recording of a single spectrum is completed in less than one minute. Since the χ^2_{r}-test is successful for the LSM fits, but fails for the linear extrapolation, this hints at the presence of systematic effects that shift the line centers on a rather slow time scale. The systematic effects of the nozzle freezing, and an unsteady excitation power calibration as presented in the sections below, are two examples of such possible effects.

As the χ^2_{r}-test yields no acceptable confidence level on the basis of the purely statistical uncertainties of the data, it is also not advisable to choose the χ^2_{r} as the figure of merit to be minimized in the fit. An unweighted fit, ignoring the individual uncertainties is therefore appropriate at stage (ii). Consequently, as the chain of purely statistical uncertainties is broken, at stage (iii) the averaging of the day results should also be performed by an unweighted fit. Of course, this procedure will have to be reconsidered in future experiments.

6.1.5 Effect of unsteady power calibration

As was experimentally observed by the MPQ group, the maximum laser power which can be reached in the enhancement resonator, as indicated by the photodiode (see Fig. 5.1), is slowly dropping in time during the measurement of several spectra. After a break, the maximum photodiode readout is restored. One possible explanation suggests that it is not the actual excitation power that drops, but that the transmittivity of the out-coupling mirror changes, as a result of a deposition of molecular hydrogen on the mirror surface. The deposited hydrogen molecules could scatter a fraction of the incident light,

reducing the transmittivity. In the following, the consequences of the transmittivity-effect are investigated, and a method to check and correct for this effect is proposed.

If the transmittivity of the out-coupling mirror changes in time, this implies that the measured voltage underestimates the true excitation power, with the discrepancy increasing in time. As a result, the power calibration would not be valid for all recorded spectra. The fact that the observed line shift coefficients k_{shift} [see Fig 5.5 (right)] exhibit significant scatter, could be a consequence of this systematic. In Fig. 6.6, the scenario of unsteady transmittivity is illustrated with exaggerated magnitude. The dots represent the line centers of $1S$–$2S$ spectra, recorded with a random excitation power in a fixed range. This simulates the scenario that the real excitation power does not suffer from a decay in maximum magnitude. However, the photodiode voltage assigned to each dot is assumed to result from one out of three different mirror transmittivities, resulting in three distinct clouds of simulated data points.

An extrapolation of the line center shifts ν_{c} to zero photodiode voltage, indicated by the solid lines, leads to mutually consistent results, if only the data points corresponding to a constant transmittivity are taken into account. However, if all data are included, a systematically higher value for the extrapolated result is obtained. This shows that the knowledge of the absolute value of the transmittivity is not crucial for the extrapolation, but that an unsteady mirror transmittivity results in a systematic upwards shift of the result of one day of measurement.

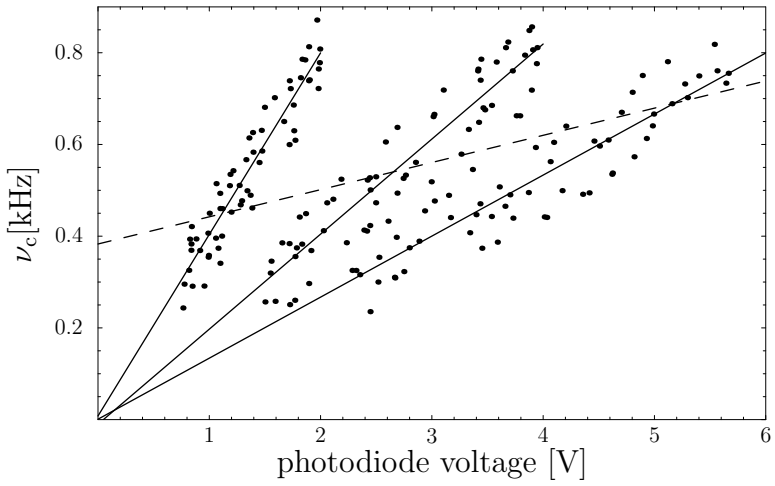

Figure 6.6: Exaggerated illustration of the effect of a possible unsteady transmittivity of the out-coupling cavity mirror. The shifts of the line centers, ν_{c}, are distributed in a fixed range, corresponding to a constant range of true excitation powers. The corresponding voltage values are distributed in three differently scaled ranges, representing three different mirror transmittivities. Linear zero-voltage extrapolations of the simulated data points belonging to a specific transmittivity are shown as solid lines, a linear extrapolation of all simulated data is indicated by the dashed line. A varying transmittivity results in an upward shift of the extrapolation to zero voltage.

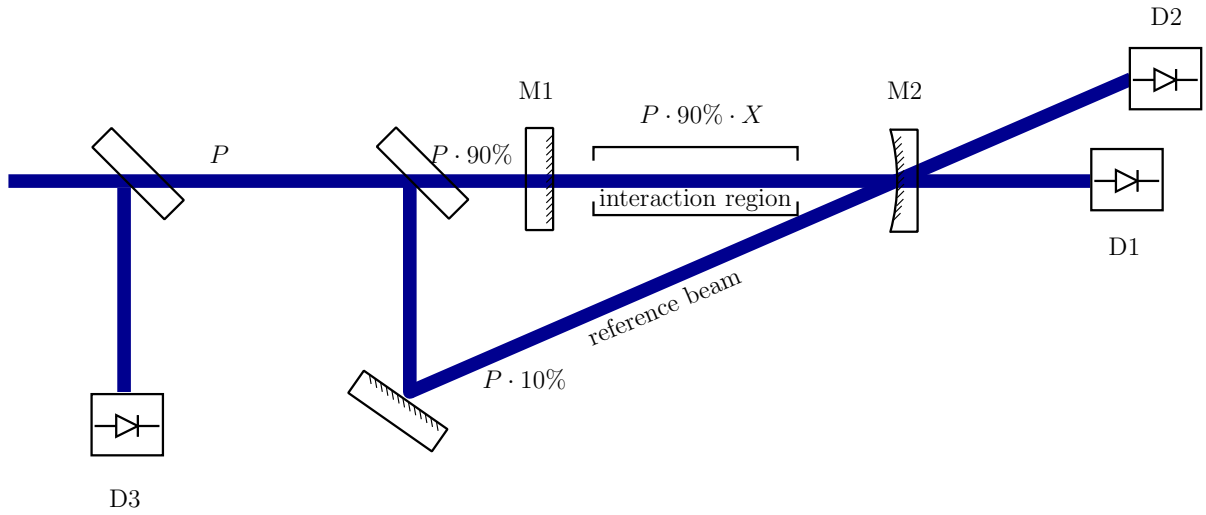

Figure 6.7: Proposal for an improved cavity power measurement scheme. A reference beam is used to probe the transmittivity T of the out-coupling mirror M2. Detector D1 measures the power $P_1 = P \cdot 90\% \cdot X \cdot T$, detector D2 is exposed to the power $P_2 = P \cdot 10\% \cdot T$, and D3 detects the power P_3 in front of the first beam splitter. From the three signals, the power enhancement X and the transmittivity T can be obtained, without inserting an optical element into the interaction zone. The 9:1 power splitting ratio is chosen arbitrarily to illustrate the principle.

Assuming that deposited hydrogen molecules scatter part of the incident light, not only the transmittivity T of the out-coupling mirror is affected, but also the power enhancement X itself is influenced, because the incoherently scattering hydrogen removes power from the resonator mode. To account for these two separate effects, an extension to the power measurement setup is proposed as depicted in Fig. 6.7. It has the advantage of providing both a quantitative measure for the transmittivity and for the actual power stored in the resonator. In addition, this is achieved without inserting any device inside the interaction zone.

From the primary beam coupled into the cavity, a small part is diverted by means of a beam splitter, before it reaches the in-coupling mirror. This reference beam is then directed through the out-coupling mirror at some angle with respect to the cavity axis, bypassing the interaction region and passing through the out-coupling mirror at the same spot, where the axis of the cavity mode is situated. In this way, the reference beam is attenuated by the same amount as the light power per direction in the cavity, before reaching the respective detectors. By dividing the power P_1 measured by detector D1, by the power P_2 of the detector D2 monitoring the transmitted reference beam, the power enhancement factor X can be obtained. By means of an additional power measurement on the primary beam with detector D3, the absolute excitation power in the cavity can be monitored, as well as the transmittivity.

There are however some experimental challenges with this approach, which need to be

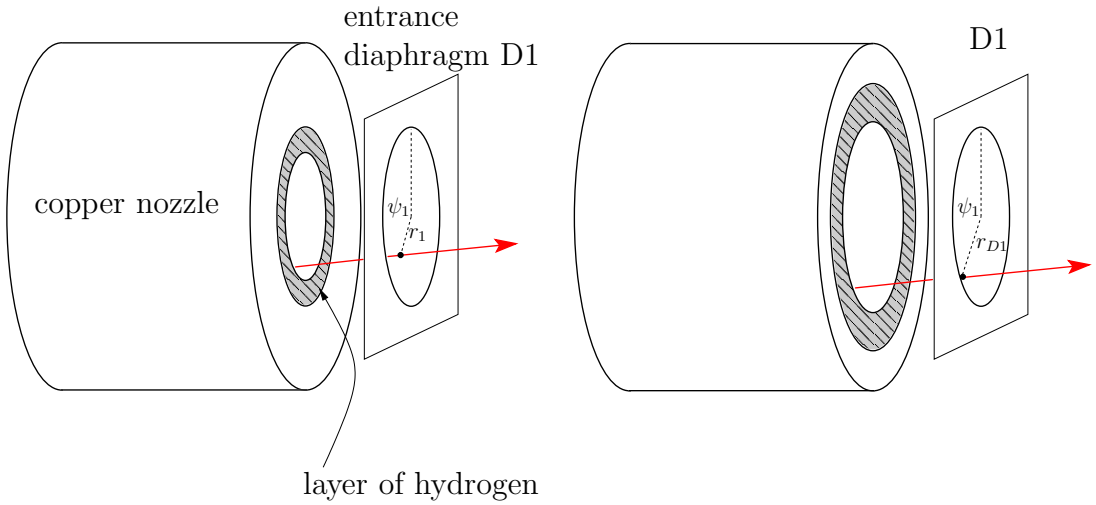

Figure 6.8: Proposal for a nozzle with a radius larger than the radius of the entrance diaphragm D1. Only atoms passing the entrance diaphragm D1 can contribute to the signal. The adhering layer of molecular hydrogen restricts the atomic trajectories in the present setup (left), whereas in a larger nozzle there would be room for some unavoidable hydrogen frost, without changing the conditions at the entrance D1 to the interaction region (right).

mentioned. First, the calibration of the power detectors must be much more stable than the suspected unsteady transmittivity. In addition, the use of three detectors instead of one renders this aspect even more important, especially because the quotient of a strong and a weak signal is involved. Second, to align the invisible reference beam to the right spot on the out-coupling mirror might prove to be difficult. Finally, the absorption of the additional beam splitters and mirrors introduced need to be taken into account, at least if the goal of an absolute power measurement is aimed for in future experiments.

6.1.6 Freezing nozzle

As has been investigated in detail in Sec. 5.5, an uncontrolled congestion of the hydrogen nozzle can have an effect on the line center of the collective 2S spectrum via the dynamic Stark shift. The film of hydrogen adhering to the nozzle can restrict the trajectories, which contribute to the signal, closer to the center of the Gaussian laser mode at the entrance to the interaction region. As a consequence, the atoms are on average subject to a larger dynamic Stark shift, suffering a systematic shift upwards in frequency.

Since the hydrogen layer thickness is difficult to quantify, a solution to this problem which could tolerate a moderate amount of hydrogen frost is proposed in Fig. 6.8. The use of a nozzle that is somewhat larger than the entrance diaphragm, as depicted, would present an inexpensive way to reduce the possible systematic effects from the nozzle freezing. In this setup, the growth of a layer of hydrogen frost, which is probably unavoidable, would not influence the trajectories of the atoms contributing to the signal, as long as the layer thickness does not reach the difference of nozzle radius and radius of the diaphragm.

6.1.7 Power-dependent line shape model

The original LSM relies on the numerical integration of the master equations (2.11) without the ionization terms involving γ_i and for a fixed intensity of 450 mW per direction. As the actual excitation power in the setup varies from about 60 mW to 660 mW, the LSM accounts for this discrepancy by scaling the overall amplitude A of the theoretical model fitted to the data. If the proposed excitation power measurement scheme in Fig 6.7 is implemented, or the absolute excitation power is determined with a different method, the numerical integration of (2.11) can be performed including the corresponding intensity distribution, and a set of improvements can be integrated into the LSM program, as proposed in the following.

As already mentioned above, the MPQ line shape model involves a phenomenological width parameter. A normalized Lorentzian function with full width at half maximum $\mathrm{FWHM}_\mathrm{Lor}$ is convoluted with the result of the numerical quantum dynamics calculation in order to account for the total width observed in the experiment. This parameter is needed because there are at least two broadening effects, which are not included in the LSM: (i) the laser line width of the driving laser and (ii) ionization broadening of the excited $2S$ state.

The ionization broadening of the collective signal can be described using the EOM (2.11) by including the excited state ionization rate $\gamma_\mathrm{i} = (2\pi\beta_\mathrm{ioni})\, I(t)$. In Sec. 5.4, it was demonstrated that this description agrees very well for the Lorentz analysis of the experimental spectra. This result suggests that the excited state ionization γ_i should also be included into the LSM, which would increase the accuracy of the LSM and would probably reduce the parameter $\mathrm{FWHM}_\mathrm{Lor}$ to $\mathrm{FWHM}_\mathrm{Laser}$.

In addition, the quantitative treatment of the excited state ionization in the framework of the LSM would implicitly generate a suppression of slow atoms in the velocity distribution contributing to the collective signal. As has been pointed out in Sec. 6.1.2, in the current LSM this suppression is modeled by the phenomenological parameters v_s and v_exp. It would be a significant simplification of the nonlinear fitting process, if these two parameters could be abandoned due to the inclusion of the ionization channel.

The main reason why the LSM is based on the master equations (2.11) for a single excitation power is that the computation of the required v-$\Delta\nu$-matrices takes a significant amount of time. In these matrices, the signal contribution for a class of atoms with fixed velocity v and laser detuning $\Delta\nu$ is stored, as it is obtained from a numerical integration of (2.11) with $\gamma_\mathrm{i} = \gamma_\mathrm{s} = 0$. During the integration, a large number of trajectories is taken into account for atoms with 95 velocities in the range $[3 \ldots 3400]$ m/s and at 40 detunings spanning ± 50 kHz. The LSM fitting program *FitAll* then constructs the collective theoretical line shape from these matrix contributions, weighted with the respective velocity distribution and shifted by $\Delta\,\mathrm{det}$ in order to find the optimal values for the fit parameters. This method avoids integrating the master equations for every iteration in the fitting procedure and should of course be maintained. However, the increase in computation power has reduced the time needed to generate a set of matrices (one for each delay τ) to about 20 hours on a single processor of the MPI-K computer cluster in 2006

as compared to M. Fischer's evaluation in 2003, which needed about one week [23], and A. Huber's original runs in 1997, which took several weeks [102].

A power-dependent LSM could therefore be implemented in the existing framework as follows. A set of matrices for different excitation powers could be generated, e.g., for a set of excitation powers $\{50{,}100, \ldots, 700\}$ mW per direction, in parallel on several nodes of the cluster. The recorded experimental spectra could then be sorted into the corresponding excitation power bin and the LSM analysis would be performed with the v-$\Delta\nu$-matrices which were generated for the excitation power closest to the measured power. In this approach, the generation of the power-dependent matrices would take 280 processor hours instead of 20, but only once, while time needed by the LSM fitting procedure for each spectrum would not increase.

6.2 Test of the drift of fundamental constants[1]

6.2.1 Introduction

When P. A. M. Dirac first proposed his large number hypothesis in 1937 [104], it was motivated by the observation that the ratio of the gravitational force and the electromagnetic force acting on, e.g., a proton and an electron, is on the same order of magnitude as the ratio of a natural atomic time scale and the age of the universe. Following Dirac, this could be an indication that so-called large numbers, like this ratio of 10^{39}, would not have to be explained ab initio by a unified theory of all interactions, as opposed to small numbers like, e.g., the mass ratio of the proton and the electron. Instead, the coupling strengths of the fundamental interactions could be related in some functional form to the age of the universe. As a consequence, the "constants" like the fine structure constant or the gravitational constant would be subject to a temporal change.

In some approaches to unification of the fundamental interactions [105], generalized Kaluza-Klein (KK) theories, and more recently string theories, suggest the existence of extra spatial dimensions, extending the 4-dimensional manifold of general relativity to $4+N$ dimensions. With $N \geq 7$ extra compact dimensions with a mean radius R_{KK} on the order of the Planck length, the metric tensor of a Kaluza-Klein model can incorporate general relativity as well as the gauge symmetries of the strong, weak and electromagnetic interactions [106]. As it is generally accepted that the observable universe is expanding, i.e., the scale of the three extended dimensions of space is increasing, it is natural to suggest that also the scale of the compact dimensions should vary in time [107]. This variation $\dot{R}_{\mathrm{KK}} \neq 0$ of the hypothetical extra dimensions, would lead to a variation of fundamental constants as observed in the 4-dimensional world [105].

The fine structure constant α, with

$$\alpha^{-1} = 137.035\,999\,11(46) \tag{6.18}$$

(2002 CODATA recommended value [12]), is an especially attractive candidate for investigations of a possible drift, because it is dimensionless. Any possible drift of a constant involving units cannot be interpreted without additional assumptions, since the reference unit could also be subject to drift. Vice versa, a zero drift within the observational uncertainties could be the result of two cancelling drifts, which might have been observable separately.

Astronomical measurements with the HIRES spectrograph on the Keck I telescope in Hawai'i [25, 108], have found strong indications that far back in the past, the fine structure constant α was different from today's value (6.18), which is known with a relative uncertainty of 3.3×10^{-9}. Investigating the absorption spectra of intergalactic gas clouds in the line of sight towards an even more distant quasar, in a first step the above authors determined the redshift of each cloud, from which the look-back time can be obtained via the Hubble relation. In a second step, transition frequencies of absorption lines due

[1] The results of this section have been obtained in close cooperation with the hydrogen spectroscopy group of T. Hänsch at the Max-Planck-Institut für Quantenoptik, Garching

to the presence of a number of heavy ions were measured. Since in the non-relativistic limit, all optical transition frequencies scale with α^2, a possible drift of α cannot be observed by comparing different optical transitions in the much more abundant hydrogen or helium atoms, because in the frequency ratios, α^2 would always cancel. The critical ingredient is therefore a different functional α-dependence of the transition frequencies due to relativistic and many body effects [109] as also discussed below. The result of the quasar absorption spectroscopy in a look-back time interval of 0.4 to 0.9 times the age of the universe, is [25, 108]

$$\frac{\Delta\alpha}{\alpha} = (-5.42 \pm 1.16) \times 10^{-6} \tag{6.19}$$

for an assumed constant difference $\Delta\alpha$ of the past and the present values, and

$$\frac{\dot{\alpha}}{\alpha} = (6.40 \pm 1.35) \times 10^{-16}/\mathrm{yr} \tag{6.20}$$

for an assumed linear drift. One should mention that astronomical measurements have the disadvantage that a possible spatial variation of the fine structure constant could mimic the observed results, interpreted as a temporal variation (6.20), because the distances of the gas clouds under study from the Earth are on a cosmological length scale, and in addition they are observed in different directions.

Other groups have investigated a phenomenon which occurred about 2×10^9 years ago, here on the Earth. In these early times, a natural fission reactor was in operation in a uranium deposit at Oklo, Gabon, and the resulting neutron flux changed the isotope ratios of several lanthanoids like samarium and gadolinium from the natural abundance ratios, as they can be observed outside the uranium deposit [26, 110, 111]. Although the relevant nuclear transmutation $\mathrm{n} + {}^{149}\mathrm{Sm} \rightarrow {}^{150}\mathrm{Sm} + \gamma$ is mediated by the strong interaction, the cross-section for this process very sensitively depends on the Coulomb energy of the excited intermediate state of ^{150}Sm, bringing the electromagnetic interaction, and therefore α, into play. Depending on different models used in the interpretation, either a null result or a significant drift of α is obtained, both on the level of 10^{-17}/year. The additional inclusion of gadolinium abundance ratios supports the null result [26]. This shows one major difficulty that is characteristic for experiments that look far back in time. Some systematic effects must be taken into account on the basis of assumptions, and the experiment cannot be repeated under improved conditions.

In contrast, in the laboratory, systematic effects can be assessed in a much more direct fashion and actively suppressed in an improved setup. In the following, the results of such a project, which has taken place in collaboration with the hydrogen spectroscopy group at the MPQ [112] are reported.

6.2.2 Analysis of the laboratory measurements

As opposed to the observations reported by [25, 26, 108, 110, 111], high-precision spectroscopy of atomic resonances can test the drift of fundamental constants at present times and restricted to a comparably small part of the universe. If the constants under consideration were truly fixed, one should obtain a zero drift in experiments sensitive to

every time scale. However, if a drift was real, its magnitude might be different at different times, as was already pointed out by Dirac [104]. It is at least not unintuitive to conceive a large drift of fundamental constants in the past, while during the ageing and cooling of the universe, the constants "settle" and today's drift is small.

In the experiments at the MPQ [6,112] in the years 1999 and 2003, the absolute frequency of the $1S$–$2S$ two-photon transition in atomic hydrogen has been very accurately compared to the time standard, the SI second, which is defined in terms of the ^{133}Cs ground state hyperfine transition frequency, ν_{Cs}, and was realized by means of a cesium fountain clock. From these observations, a limit on the drift of the $1S$–$2S$ transition frequency relative to the cesium clock over a time interval of 44 months could be derived. In combination with the limit on the drift of another optical transition frequency in mercury [24] separate statements on the drift of the fine structure constant and the cesium nuclear magnetic moment can be derived.

The transformation of these observed independent limits on the drift of two optical transition frequencies to separate limits on the drift of fundamental constants is presented in the following. The 1999 and 2003 results of the MPQ measurements of the absolute frequency of the hydrogen $1S(F=1, m_F=\pm1) \Leftrightarrow 2S(F'=1, m'_F=\pm1)$ transition read [112]

$$\nu_{\mathrm{H},1999} = 2\,466\,061\,102\,474\,880(36)(28)\,\mathrm{Hz}\,, \tag{6.21}$$

$$\nu_{\mathrm{H},2003} = 2\,466\,061\,102\,474\,851(25)(23)\,\mathrm{Hz}\,. \tag{6.22}$$

Here the uncertainties given in the first brackets are the statistical uncertainties, while the second brackets denote the systematic uncertainties. In the data analysis of the 2003 result, the same fitting procedure was used as for the 1999 analysis, to ensure the comparability of both values. As a consequence of the definition of the SI second, the definition of the Hz reads

$$\mathrm{Hz} = \frac{\nu_{\mathrm{Cs}}}{9\,192\,631\,770}\,, \tag{6.23}$$

therefore the results (6.21) and (6.22) directly yield the values of the frequency ratio $\nu_{\mathrm{Cs}}/\nu_{\mathrm{H}}$, at two points in time. From these values one obtains

$$\nu_{\mathrm{H},2003} - \nu_{\mathrm{H},1999} = (-29 \pm 57)\,\mathrm{Hz}\,, \tag{6.24}$$

$$\frac{\partial}{\partial t} \ln\left(\frac{\nu_{\mathrm{Cs}}}{\nu_{\mathrm{H}}}\right) = (3.2 \pm 6.3) \times 10^{-15}/\mathrm{yr}\,, \tag{6.25}$$

assuming a possible drift to be linear on the time scale of a few years, and using the notation

$$\frac{\partial}{\partial t}\,\ln(\kappa) = \frac{\dot{\kappa}}{\kappa} \tag{6.26}$$

to describe the relative temporal change, or relative drift, of an entity κ. In order to connect the possible drift of the $1S$–$2S$ transition frequency to a drift of fundamental constants, consider the following form, in which any optical transition frequency ν can be written:

$$\nu = A\,\mathrm{Ry}\,F_{\mathrm{rel}}(\alpha) = \nu_0 F_{\mathrm{rel}}(\alpha)\,. \tag{6.27}$$

Here, A is a numerical prefactor which is independent of physical constants, and Ry is the Rydberg frequency. The factor $F_{\rm rel}$ describes the dependence of ν on relativistic effects as discussed below and is essentially unity for hydrogen. Analogously, the frequency of the ^{133}Cs ground state hyperfine transition can be written as

$$\nu_{\rm Cs} = A' \,{\rm Ry}\, \alpha^2 \, \frac{\mu_{\rm Cs}}{\mu_B} \, F_{\rm rel,Cs}(\alpha) \,. \tag{6.28}$$

In the measured frequency ratio $\nu_{\rm Cs}/\nu_{\rm H}$, if expressed by (6.28) and (6.27), the Ry cancels out, and since the numerical constants A and A' are time-independent, the relative drift of the frequency ratio $\nu_{\rm Cs}/\nu_{\rm H}$ can be written as

$$\begin{aligned} \frac{\partial}{\partial t} \ln\left(\frac{\nu_{\rm Cs}}{\nu_{\rm H}}\right) =& \frac{\partial}{\partial t} \ln\left(\alpha^2\right) + \frac{\partial}{\partial t} \ln\left(\frac{\mu_{\rm Cs}}{\mu_B}\right) + \frac{\partial}{\partial t} \ln\left(\frac{F_{\rm rel,Cs}(\alpha)}{F_{\rm rel,H}(\alpha)}\right) && (6.29) \\ =& \frac{\partial}{\partial t} \ln\left(\frac{\mu_{\rm Cs}}{\mu_B}\right) \\ &+ \left(2 + \frac{\alpha}{F_{\rm rel,Cs}(\alpha)} \frac{\partial}{\partial \alpha} F_{\rm rel,Cs}(\alpha) - \frac{\alpha}{F_{\rm rel,H}(\alpha)} \frac{\partial}{\partial \alpha} F_{\rm rel,H}(\alpha)\right) \frac{\partial}{\partial t} \ln(\alpha) \,. && (6.30) \end{aligned}$$

From this relation, it is clear that a statement concerning a possible drift of α cannot be extracted from the measured result of $\nu_{\rm Cs}/\nu_{\rm H}$ alone, because the cesium nuclear moment in units of the Bohr magneton, $\mu_{\rm Cs}/\mu_B$, can also be subject to drift. In addition, a zero drift of the frequency ratio might be caused by a cancelling drift of α and $\mu_{\rm Cs}$. This missing information therefore has to be provided by another frequency comparison. For energy levels in atoms like hydrogen with very small relativistic effects and no many-body corrections, $F_{\rm rel,H}(\alpha) \approx 1$ and using, e.g., another transition in hydrogen, would add no additional uncorrelated information.

Therefore, a second measurement was taken into account, performed with a single mercury ion, by the group of J. Bergquist at NIST between July 2000 and December 2002 [24]. In this experiment, the $^{199}{\rm Hg}^+$ $5d^{10}6s\ {}^2S_{1/2}(F=0) \rightarrow 5d^9 6s^2\, {}^2D_{5/2}(F'=2)$ electric quadrupole transition was investigated and a relative drift with respect to the cesium standard of

$$\frac{\partial}{\partial t} \ln\left(\frac{\nu_{\rm Cs}}{\nu_{\rm Hg}}\right) = (0.2 \pm 7) \times 10^{-15}/{\rm yr} \,, \tag{6.31}$$

was obtained. The advantage of including the mercury result is, that $F_{\rm rel}$ of this particular transition frequency has a very strong α-dependence, which will turn out to provide an independent restriction to the drift of the fine structure constant, in combination with the weak α-dependence of the hydrogen transition frequency.

The α-dependence of atomic energy levels can obviously not be directly measured experimentally. In Ref. [109], ab initio calculations of transition frequencies are performed for a set of transitions in heavy ions, including mercury, and successfully compared to experiments. These numerical calculations include relativistic and many-body effects using a relativistic Hartree-Fock Hamiltonian and many-body perturbation theory. In addition, these calculations have been repeated for different values of the fine structure constant, and the resulting α-dependence of the transition frequency ω_0 (in the notation of [109])

is given in the form of the expansion

$$\omega(\alpha) = \omega_0 \left\{ 1 + \frac{q_1}{\omega_0} \left[\left(\frac{\alpha}{\alpha_l} \right)^2 - 1 \right] + \frac{q_2}{\omega_0} \left[\left(\frac{\alpha}{\alpha_l} \right)^4 - 1 \right] \right\}$$
$$=: \omega_0 \, F_{\rm rel}(\alpha) \,, \tag{6.32}$$

where α_l is the reference value (6.18), as determined in the laboratory at present, ω_0 is the corresponding transition frequency and the coefficients q_1 and q_2 are listed in Tabs. III and IV of [109]. From the expansion (6.32), the terms involving $F_{\rm rel}(\alpha)$ in (6.30) can be obtained:

$$\alpha \frac{\partial}{\partial \alpha} \ln F_{\rm rel}(\alpha) \bigg|_{\alpha=\alpha_l} \equiv \frac{\alpha}{F_{\rm rel}(\alpha)} \, \frac{\partial}{\partial \alpha} F_{\rm rel}(\alpha) \bigg|_{\alpha=\alpha_l} = \frac{2\,q_1 + 4\,q_2}{\omega_0} \,. \tag{6.33}$$

Specifically, for the α-dependencies of the mercury transition and the cesium ground state hyperfine splitting, one obtains from the expansion around the present value α_l

$$\alpha \frac{\partial}{\partial \alpha} \ln[F_{\rm rel,Hg}(\alpha)] = -3.19 \,, \tag{6.34}$$
$$\alpha \frac{\partial}{\partial \alpha} \ln[F_{\rm rel,Cs}(\alpha)] = 0.83 \,, \tag{6.35}$$
$$\alpha \frac{\partial}{\partial \alpha} \ln[F_{\rm rel,H}(\alpha)] \approx 0 \,. \tag{6.36}$$

Summarizing the above considerations, one arrives at the following relations between the possible drifts of the transition frequencies, α and $\mu_{\rm Cs}$:

$$\frac{\partial}{\partial t} \ln \left(\frac{\nu_{\rm Cs}}{\nu_{\rm H}} \right) = (3.2 \pm 6.3) \times 10^{-15}/{\rm yr} = \frac{\partial}{\partial t} \ln \left(\frac{\mu_{\rm Cs}}{\mu_B} \right) + (2 + 0.8 + 0.0) \frac{\partial}{\partial t} \ln(\alpha) \,, \tag{6.37}$$

$$\frac{\partial}{\partial t} \ln \left(\frac{\nu_{\rm Cs}}{\nu_{\rm Hg}} \right) = (0.2 \pm 7) \times 10^{-15}/{\rm yr} = \frac{\partial}{\partial t} \ln \left(\frac{\mu_{\rm Cs}}{\mu_B} \right) + (2 + 0.8 + 3.2) \frac{\partial}{\partial t} \ln(\alpha) \,. \tag{6.38}$$

The numerical precision is restricted by the relative uncertainty of 7×10^{-15} of the mercury measurement, therefore all other values are taken into account with only one more significant digit. With the abbreviations for the relative drift of the fine structure constant, x, and the relative drift of the cesium nuclear magnetic moment, y,

$$x = \frac{\partial}{\partial t} \ln(\alpha) \,, \qquad y = \frac{\partial}{\partial t} \ln \left(\frac{\mu_{\rm Cs}}{\mu_B} \right) \,, \tag{6.39}$$

one obtains

$$y + 6.0\, x = (0.2 \pm 7) \times 10^{-15}/{\rm yr} \,, \tag{6.40a}$$
$$y + 2.8\, x = (3.2 \pm 6.3) \times 10^{-15}/{\rm yr} \,. \tag{6.40b}$$

In Fig. 6.9, the x-y plane of possible independent drifts of α and μ_{Cs}/μ_B is depicted. The linear restrictions (6.40) are indicated by a solid line, and the dashed lines mark the stripe of 1σ uncertainty, assuming a Gaussian probability density for the observed restrictions (6.25) and (6.31) of the drift of the transition frequencies.

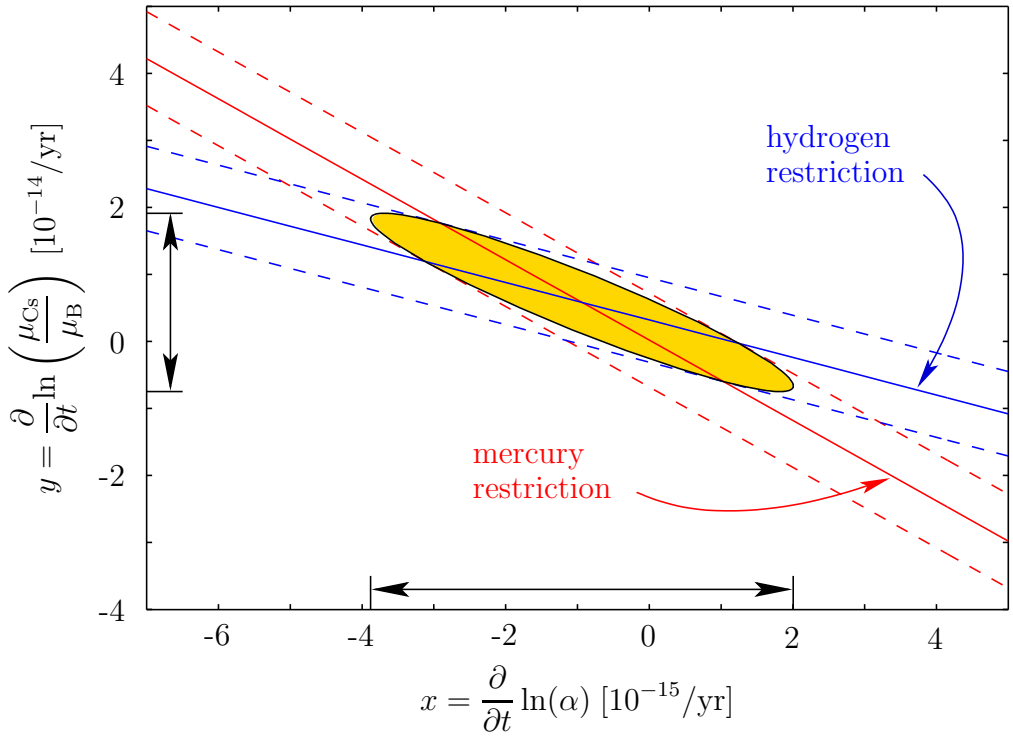

Figure 6.9: Combination of two independent experimental restrictions to the possible drifts of the fine structure constant α and the drift of the cesium nuclear magnetic moment μ_{Cs}/μ_B. The x-y plane corresponds to all possible combinations of independent relative drifts of the fine structure constant, $x = \dot{\alpha}/\alpha = \partial \ln(\alpha)/\partial t$, and the cesium magnetic moment, y. The restriction obtained from the repeated absolute frequency measurement of the hydrogen $1S$–$2S$ transition is marked by the blue solid line, including a 1σ-uncertainty as indicated by the blue dashed lines. The restriction imposed by the experiment investigating a mercury quadrupole transition is given by the corresponding red lines. The possible drift of μ_{Cs}/μ_B comes into play, because both optical transition frequencies are compared to the SI time normal, which is a cesium atomic clock. The 1σ-ellipse of the intersection, when projected onto the axes, yields the 1σ-intervals for the drift of the fine structure constant and the cesium nuclear magnetic moment (black arrows).

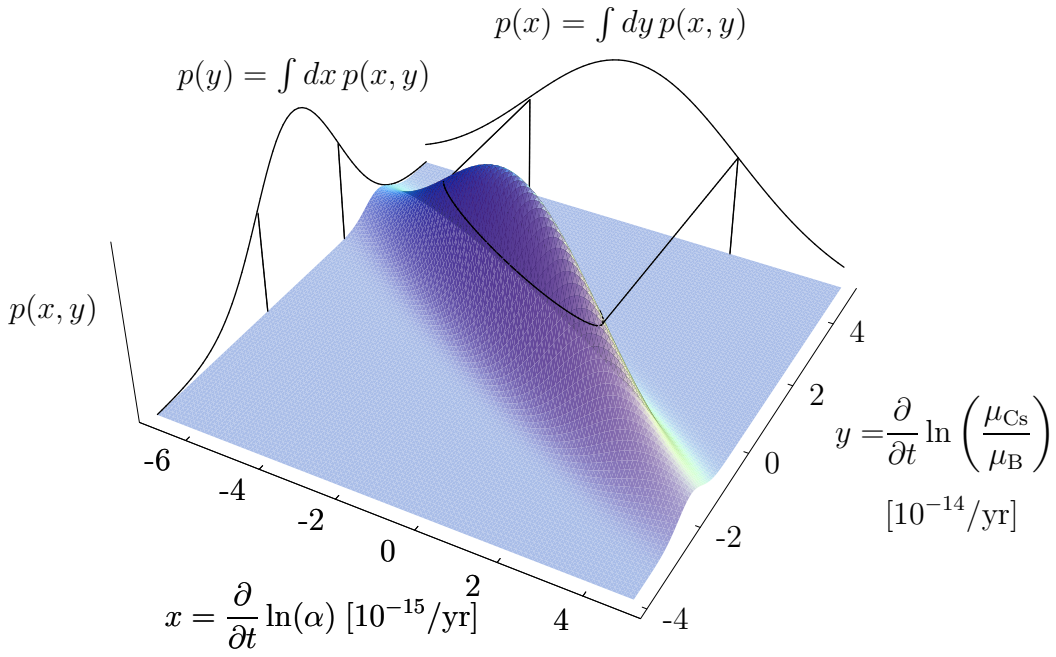

Figure 6.10: Joint probability density $p(x, y)$ and corresponding marginal probability densities $p(x)$ for x and $p(y)$ for y. The projections of the 1σ-ellipse of the joint distribution, containing both true values for (x,y) with a probability of 39.3%, yield the 1σ-intervals of the marginal distributions, in which the true values of x and y are contained with 68.3% probability, respectively.

6.2.3 Results

Solving Eqs. (6.40) for x and y, one obtains for the most probable values

$$x_m = -0.9 \times 10^{-15}/\text{yr}\,, \qquad y_m = 0.6 \times 10^{-14}/\text{yr}\,. \tag{6.41}$$

The joint probability density for x and y to be the true values of the respective relative drift, therefore reads

$$p(x,y) = \frac{1}{2\pi\sigma_H\sigma_{Hg}} \exp\left[-R(\Delta x, \Delta y)\right]\,, \tag{6.42}$$

$$R(\Delta x, \Delta y) = \frac{(\Delta y + 2.8\Delta x)^2}{2\sigma_H^2} + \frac{(\Delta y + 6\Delta x)^2}{2\sigma_{Hg}^2}\,, \tag{6.43}$$

with $\Delta x = x - x_m$, $\Delta y = y - y_m$ and the corresponding uncertainties of the frequency drift measurements, $\sigma_H = 6.3 \times 10^{-15}/\text{yr}$ and $\sigma_{Hg} = 7 \times 10^{-15}/\text{yr}$. The 1σ-ellipse in Fig. 6.9 is defined to be the set of values (x, y) for which $R(\Delta x, \Delta y) = 1/2$, in accordance with a one-dimensional Gaussian distribution, where the 1σ-interval is given by the exponents of $\pm 1/2$.

Integrating the bivariate Gaussian probability density (6.42) over one of the arguments, e.g., y, one obtains a univariate Gaussian probability density [103] for the other random variable, x. From this marginal distribution, one can easily obtain the most probable value including the 1σ-uncertainty, irrespective of the actual value of y. In this way, one obtains

$$x = \frac{\partial}{\partial t} \ln(\alpha) = (-0.9 \pm 2.9) \times 10^{-15}/\mathrm{yr}\,, \tag{6.44a}$$

$$y = \frac{\partial}{\partial t} \ln\left(\frac{\mu_{\mathrm{Cs}}}{\mu_B}\right) = (0.6 \pm 1.3) \times 10^{-14}/\mathrm{yr}\,. \tag{6.44b}$$

In Fig. 6.10 this extraction of the 1σ-intervals is illustrated, which are given by the projection of the 1σ-ellipse on the respective axis. The final results (6.44) for the drift of the fine structure constant and the cesium nuclear magnetic moment are separate limits for the two drifts and both are compatible with zero within one standard uncertainty. The only assumptions made in the laboratory measurement approach are, that a possible temporal change of α is not by chance cancelled by a spacial drift of α due to the Earth's trajectory in space, and that a possible drift can be described in good approximation as linear on the timescale of about three years.

In conclusion, laboratory experiments can provide complementary results to astronomical and geological investigations for the drift of fundamental constants, with comparable relative precision. Two stringent, separate upper limits are given on the present relative drifts of the fine structure constant and the cesium nuclear magnetic moment, derived from the results of independent high-precision spectroscopy laboratory experiments. No assumption regarding the exclusive drift of any single constant was needed in the derivation, and both results agree well with a zero drift within the observational uncertainties. Further developments in the experimental control, and in the theoretical understanding of systematic effects as undertaken in this thesis, as well as simply the passage of time, will help to make these limits even more stringent or make it possible to detect a nonzero drift, if it exists.

Chapter 7

Conclusion

7.1 General conclusion

In this thesis, the excitation dynamics of two-photon transitions in bound two-body Coulomb systems, and in particular the hydrogen $1S$–$2S$ transition, has been examined theoretically and high-precision matrix elements have been calculated. The modeling of the experimentally observed line shape has been improved and a thorough search for small systematic effects has been conducted in order to further improve the control of systematics in the future. From the analysis of experimental results, stringent limits on the drift of two fundamental constants have been derived.

Starting from first principles, the quantum dynamics and the atomic constants describing the two-photon excitation process in ongoing and planned high-precision experiments were presented in a unified treatment, including the dependence on Z, the reduced mass and hyperfine structure of the system. By generalizing the usual master equations, the special circumstances of a typical standing wave field configuration were taken into account, and an analytic solution for the time-dependent excited state line shape for constant driving intensity was derived. The relative importance of ionization losses and spontaneous decay of the excited state have been discussed in detail for hydrogenlike systems with different nuclear charge numbers. Ionization has been identified as a decisive feature of the quantum dynamics which has to be taken into account in future line shape models of high-precision experiments.

Leading-order relativistic and radiative corrections to the excitation dynamics and to the dynamic Stark effect have been calculated in anticipation of increasing experimental precision. Especially in the case of the dynamic Stark shift, which consists a major systematic effect in high-precision two-photon spectroscopy, the quantitative calculation of these corrections is important. In addition, corrections beyond the dipole approximation as they occur in a standing-wave setup in the context of first-order Doppler free excitation have been obtained. These are especially important for highly excited states.

A Monte Carlo simulation implementing the experimental setup of the hydrogen $1S$–$2S$ absolute frequency measurement at the Max–Planck–Institut für Quantenoptik (MPQ)

has been developed and the simulation results were found to agree very well with experimental data. In particular, the photoionization broadening of the $1S$–$2S$ transition as a function of excitation power could be quantitatively reproduced for the first time. This comparison also constitutes an indirect verification of the calculated transition matrix elements and dynamic polarizabilities. By means of the numerical simulation, systematic effects were studied which are difficult to assess in the laboratory, like the freezing of the hydrogen nozzle and the effect of a small misalignment of the in-coupling laser beam with respect to the power enhancement cavity.

The program performing the nonlinear regression in the data analysis at the MPQ was directly checked in great detail, and has also been validated by comparison with a new data analysis procedure, carried out with the same raw data but completely independent otherwise. This comparison also allowed to exclude the numerical line shape model as a major source of scatter observed in the data and supported the suspicion that uncontrolled systematic effects are still present in the experimental setup, possible sources of which are briefly summarized in the section below.

By analyzing the repeated high-precision measurements of the hydrogen $1S$–$2S$ absolute frequency at the MPQ, and the results of a mercury quadrupole clock transition experiment at NIST, separate stringent limits on the relative drift of the fine structure constant and the cesium nuclear magnetic moment have been derived in cooperation with the MPQ group, which are comparable with the precision of existing astronomical and geological measurements, and require only very basic assumptions. The relative temporal change in the course of three years has been found to be compatible with zero, within one standard deviation, on the level of 10^{-15}/yr.

7.2 Proposals for future experiments

The analysis carried out in this thesis suggests the following proposals for the experiments carried out in the high-precision spectroscopy group at the MPQ, aiming at a further improvement of resolution.

It has been found that the scatter which is exhibited in the fitted line centers of spectra recorded in one day, and in the zero-power extrapolated day values, cannot be attributed to the line shape model developed by A. Huber [102]. Both thorough checks of the program and a comparison with the Lorentz data analysis support this conclusion. A number of alternative systematic effects have been examined and the following have been identified as possible contributions to the scatter.

The freezing of the hydrogen nozzle during consecutive measurements of several spectra can lead to a different inhomogeneous Stark shift than that taken into account by the line shape model. Although the general trend of this effect is an upward shift, the zero-power extrapolated value is not systematically shifted in a specific direction, because the excitation power is varied randomly. However, the scatter of the line centers may be a limiting factor for a further increase in precision. A proposal for a different geometry of the nozzle avoiding this effect, is given in Sec. 6.1.6.

The misalignment of the in-coupling laser beam with respect to the cavity axis can lead to two different systematic contributions, both originating in a residual first-order Doppler shift from the absorption of photons that are not perfectly counter-propagating. One of these misalignment effects averages as a function of misalignment angle, while the other entails a small systematic shift towards a higher observed transition frequency. A cavity with an increased power enhancement factor will reduce both these effects.

In view of the Monte Carlo results, displaying quantitative agreement of the photoionization broadening with the experimental data, it is advisable to take into account the ionization rate and the varying excitation powers into the line shape model. Also the ionization losses from the initial velocity distributions, incorporated phenomenologically in the current line shape model, are likely to be described more appropriately in this way. To take advantage from a power-dependent line shape model, a reliable power measurement and an improved power stabilization are required. A proposal for a non-invasive power measurement scheme, using a reference beam to probe the transmittivity of a cavity mirror, is given in Sec. 6.1.5.

For the $1S$–$3S$ experiment, the inconsistencies found in the literature concerning the transition matrix elements have been resolved and all relevant matrix elements are explicitly given in appendix B.

The detection of ionization products is a promising alternative to the current detection of atoms in the excited state, because charged particles can be detected with higher quantum efficiency. This scheme could be applied in the hydrogen experiments as well as in the planned He^+ spectroscopy [113]. The relevant ionization coefficients and the time-dependent line shape have been derived and can be directly used in a power-dependent line shape model for the evaluation of the expected signal and for the data analysis.

For the future, it may be worthwhile to examine more closely the excitation with very short pulses, e.g., to the benefit of the ongoing $1S$–$3S$ experiment, and the possible consequences of chirps which the pulses acquire by passing through the dispersive media of the setup. The high-precision spectroscopy experiment with trapped hydrogenlike helium, which is currently in preparation at the MPQ, will also present new challenges for theoretical investigations.

Further, the development of a power-dependent line shape model, taking into account the excitation power and ionization from the excited state would be desirable, especially in view of the alternative ionization detection scheme. An implementation using the existing data analysis framework is proposed in Sec. 6.1.7.

Continuing efforts, both experimentally and theoretically as undertaken in this thesis, are required to further enhance the precision of the determination of absolute transition frequencies and fundamental constants.

Appendix A

Some comparisons with the literature

A.1 The $1S$–$2S$ transition

This section is dedicated to a comparison of the results given in this thesis and previous work. For the convenience of the reader, all the prefactors are described in detail, where different conventions and units are used. The collection of articles covered in the following is not claimed to be complete.

For the $1S$–$2S$ two-photon transition matrix element, the result of this thesis reads $\beta_{ge} = 3.68111 \times 10^{-5}\,\mathrm{Hz}/(\mathrm{W/m^2})$, see Tab. 3.1, with

$$\begin{aligned}\beta_{ge} = &- \frac{e^2}{2\,h\,c\,\epsilon_0} \left\langle 2S \left| z \frac{1}{H_0 - (E_{1S} + \hbar\omega_\mathrm{L})} z \right| 1S \right\rangle = \\ &- \frac{e^2}{2\,h\,c\,\epsilon_0} \sum_n \frac{\langle 2S\,|z|n\rangle\langle n|z|\,1S\rangle}{E_n - E_{1S} - \hbar\omega_\mathrm{L}}\,,\end{aligned} \tag{A.1}$$

and with intermediate states $|n\rangle$. To relate this result in SI units to atomic units, where $\hbar = a_0 = e = m_\mathrm{e} = 1$, one has to apply the conversion

$$\beta_{ge}\,[\mathrm{at.u.}] = \beta_{ge}\,[\mathrm{SI}]\,\frac{\hbar^2}{m_\mathrm{e}\,a_0^4\,\alpha}\,, \tag{A.2}$$

in which these constants are reinstated, resulting in a value of $\beta_{ge} = 7.85366$ atomic units. In Ref. [49], the authors define

$$D[J_0] = \frac{3}{2}\sum (1 + P_{12}) \frac{\hat{\boldsymbol{e}}_1 \cdot \langle 2S|\boldsymbol{r}/a_0|n\rangle\langle n|\boldsymbol{r}/a_0|1S\rangle \cdot \hat{\boldsymbol{e}}_2}{\nu(n) - \nu(1s) - \nu_2} \tag{A.3}$$

as the two-photon transition probability amplitude and obtain a value of -11.7805 atomic units, which differs precisely by a factor of - 3/2 from the result of this work. The opposite sign obviously is just a consequence of a different definition of the Green's function.

The operator P_{12} interchanges the polarization vectors $\hat{\boldsymbol{e}}_1$ and $\hat{\boldsymbol{e}}_2$ and the frequencies of the two photons. The authors of Ref. [49] treat the light fields more generally to have different frequencies. This makes the photons distinguishable, and therefore there are two different ways to excite the atom, one path with first low-frequency, then high-frequency photon absorption and another with first high-frequency and then low-frequency photon absorption.

To reduce definition (A.3) to the case of equal polarizations and equal frequencies, as considered in this thesis, one needs to set the polarization vectors $\hat{\boldsymbol{e}}_1 = \hat{\boldsymbol{e}}_2 = \hat{\boldsymbol{e}}_z$ and one has to omit the part where the polarizations and frequencies are interchanged, because the photons are indistinguishable. Then the manifest prefactor of 3/2 in Eq. (A.3) explains the numerical difference as being only a matter of definition, while the physical results agree. This value of $D[J_0]$ is cited and used by Ref. [50], therefore the same considerations apply there.

A.2 The $1S$–$3S$ transition

The result of this work for the $1S$–$3S$ transition matrix element (see Tab. 3.1) reads $\beta_{ge} = 1.00333 \times 10^{-5}\,\mathrm{Hz}/(\mathrm{W/m^2})$, or when converted to atomic units: $\beta_{ge} = 2.14061$. This equals the value given in Ref. [52]. Also, the other S–S transition matrix elements calculated there, namely for the $2S$–$6S$ and $2S$–$8S$ transitions, are equal to the results presented here, if converted according to Eq. (A.2).

In Ref. [51], Tab. 20, the square of the transition matrix elements, called M, for the transitions $1S$–nS, $1S$–nD, $2S$–nS and $2S$–nD with n up to 6 are given. Out of these 18 squared matrix elements (given in atomic units), the results of this thesis are in agreement with 16 values. The cases in which differences occur, are the values for the $1S$–$3S$ and the $2S$–$6S$ transition (see Tab. A.1). The value for $M(1S$–$3S)$ given by Tung *et al.* [51] is equal to the double of the transition matrix element from this work (2.14061), not the square. Also in view of the agreement of this thesis with Ref. [52], it is likely that Tung *et al.* inadvertently doubled their correct result for the transition matrix element instead of squaring it. The second inconsistency might be explained by a twist of digits.

Table A.1: Comparison of squared transition matrix elements M, as defined in Ref. [51], with the corresponding results from this thesis.

Literature source	Transition	M
Tung *et al.* [51]	$1S$–$3S$	4.2812
this work	$1S$–$3S$	4.5822
Tung *et al.* [51]	$2S$–$6S$	261.44
this work	$2S$–$6S$	216.4420

In an even older study [53], the authors work in the velocity gauge, as opposed to the length gauge used in all articles considered here. Tung *et al.* agree with their results for the absorption cross section, which is related to the transition matrix element. This supports the assumption that Tung *et al.* indeed have obtained matrix elements in agreement with the results presented here, while the numerical differences originated in the compilation process.

A.3 Light shifts

The complete set of results for the light shifts of S states, for transitions where the $2S$ state acts as the ground state (see Tab. 3.4), agree with Tab. Ic of Ref. [31]. In that work, where atomic units are used, only the real parts of the dynamic Stark shifts are presented; the light shift of $20S$ in the $2S$–$20S$ transition for example is 261.18 atomic units in Ref. [31], which can be converted via relation (A.2), into $\beta_{\mathrm{AC}}(20S) = 1.2242 \times 10^{-3}\,\mathrm{Hz}/(\mathrm{W}/\mathrm{m}^2)$ in agreement with the value given in Tab. 3.4. The light shifts of the gross structure D states given in the same table in Ref. [31], agree with the values obtained in this thesis, reduced to the special case where the atomic fine structure and hyperfine structure are not taken into account.

Appendix B

Explicit Polarizabilities and Transition Matrix Elements

This appendix lists explicit expressions for the transition matrix elements and dynamic polarizabilities relevant for the $1S$–$2S$ and the $1S$–$3S$ transitions in hydrogenic systems, as a function of the intermediate state energies. The energy parameterization $E(\eta)$ is defined in Eq. (3.30). The Bohr radius is denoted by a_0, m_e is the electron mass, and H_0 the unperturbed Hamiltonian (3.1b). The purpose of giving the matrix elements in this general form is to enable the reader to evaluate the polarizabilities also at other frequencies than the two-photon resonance frequency. This is particularly useful for a planned detection scheme in the MPQ $1S$–$3S$ experiment, where excited $3S$ atoms are detected via the observation of ionization products. An additional dedicated laser, tuned slightly above the frequency needed to ionize the $3S$ state, increases the ionization rate, because close to the continuum threshold, ionization is very efficient. The corresponding ionization rate, for a laser with arbitrary frequency can be obtained from the imaginary part of the excited state polarizability below, as defined in Eq. (3.64).

$$\left\langle 1S \left| z \frac{1}{H_0 - E(\eta)} z \right| 2S \right\rangle = \frac{m_\mathrm{e}\, {a_0}^4}{Z^4\, \hbar^2} \frac{512\sqrt{2}\,\eta^2}{729\,(\eta^2-4)^3(\eta^2-1)^2} \tag{B.1}$$
$$\times \Bigg[128 - 272\,\eta^2 + 120\,\eta^4 + 253\,\eta^6 + 972\,\eta^7 + 419\,\eta^8$$
$$-1944\,\eta^7\, {}_2F_1\left(1, -\eta, 1-\eta, \frac{(1-\eta)(2-\eta)}{(1+\eta)(2+\eta)}\right)\Bigg]$$

$$\left\langle 1S \left| z \frac{1}{H_0 - E(\eta)} z \right| 3S \right\rangle = \frac{m_\mathrm{e}\, {a_0}^4}{Z^4\, \hbar^2} \frac{9\sqrt{3}\,\eta^2}{64(\eta^2-9)^4(\eta^2-1)^2} \tag{B.2}$$
$$\times \Bigg[-19683 + 37179\,\eta^2 - 6318\,\eta^4 - 62586\,\eta^6 - 221184\,\eta^7 - 47487\,\eta^8 + 57344\,\eta^9$$
$$+16975\,\eta^{10} - 16384\,\eta^7(7\,\eta^2 - 27)\, {}_2F_1\left(1, -\eta, 1-\eta, \frac{(1-\eta)(3-\eta)}{(1+\eta)(3+\eta)}\right)\Bigg]$$

$$\left\langle 1S \left| z \frac{1}{H_0 - E(\eta)} z \right| 1S \right\rangle = \frac{m_e {a_0}^4}{Z^4 \hbar^2} \frac{2\,\eta^2}{3(\eta^2-1)^5} \tag{B.3}$$
$$\times \left[-3 + 15\,\eta^2 - 31\,\eta^4 + 45\,\eta^6 + 64\,\eta^7 + 38\,\eta^8 - 128\,\eta^7\, {}_2F_1\left(1, -\eta, 1-\eta, \left(\frac{1-\eta}{1+\eta}\right)^2\right)\right]$$

$$\left\langle 2S \left| z \frac{1}{H_0 - E(\eta)} z \right| 2S \right\rangle = \frac{m_e {a_0}^4}{Z^4 \hbar^2} \frac{16\,\eta^2}{3(\eta^2-4)^6} \tag{B.4}$$
$$\times \left[21504 - 28416\,\eta^2 + 15488\,\eta^4 - 5344\,\eta^6 - 4096\,\eta^7 + 2148\,\eta^8 \right.$$
$$\left. +4096\,\eta^9 + 1181\,\eta^{10} - 8192\,\eta^7\,(\eta^2-1)\, {}_2F_1\left(1, -\eta, 1-\eta, \left(\frac{2-\eta}{2+\eta}\right)^2\right)\right]$$

$$\left\langle 3S \left| z \frac{1}{H_0 - E(\eta)} z \right| 3S \right\rangle = \frac{m_e {a_0}^4}{Z^4 \hbar^2} \frac{54\,\eta^2}{(\eta^2-9)^8} \tag{B.5}$$
$$\times \left[110008287 - 87156324\,\eta^2 + 29819745\,\eta^4 - 6022998\,\eta^6 - 1259712\,\eta^7 \right.$$
$$+ 2106081\,\eta^8 + 1912896\,\eta^9 - 504792\,\eta^{10} - 737856\,\eta^{11} - 31041\,\eta^{12} + 84672\,\eta^{13}$$
$$\left. +15538\,\eta^{14} + 3456\,\eta^7\left(27 - 7\,\eta^2\right)^2\left(1-\eta^2\right)\, {}_2F_1\left(1, -\eta, 1-\eta, \left(\frac{3-\eta}{3+\eta}\right)^2\right)\right]$$

For higher excited states, the analytic results rapidly increase in length, which necessitates the use of a computer algebra system [78]. The ${}_2F_1$ hypergeometric function often occurs in the result for integrals containing the Schrödinger-Coulomb Green's function in the above form [56].

Bibliography

[1] W. E. Lamb and R. C. Retherford, Phys. Rev. **72**, 241 (1947).

[2] H. A. Bethe, Phys. Rev. **72**, 339 (1947).

[3] R. S. Van Dyck, Jr., P. B. Schwinberg, and H. G. Dehmelt, Phys. Rev. Lett. **59**, 26 (1987).

[4] G. W. Bennett, B. Bousquet, H. N. Brown, G. Bunce, R. M. Carey, P. Cushman, G. T. Danby, P. T. Debevec, M. Deile, H. Deng, S. K. Dhawan, V. P. Druzhinin, L. Duong, F. J. M. Farley, G. V. Fedotovich, F. E. Gray, D. Grigoriev, M. Grosse-Perdekamp, A. Grossmann, M. F. Hare, D. W. Hertzog, X. Huang, V. W. Hughes, M. Iwasaki, K. Jungmann, D. Kawall, B. I. Khazin, F. Krienen, I. Kronkvist, A. Lam, R. Larsen, Y. Y. Lee, I. Logashenko, R. McNabb, W. Meng, J. P. Miller, W. M. Morse, D. Nikas, C. J. G. Onderwater, Y. Orlov, C. S. Ozben, J. M. Paley, Q. Peng, C. C. Polly, J. Pretz, R. Prigl, G. zu Putlitz, T. Qian, S. I. Redin, O. Rind, B. L. Roberts, N. Ryskulov, Y. K. Semertzidis, P. Shagin, Y. M. Shatunov, E. P. Sichtermann, E. Solodov, M. Sossong, L. R. Sulak, A. Trofimov, P. von Walter, and A. Yamamoto, Phys. Rev. Lett. **92**, 161802 (2004).

[5] M. Weitz, A. Huber, F. Schmidt-Kaler, D. Leibfried, W. Vassen, C. Zimmermann, K. Pachucki, T. W. Hänsch, L. Julien, and F. Biraben, Phys. Rev. A **52**, 2664 (1995).

[6] M. Niering, R. Holzwarth, J. Reichert, P. Pokasov, Th. Udem, M. Weitz, T. W. Hänsch, P. Lemonde, G. Santarelli, M. Abgrall, P. Laurent, C. Salomon, and A. Clairon, Phys. Rev. Lett. **84**, 5496 (2000).

[7] K. Pachucki, D. Leibfried, M. Weitz, A. Huber, W. König, and T. W. Hänsch, J. Phys. B **29**, 177 (1996).

[8] A. Antognini, F. D. Amaro, F. Biraben, U. Brauch, J. M. R. Cardoso, C. A. N. Conde, A. Dax, S. Dhawan, L. M. P. Fernandes, A. Giesen, T. W. Hänsch, P. Indelicato, L. Julien, P. E. Knowles, F. Kottmann, Y. W. Liu, J. A. M. Lopes, L. Ludhova, C. M. B. Monteiro, F. Mulhauser, F. Nez, R. Pohl, P. Rabinowitz, J. M. F. dos Santos, L. A. Schaller, C. Schwob, C. Stolzenburg, D. Taqqu, and J. F. C. A. Veloso, AIP Conf. Proc. **796**, 253 (2005).

[9] U. D. Jentschura, S. Kotochigova, E.-O. Le Bigot, P. J. Mohr, and B. N. Taylor, Phys. Rev. Lett. **95**, 163003 (2005).

[10] B. de Beauvoir, F. Nez, L. Julien, B. Cagnac, F. Biraben, D. Touahri, L. Hilico, O. Acef, A. Clairon, and J. J. Zondy, Phys. Rev. Lett. **78**, 440 (1997).

[11] C. Schwob, L. Jozefowski, B. de Beauvoir, L. Hilico, F. Nez, L. Julien, F. Biraben, O. Acef, A. Clairon, and J. J. Zondy, Phys. Rev. Lett. **82**, 4960 (1999).

[12] P. J. Mohr and B. N. Taylor, Rev. Mod. Phys. **77**, 1 (2005).

[13] G. Santarelli, Ph. Laurent, P. Lemonde, A. Clairon, A. G. Mann, S. Chang, A. N. Luiten, and C. Salomon, Phys. Rev. Lett. **82**, 4619 (1999).

[14] H. Schnatz, B. Lipphardt, J. Helmcke, F. Riehle, and G. Zinner, Phys. Rev. Lett. **76**, 18 (1996).

[15] Th. Udem, A. Huber, B. Gross, J. Reichert, M. Prevedelli, M. Weitz, and T. W. Hänsch, Phys. Rev. Lett. **79**, 2646 (1997).

[16] K. Evenson, J. Wells, F. Petersen, B. Danielson, and G. Day, Appl. Phys. Lett. **22**, 192 (1973).

[17] T. Udem, J. Reichert, R. Holzwarth, and T. W. Hänsch, Phys. Rev. Lett. **82**, 3568 (1999).

[18] Th. Udem, R. Holzwarth, and T. W. Hänsch, Nature (London) **416**, 233 (2002).

[19] J. M. Overduin and P. S. Wesson, Phys. Rep. **283**, 303 (1997).

[20] E. Witten, Phys. Lett. B **149**, 351 (1986).

[21] J. Polchinski, *Superstring Theory* (Cambridge University Press, Cambridge, UK, 1997).

[22] J.-P. Uzan, Rev. Mod. Phys. **75**, 403 (2003).

[23] M. Fischer, *Höchstauflösende Laserspektroskopie an atomarem Wasserstoff*, PhD thesis, Ludwig–Maximilians–Universität München (2004).

[24] S. Bize, S. A. Diddams, U. Tanaka, C. E. Tanner, W. H. Oskay, R. E. Drulling, T. E. Parker, T. P. Heavner, S. R. Jefferts, L. Hollberg, W. M. Itano, and J. C. Bergquist, Phys. Rev. Lett. **90**, 150802 (2003).

[25] J. K. Webb, M. T. Murphy, V. V. Flambaum, V. A. Dzuba, J. D. Barrow, C. W. Churchill, J. X. Prochaska, and A. M. Wolfe, Phys. Rev. Lett. **87**, 091301 (2001).

[26] Y. Fujii, A. Iwamoto, T. Fukahori, T. Ohnuki, M. Nakagawa, H. Hidaka, Y. Oura, and P. Möller, Nucl. Phys. B **573**, 377 (2000).

[27] A. Huber, B. Gross, M. Weitz, and T. W. Hänsch, Phys. Rev. A **59**, 1844 (1999).

[28] M. Fischer, N. Kolachevsky, M. Zimmermann, R. Holzwarth, Th. Udem, T. W. Hänsch, M. Abgrall, J. Grünert, I. Maksimovic, S. Bize, H. Marion, F. P. D. Santos, P. Lemonde, G. Santarelli, P. Laurent, A. Clairon, and C. Salomon, e-print physics/0311128, 2003.

[29] M. Scully and M. Zubairy, *Quantum Optics* (Cambridge University Press, Cambridge, UK, 1999).

[30] W. Vogel, D.-G. Welsch, and S. Wallentowitz, *Quantum Optics. An Introduction* (WILEY–VCH, Berlin, 2001).

[31] J. C. Garreau, M. Allegrini, L. Julien, and F. Biraben, J. Phys. (France) **51**, 2275 (1990).

[32] F. Bloch and A. Siegert, Phys. Rev. **57**, 522 (1940).

[33] H. F. Beyer, H.-J. Kluge, and V. P. Shevelko, *X-Ray Radiation of Highly Charged Ions* (Springer, Berlin-Heidelberg, 1997).

[34] V. Yakhontov, R. Santra, and K. Jungmann, J. Phys. B **32**, 1615 (1999).

[35] B. J. Shortt, P. J. M. van der Burgt, and F. Giammanco, Las. Phys. **12**, 1402 (2002).

[36] P. Zoller, Phys. Rev. A **19**, 1151 (1979).

[37] G. S. Agarwal, Phys. Rev. Lett. **37**, 1383 (1976).

[38] W. Demtröder, *Laser Spectroscopy*, 3rd ed. (Springer, Berlin, 2003).

[39] B. L. Beers and L. Armstrong, Phys. Rev. A **12**, 2447 (1975).

[40] U. D. Jentschura, Phys. Rev. A **69**, 052118 (2004).

[41] J. D. Cresser, A. Z. Tang, G. J. Salamo, and F. T. Chan, Phys. Rev. A **33**, 1677 (1986).

[42] V. Florescu, I. Schneider, and I. N. Mihailescu, Phys. Rev. A **38**, 2189 (1988).

[43] H. A. Bethe and E. E. Salpeter, *Quantum Mechanics of One- and Two-Electron Atoms* (Springer, Berlin, 1957).

[44] W. H. Press, B. P. Flannery, S. A. Teukolsky, and W. T. Vetterling, *Numerical Recipes in C: The Art of Scientific Computing*, 2nd ed. (Cambridge University Press, Cambridge, UK, 1993).

[45] C. E. Theodosiou, L. Armstrong, M. Crance, and F. Feneuille, Phys. Rev. A **19**, 766 (1979).

[46] J. L. F. de Meijere and J. H. Eberly, Phys. Rev. A **17**, 1416 (1978).

[47] G. S. Agarwal, S. L. Haan, K. Burnett, and J. Cooper, Phys. Rev. Lett. **48**, 1164 (1982).

[48] G. S. Agarwal, S. L. Haan, and J. Cooper, Phys. Rev. A **29**, 2552 (1984).

[49] F. Bassani, J. J. Forney, and A. Quattropani, Phys. Rev. Lett. **39**, 1070 (1977).

[50] M. G. Boshier, P. E. G. Baird, C. J. Foot, E. A. Hinds, M. D. Plimmer, D. N. Stacey, J. B. Swan, D. A. Tate, D. M. Warrington, and G. K. Woodgate, Phys. Rev. A **40**, 6169 (1989).

[51] J. H. Tung, A. Z. Tang, G. J. Salomo, and F. T. Chan, J. Opt. Soc. Am. B **3**, 837 (1986).

[52] B. de Beauvoir, C. Schwob, O. Acef, L. Jozefowski, L. Hilico, F. Nez, L. Julien, A. Clairon, and F. Biraben, Eur. Phys. J. D **12**, 61 (2000).

[53] Y. Gontier and M. Trahin, Phys. Lett. A **36**, 463 (1971).

[54] C. Cohen-Tannoudji, J. Dupont-Roc, and G. Grynberg, *Atom–Photon Interactions* (J. Wiley & Sons, New York, 1992).

[55] W. Kuhn and J. Strnad, *Quantenfeldtheorie* (Vieweg, Wiesbaden, Germany, 1995).

[56] M. Gavrila and A. Costescu, Phys. Rev. A **2**, 1752 (1970).

[57] K. Pachucki, Ann. Phys. (N.Y.) **226**, 1 (1993).

[58] U. D. Jentschura, *Bound state QED*, Lecture course, Ruprecht-Karls-Universität, Heidelberg, WS 2005/06.

[59] A. Czarnecki, U. D. Jentschura, and K. Pachucki, Phys. Rev. Lett. **95**, 180404 (2005).

[60] K. Pachucki, A. Czarnecki, U. D. Jentschura, and V. A. Yerokhin, Phys. Rev. A **72**, 022108 (2005).

[61] D. H. Kobe, J. Phys. B **16**, 1159 (1983).

[62] S. Salomonson and P. Öster, Phys. Rev. A **40**, 5559 (1989).

[63] V. Yakhontov, Phys. Rev. Lett. **91**, 093001 (2003).

[64] R. A. Swainson and G. W. F. Drake, J. Phys. A **24**, 79 (1991).

[65] R. A. Swainson and G. W. F. Drake, J. Phys. A **24**, 95 (1991).

[66] R. A. Swainson and G. W. F. Drake, J. Phys. A **24**, 1801 (1991).

[67] A. R. Edmonds, *Angular Momentum in Quantum Mechanics* (Princeton University Press, Princeton, NJ, 1957).

[68] J. J. Sakurai, *Modern Quantum Mechanics* (Addison-Wesley, Reading, MA, 1994).

[69] P. J. Mohr, G. Plunien, and G. Soff, Phys. Rep. **293**, 227 (1998).

[70] U. D. Jentschura and C. H. Keitel, Ann. Phys. (N.Y.) **310**, 1 (2004).

[71] K. Pachucki, J. Phys. B **31**, 5123 (1998).

[72] B. R. Holstein, Am. J. Phys. **72**, 333 (2004).

[73] H. Bateman, *Higher Transcendental Functions* (McGraw-Hill, New York, NY, 1953), Vol. 1.

[74] J. C. Garreau, M. Allegrini, L. Julien, and F. Biraben, J. Phys. (France) **51**, 2263 (1990).

[75] J. C. Garreau, M. Allegrini, L. Julien, and F. Biraben, J. Phys. (France) **51**, 2293 (1990).

[76] B. de Beauvoir, C. Schwob, O. Acef, L. Jozefowski, L. Hilico, F. Nez, L. Julien, A. Clairon, and F. Biraben, Eur. Phys. J. D **12**, 61 (2000).

[77] Ch. Gohle, Th. Udem, M. Herrmann, J. Rauschenberger, R. Holzwarth, H. A. Schuessler, F. Krausz, and T. W. Hänsch, Nature (London) **436**, 234 (2005).

[78] S. Wolfram, *Mathematica - A System for Doing Mathematics by Computer* (Addison-Wesley, Reading, MA, 1988).

[79] J. C. de Vries, *A precision millimeter-wave measurement of the Rydberg frequency*, PhD thesis, MIT Report 658 (2002).

[80] U. D. Jentschura, E.-O. Le Bigot, J. Evers, P. J. Mohr, and C. H. Keitel, J. Phys. B **38**, S97 (2005).

[81] M. Stobbe, Ann. Phys. (Leipzig) **7**, 661 (1930).

[82] S. A. Lee, *Measurement of the ground state Lamb shift of atomic hydrogen and deuterium by laser spectroscopy*, PhD thesis, Stanford University, M. L. Report No. 2460 (1975).

[83] W. E. Caswell and G. P. Lepage, Phys. Lett. B **167**, 437 (1986).

[84] L. L. Foldy and S. A. Wouthuysen, Phys. Rev. **78**, 29 (1950).

[85] J. J. Sakurai, *Advanced Quantum Mechanics* (Addison-Wesley, Reading, MA, 1967).

[86] D. Hestenes, Found. Phys. **20**, 1213 (1990).

[87] U. D. Jentschura, Phys. Rev. A **70**, 052108 (2004).

[88] K. Pachucki and U. D. Jentschura, Phys. Rev. Lett. **91**, 113005 (2003).

[89] I. S. Gradshteyn and I. M. Ryzhik, *Table of Integrals, Series, and Products* (Academic Press, New York, 1980).

[90] V. Gates, E. Kangaroo, M. Roachcock, and W. C. Gall, Physica D **15**, 289 (1985).

[91] J. Evers, U. D. Jentschura, and C. H. Keitel, Phys. Rev. A **70**, 062111 (2004).

[92] C. Cohen-Tannoudji, in *Aux frontières de la spectroscopie laser/Frontiers in Laser Spectroscopy*, edited by R. Balian, S. Haroche, and S. Liberman (North-Holland, Amsterdam, 1975), pp. 4–104.

[93] B. R. Mollow, Phys. Rev. **188**, 1969 (1969).

[94] U. D. Jentschura, J. Evers, M. Haas, and C. H. Keitel, Phys. Rev. Lett. **91**, 253601 (2003).

[95] K. S. E. Eikema, J. Walz, and T. W. Hänsch, Phys. Rev. Lett. **86**, 5679 (2001).

[96] M. Niering, *Doppler-freie Zweiphotonen-Spektroskopie an atomarem Wasserstoff*, PhD thesis, MPQ Report 252 (2000).

[97] M. Abgrall, *Evaluation des performances de la fontaine atomique PHARAO, participation à l'étude de l'horloge spatiale PHARAO*, PhD thesis, Université Paris VI (2003).

[98] G. Scoles, D. Bassi, U. Buck, and D. C. Lainé, *Atomic and Molecular Beam Methods* (Oxford University Press, New York, 1988), Vol. I.

[99] M. Fischer, N. Kolachevsky, S. G. Karshenboim, and T. W. Hänsch, Can. J. Phys. **80**, 1225 (2002).

[100] H. Kogelnik and T. Li, Proc. IEEE **54**, 1312 (1966).

[101] MTR Software, http://www.fitall.com.

[102] A. Huber, *Höchstauflösende Präzisionsspektroskopie am atomaren Wasserstoff*, PhD thesis, MPQ Report 227 (1997).

[103] J. Honerkamp, *Statistical Physics* (Springer, Berlin, 2002).

[104] P. A. M. Dirac, Nature (London) **139**, 323 (1937).

[105] W. J. Marciano, Phys. Rev. Lett. **52**, 489 (1984).

[106] E. Witten, Nucl. Phys. B **186**, 412 (1981).

[107] A. Chodos and S. Detweiler, Phys. Rev. D **21**, 2167 (1980).

[108] M. T. Murphy, J. K. Webb, and V. V. Flambaum, Mon. Not. Roy. Astron. Soc. **345**, 609 (2003).

[109] V. A. Dzuba, V. V. Flambaum, and J. K. Webb, Phys. Rev. A **59**, 230 (1999).

[110] A. I. Shlyakhter, Nature (London) **264**, 340 (1976).

[111] T. Damour and F. Dyson, Nucl. Phys. B **480**, 37 (1996).

[112] M. Fischer, N. Kolachevsky, M. Zimmermann, R. Holzwarth, Th. Udem, T. W. Hänsch, M. Abgrall, J. Grünert, I. Maksimovic, S. Bize, H. Marion, F. Pereira Dos Santos, P. Lemonde, G. Santarelli, P. Laurent, A. Clairon, C. Salomon, M. Haas, U. D. Jentschura, and C. H. Keitel, Phys. Rev. Lett. **92**, 230802 (2004).

[113] M. Herrmann, Th. Udem, and T. W. Hänsch, private communication.

Thanks

I would like to thank first of all Christoph H. Keitel for the assignment of the thesis subject and the excellent working conditions, which you provided both in the Nachwuchsgruppe in Freiburg and in your research group at the Max–Planck–Institut in Heidelberg. Your continued encouragement and support for my projects, which somewhat moved away from the original ideas, was and is very important for me.

To Ulrich D. Jentschura I want to express my sincerest gratitude for the very intensive supervision during the whole PhD project, and the enthusiasm with which you introduced me to high-precision physics. Without your personal commitment and support, both the theory and the cooperation with the experimentalist group at the MPQ would not have progressed to the present state.

Also I would like to thank both Christoph H. Keitel and Ulrich D. Jentschura for helping me overcome my slight reluctance for giving presentations on conferences. I would have missed a great deal of interesting and exciting physics and places!

I am very much obliged to Theodor W. Hänsch and Thomas Udem for letting me take part in the exciting hydrogen spectroscopy project and for many lively and fruitful discussions, both at a distance and at our various meetings. Nikolai N. Kolachevsky and Marc Fischer I would like to thank for the long and fruitful cooperation, and the patience with which you explained me the many details of your sophisticated setup. Many thanks also to Maximilian Herrmann, Peter Fendel and Markus Zimmermann, I enjoyed many a pleasant and productive time with you.

To all my other colleagues and friends, both from Freiburg and Heidelberg, I would like to say "thank you" for many things which I cannot all list here. With Jörg Evers, Mario Verschl, Martin Kiffner, Robert Fischer and Peter Orth, I was happy to have very nice and sociable roommates, and together with you and Andreas Staudt, Guido Mocken, Mihai Macovei, Alexander Eisfeld, Jens Götz, Mark Santer, Stefan Pieper, Matthias Ruf, Martina Weizmann and Carsten Müller, I spent quiz nights, happy hours, movie sessions, "Adventskaffees", and more the like.

What would a theorist do today without a reliable computing environment? Thanks to Peter Brunner and Rainer Heintzmann, I did not need to worry about the hardware and software which actually did all the work performing my simulations.

My most personal thanks go to my parents, my sisters, my brother and my beloved Elisabeth. Thank you for always being a safe haven for me and for cheering me up, when at times my road was gloomy and difficult. Especially I thank you, Elisabeth, for supporting my move to Heidelberg in the middle of my PhD project, while you had to remain in Freiburg.